

AFRL-PR-WP-TR-2006-2176

**HIGH TEMPERATURE PROPERTIES
AND AGING-STRESS RELATED
CHANGES OF FeCo MATERIALS**



**John Horwath
Zafer Turgut
Richard Fingers**

**Power Generation Branch (AFRL/PRPG)
Power Division
Propulsion Directorate
Air Force Materiel Command, Air Force Research Laboratory
Wright-Patterson Air Force Base, OH 45433-7251**

JULY 2006

Final Report for 01 October 2001 – 30 May 2006

Approved for public release; distribution is unlimited.

STINFO COPY

**PROPULSION DIRECTORATE
AIR FORCE MATERIEL COMMAND
AIR FORCE RESEARCH LABORATORY
WRIGHT-PATTERSON AIR FORCE BASE, OH 45433-7251**

NOTICE AND SIGNATURE PAGE

Using Government drawings, specifications, or other data included in this document for any purpose other than Government procurement does not in any way obligate the U.S. Government. The fact that the Government formulated or supplied the drawings, specifications, or other data does not license the holder or any other person or corporation; or convey any rights or permission to manufacture, use, or sell any patented invention that may relate to them.

This report was cleared for public release by the Air Force Research Laboratory Wright Site (AFRL/WS) Public Affairs Office and is available to the general public, including foreign nationals. Copies may be obtained from the Defense Technical Information Center (DTIC) (<http://www.dtic.mil>).

AFRL-PR-WP-TR-2006-2176 HAS BEEN REVIEWED AND IS APPROVED FOR PUBLICATION IN ACCORDANCE WITH ASSIGNED DISTRIBUTION STATEMENT.

*/Signature/

John C. Horwath
Electrical Engineer
Power Division

//Signature//

Paul N. Barnes
Acting Branch Chief
Power Division

//Signature//

Kirk L. Yerkes, Ph.D.
Deputy for Science
Power Division

This report is published in the interest of scientific and technical information exchange, and its publication does not constitute the Government's approval or disapproval of its ideas or findings.

Disseminated copies will show “/Signature/” stamped or typed above the signature blocks.

REPORT DOCUMENTATION PAGE					Form Approved OMB No. 0704-0188	
<p>The public reporting burden for this collection of information is estimated to average 1 hour per response, including the time for reviewing instructions, searching existing data sources, gathering and maintaining the data needed, and completing and reviewing the collection of information. Send comments regarding this burden estimate or any other aspect of this collection of information, including suggestions for reducing this burden, to Department of Defense, Washington Headquarters Services, Directorate for Information Operations and Reports (0704-0188), 1215 Jefferson Davis Highway, Suite 1204, Arlington, VA 22202-4302. Respondents should be aware that notwithstanding any other provision of law, no person shall be subject to any penalty for failing to comply with a collection of information if it does not display a currently valid OMB control number. PLEASE DO NOT RETURN YOUR FORM TO THE ABOVE ADDRESS.</p>						
1. REPORT DATE (DD-MM-YY) July 2006		2. REPORT TYPE Final		3. DATES COVERED (From - To) 10/01/2001 – 05/30/2006		
4. TITLE AND SUBTITLE HIGH TEMPERATURE PROPERTIES AND AGING-STRESS RELATED CHANGES OF FeCo MATERIALS				5a. CONTRACT NUMBER In-house		
				5b. GRANT NUMBER		
				5c. PROGRAM ELEMENT NUMBER 62203F		
6. AUTHOR(S) John Horwath Zafer Turgut Richard Fingers				5d. PROJECT NUMBER 3145		
				5e. TASK NUMBER 01		
				5f. WORK UNIT NUMBER CD		
7. PERFORMING ORGANIZATION NAME(S) AND ADDRESS(ES) Power Generation Branch (AFRL/PRPG) Power Division Propulsion Directorate Air Force Materiel Command, Air Force Research Laboratory Wright-Patterson Air Force Base, OH 45433-7251				8. PERFORMING ORGANIZATION REPORT NUMBER AFRL-PR-WP-TR-2006-2176		
9. SPONSORING/MONITORING AGENCY NAME(S) AND ADDRESS(ES) Propulsion Directorate Air Force Research Laboratory Air Force Materiel Command Wright-Patterson AFB, OH 45433-7251				10. SPONSORING/MONITORING AGENCY ACRONYM(S) AFRL-PR-WP		
				11. SPONSORING/MONITORING AGENCY REPORT NUMBER(S) AFRL-PR-WP-TR-2006-2176		
12. DISTRIBUTION/AVAILABILITY STATEMENT Approved for public release; distribution is unlimited.						
13. SUPPLEMENTARY NOTES PAO case number: AFRL/WS 06-1683; Date cleared: 07 Jul 2006.						
14. ABSTRACT This publication focuses on high temperature magnetic, mechanical, and electrical properties of three Fe-Co alloys intended for use in high stress and high temperature environments. The specific alloys of interest are Hiperc® Alloy 27, Hiperc® Alloy 50 and Hiperc® Alloy 50 HS. Aging related changes in magnetic, mechanical, and electrical performance throughout the material's lifetime are documented. The effect of compressive and tensile stresses that may originate from product assembly and rotational forces during operation was also studied. Information contained in this publication is only specific to the alloys with given annealing conditions since magnetic and mechanical properties depend greatly on the annealing conditions performed after cold deformation. However, absence of any grain growth during 500 °C aging up to 5,000 hours indicates that the observed trends should be representative for the same alloy compositions with different annealing histories.						
15. SUBJECT TERMS soft magnetic materials, iron cobalt laminates, aging studies						
16. SECURITY CLASSIFICATION OF:			17. LIMITATION OF ABSTRACT: SAR	18. NUMBER OF PAGES 134	19a. NAME OF RESPONSIBLE PERSON (Monitor) John Horwath 19b. TELEPHONE NUMBER (Include Area Code) N/A	
a. REPORT Unclassified	b. ABSTRACT Unclassified	c. THIS PAGE Unclassified				

Table of Contents

Section	Page
Preface.....	iv
1. Introduction	1
2. FeCo Alloy System	3
3. Aging and Related Property Changes	7
3.1 Magnetic Properties	8
3.2 Mechanical Properties	52
3.3 Electrical Properties	67
3.4 Microstructure.....	72
4. Effect of Stress on Magnetic Properties.....	78
4.1 Effect of Tensile Stress.....	78
4.1.1 DC Magnetic Properties Under Tensile Stress	80
4.1.2 Core Losses Under Tensile Stress.....	82
4.2 Effect of Compressive Stress.....	110
4.2.1 DC Magnetic Properties Under Compressive Stress	111
4.2.2 Core Losses Under Compressive Stress	114
5. Summary	124
6. References.....	125

PREFACE

This publication focuses on high temperature magnetic, mechanical, and electrical properties of three Fe-Co alloys intended for use in high stress and high temperature environments. The specific alloys of interest are Hiperco[®] Alloy 27, Hiperco[®] Alloy 50 and Hiperco[®] Alloy 50HS, which are commercially available from Carpenter Specialty Alloys. A great amount of effort was spent on determining the aging related changes in magnetic, mechanical, and electrical performance throughout the material's lifetime. The effect of compressive and tensile stresses that are mainly originated from product assembly and rotational forces during operation was also studied and documented. Where relevant, results of a literature search were incorporated into this study to explain the mechanisms behind the observed trends. These studies were conducted as part of an in-house research effort under the Power Generation Branch (PRPG) of the Power Division (PR) at AFRL.

While the related research efforts to develop materials with better performance at high temperature, high stress environments are being pursued; it is the goal of this study to provide a thorough performance analysis on the existing Fe-Co materials within the desired operation environment and the anticipated lifetime. A description of the temperature dependent magnetic, mechanical, and electrical performance throughout the material's lifetime would be of great value to the designers of high temperature electromachines. A thorough understanding of the corresponding degradation mechanisms may lead new alloy designs.

Information contained in this publication is only specific to the alloys with given annealing conditions since magnetic and mechanical properties depend greatly on the annealing conditions performed after cold deformation. However, absence of any grain growth during 500 ° C aging up to 5000 hours indicates that the observed trends should be representative for the same alloy compositions with different annealing histories.

CHAPTER I

Introduction

As the demand for energy savings and miniaturized devices continues to accelerate, the Air Force need for high-power-density power generation capabilities has dictated the utilization of advanced soft magnetic materials in high temperature, high stress environments. Development and utilization of these highly functional materials will increase military aircraft reliability, maintainability, and supportability and drastically reduce the need for ground support equipment. This advancement will be accomplished through the continued development of magnetic bearings as well as aircraft Integrated Power Units and Internal Starter/Generators for main propulsion engines. These key technologies are the driving force for the new emphasis on the development of high temperature magnets. Current power generation systems for airborne applications such as starter and generator components of the aircraft engines utilize FeCo based soft magnetic alloys. Despite the fact that these classes of alloys have relatively higher magnetic losses than many in this category, they have the best performance in terms of combined temperature-induction-mechanical capabilities. Some of these advanced applications require the soft magnetic Fe-Co materials to be stable at temperatures as high as 500 °C in a 0.15-mm thick laminate configuration. Hence, they must be capable of maintaining structural integrity in a high stress and high temperature environment for the anticipated life of the component. This temperature range and the anticipated lifetime may be sufficiently high enough for aging related property changes. Among the other properties, creep resistance and yield strength become the most important material properties due to the high temperatures and high rotational forces.

The manufacturer generally provides Fe-Co in the form of cold rolled sheets. Therefore, a post-cold deformation annealing is always necessary to develop a stress free microstructure and good magnetic properties at the expense of the mechanical strength of the material. This annealing is usually performed at or above the order-disorder phase transformation temperature of the FeCo alloys. The desired properties (mechanical versus magnetic) determine the annealing time and temperature, and a slow cooling to room temperature is necessary to obtain an ordered structure for optimum magnetic properties. Material suppliers typically specify only the room temperature properties, and only a few reports have been published on the properties at elevated temperatures. Little information was found relating to high temperature performance as a function of time.

The remaining parts of this report are organized as follows:

Chapter II provides brief, general information on the FeCo alloy system and properties of the alloys of interest.

Chapter III is designated for high temperature aging and related changes in a material's magnetic, electrical and mechanical properties. Data on specimens aged at 500 ° C up to 5000 hours under air and argon atmospheres are documented. Specimen preparation and procedures are also included.

Chapter IV focuses on the effect of compressive and tensile stress on magnetic properties. Changes in DC magnetic properties as well as total magnetic losses are given in a stress window of –25.7 MPa to 200 MPa at room temperature.

Chapter V presents the conclusions of this work as a whole.

CHAPTER II

FeCo Alloy System

The technical importance of FeCo alloys arises from their high saturation magnetization and high Curie temperature, which can not be matched by any other alloy system. The high saturation magnetization of up to 2.4 T and the Curie temperature of about 950 °C are characteristics for the FeCo alloys with compositions 25-50 % Co. The FeCo phase diagram is shown in Figure 2.1. Maximum saturation magnetization occurs at about 35 % Co. The permeability of Fe-Co alloys exhibits considerable variation with composition. Alloys near equiatomic compositions are particularly soft and exhibit large permeabilities (Figure 2.2) [2.1], which can be attributed to a zero crossing of the first order magnetic anisotropy constant, K_1 , near this composition (Figure 2.3) [2.2].

Alloys in the composition range of about 30% - 70% Co undergo a continuous (i.e. higher than first order) order-disorder phase transformation at a maximum temperature of 730 °C at the equiatomic composition. The change in the structure from the disordered α -bcc (*A1*) to the ordered α' -CsCl (*B2*) appears as a λ type anomaly in the heat temperature spectra. Compositional dependence of this order-disorder transformation of bulk Fe-Co alloys is well established by specific heat measurements [2.3], thermal analysis [2.4] and neutron diffraction [2.5]. Deviations from the equiatomic composition results in a decrease in the order-disorder transformation temperature and the transformation exist over a considerable range in both sides of the stoichiometric composition. The transformation also reflects itself as a small change in saturation magnetization (~4 %) and no satisfactory explanation had been made until the proper neutron diffraction measurements were conducted by Collins and Forsyth [2.6]. They found that upon ordering, the atomic moments of Fe increased from 2.2 μ_B in pure Fe to over 3.0 μ_B in alloys of 50 at. % or more Co while the atomic moments on Co remained unchanged. The increase in μ_{Fe} is ascribed to a change in the nearest neighbor coordination of Fe atoms. Ordering brings Co atoms into the environment of each Fe atom at the maximum number.

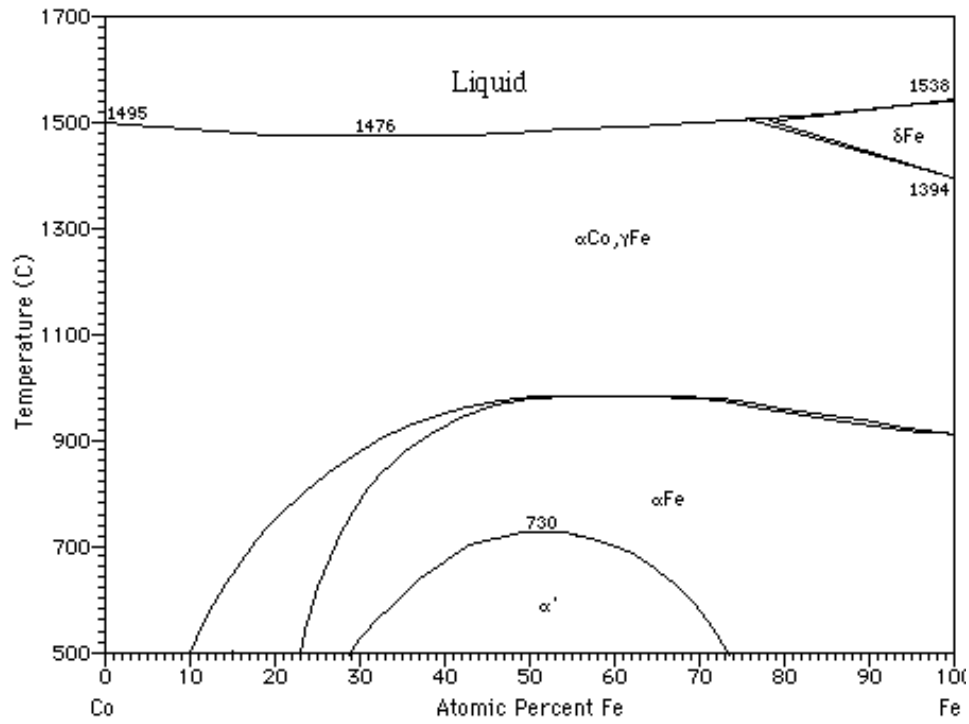


Figure 2.1 Fe-Co phase diagram showing fields for the γ -(fcc), α -(bcc) and α' -(CsCl) phases (produced using TAPP @TM software, ES Microware)

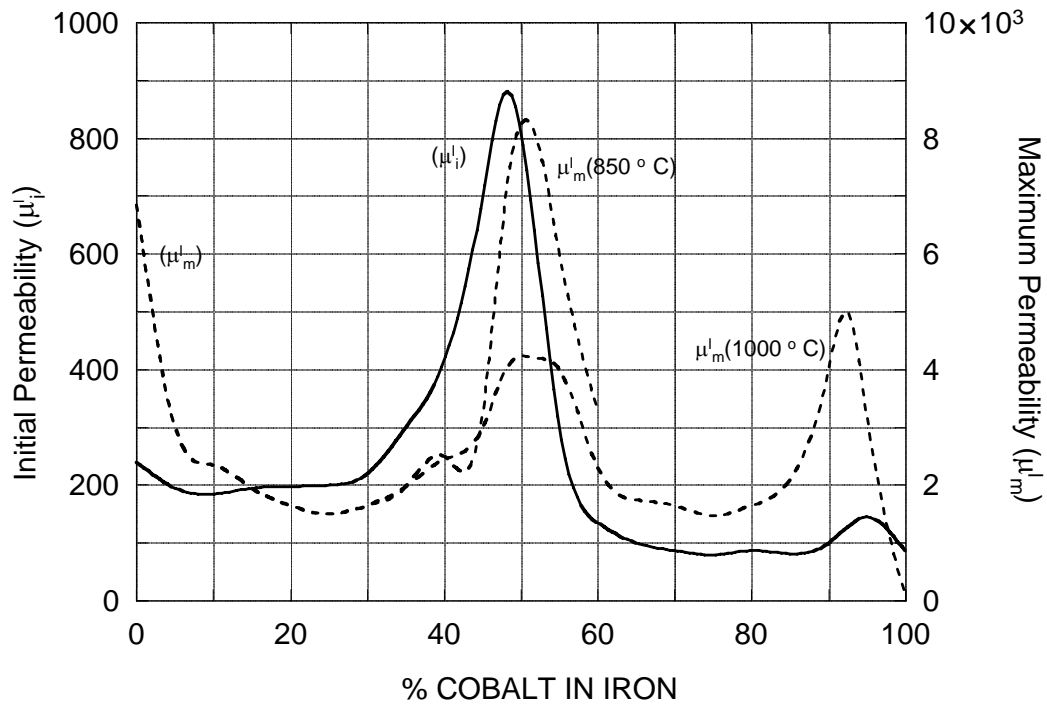


Figure 2.2 Initial and maximum relative permeabilities of the Fe-Co alloys [2.1]

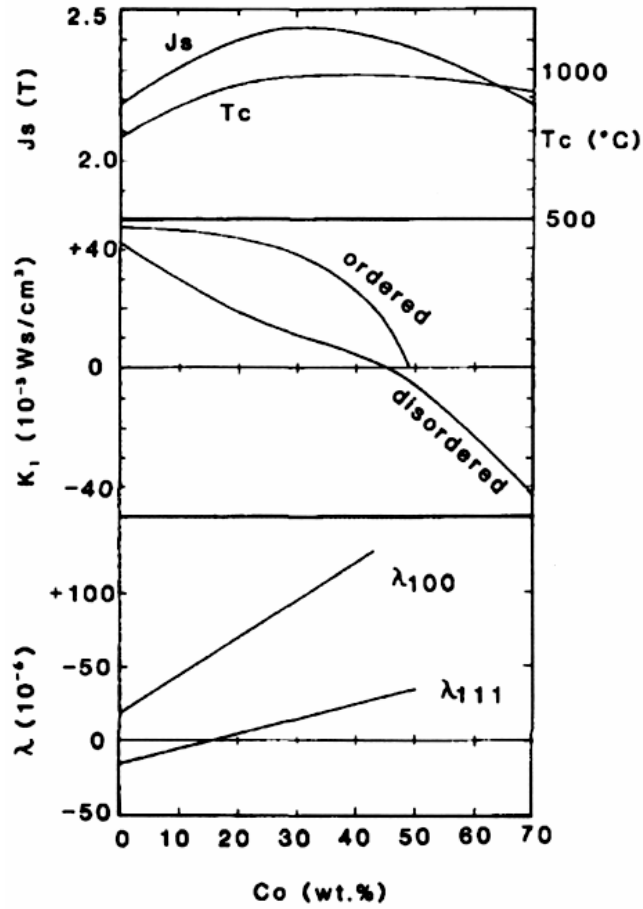


Fig. 2.3 Compositional dependence of Saturation magnetization, Curie temperature and basic magnetic constants K_1 and λ in the Fe-Co system [2.2]

Besides the mentioned magnetic properties, ordered FeCo alloys show poor cold-workability and lower resistivity values, which are important parameters in fabrication and operational purposes. This problem is solved by introducing a third alloying element such as V, Nb, Mo, W, Ti, Ta. Among those, alloys containing 2 at. % vanadium found great deal of applications. Vanadium suppresses the ordering and increases the resistivity of the system. Table I gives chemical compositions and some basic physical properties of the Hipercor alloys that are subject of this study.

Table I. Chemical compositions (in wt %) and physical properties of Hiperco alloys

ALLOY	CHEMICAL ANALYSIS									$T_{\alpha \rightarrow \gamma}$ (° C)	$T_{\text{order} \rightarrow \text{disorder}}$ (° C)	Density g/cm ³	λ_s
	C	Mn	Si	Co	V	Nb	Ni	Cr	Fe				
HIPERCO 27	0.01	0.25	0.25	27.0	—	—	0.6	0.6	Bal.	976	N/A	7.95	36×10^{-6}
HIPERCO 50	0.01	0.05	0.05	48.75	1.9	0.05	—	—	Bal.	984	730	8.12	—
HIPERCO 50 HS	0.01	0.05	0.05	48.75	1.9	0.3	—	—	Bal.	984	730	8.12	60×10^{-6}

CHAPTER III

Aging and Related Property Changes

Aging is a well known metallurgical phenomenon in which the interstitial atoms that are dissolved in a lattice at concentrations in excess of their equilibrium values slowly precipitate out if a driving force for such transformation is present. It is commonly used for precipitation hardening that enhances the mechanical strength in a variety of systems. In soft magnetic materials, however, this slow precipitation process deteriorates the magnetic properties by hindering the domain wall motion. As a result, permeability values are reduced while the coercivities are increased since those values are primarily dependent on the impurities and amount of grain boundaries that act as pinning sites for the domain wall motion. Along with the magnetocrystalline anisotropy of the system, internal stress created by formation of these precipitates may also generate a stress-induced anisotropy and effects on the permeability and coercivity.

Elimination of cooling systems and higher rotational speeds for miniaturization and improved efficiency always translate to a higher operating temperature for soft magnetic cores. The necessary rotor speeds and temperatures require a high strength magnetic material capable of sustained integrity in a high temperature environment. Rapidly changing magnetic flux with higher speeds increases the core losses in the form of Joule heating. While materials' softness benefits from increased temperatures, the attainable magnetic induction for a given applied field diminishes. The temperature dependence of magnetization for any magnetic system is an intrinsic property therefore it can be factored out while designing such systems if a sufficient magnetic induction is present for the desired temperature. Materials' electrical resistivity also benefits from increased temperatures. Increased resistivities help to reduce the eddy current component of the total power losses. A material's yield stress and creep resistance, however, suffer at elevated temperatures creating serious functionality problems.

Except the Curie temperature, all the properties mentioned above are extrinsic in nature and strongly depend on the microstructural characteristics of the materials. Hence, these properties can be tailored precisely by employing a variety of metallurgical tools. However, simultaneous realization of those properties in a single magnetic system is difficult; instead, an optimum is reached at the expense of one property for another. One question remaining is the stability of the final microstructure under given operation conditions.

3.1. Magnetic Properties

Prior to aging, cut specimens were heat-treated in a dry hydrogen atmosphere at 730°C for 45 minutes, followed by cooling to room temperature at a rate of 177 ° C/hour. Test specimens prepared for magnetic, electrical and mechanical testing subsequently underwent an aging at 500 ° C for up to 5000 hours under argon and air environments. The specimens were pulled out at intervals of 100 hours, 1000 hours, 2000 hours and 5000 hours for testing. The sole purpose of the aging in air environment was to determine the corrosion resistance of the alloys of interest. We report only mechanical properties of the air aged specimens. The rest of the data in this chapter was taken on specimens aged in an argon chamber.

Figure 3.1.1 gives the coercivity change of the three alloys over the 5000 hours aging. Total core loss values are given figures 3.1.2 through 3.1.83 at three induction levels (13-16 and 19 kG) for frequencies of 400, 500, 700, 1000, 1500 and 2000 hertz. The core loss data covers 0, 100, 1000, 2000, and 5000 hour aging intervals, and performance of these materials from room temperature up to 500 ° C.

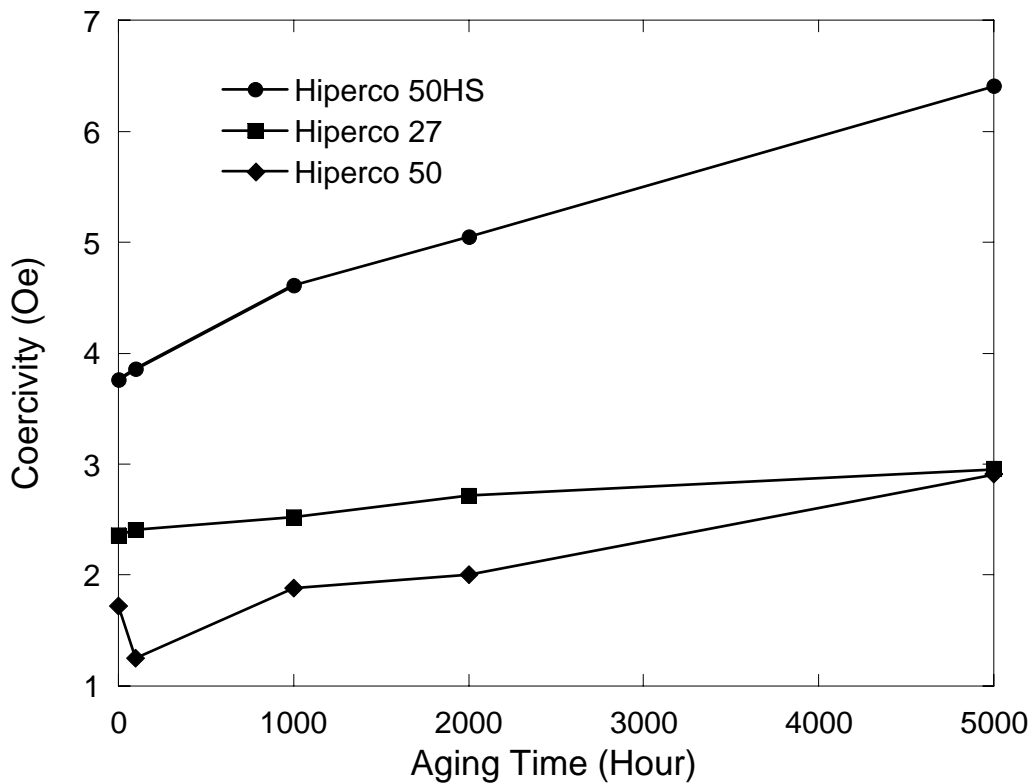


Figure 3.1.1 Coercivity change of Hiperco alloys vs aging at 500 ° C.

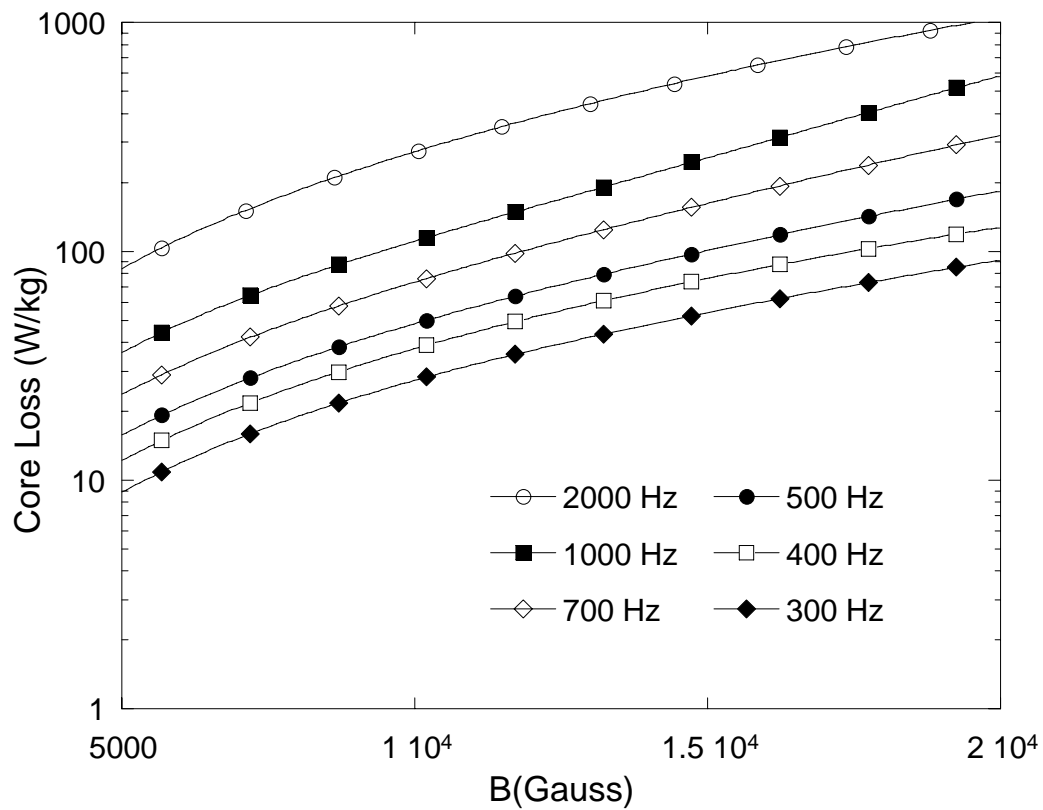


Figure 3.1.2 Core losses of unaged Hipercro 27 alloy taken at room temperature

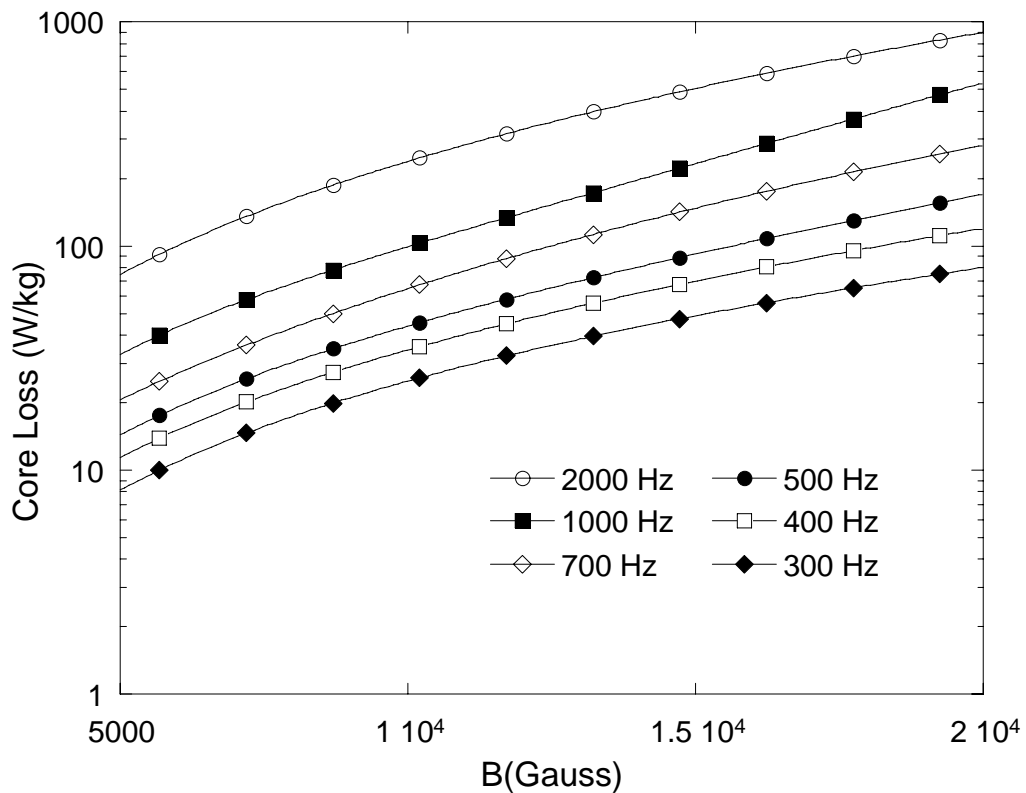


Figure 3.1.3 Core losses of unaged Hipercro 27 alloy taken at 200 °C

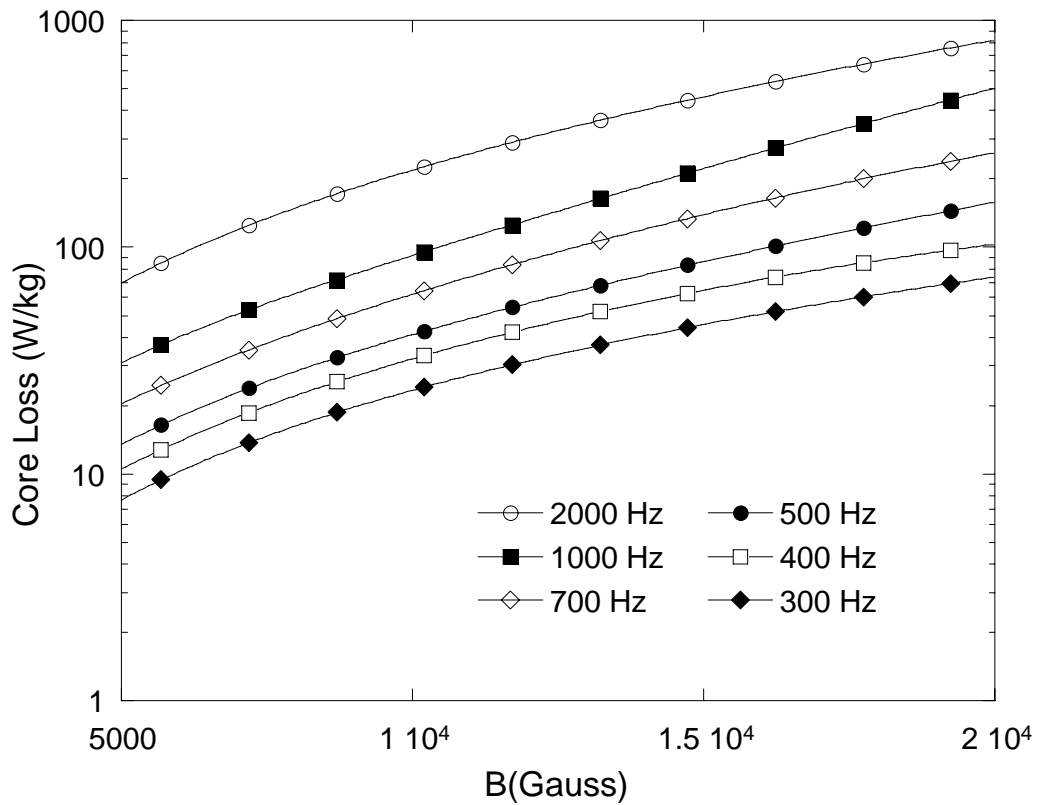


Figure 3.1.4 Core losses of unaged Hipercro 27 alloy taken at 300 ° C

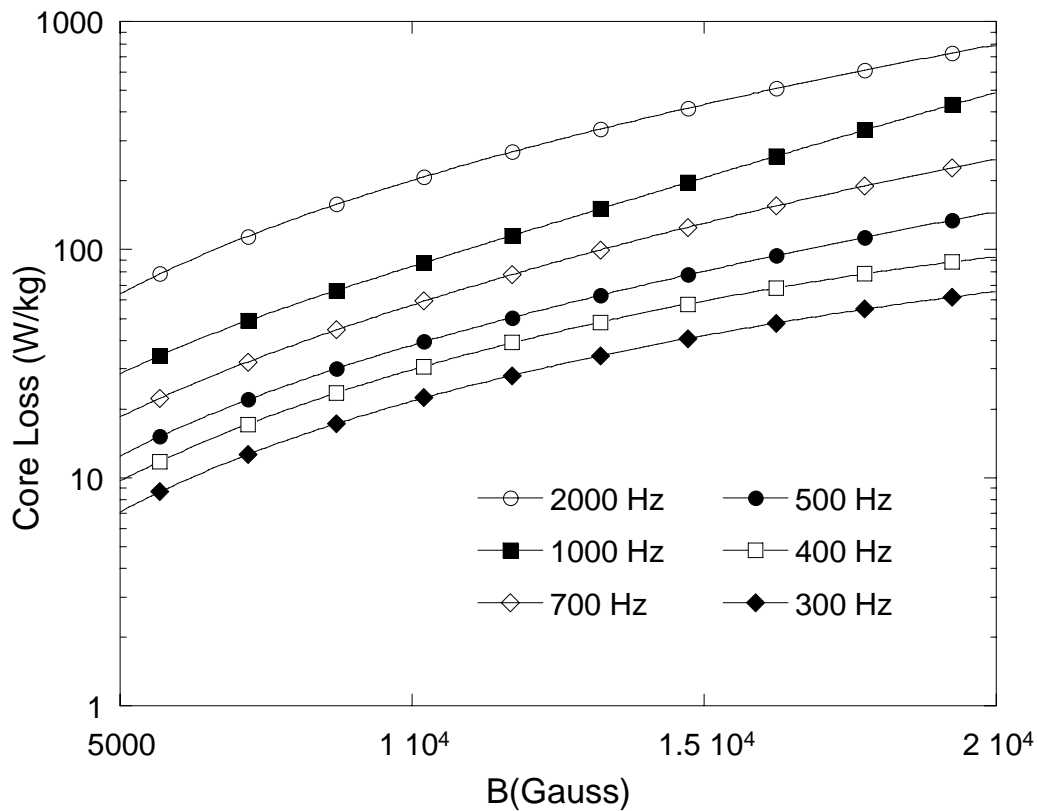


Figure 3.1.5 Core losses of unaged Hipercro 27 alloy taken at 400 ° C

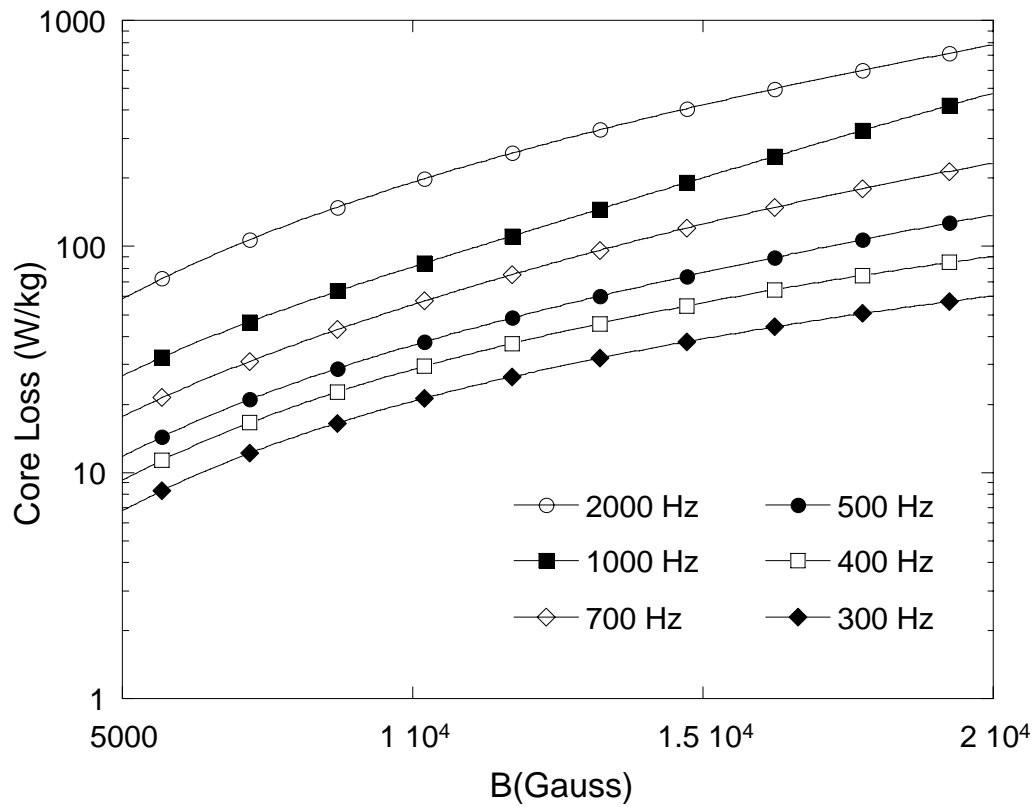


Figure 3.1.6 Core losses of unaged Hipercro 27 alloy taken at 500 ° C

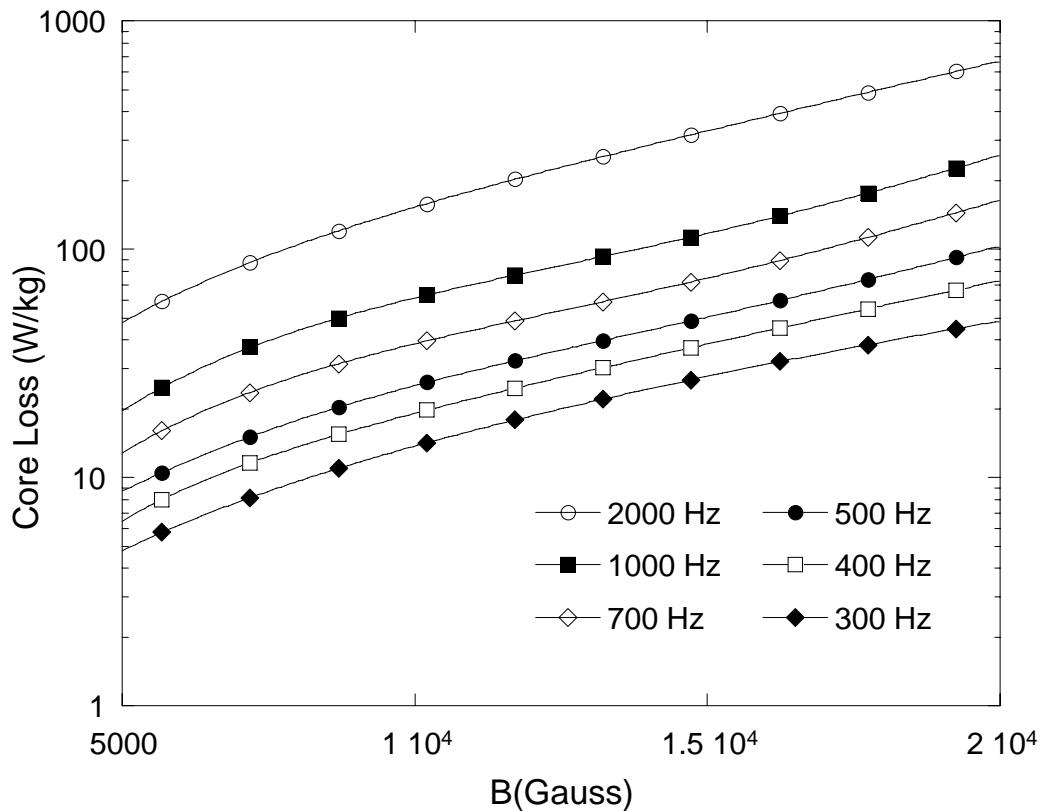


Figure 3.1.7 Core losses of unaged Hipercro 50 alloy taken at room temperature

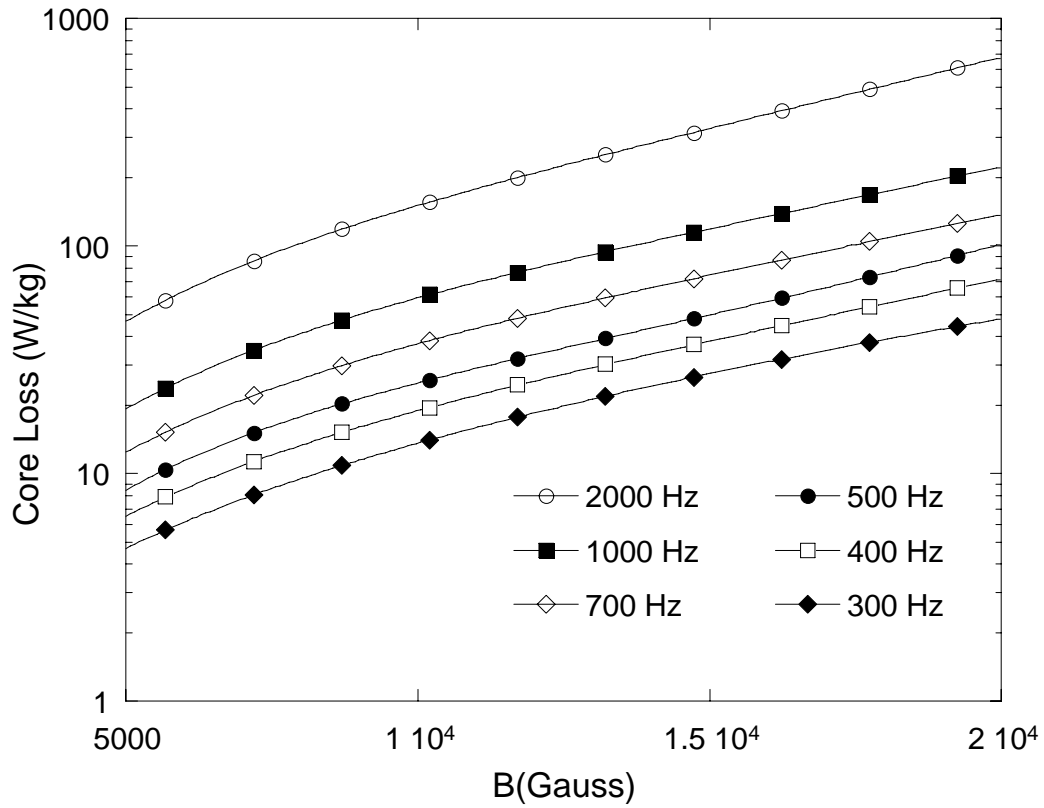


Figure 3.1.8 Core losses of unaged Hipercro 50 alloy taken at 100°C

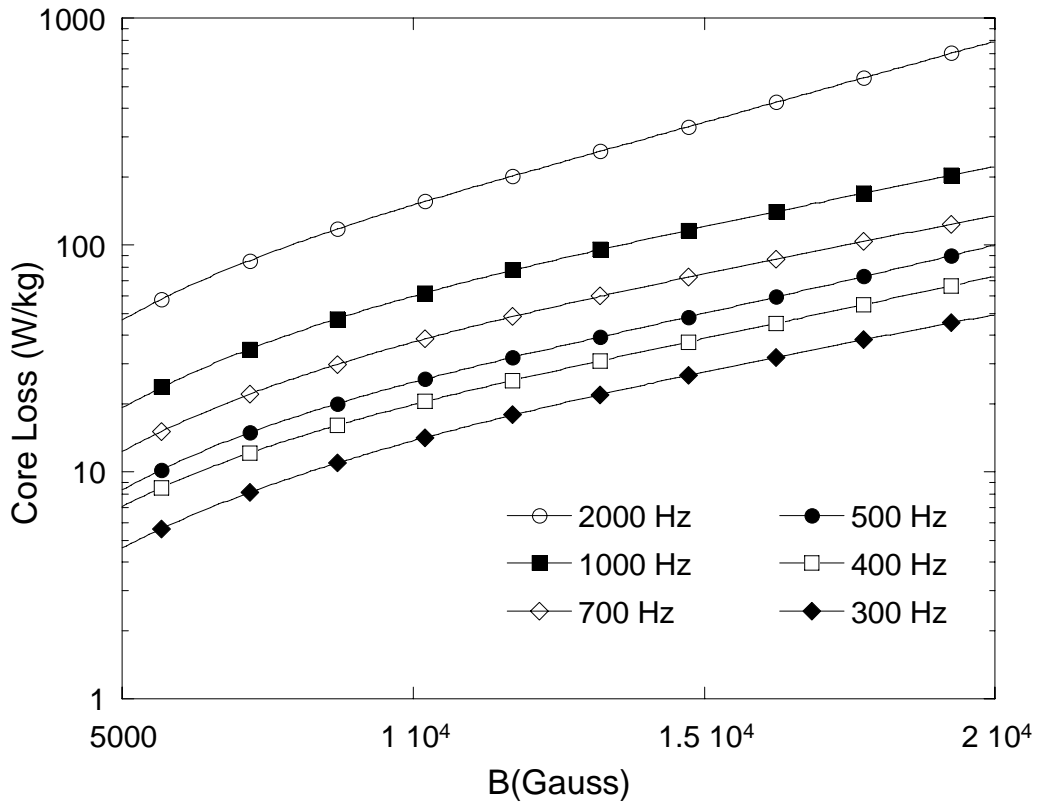


Figure 3.1.9 Core losses of unaged Hipercro 50 alloy taken at 200°C

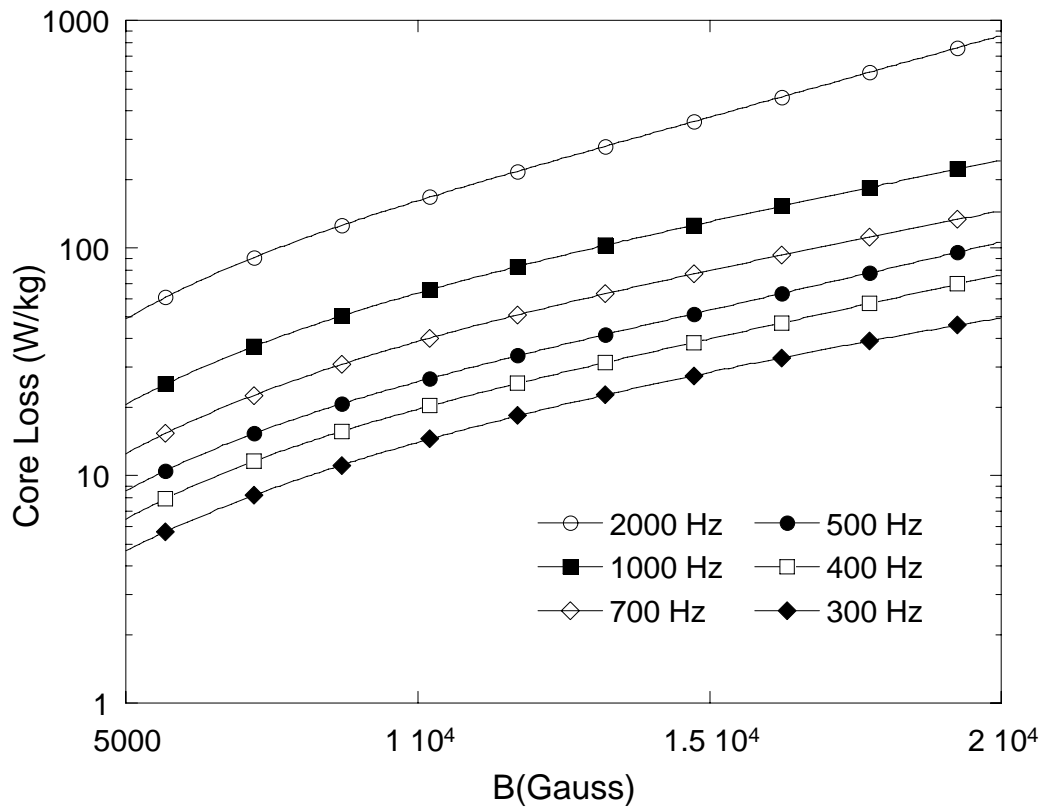


Figure 3.1.10 Core losses of unaged Hipercro 50 alloy taken at 300°C

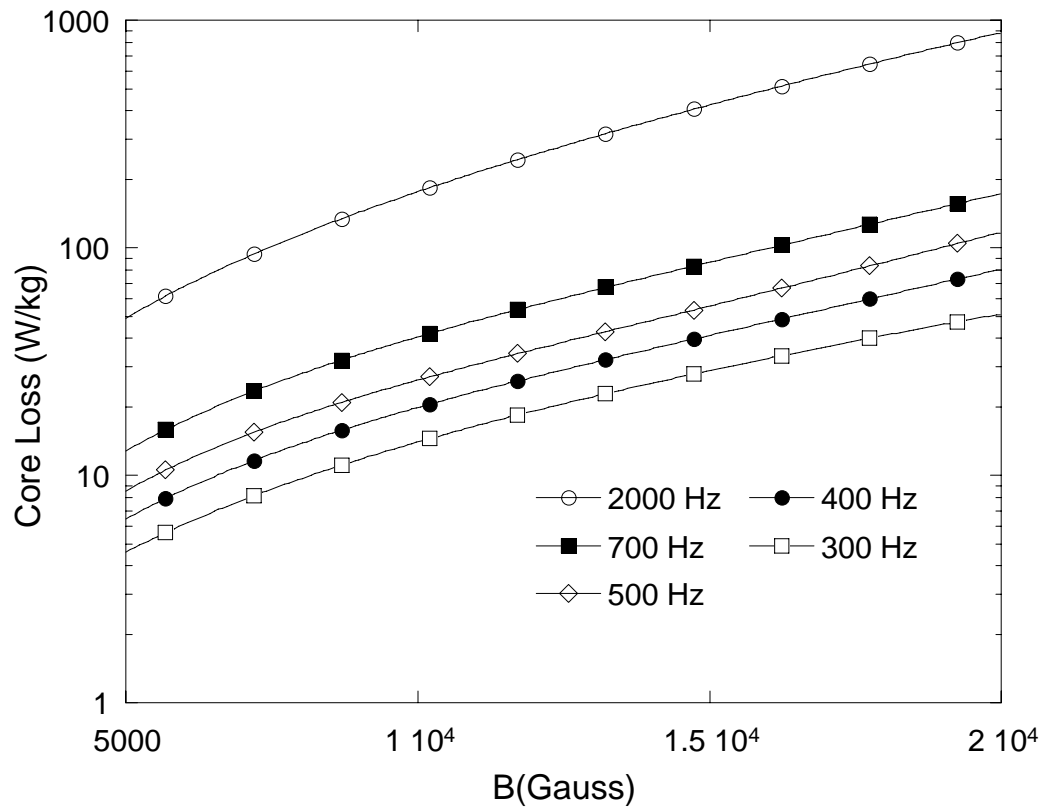


Figure 3.1.11 Core losses of unaged Hipercro 50 alloy taken at 400°C

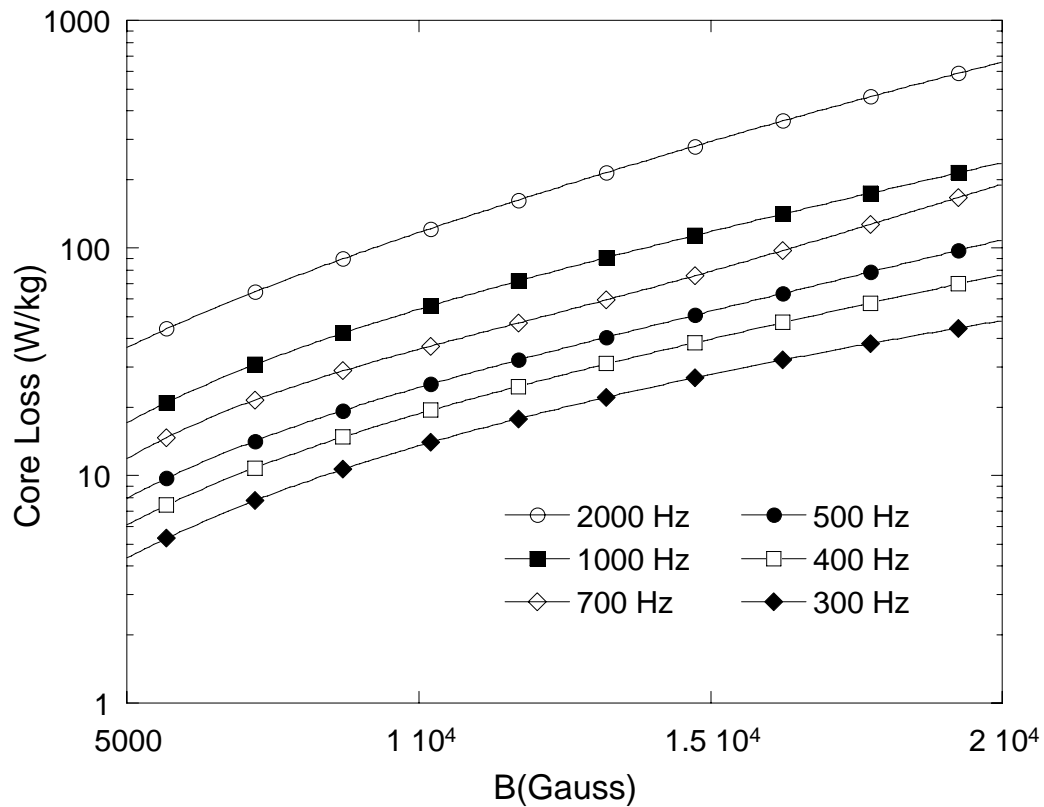


Figure 3.1.12 Core losses of unaged Hiperc 50 alloy taken at 500 ° C

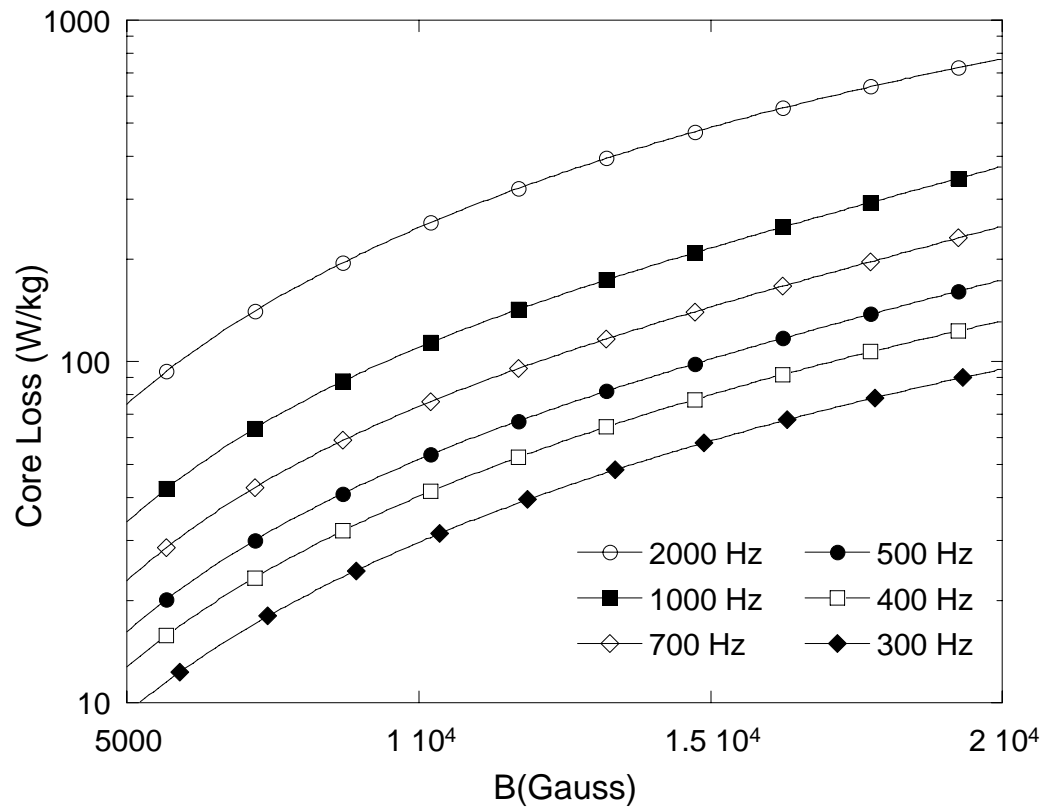


Figure 3.1.13 Core losses of unaged Hiperc 50HS alloy taken at room temperature

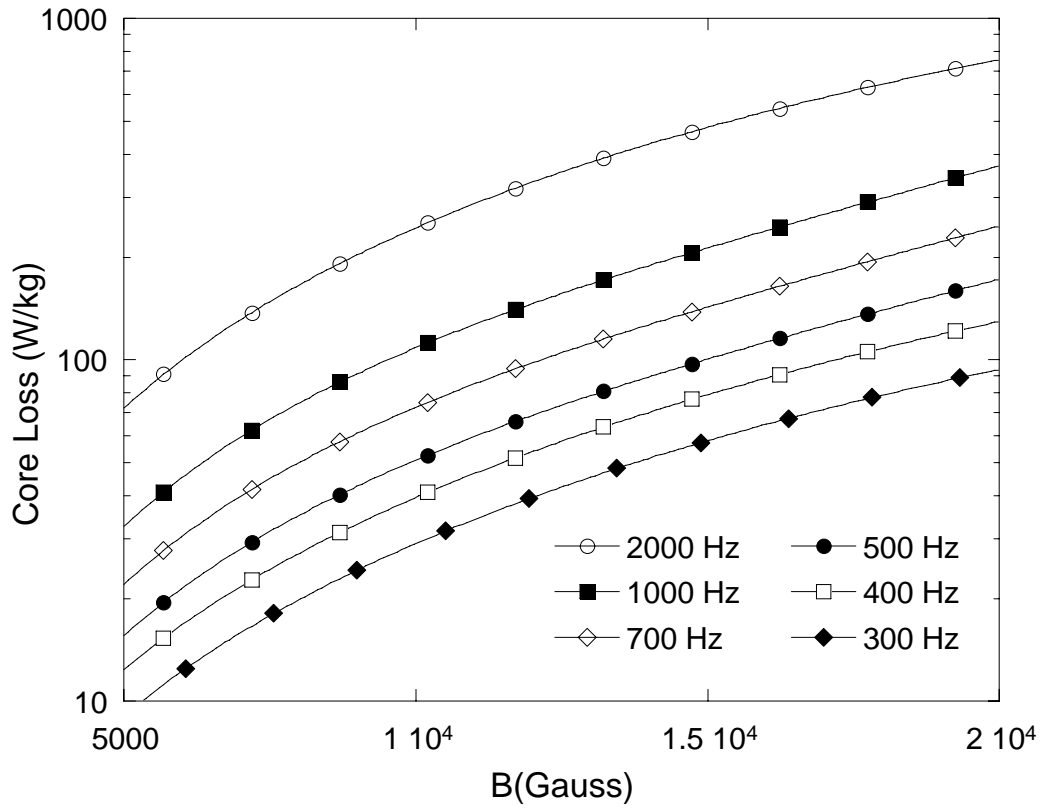


Figure 3.1.14 Core losses of unaged Hipercro 50 HS alloy taken at 100°C

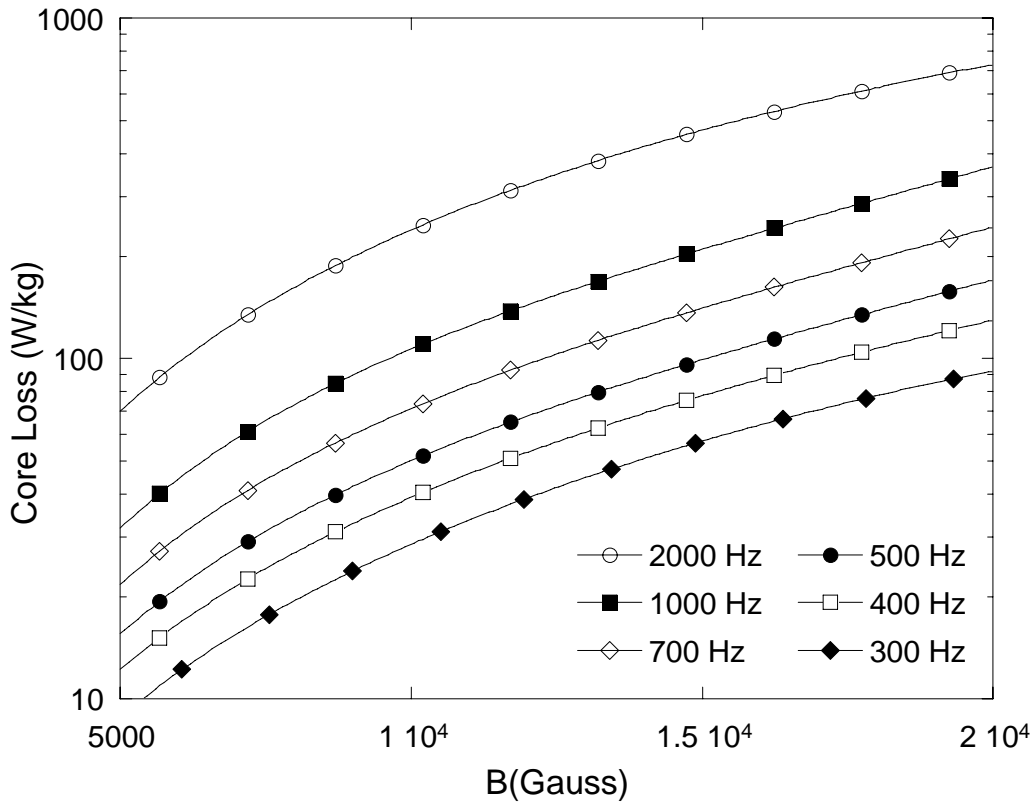


Figure 3.1.15 Core losses of unaged Hipercro 50 HS alloy taken at 200°C

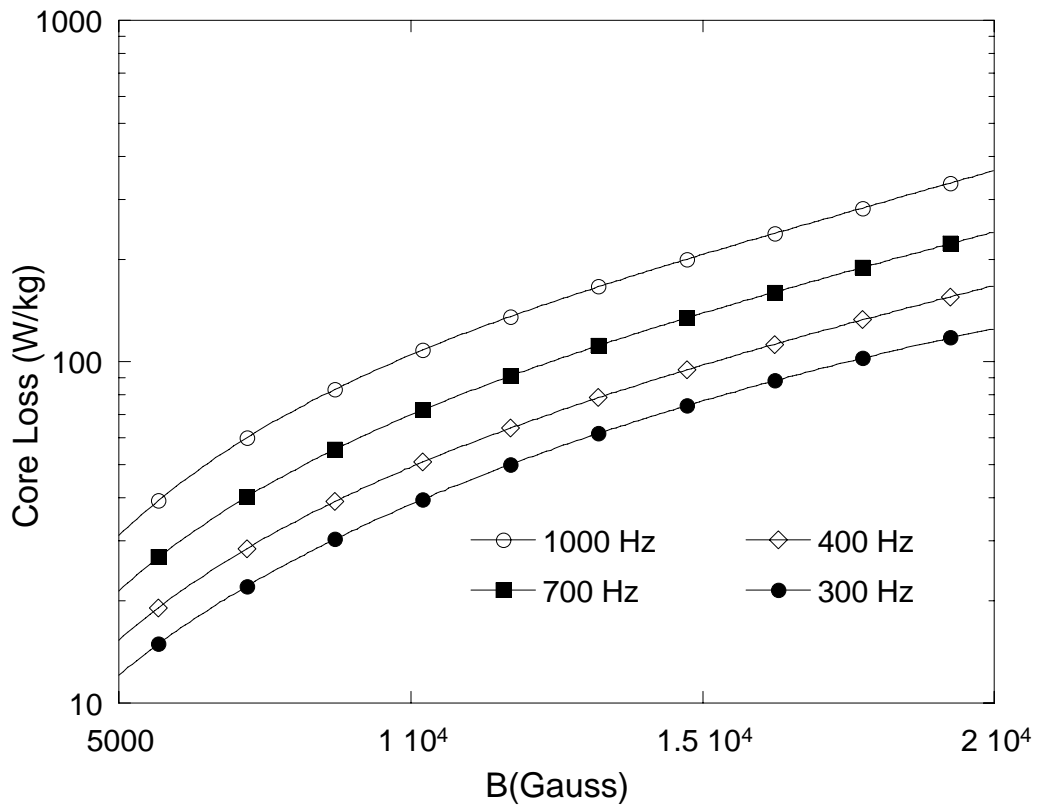


Figure 3.1.16 Core losses of unaged Hipercro 50 HS alloy taken at 300 ° C

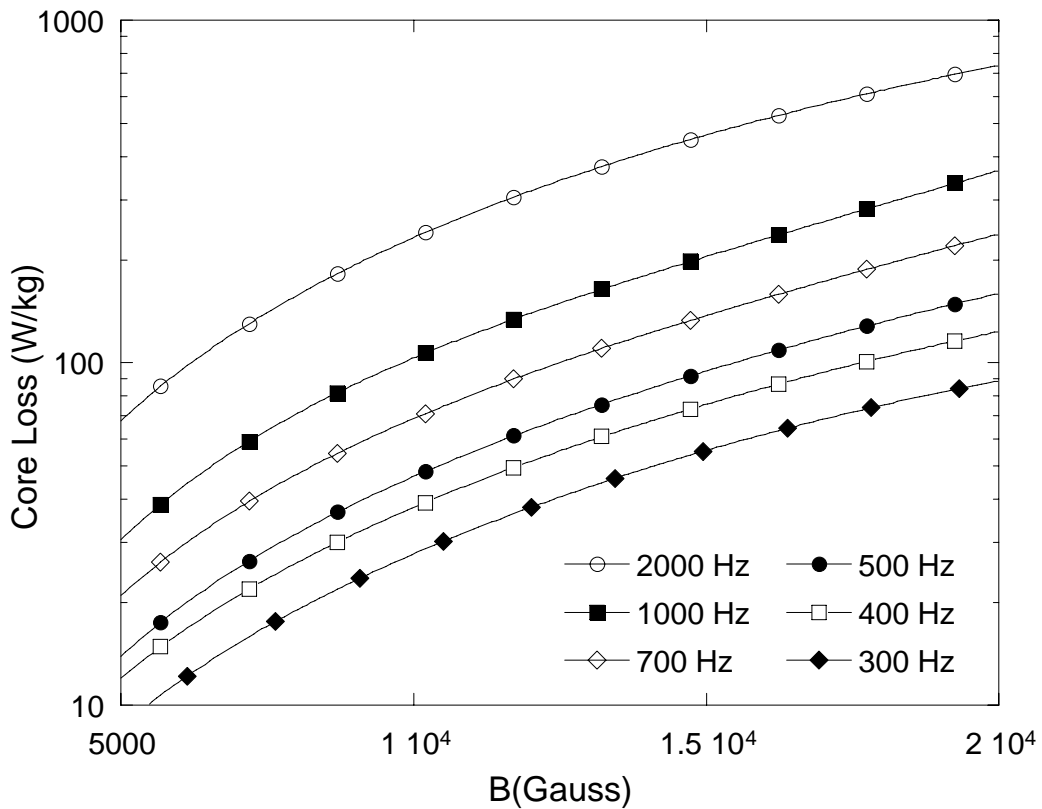


Figure 3.1.17 Core losses of unaged Hipercro 50 HS alloy taken at 400 ° C

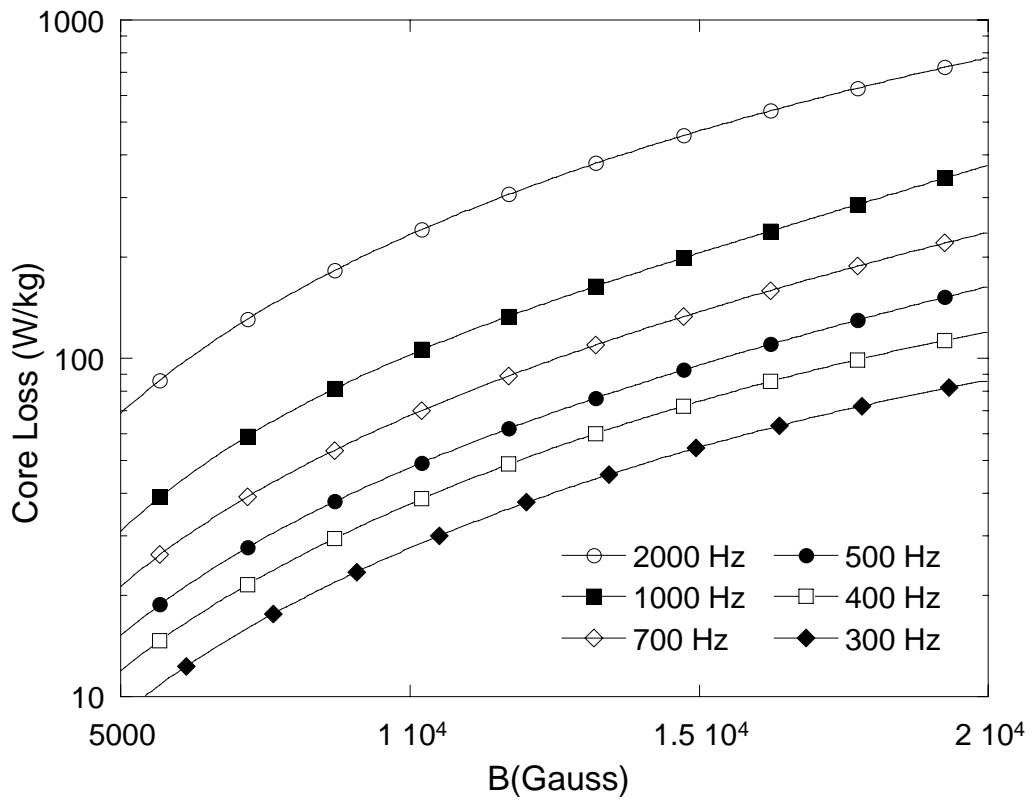


Figure 3.1.18 Core losses of unaged Hiperc 50 HS alloy taken at 500 ° C

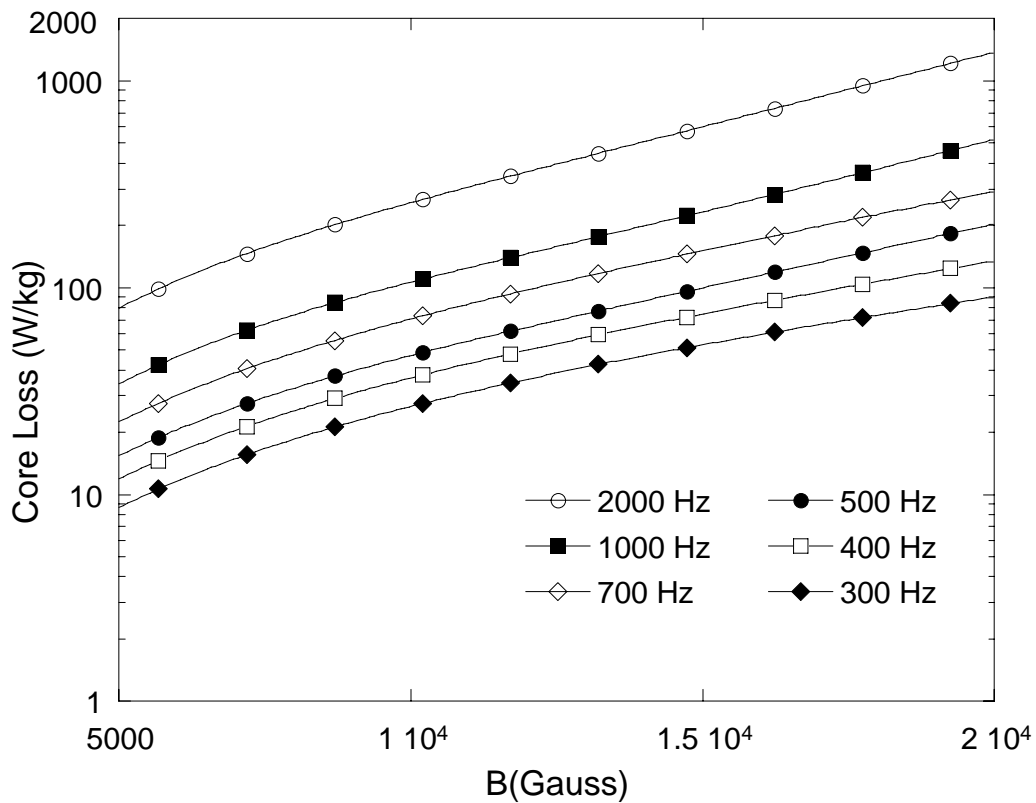


Figure 3.1.19 Core losses of 100 hours-aged Hipercro 27 alloy taken at RT

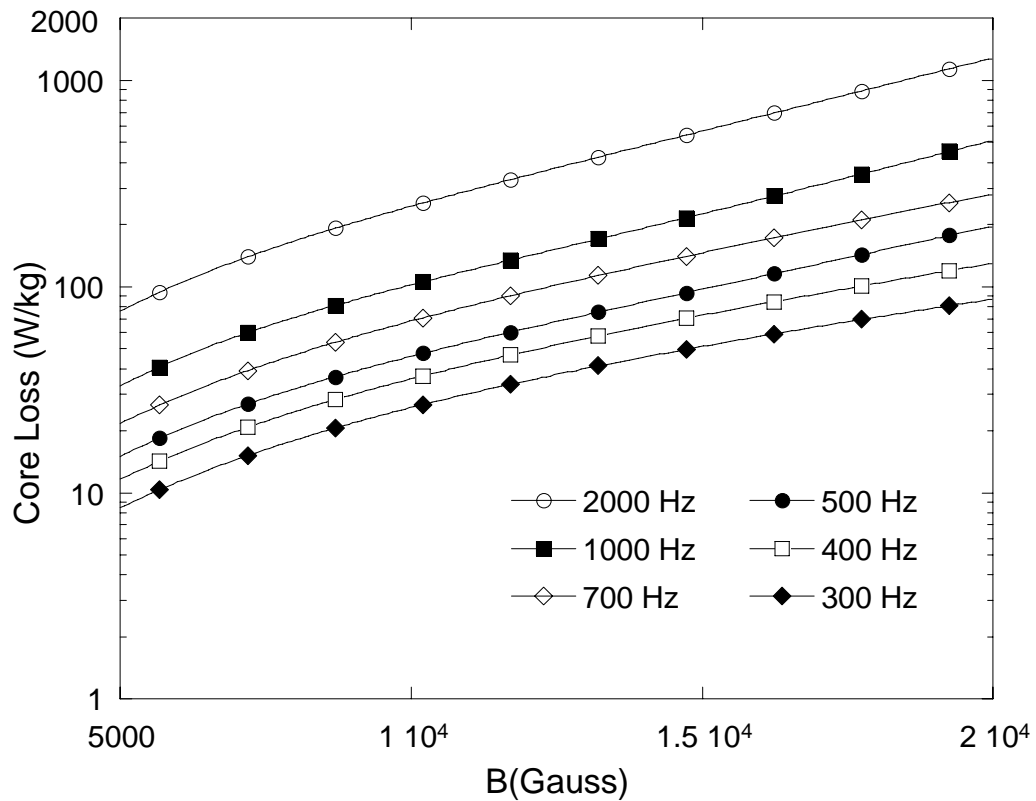


Figure 3.1.20 Core losses of 100 hours-aged Hipercro 27 alloy taken at 100 °C

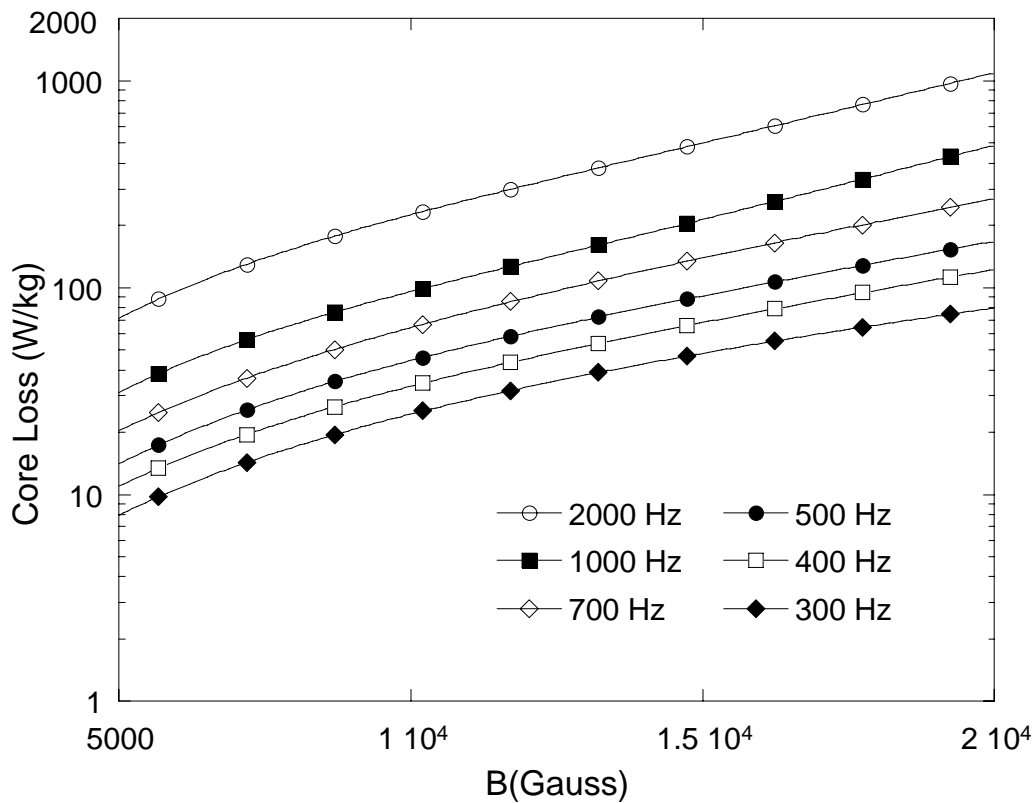


Figure 3.1.21 Core losses of 100 hours-aged Hipercro 27 alloy taken at 200 °C

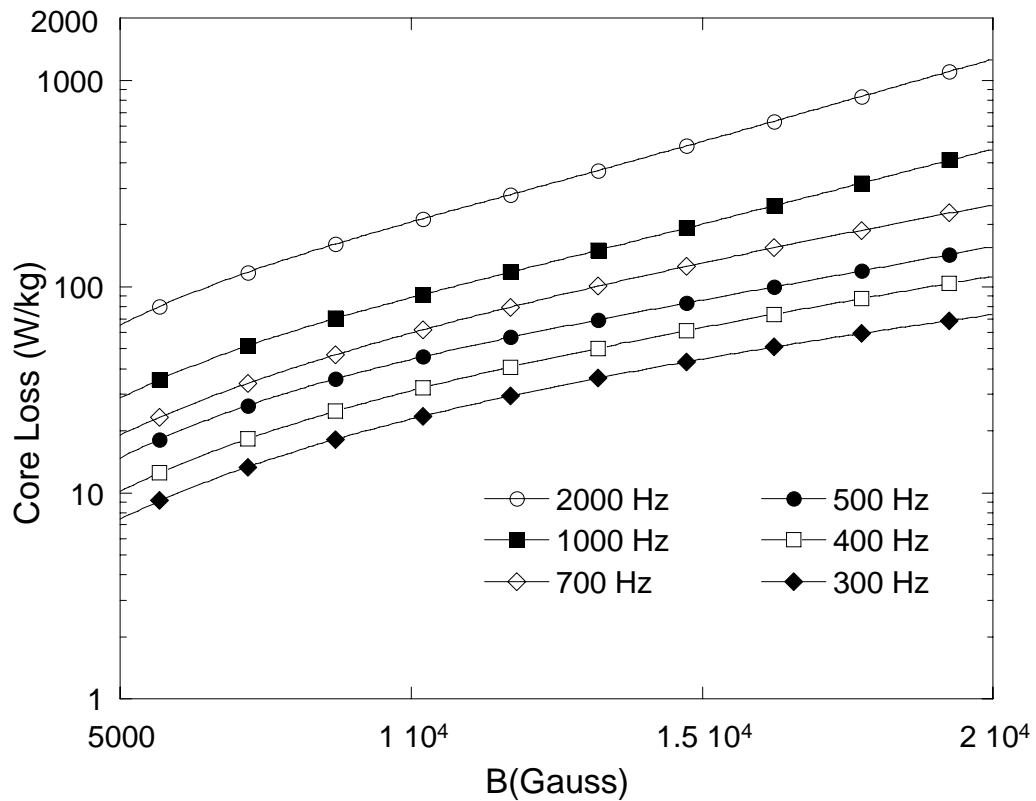


Figure 3.1.22 Core losses of 100 hours-aged Hipercro 27 alloy taken at 300 °C

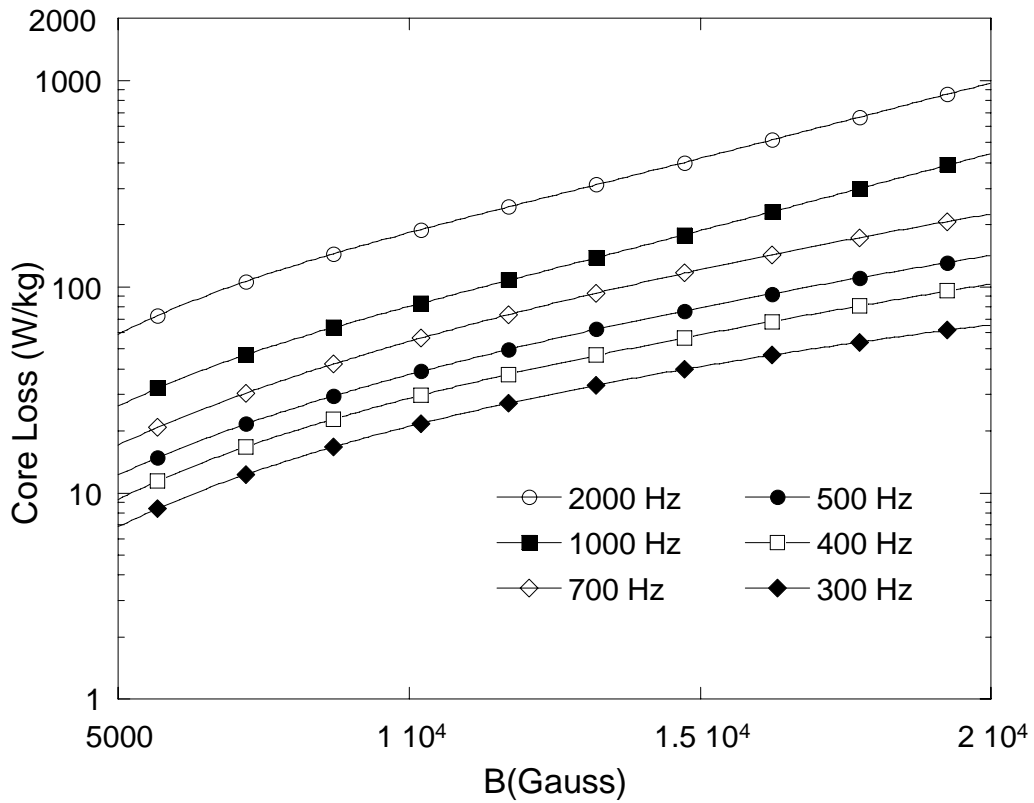


Figure 3.1.23 Core losses of 100 hours-aged Hipercro 27 alloy taken at 400 °C

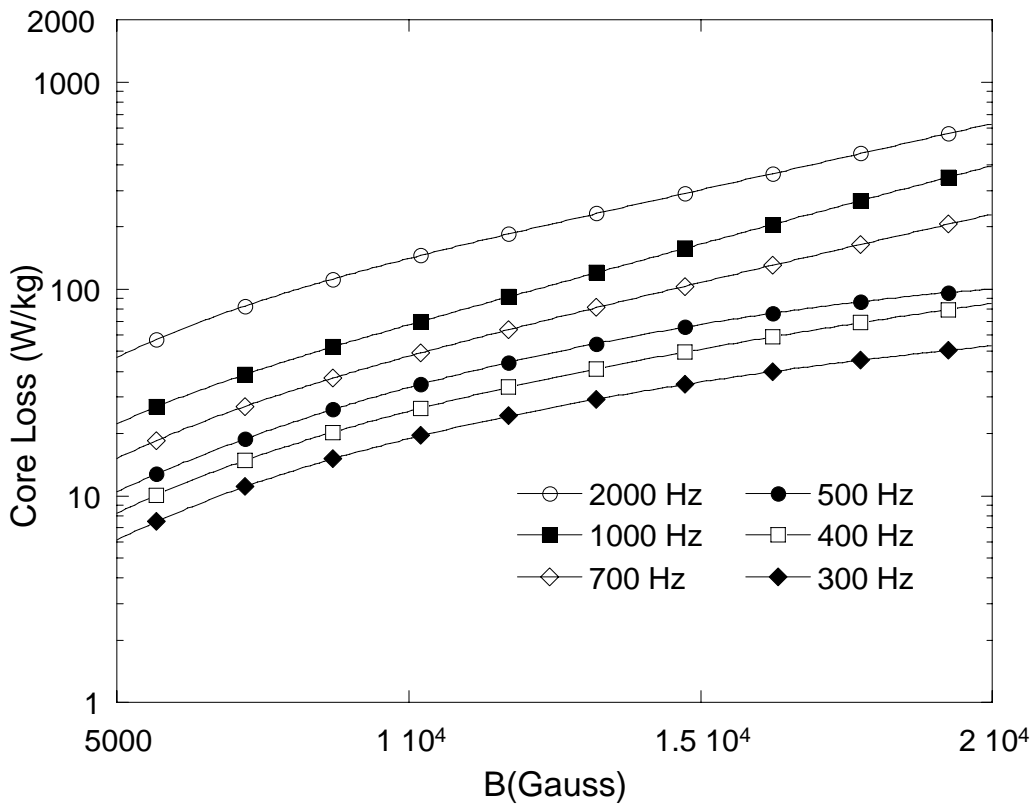


Figure 3.1.24 Core losses of 100 hours-aged Hipercro 27 alloy taken at 500 °C

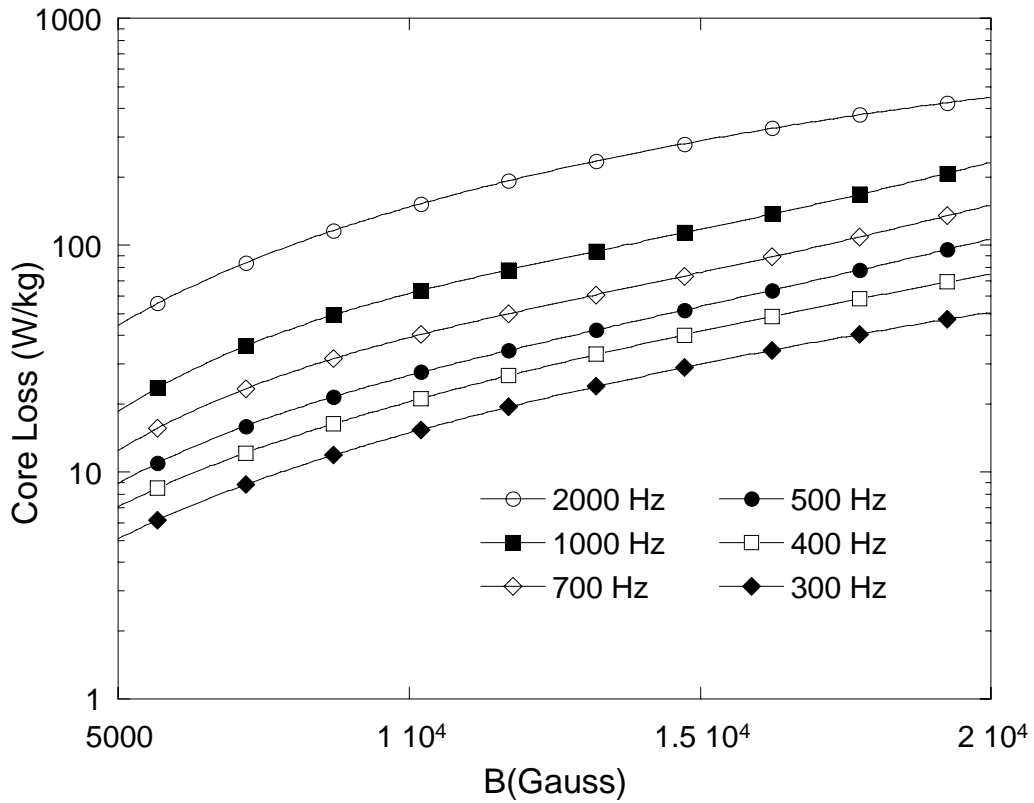


Figure 3.1.25 Core losses of 100 hours-aged Hipercro 50 alloy taken at RT

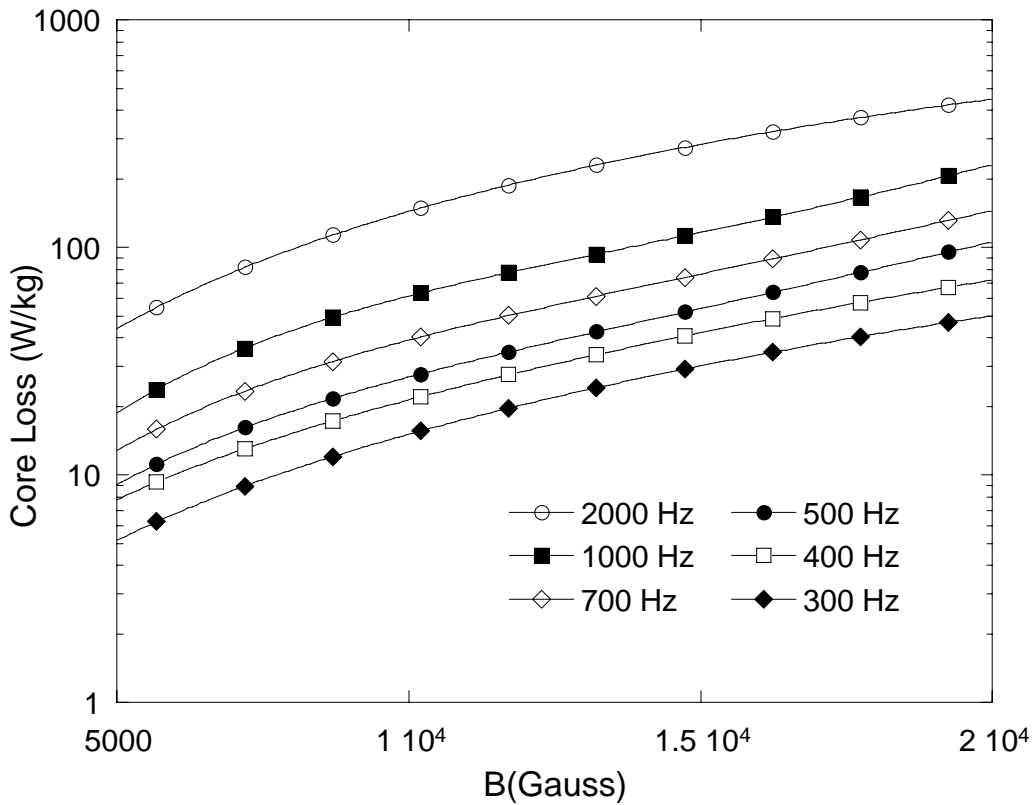


Figure 3.1.26 Core losses of 100 hours-aged Hipercro 50 alloy taken at 100 °C

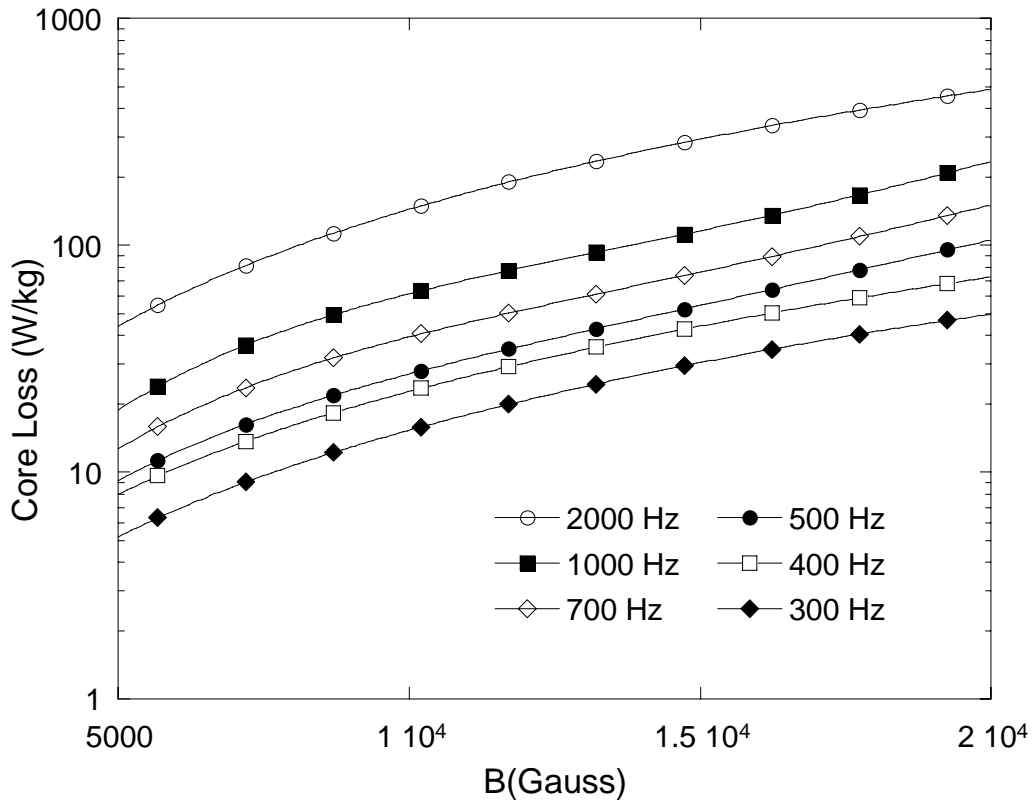


Figure 3.1.27 Core losses of 100 hours-aged Hipercro 50 alloy taken at 200°C

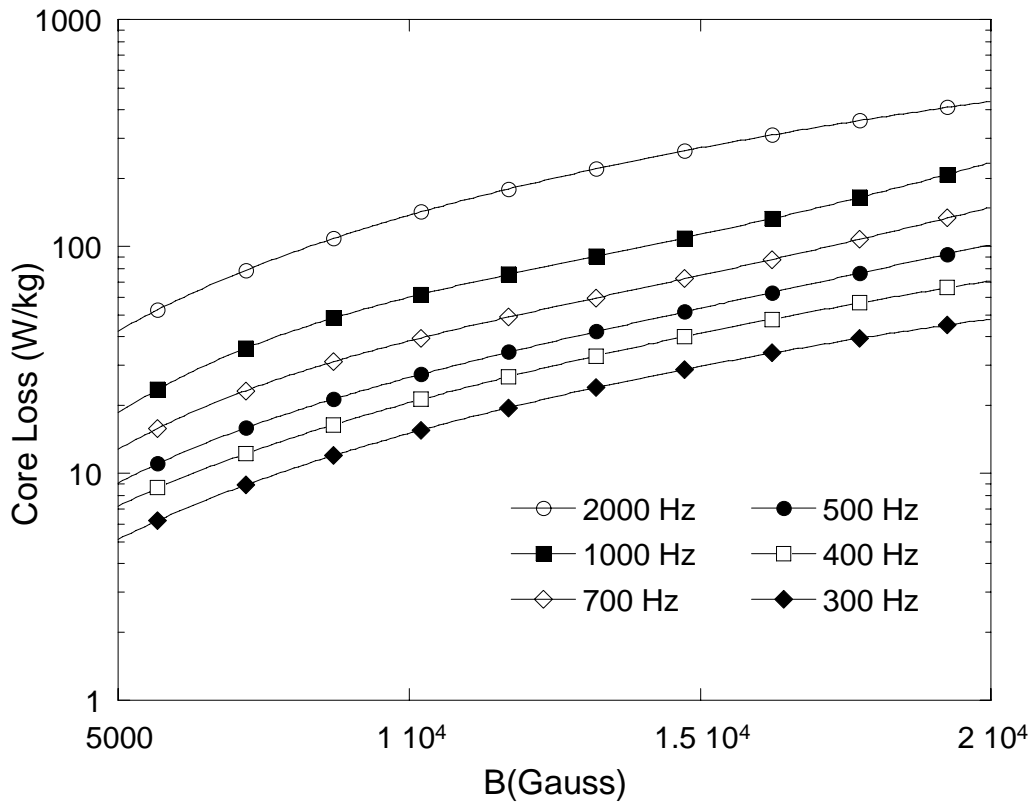


Figure 3.1.28 Core losses of 100 hours-aged Hipercro 50 alloy taken at 300°C

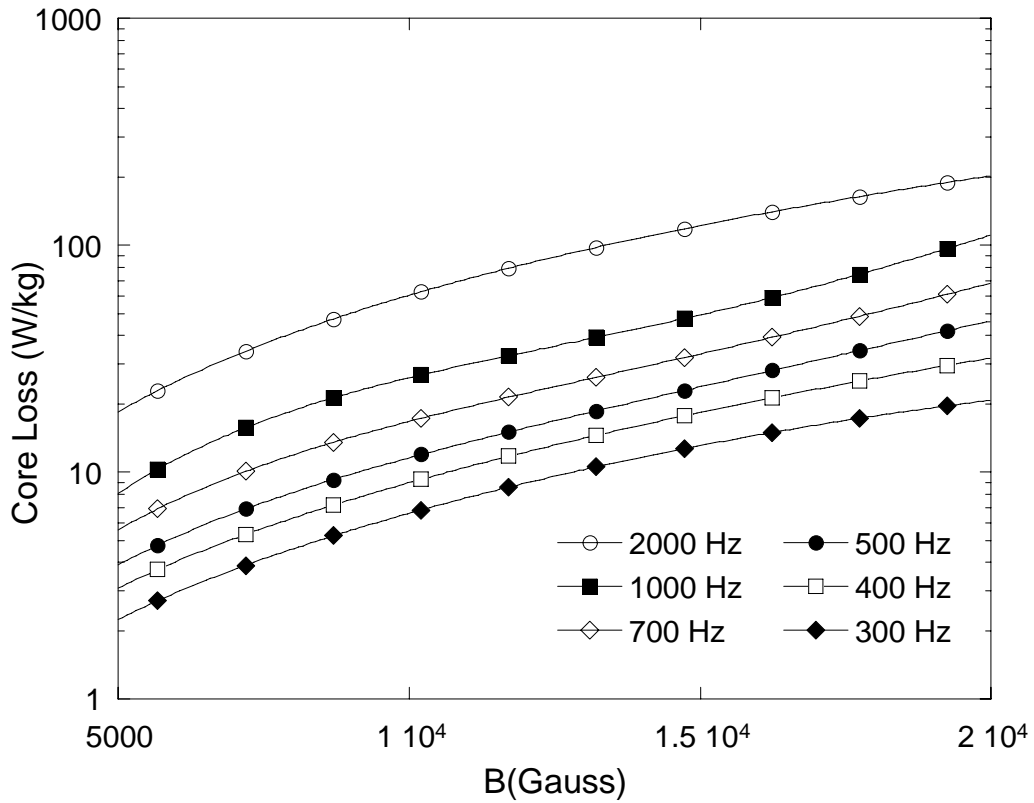


Figure 3.1.29 Core losses of 100 hours-aged Hipercro 50 alloy taken at 400°C

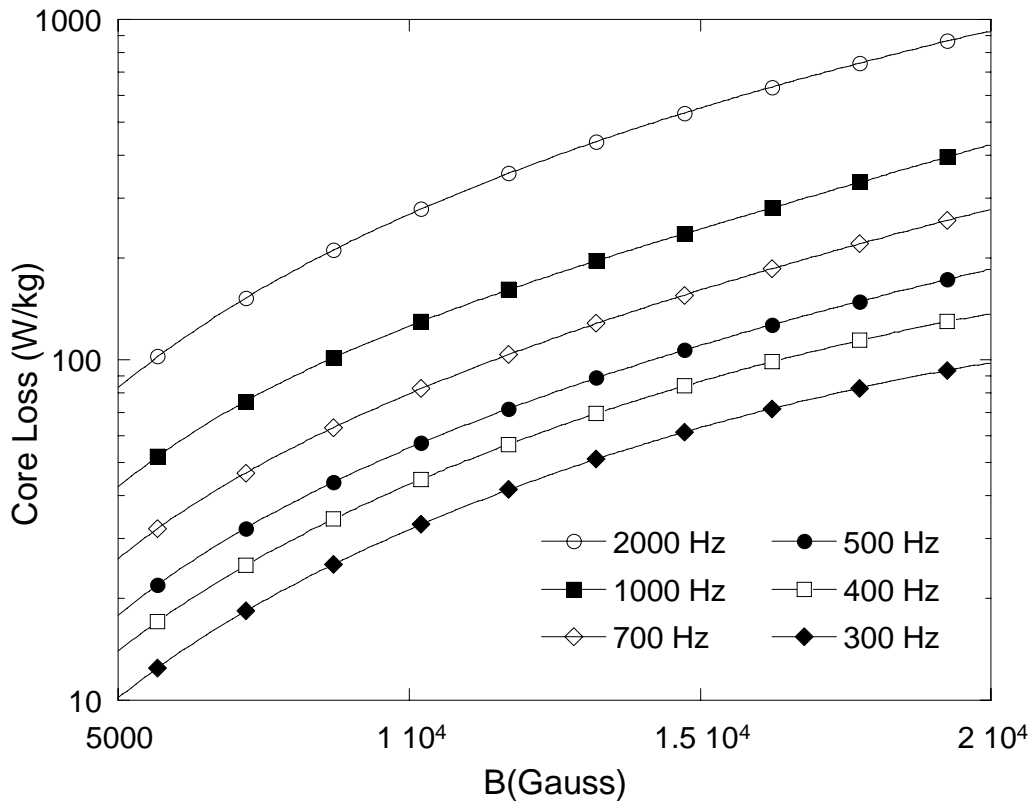


Figure 3.1.30 Core losses of 100 hours-aged Hipercro 50 HS alloy taken at RT

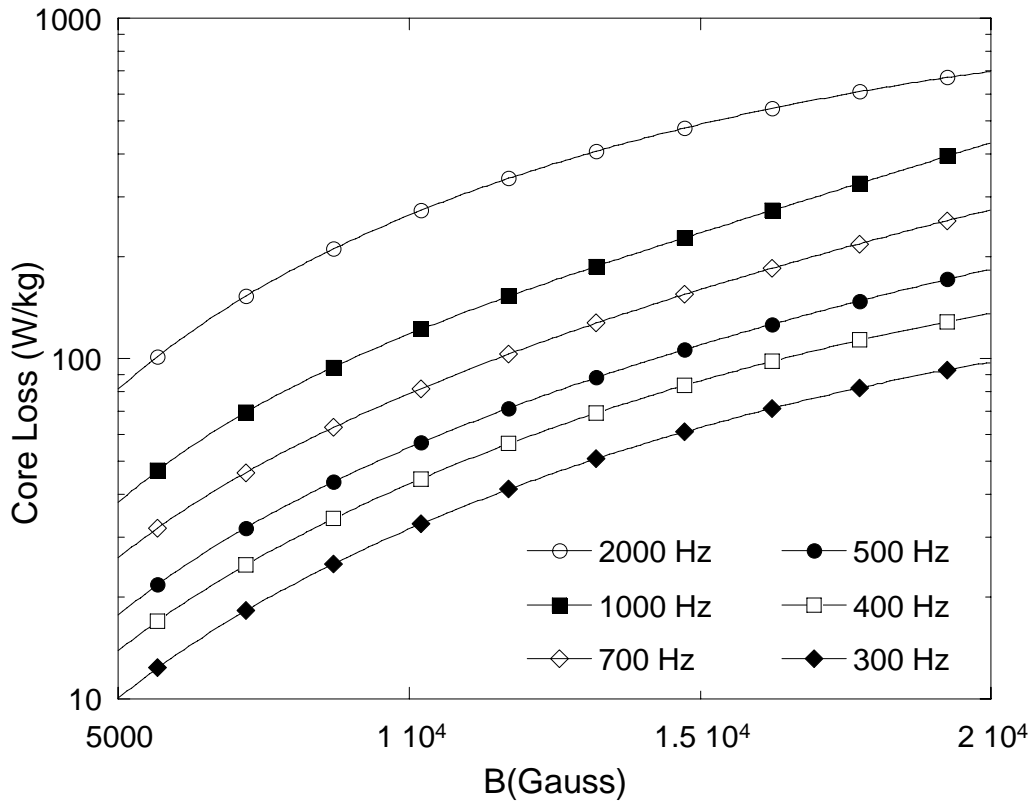


Figure 3.1.31 Core losses of 100 hours-aged Hipercro 50 HS alloy taken at 100 °C

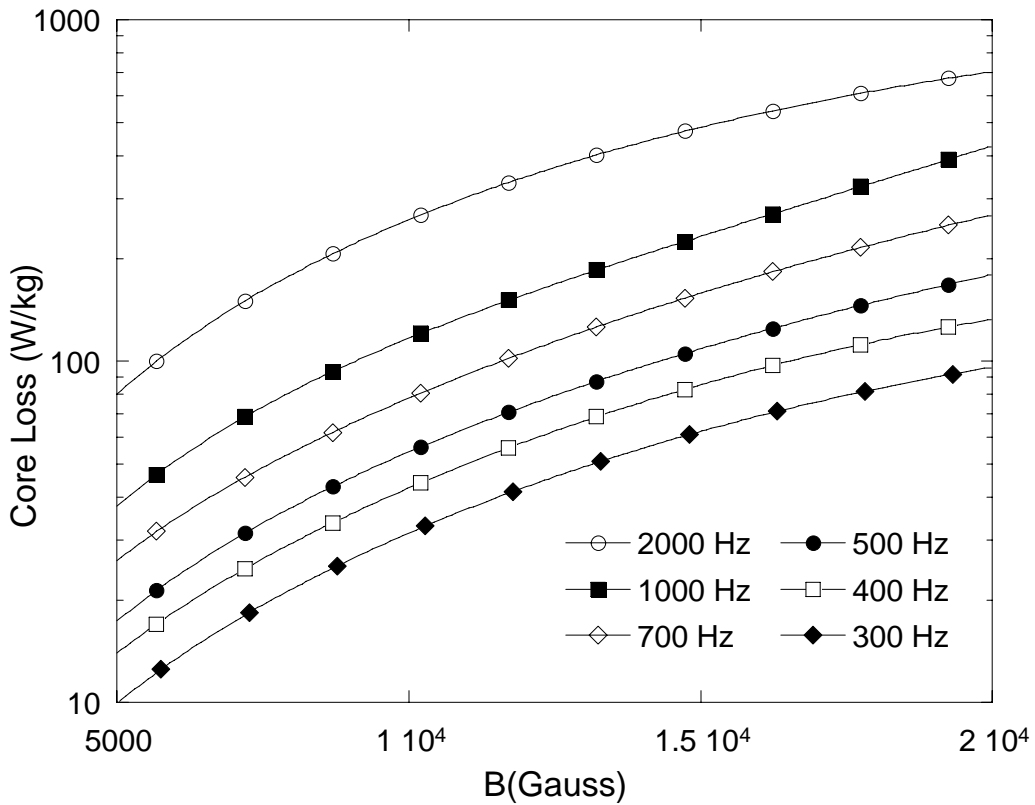


Figure 3.1.32 Core losses of 100 hours-aged Hipercro 50 HS alloy taken at 200 °C

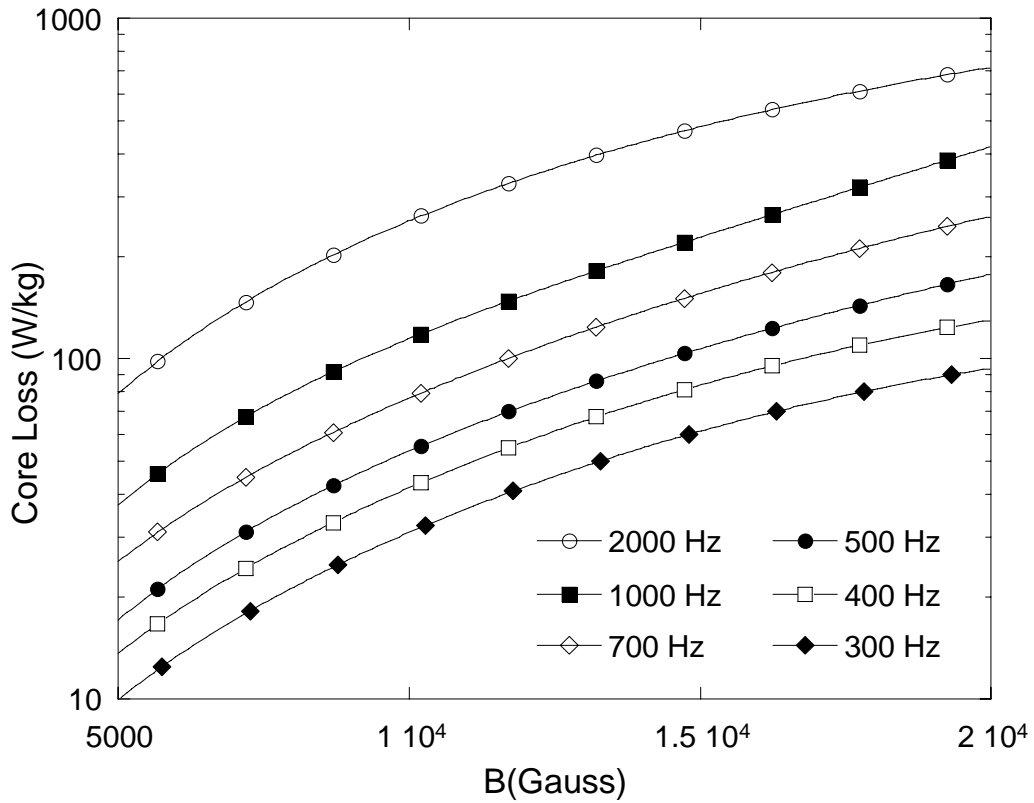


Figure 3.1.33 Core losses of 100 hours-aged Hipercro 50 HS alloy taken at 300 °C

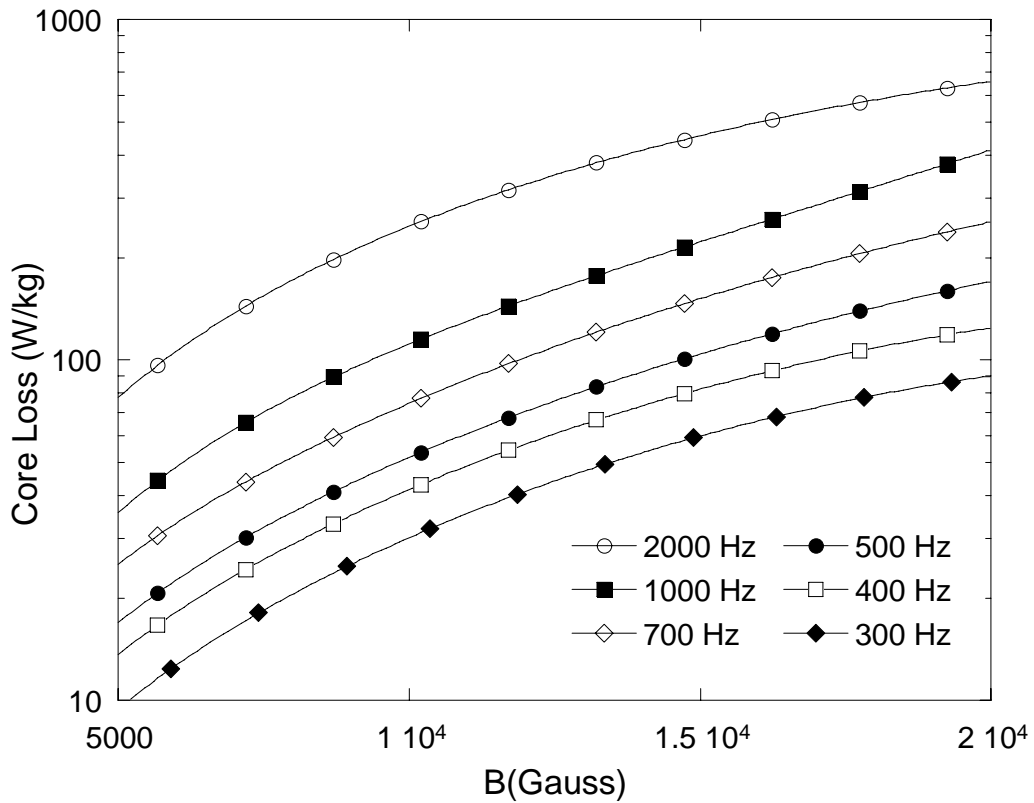


Figure 3.1.34 Core losses of 100 hours-aged Hipercro 50 HS alloy taken at 400 °C

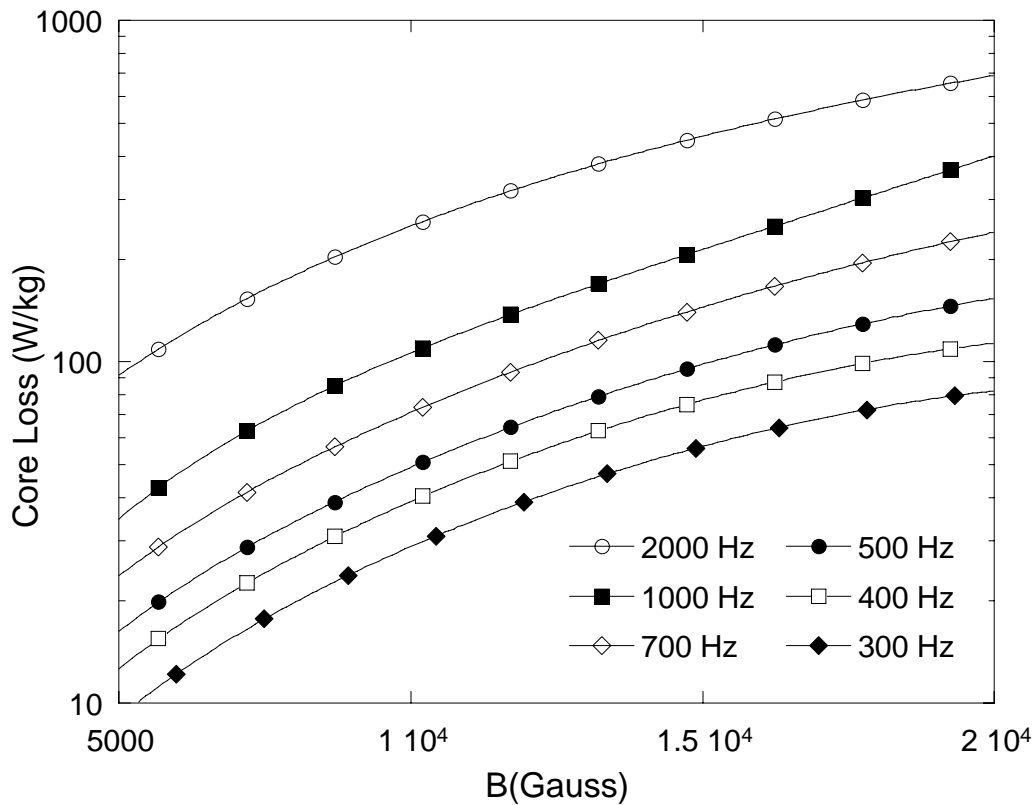


Figure 3.1.35 Core losses of 100 hours-aged Hipercro 50 HS alloy taken at 500 °C

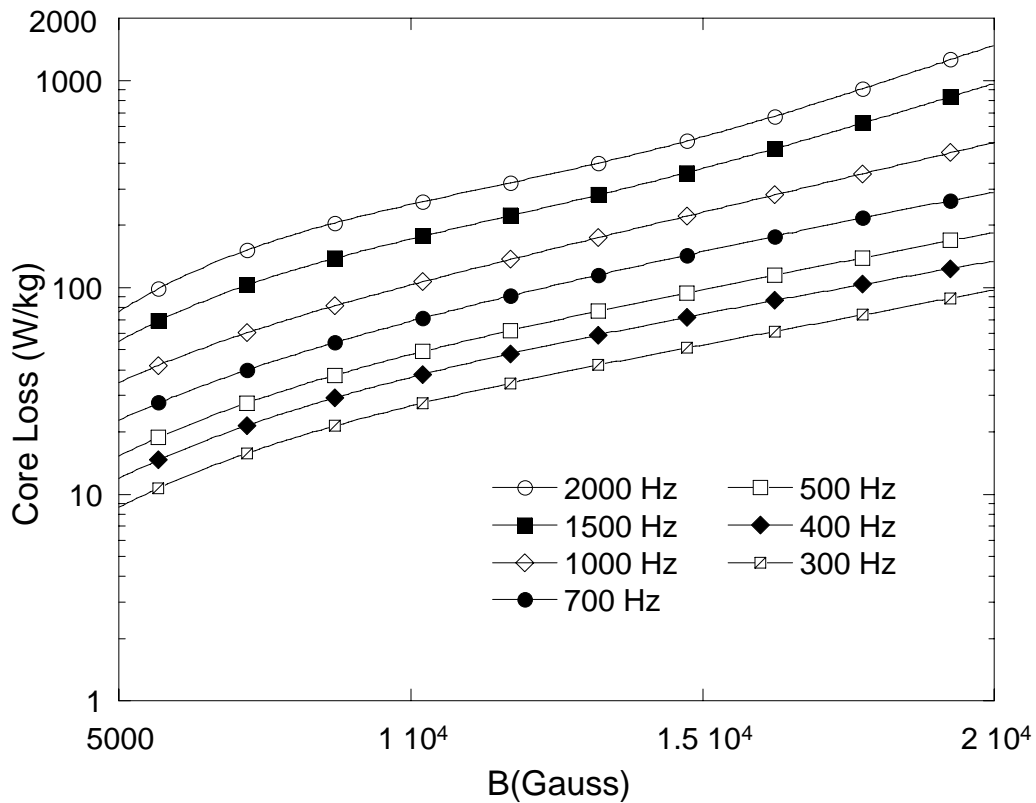


Figure 3.1.36 Core losses of 1000 hours-aged Hipercro 27 alloy taken at RT

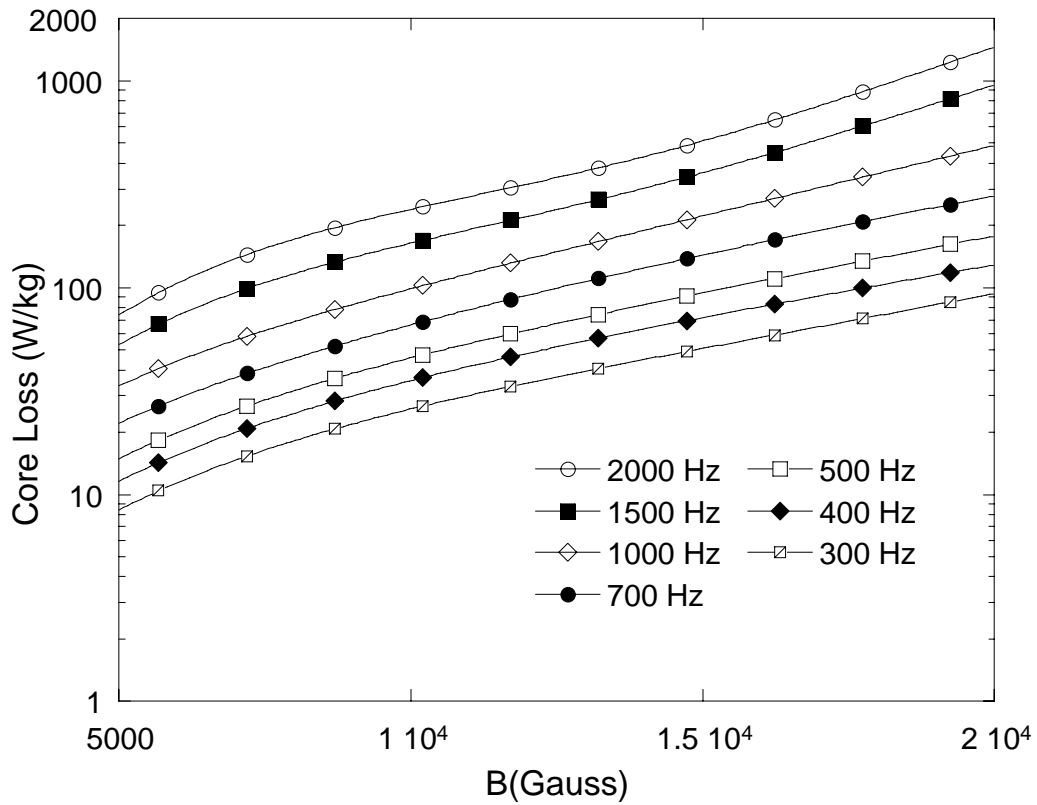


Figure 3.1.37 Core losses of 1000 hours-aged Hipercor 27 alloy taken at 100 °C

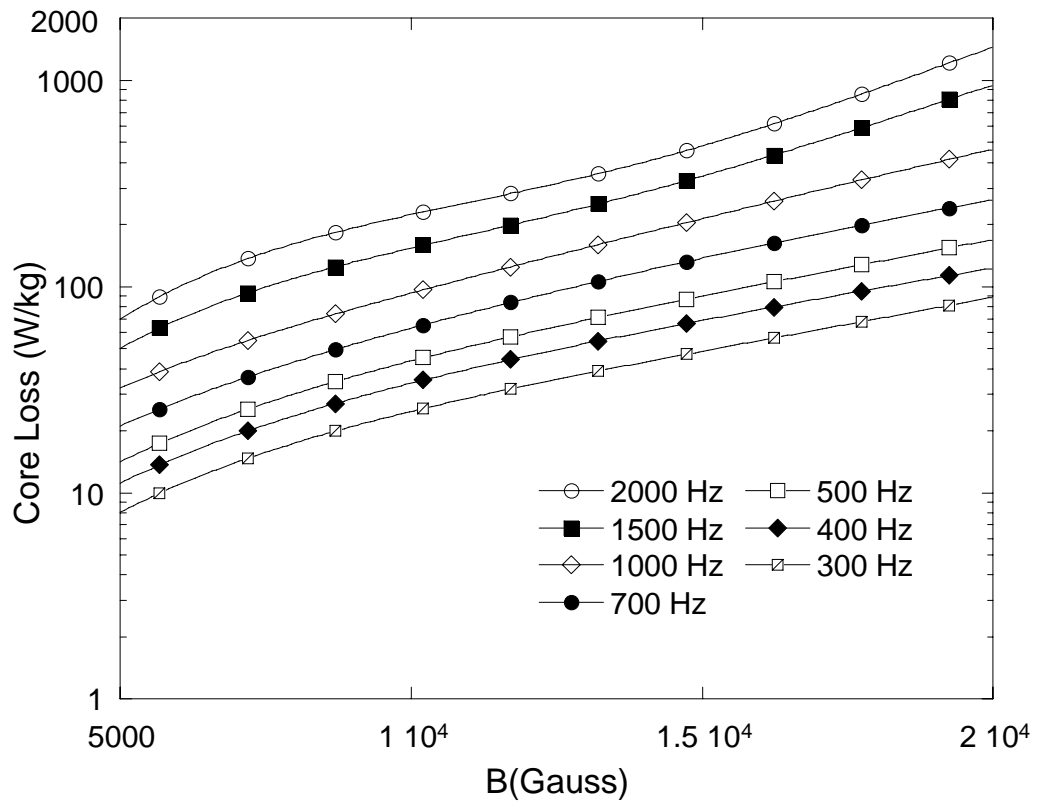


Figure 3.1.38 Core losses of 1000 hours-aged Hipercor 27 alloy taken at 200 °C

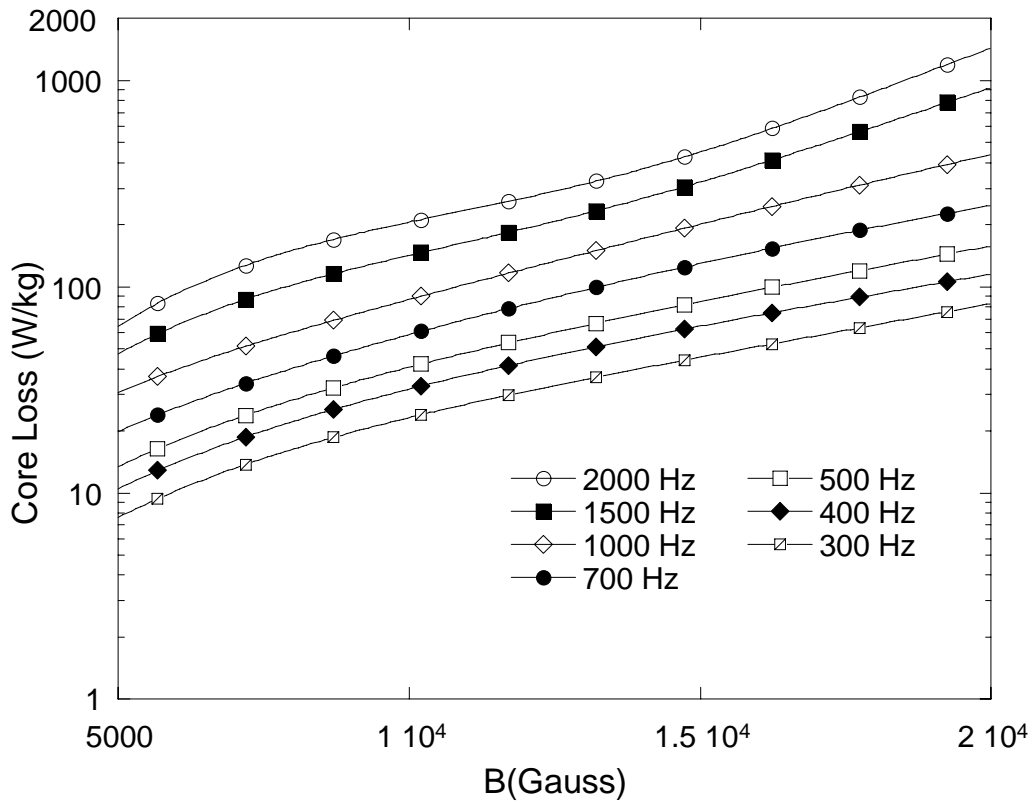


Figure 3.1.39 Core losses of 1000 hours-aged Hipercro 27 alloy taken at 300 °C

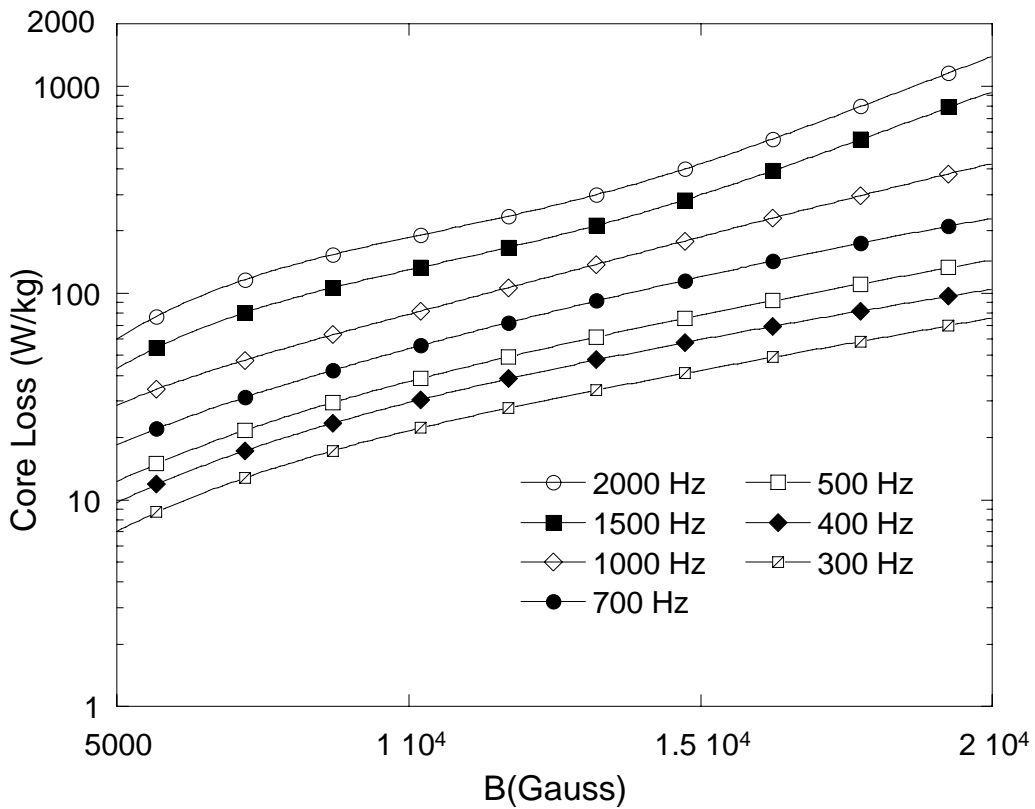


Figure 3.1.40 Core losses of 1000 hours-aged Hipercro 27 alloy taken at 400 °C

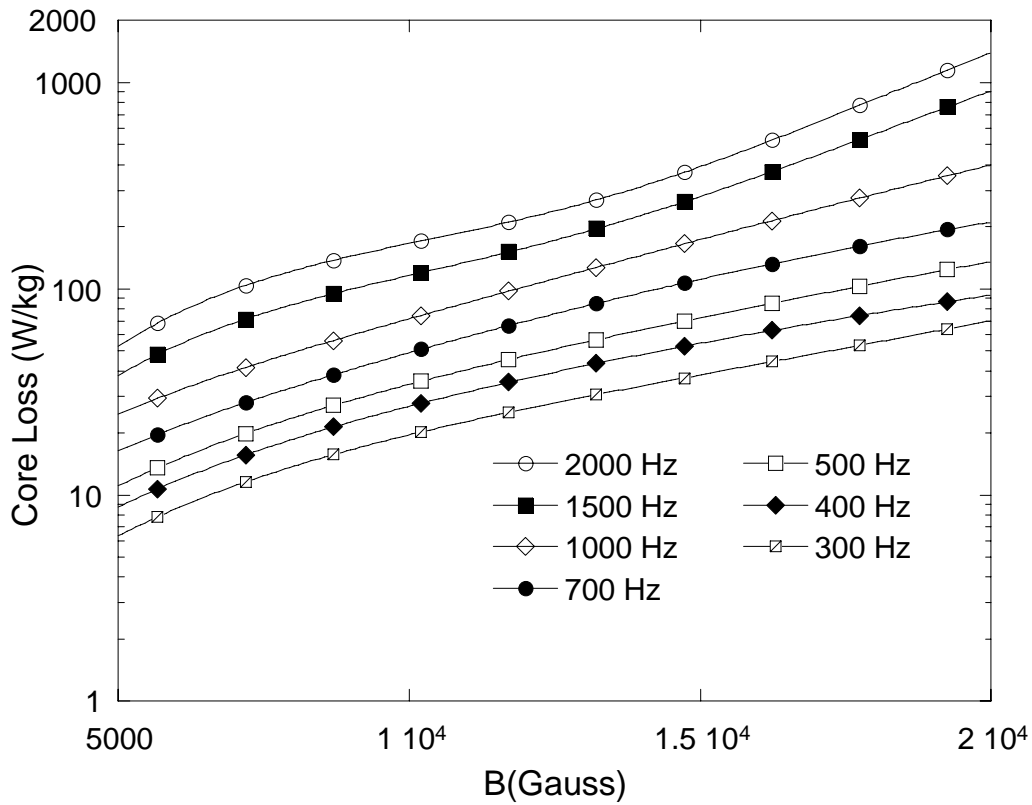


Figure 3.1.41 Core losses of 1000 hours-aged Hipercro 27 alloy taken at 500 °C

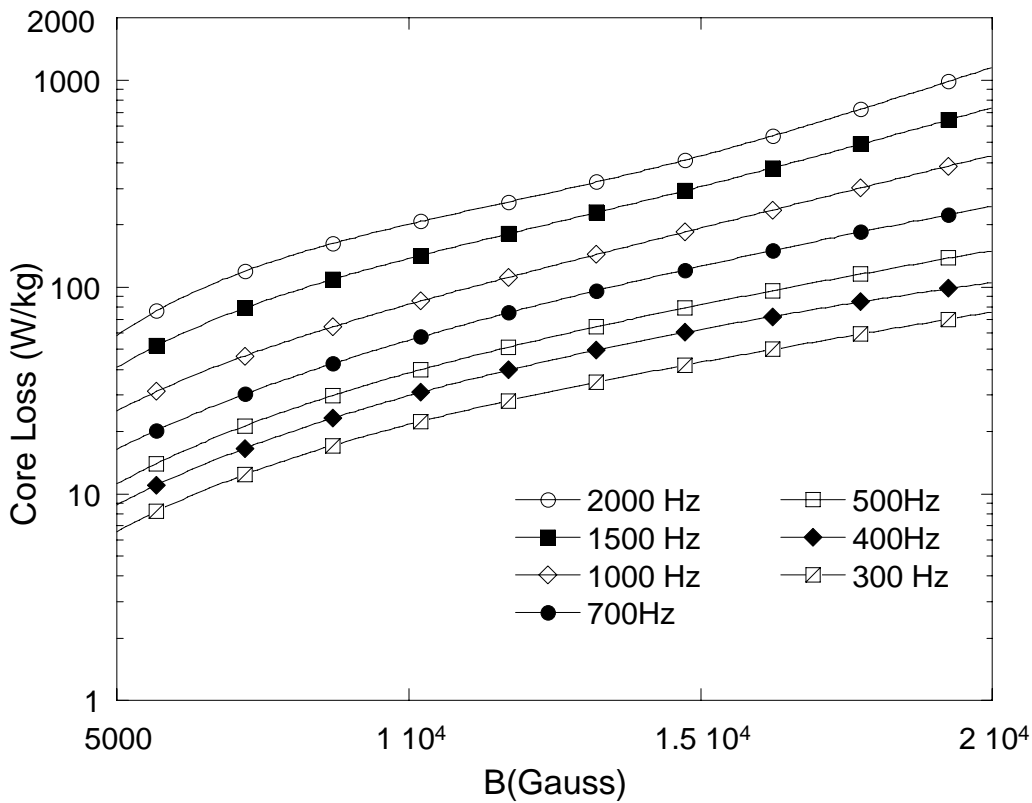


Figure 3.1.42 Core losses of 1000 hours-aged Hipercro 50 alloy taken at RT

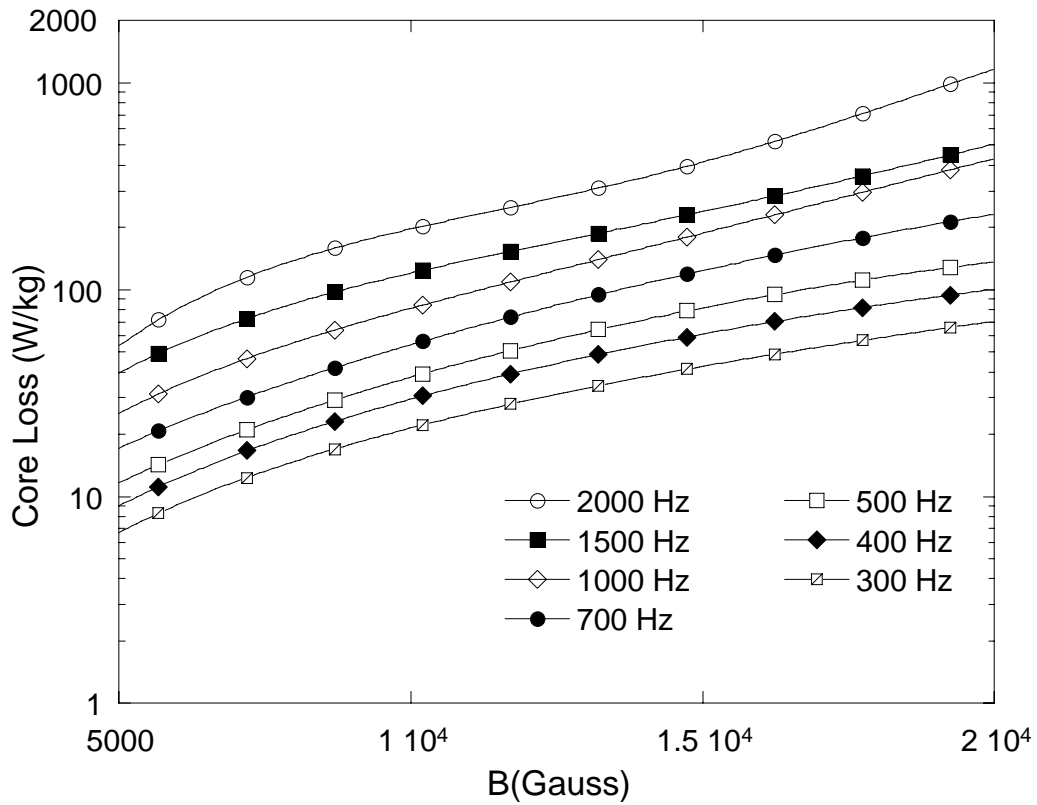


Figure 3.1.43 Core losses of 1000 hours-aged Hipercro 50 alloy taken at 200 °C

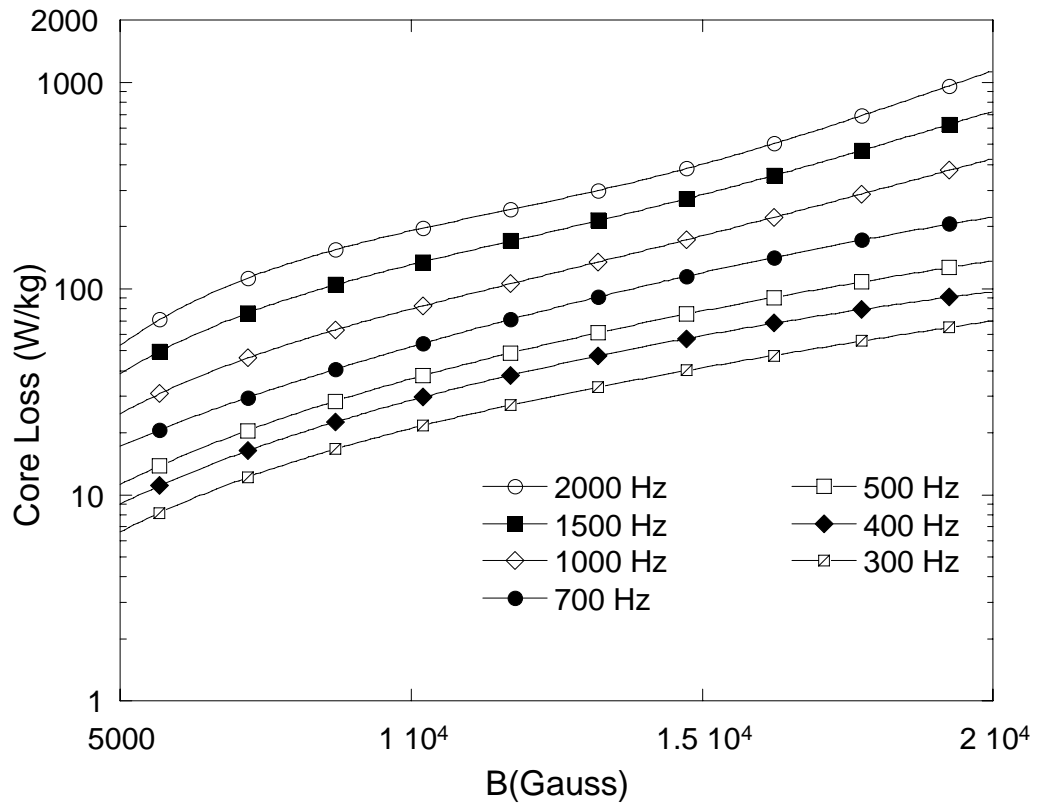


Figure 3.1.44 Core losses of 1000 hours-aged Hipercro 50 alloy taken at 300 °C

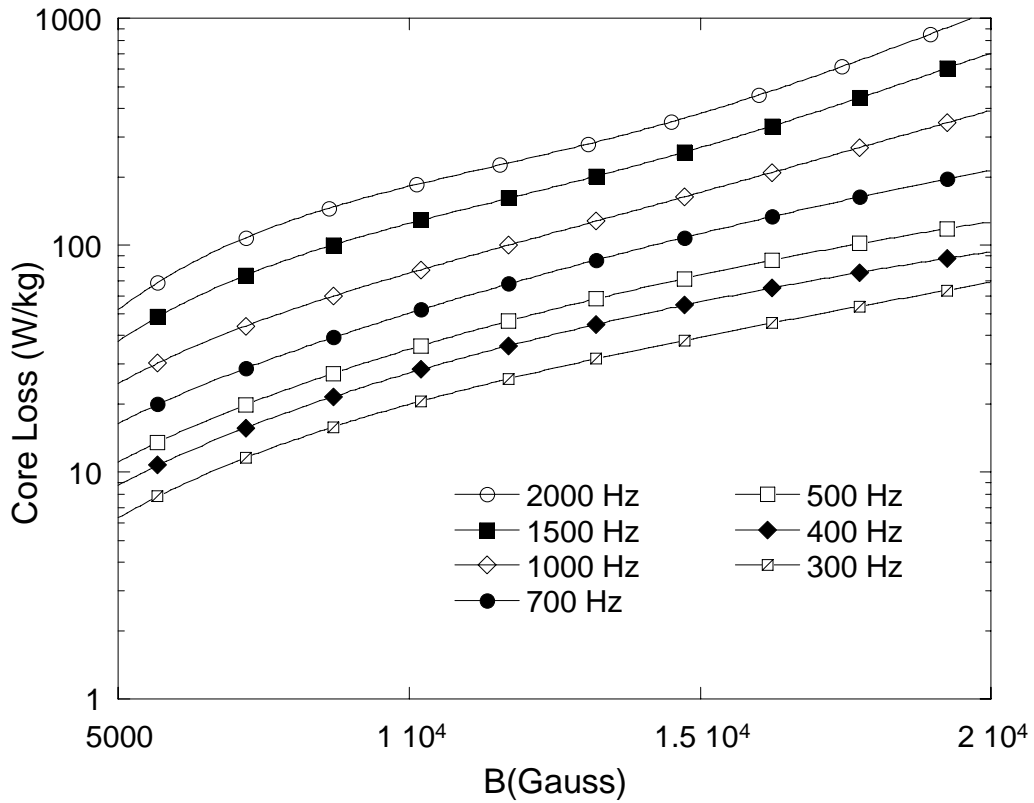


Figure 3.1.45 Core losses of 1000 hours-aged Hipercro 50 alloy taken at 400 °C

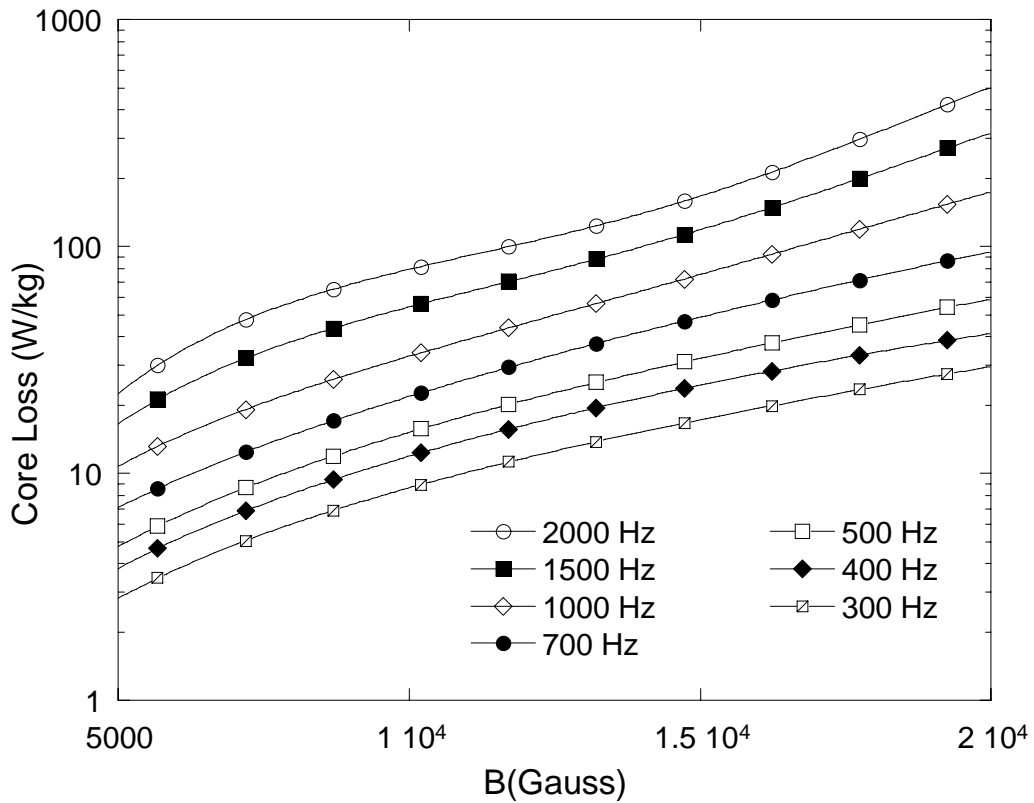


Figure 3.1.46 Core losses of 1000 hours-aged Hipercro 50 alloy taken at 500 °C

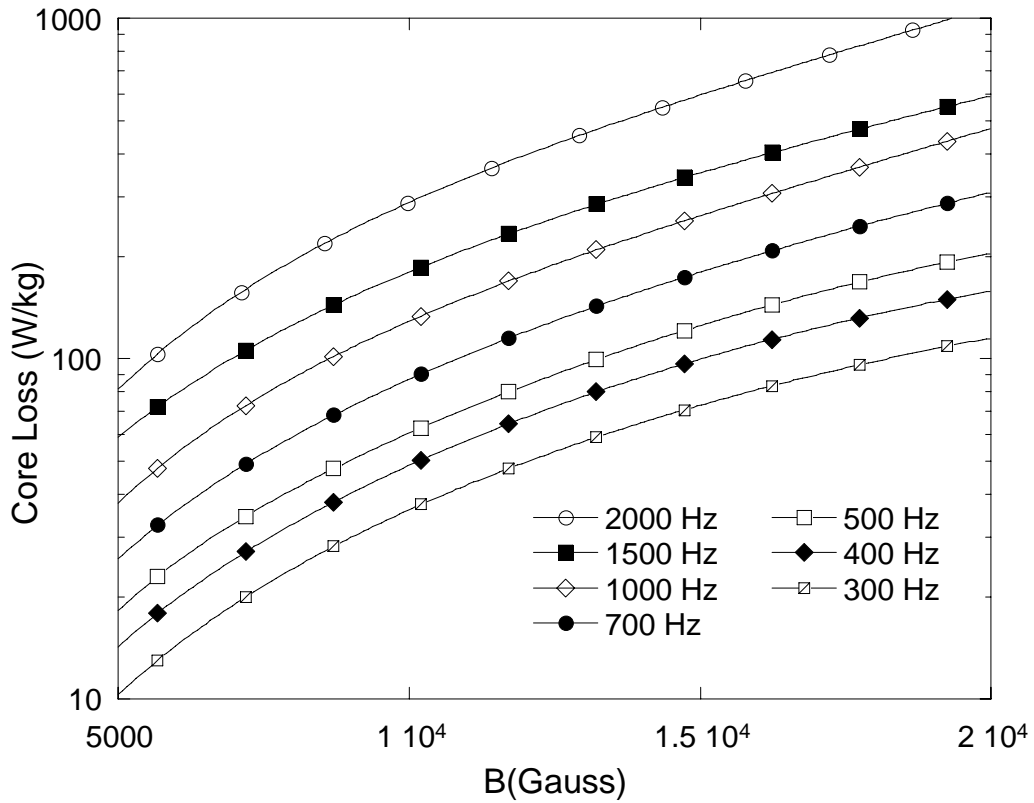


Figure 3.1.47 Core losses of 1000 hours-aged Hipercó 50 HS alloy taken at RT

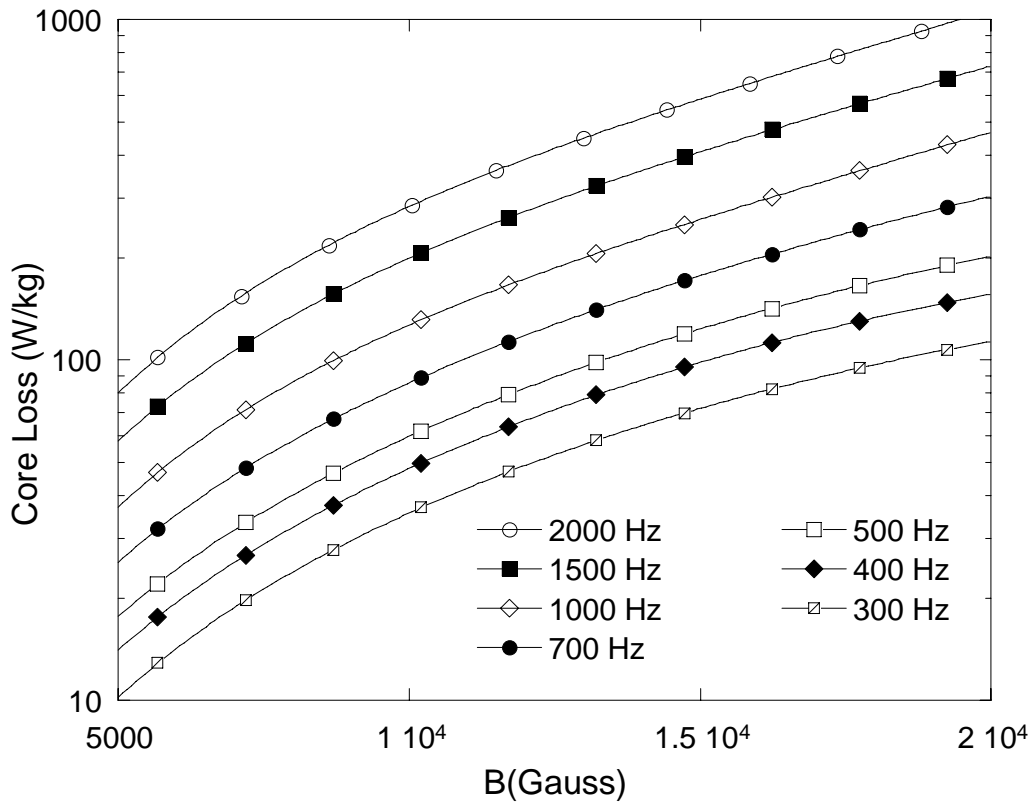


Figure 3.1.48 Core losses of 1000 hours-aged Hipercó 50 HS alloy taken at 100 °C

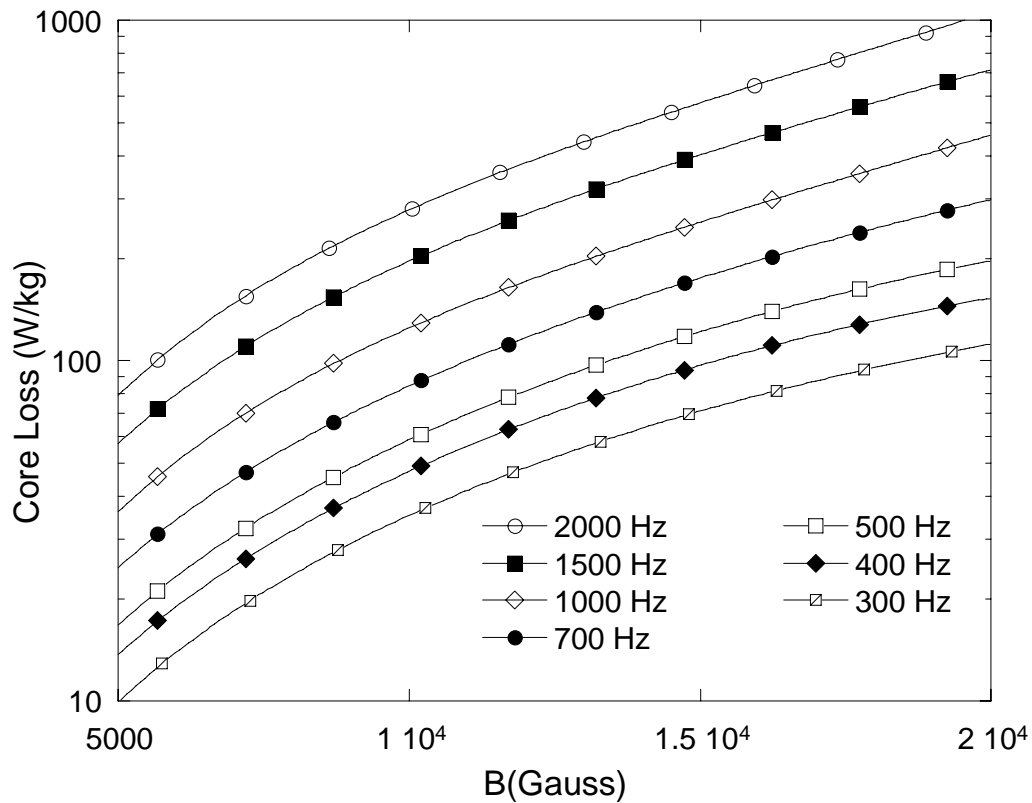


Figure 3.1.49 Core losses of 1000 hours-aged Hipercro 50 HS alloy taken at 200 °C

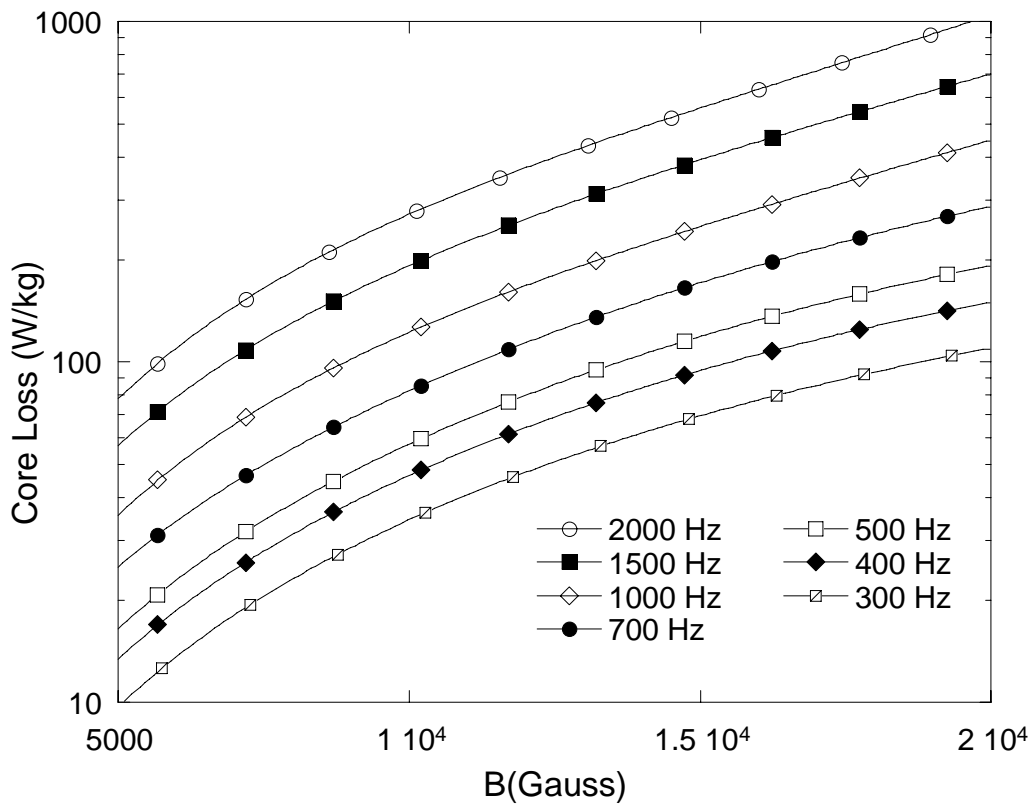


Figure 3.1.50 Core losses of 1000 hours-aged Hipercro 50 HS alloy taken at 300 °C

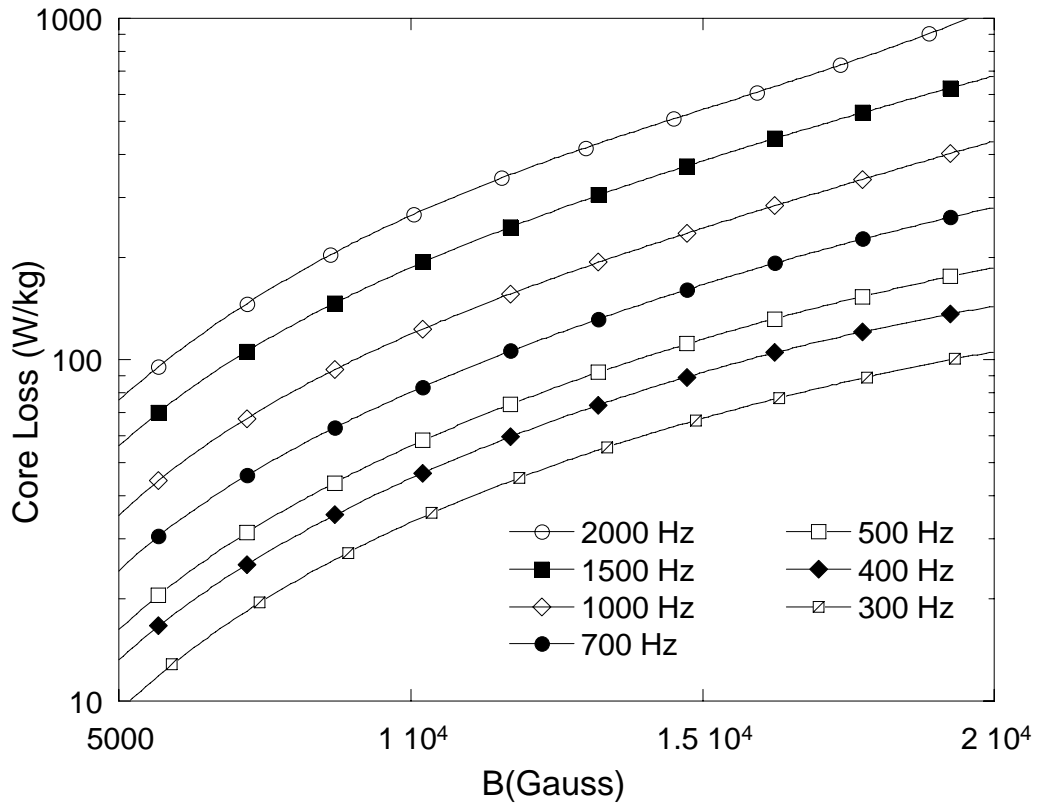


Figure 3.1.51 Core losses of 1000 hours-aged Hiperc 50 HS alloy taken at 400 °C

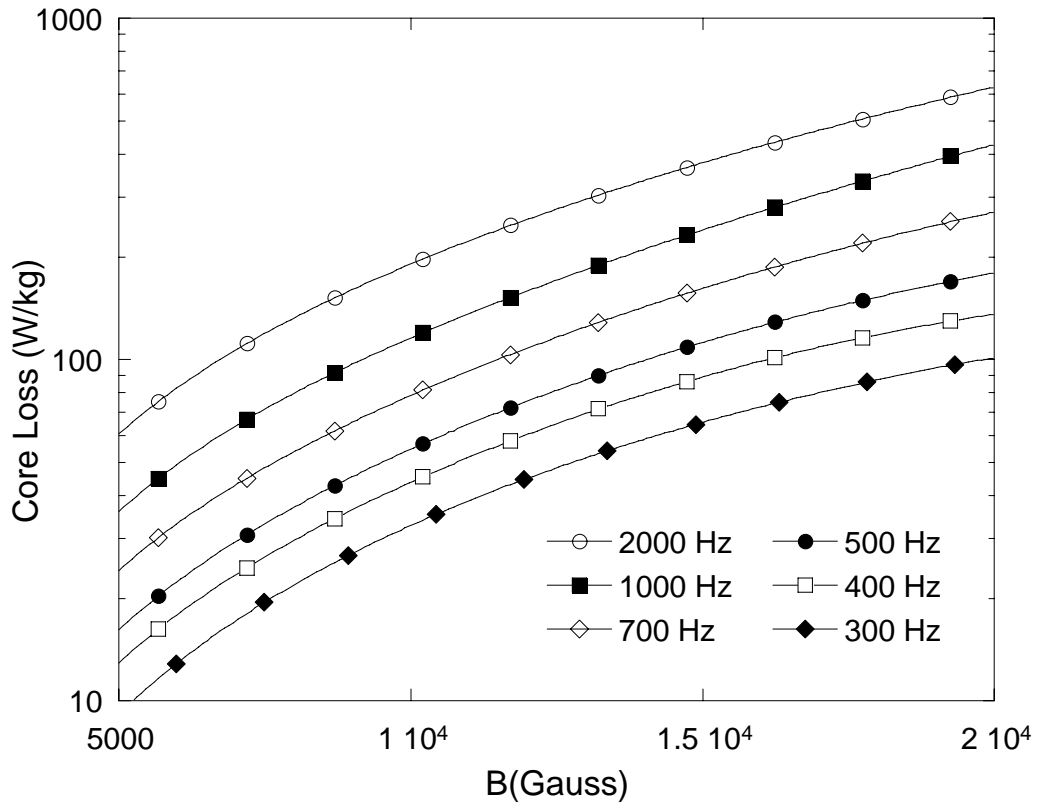


Figure 3.1.52 Core losses of 1000 hours-aged Hiperc 50 HS alloy taken at 500 °C

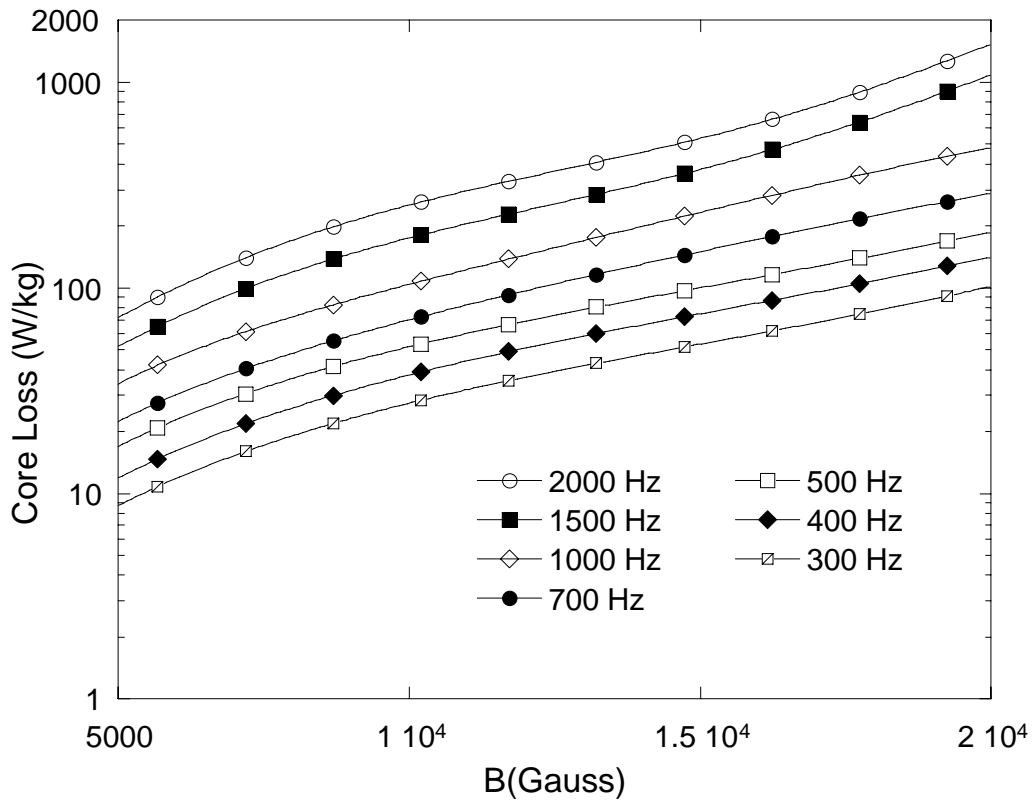


Figure 3.1.53 Core losses of 2000 hours-aged Hipercor 27 alloy taken at RT

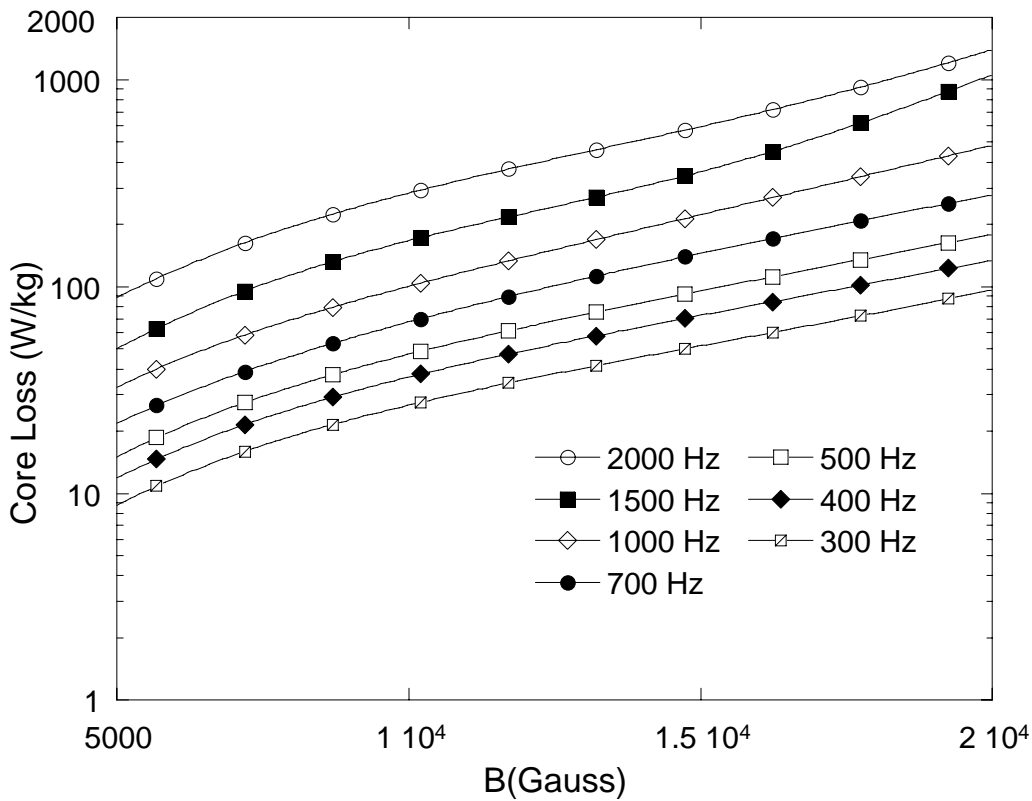


Figure 3.1.54 Core losses of 2000 hours-aged Hipercor 27 alloy taken at 100 °C

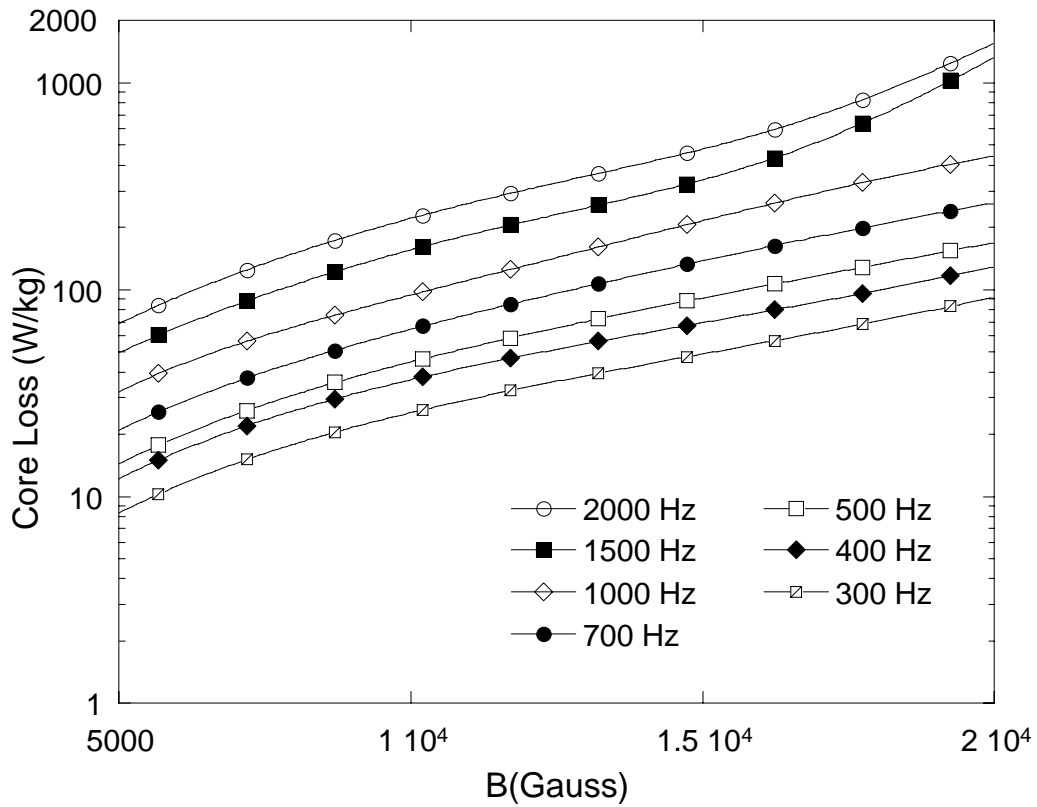


Figure 3.1.55 Core losses of 2000 hours-aged Hipercro 27 alloy taken at 200 °C

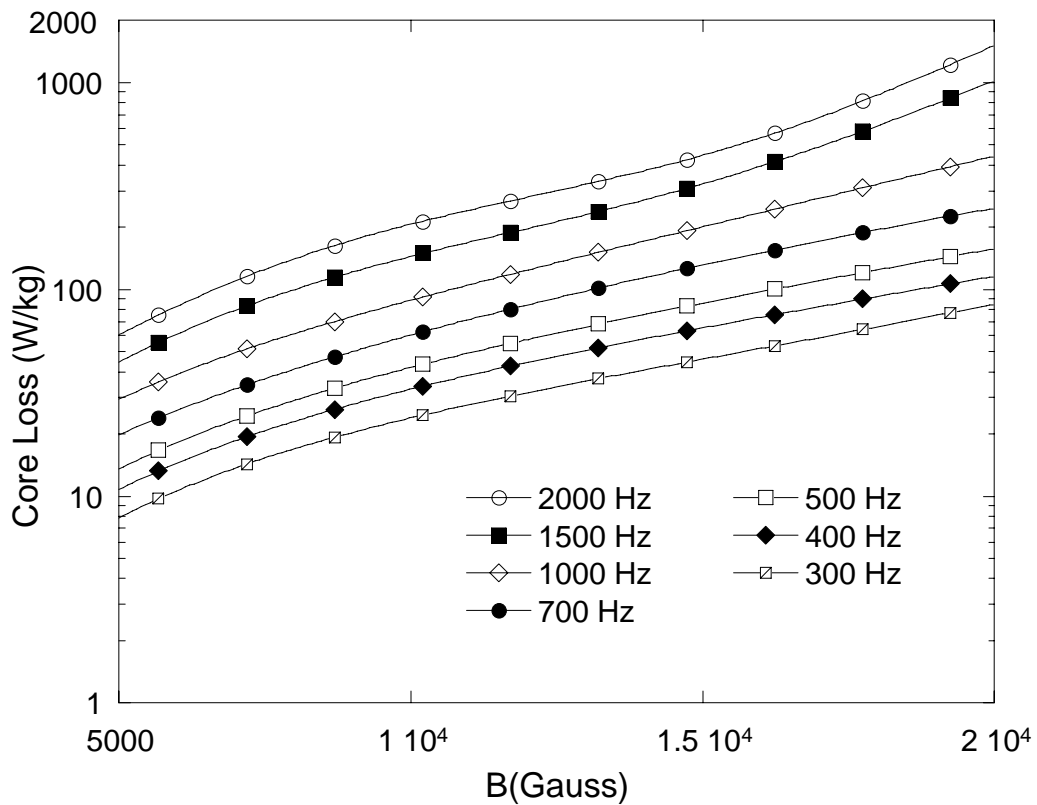


Figure 3.1.56 Core losses of 2000 hours-aged Hipercro 27 alloy taken at 300 °C

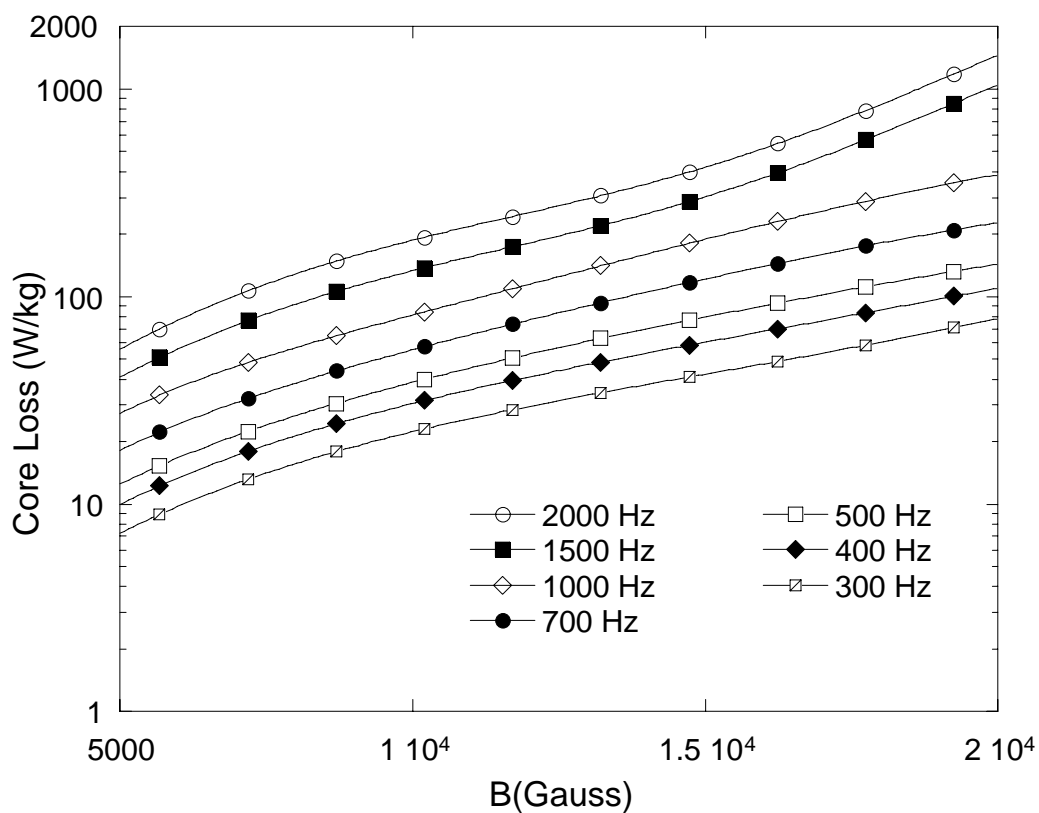


Figure 3.1.57 Core losses of 2000 hours-aged Hipercro 27 alloy taken at 400 °C

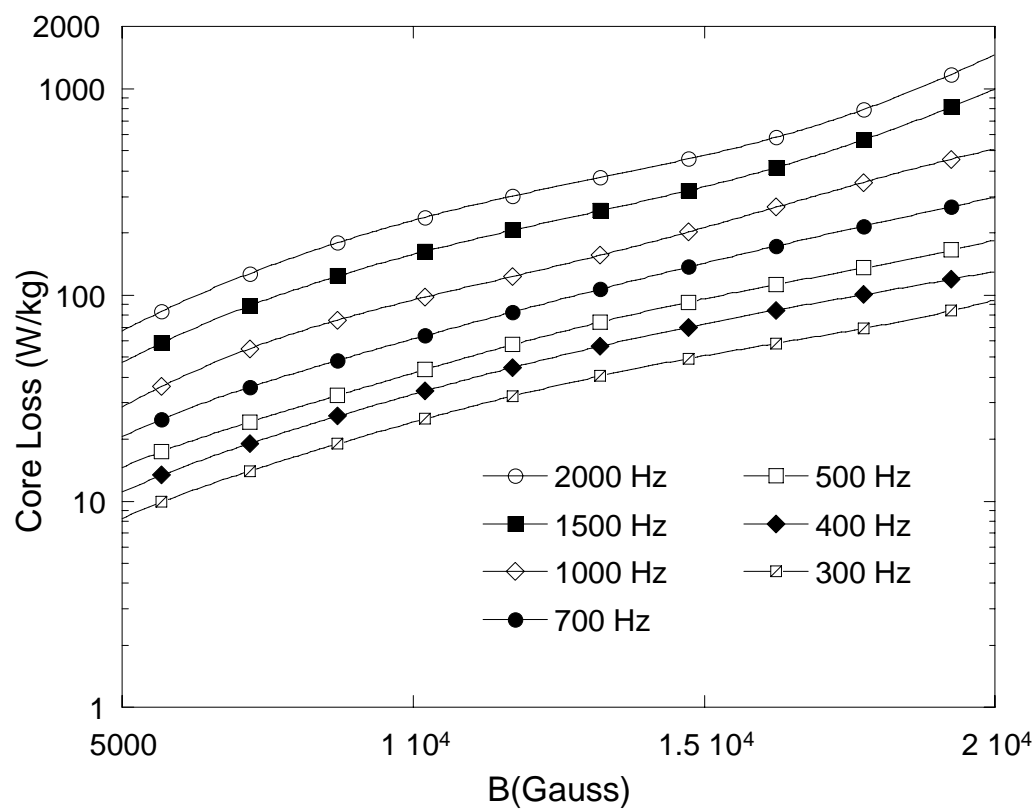


Figure 3.1.58 Core losses of 2000 hours-aged Hipercro 50 alloy taken at RT

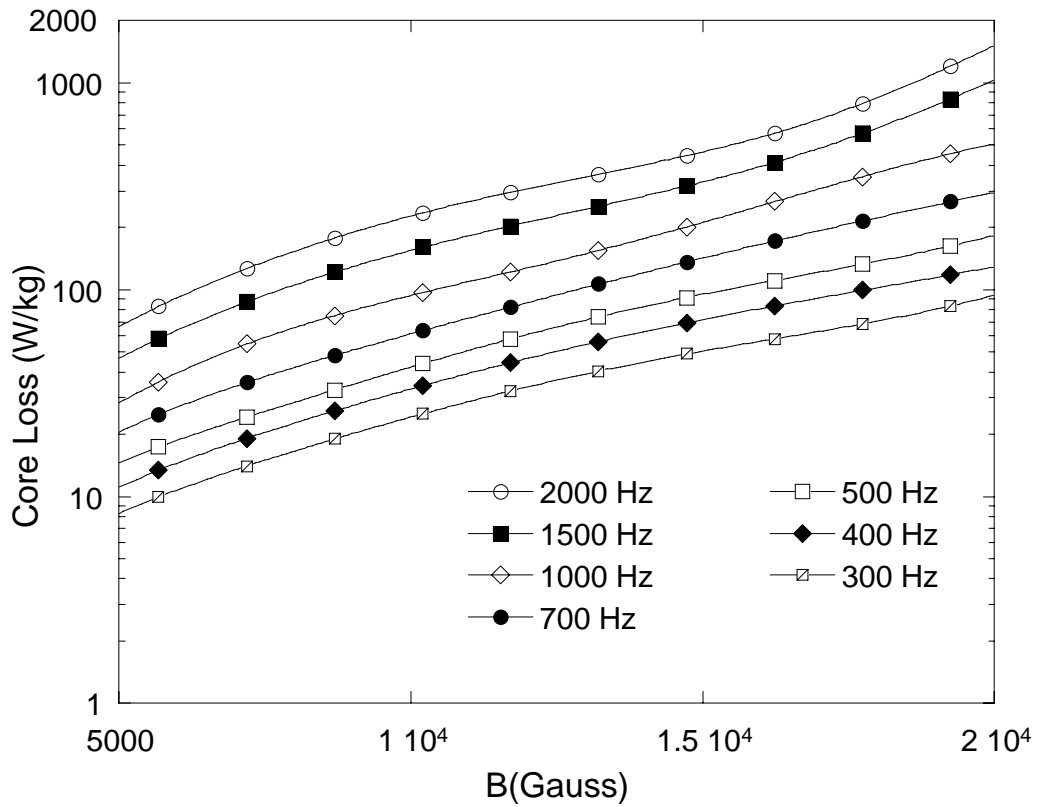


Figure 3.1.59 Core losses of 2000 hours-aged Hipercro 50 alloy taken at 100°C

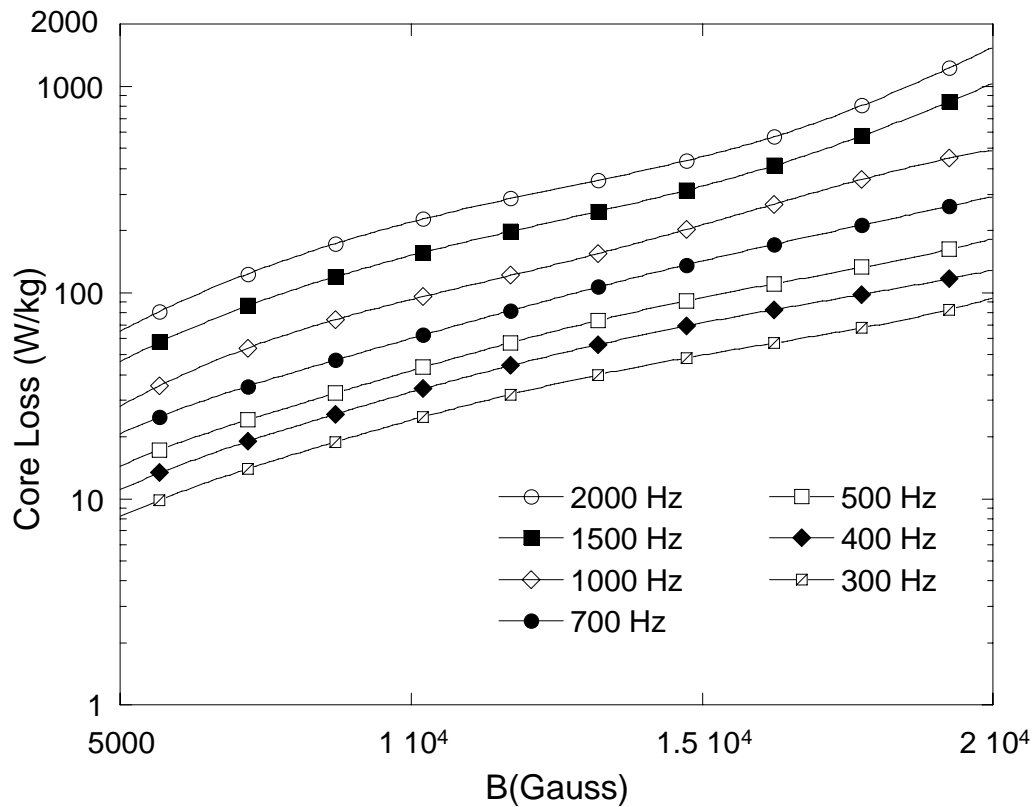


Figure 3.1.60 Core losses of 2000 hours-aged Hipercro 50 alloy taken at 200°C

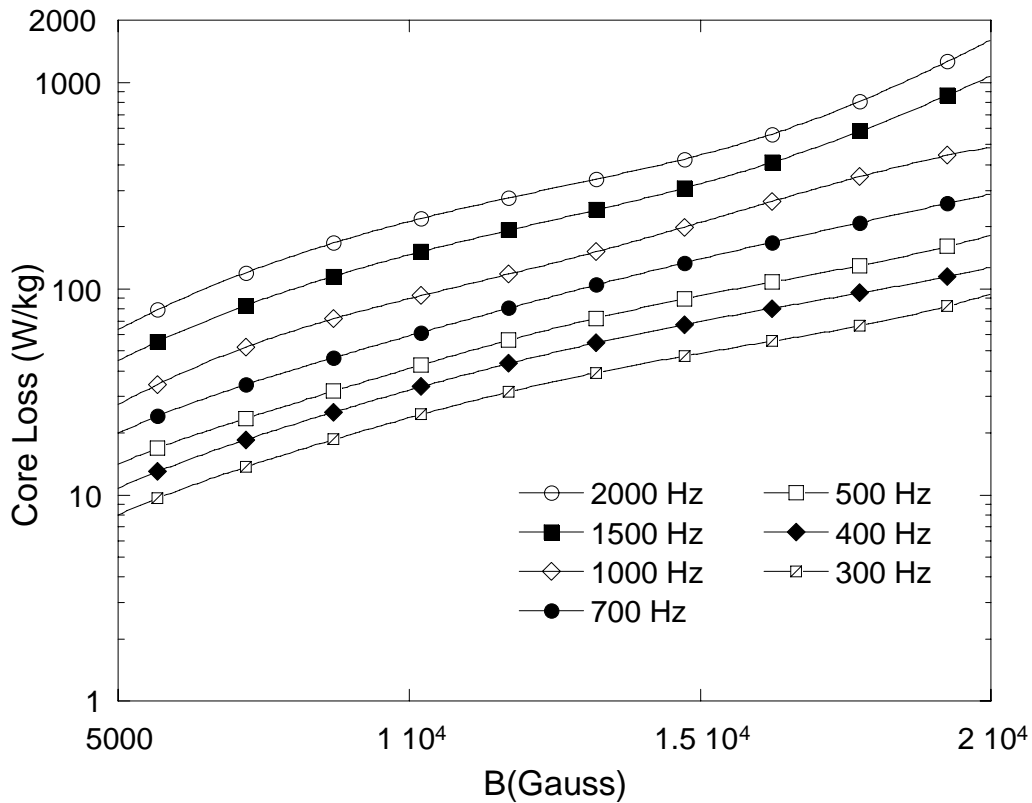


Figure 3.1.61 Core losses of 2000 hours-aged Hipercó 50 alloy taken at 300 °C

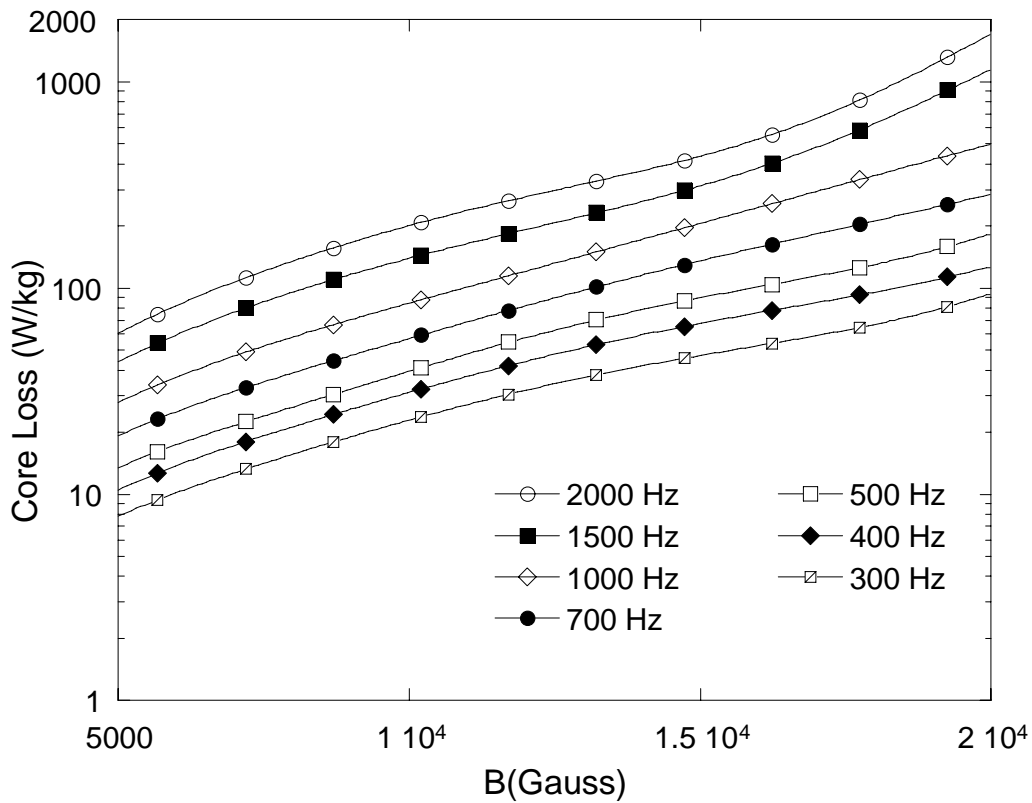


Figure 3.1.62 Core losses of 2000 hours-aged Hipercó 50 alloy taken at 400 °C

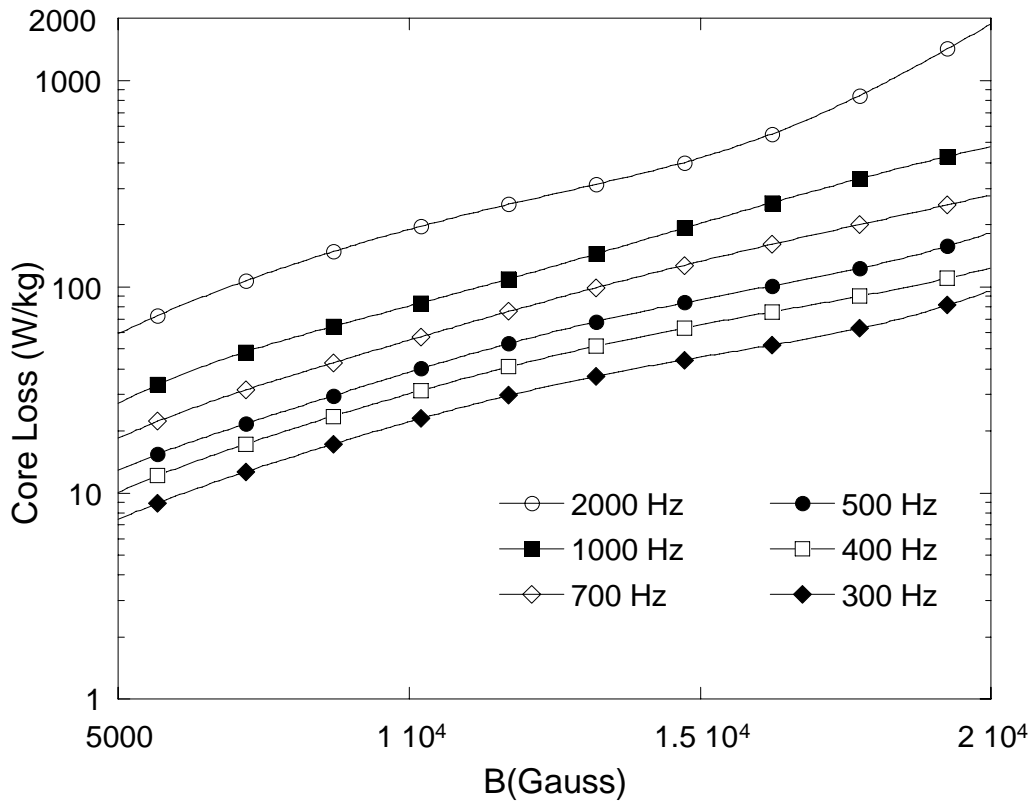


Figure 3.1.63 Core losses of 2000 hours-aged Hipercro 50 alloy taken at 500 ° C

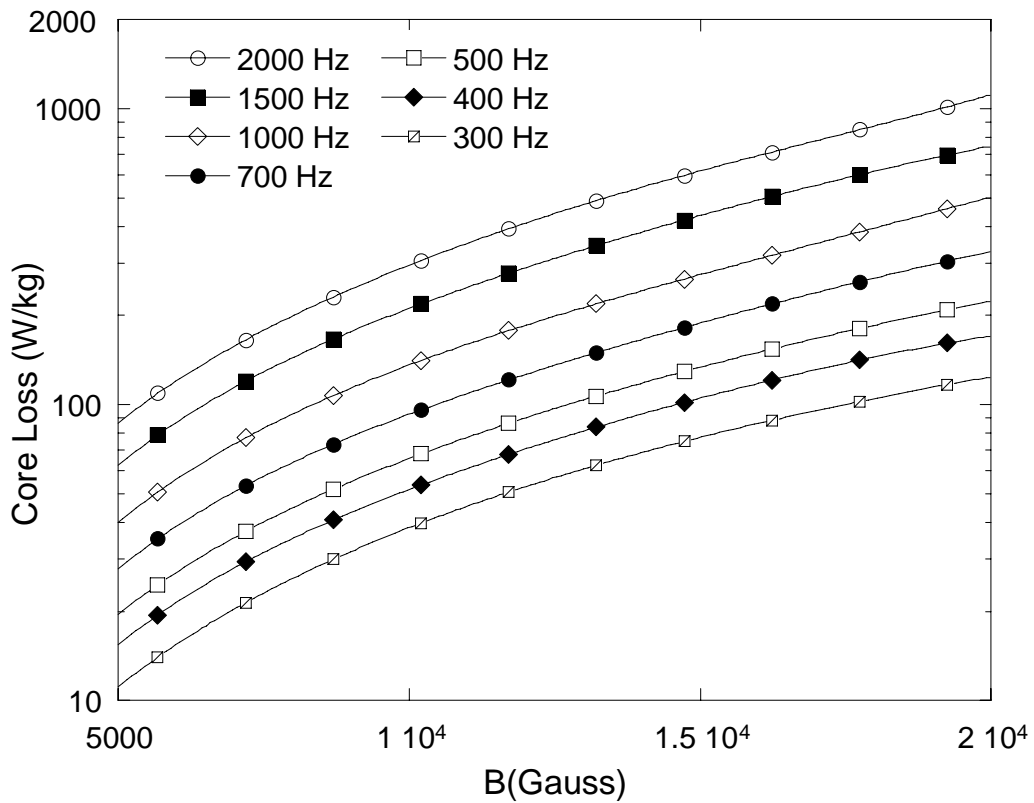


Figure 3.1.64 Core losses of 2000 hours-aged Hipercro 50 HS alloy taken at RT

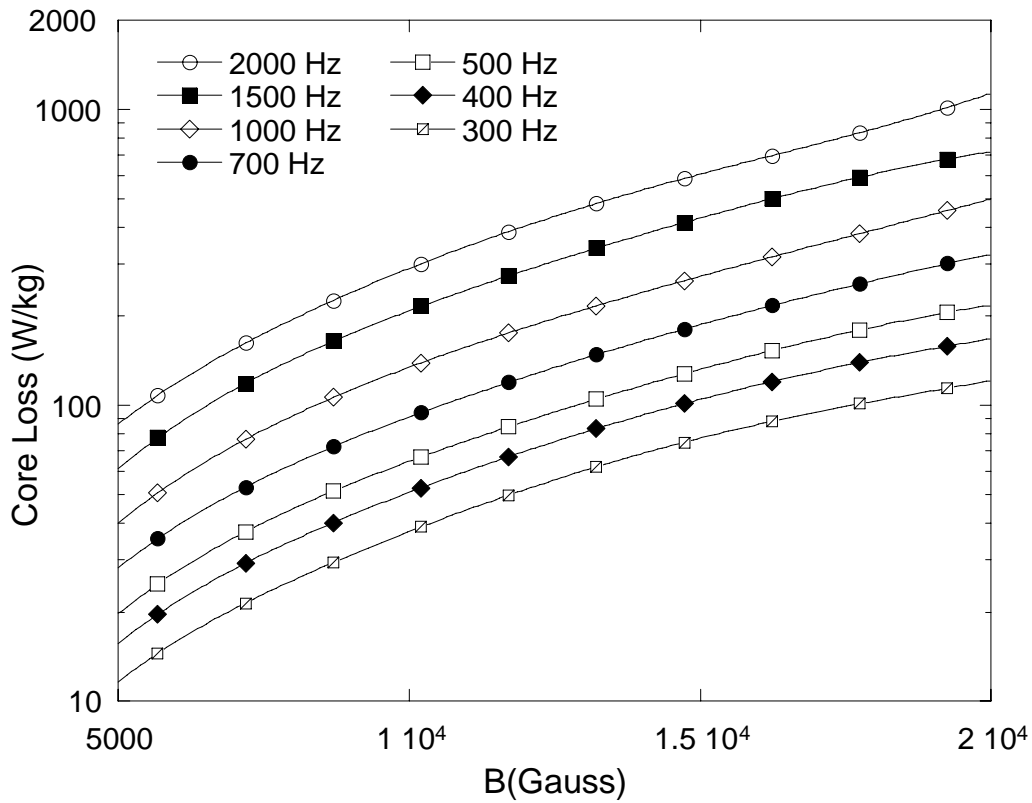


Figure 3.1.65 Core losses of 2000 hours-aged Hipercor 50 HS alloy taken at 100 °C

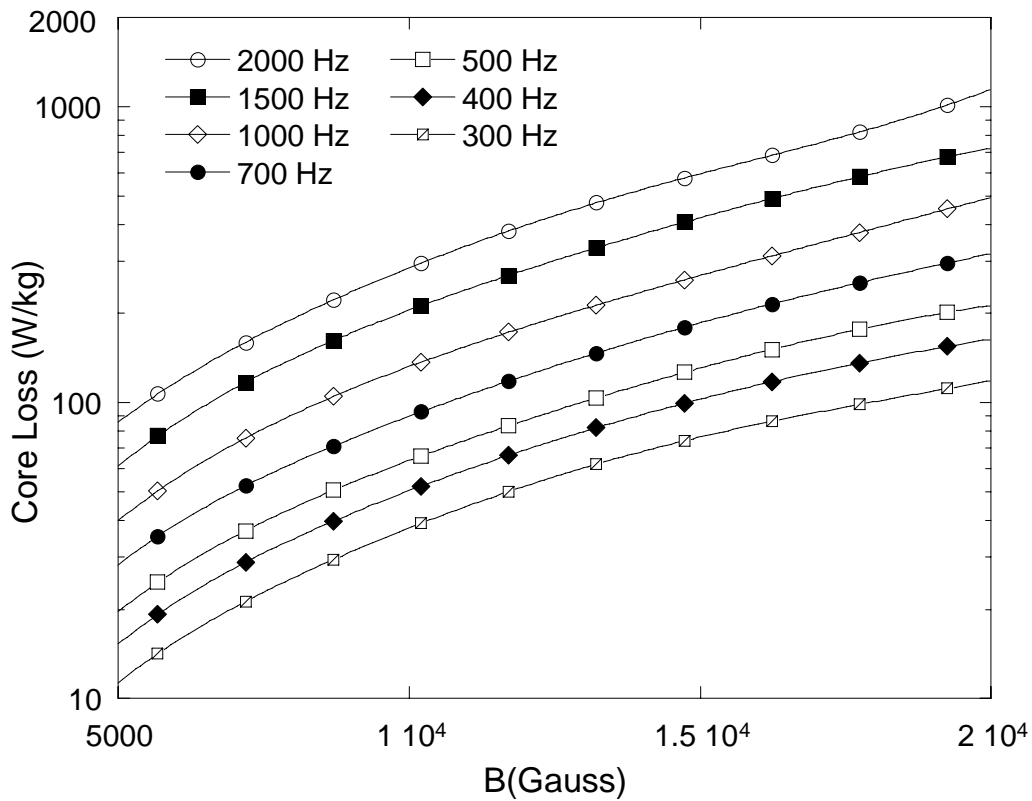


Figure 3.1.66 Core losses of 2000 hours-aged Hipercor 50 HS alloy taken at 200 °C

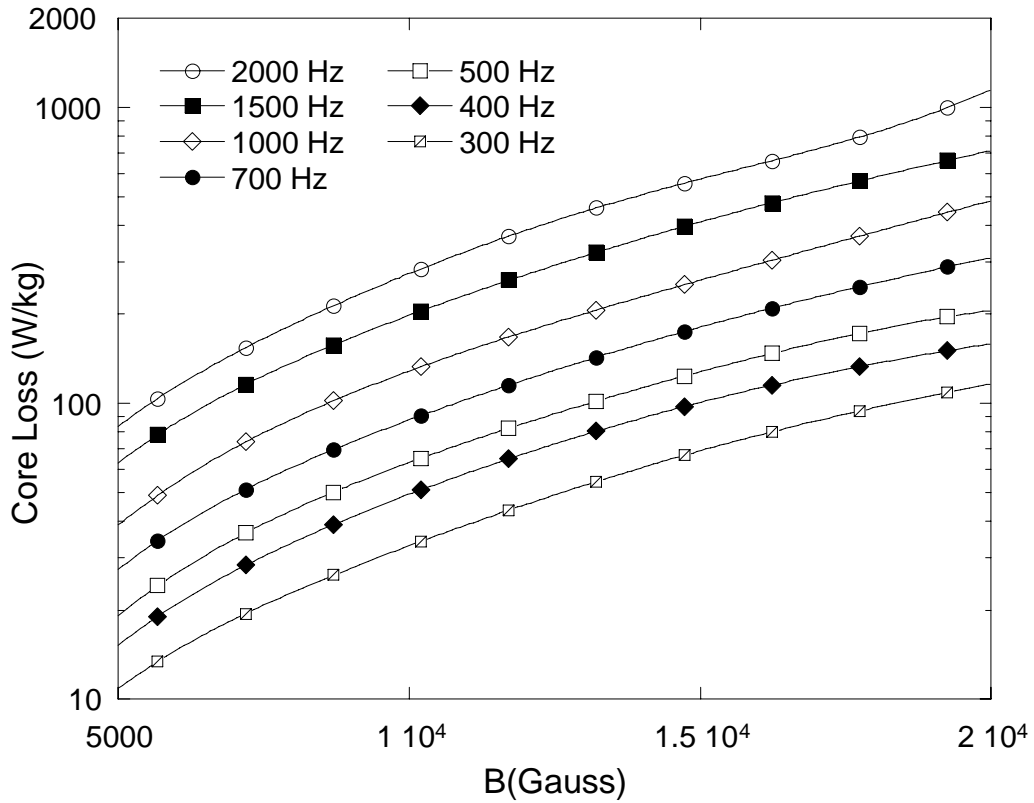


Figure 3.1.67 Core losses of 2000 hours-aged Hipercro 50 HS alloy taken at 300 °C

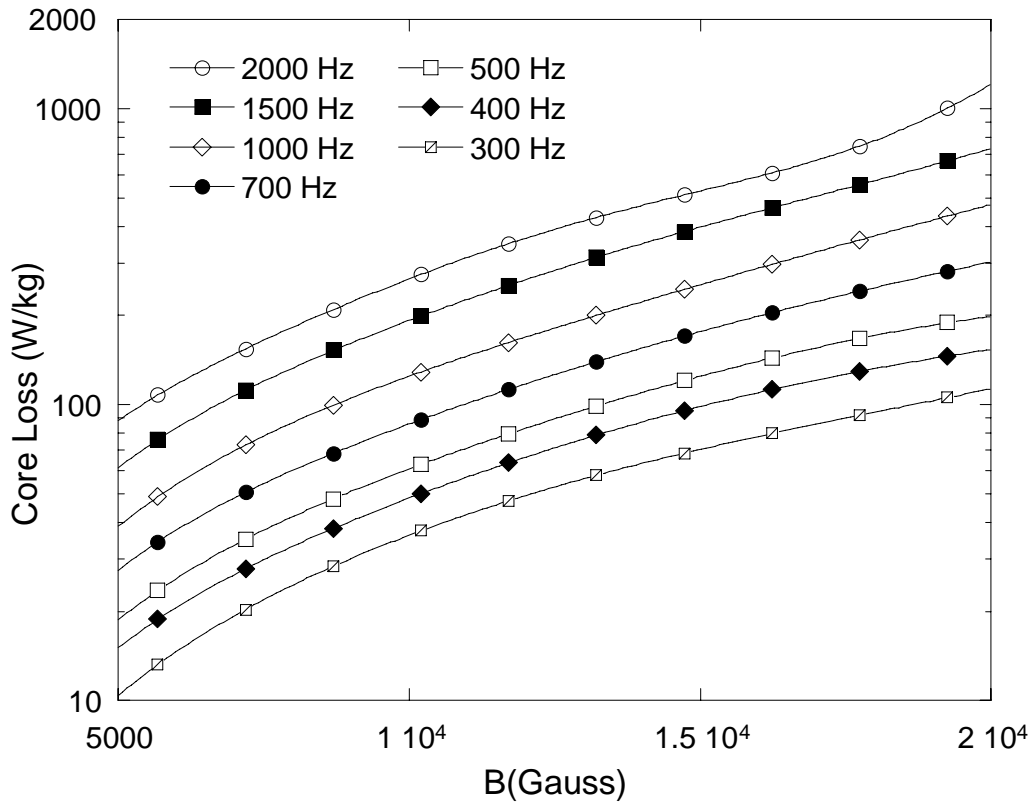


Figure 3.1.68 Core losses of 2000 hours-aged Hipercro 50 HS alloy taken at 400 °C

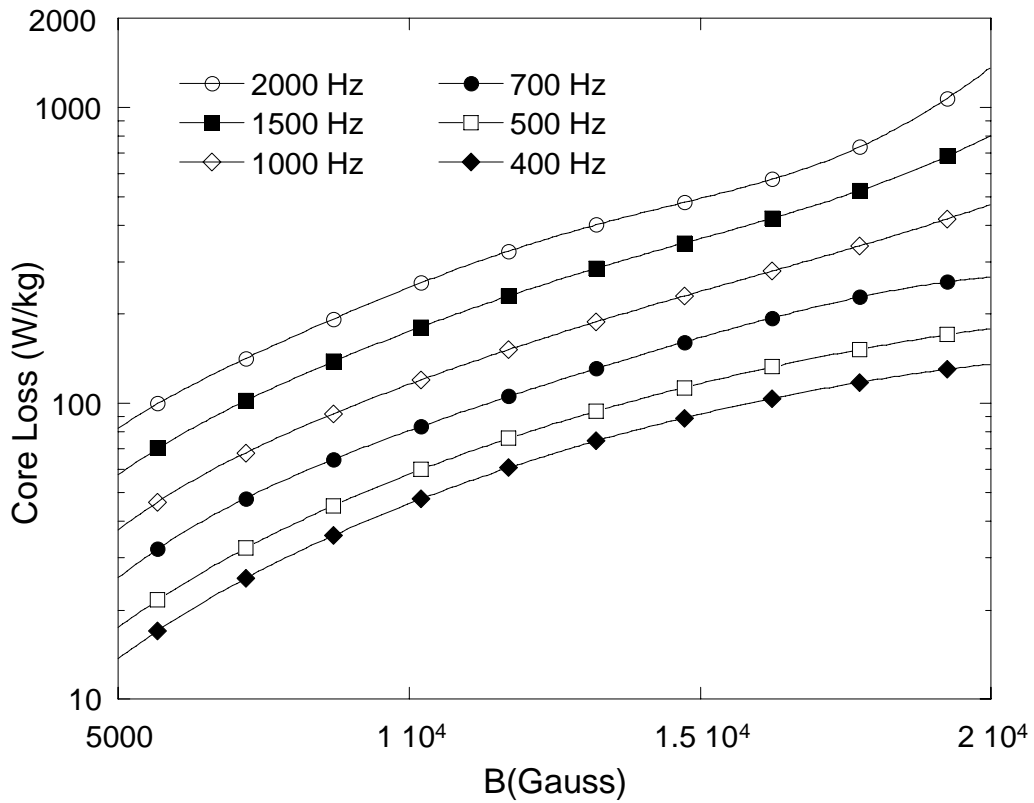


Figure 3.1.69 Core losses of 2000 hours-aged Hipercro 50 HS alloy taken at 500 °C

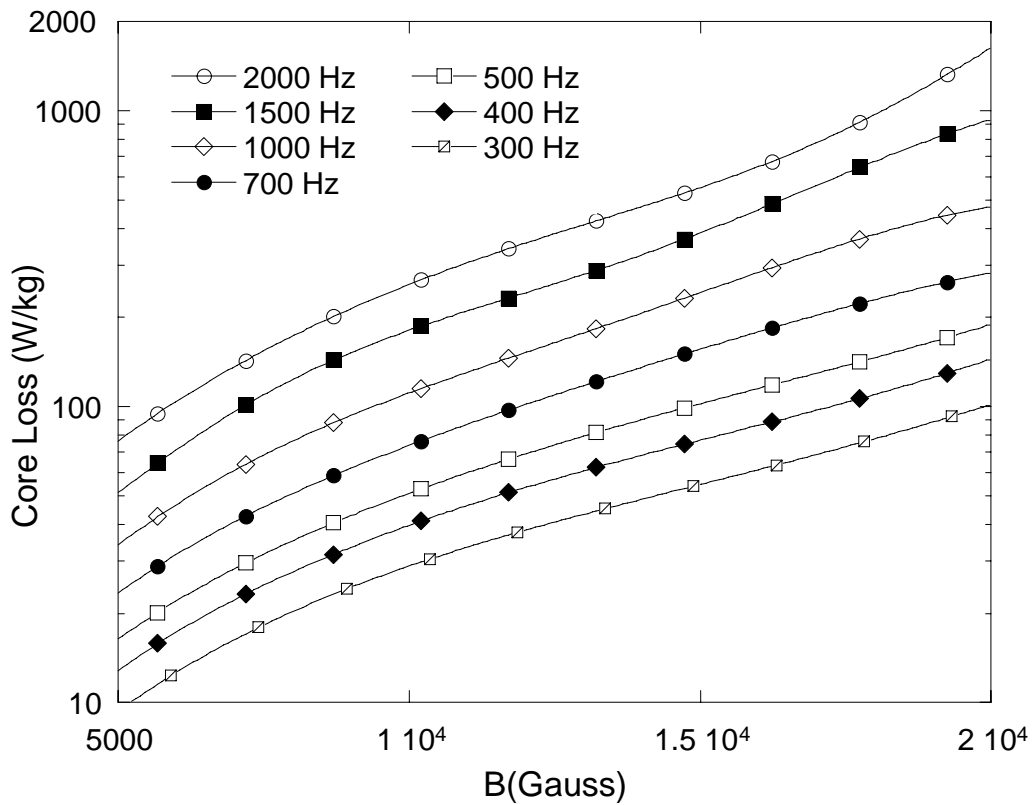


Figure 3.1.70 Core losses of 5000 hours-aged Hipercro 27 alloy taken at RT

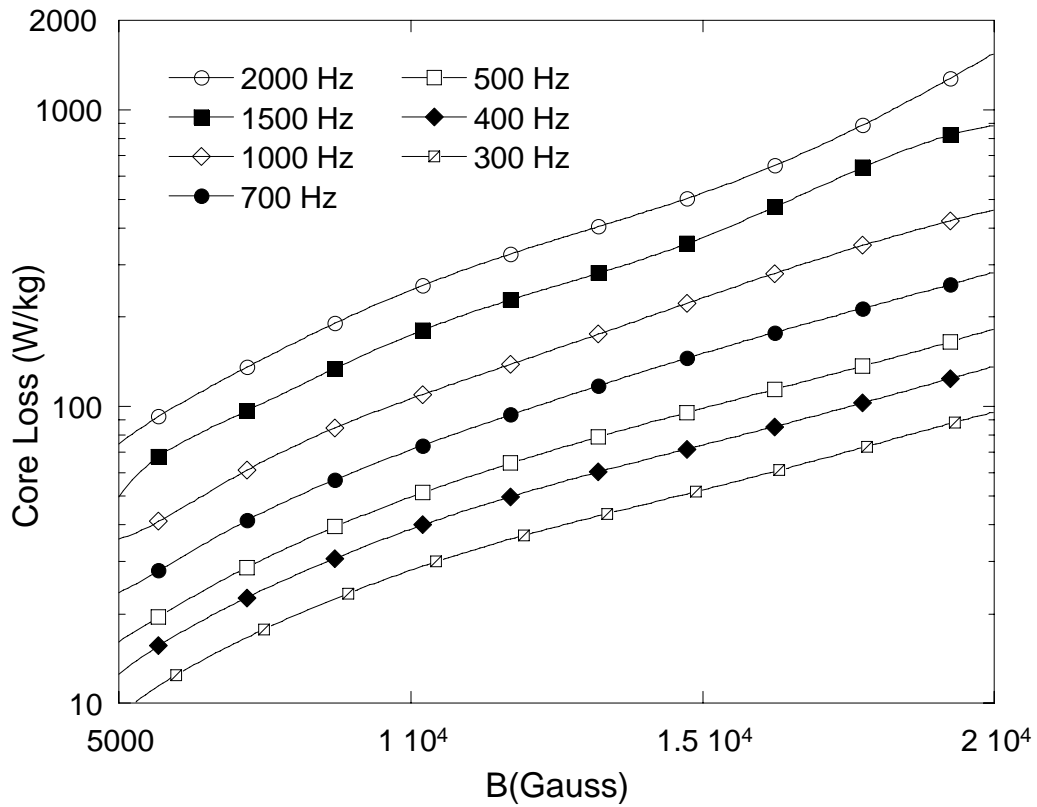


Figure 3.1.71 Core losses of 5000 hours-aged Hipercor 27 alloy taken at 100 °C

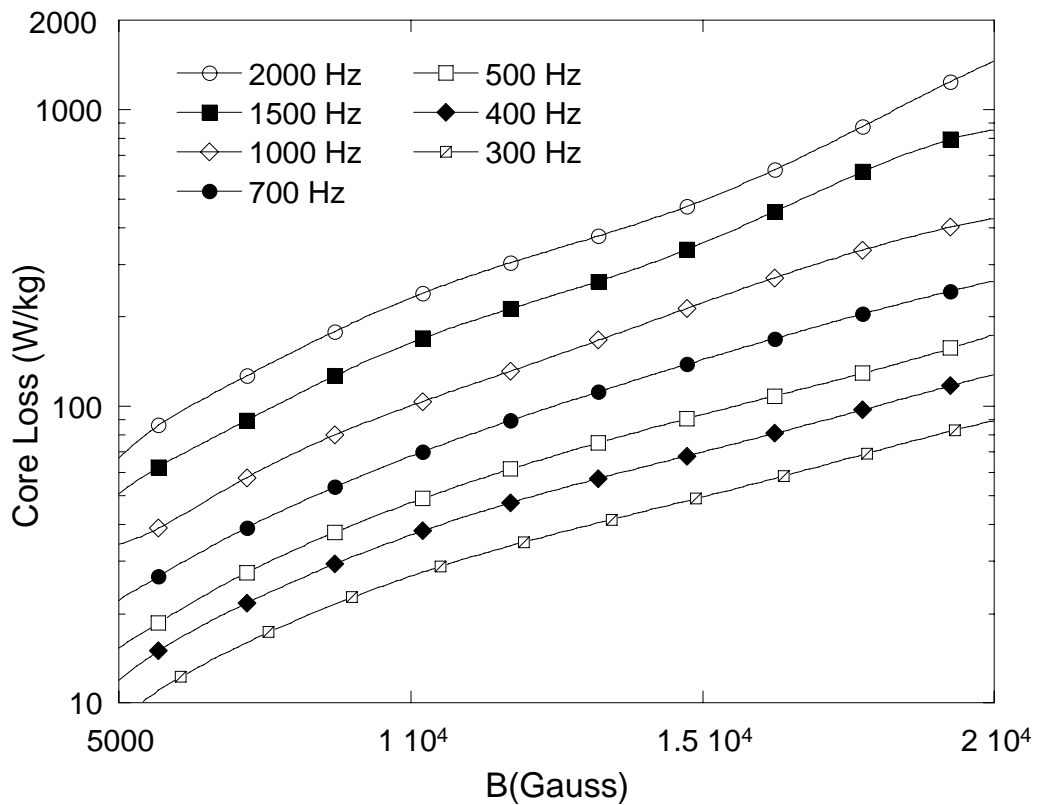


Figure 3.1.72 Core losses of 5000 hours-aged Hipercor 27 alloy taken at 200 °C

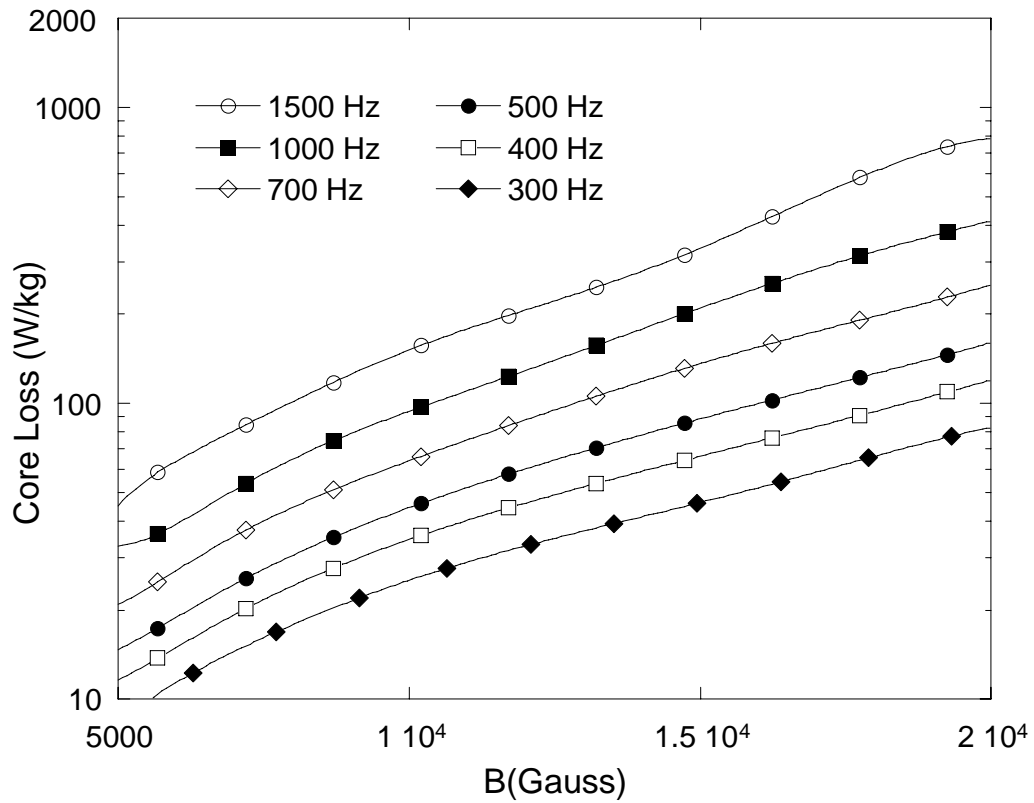


Figure 3.1.73 Core losses of 5000 hours-aged Hipercro 27 alloy taken at 300 °C

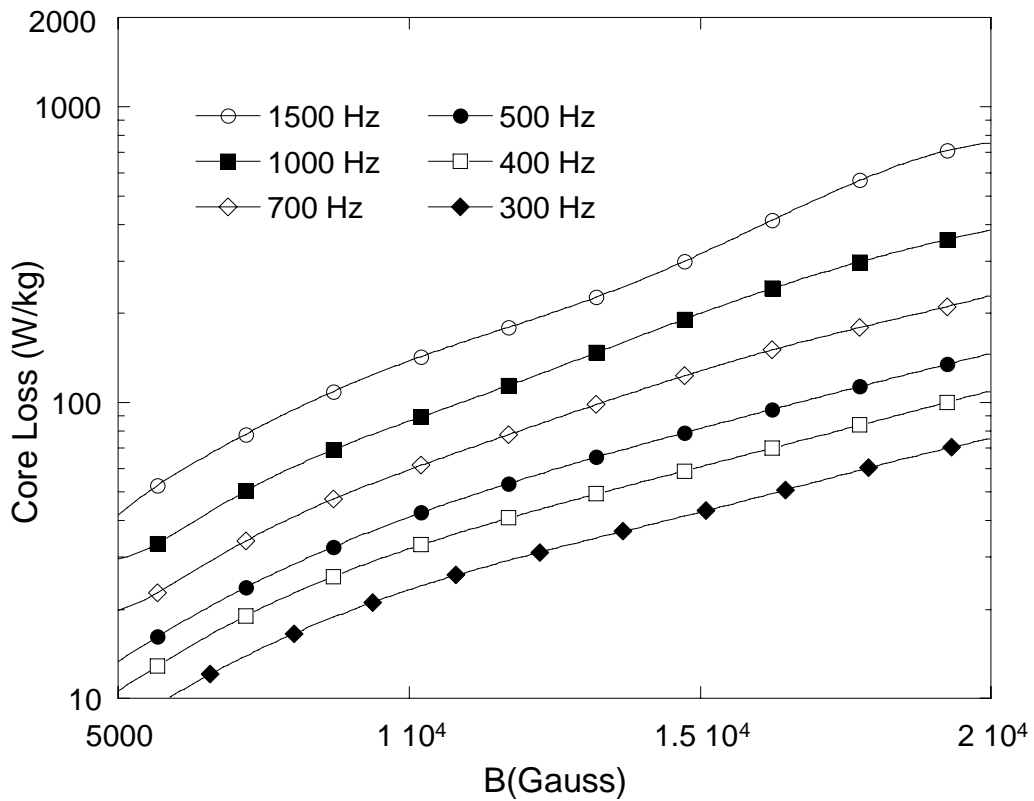


Figure 3.1.74 Core losses of 5000 hours-aged Hipercro 27 alloy taken at 400 °C

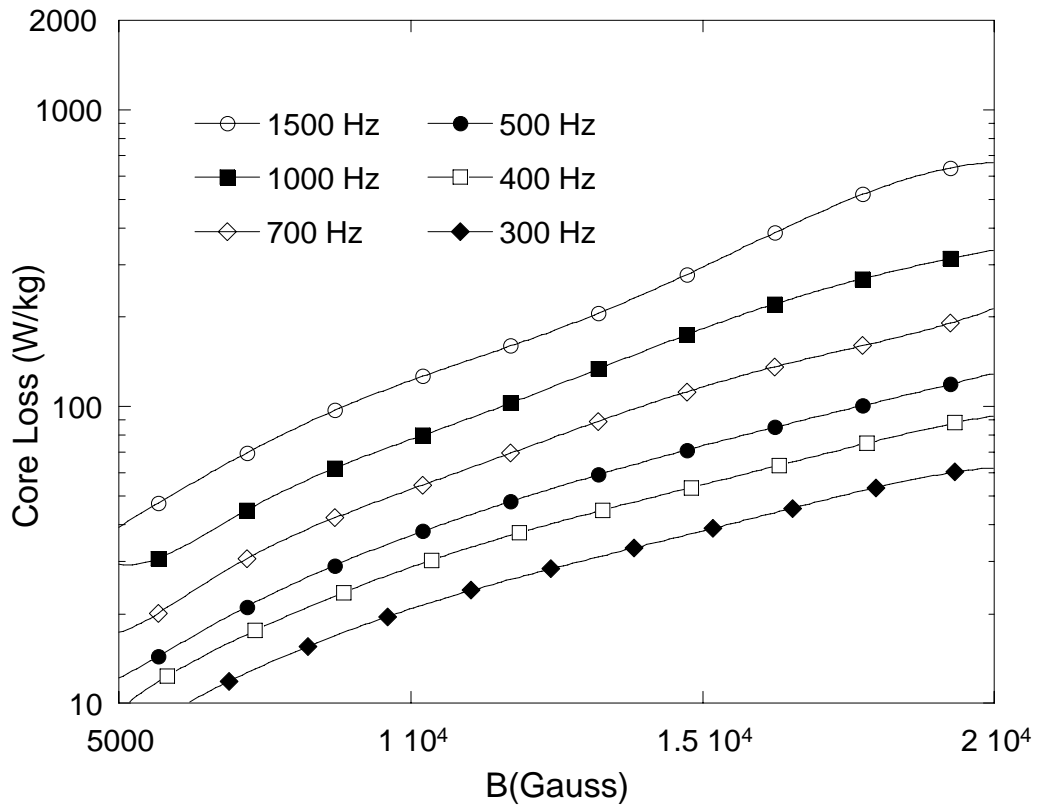


Figure 3.1.75 Core losses of 5000 hours-aged Hipercro 27 alloy taken at 500 °C

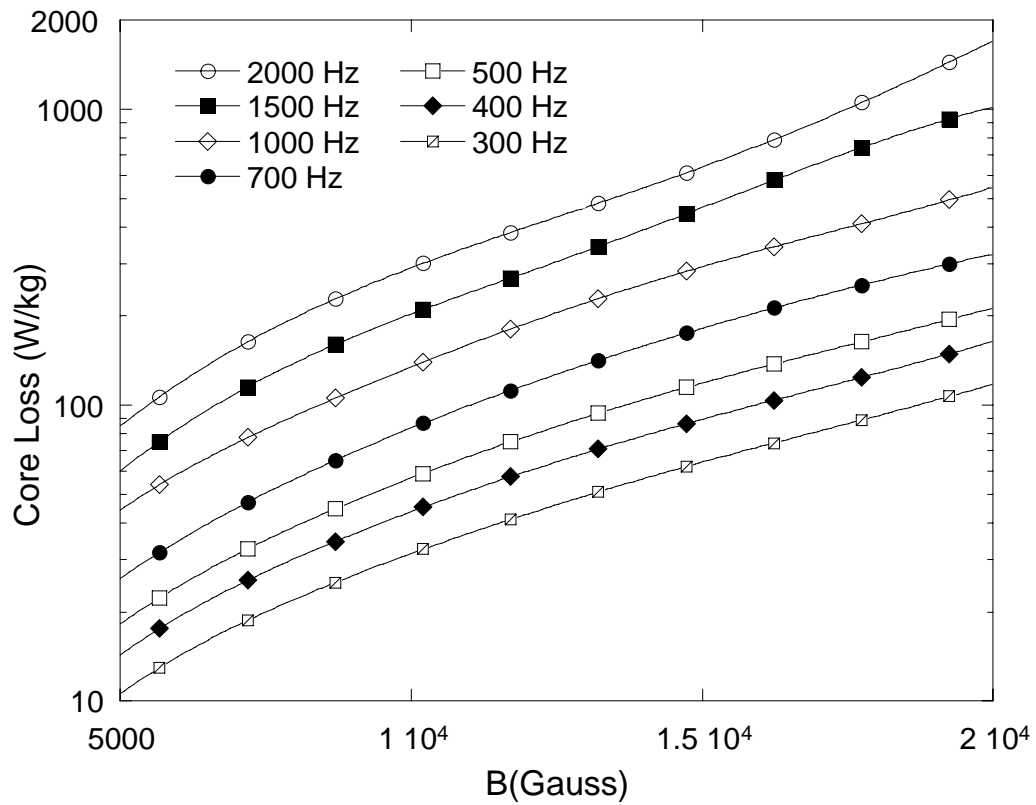


Figure 3.1.76 Core losses of 5000 hours-aged Hipercro 50 alloy taken at RT.

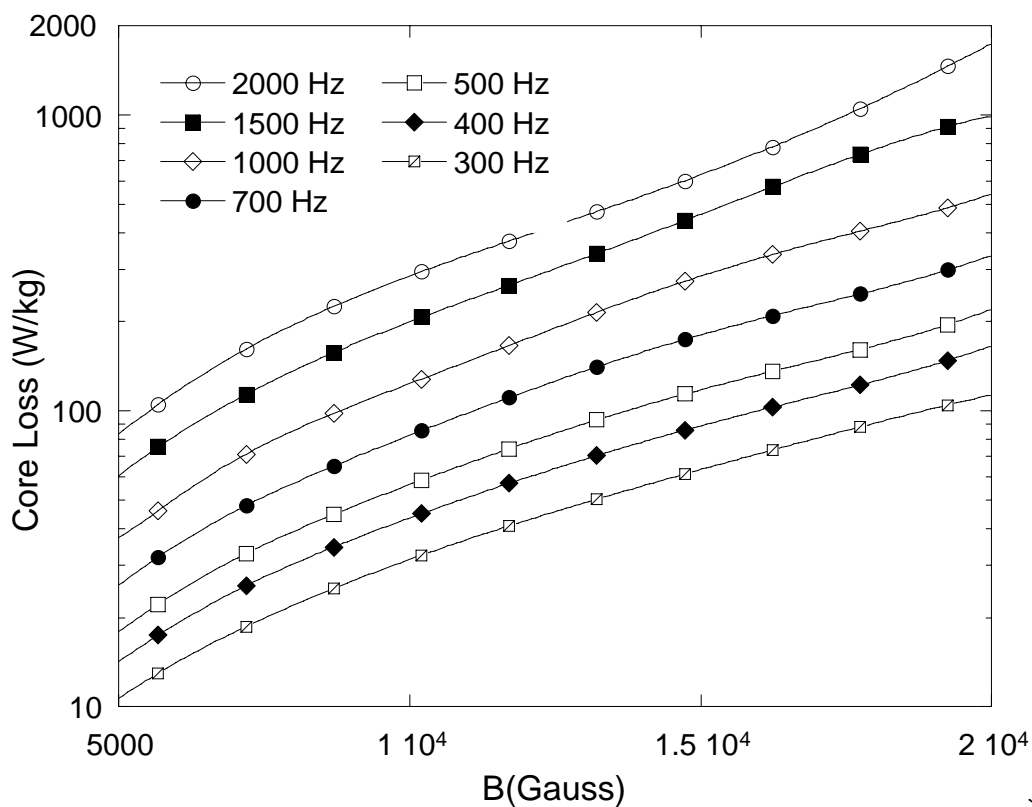


Figure 3.1.77 Core losses of 5000 hours-aged Hipercro 50 alloy taken at 100°C

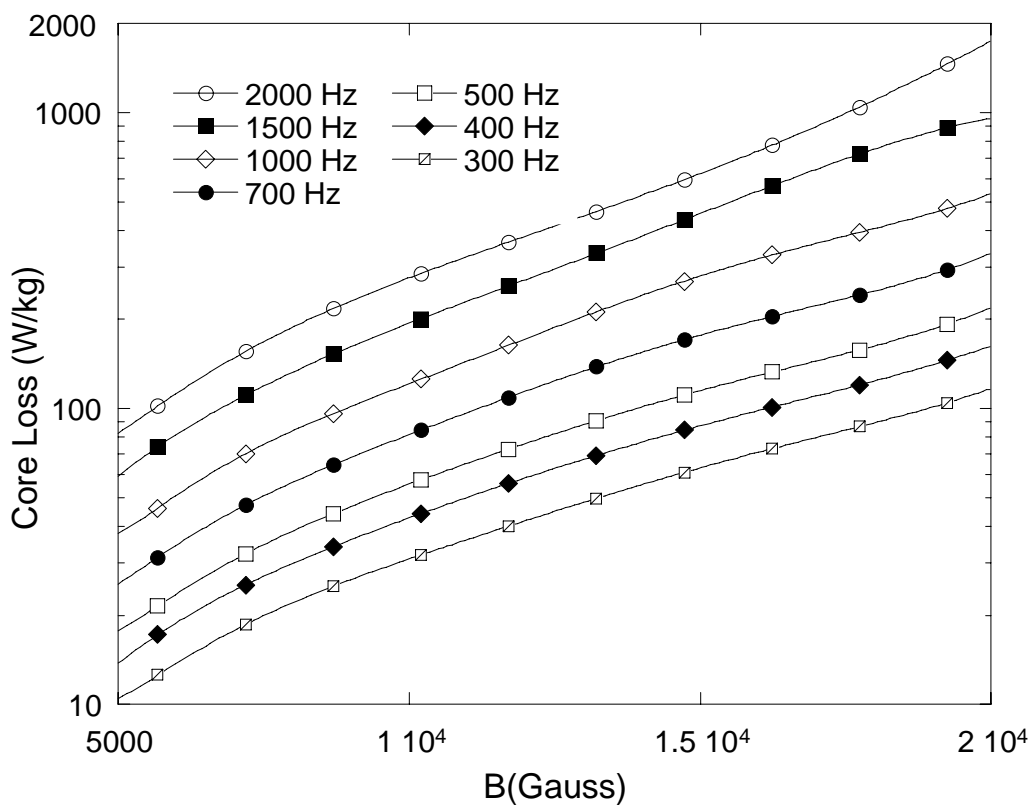


Figure 3.1.78 Core losses of 5000 hours-aged Hipercro 50 alloy taken at 200°C

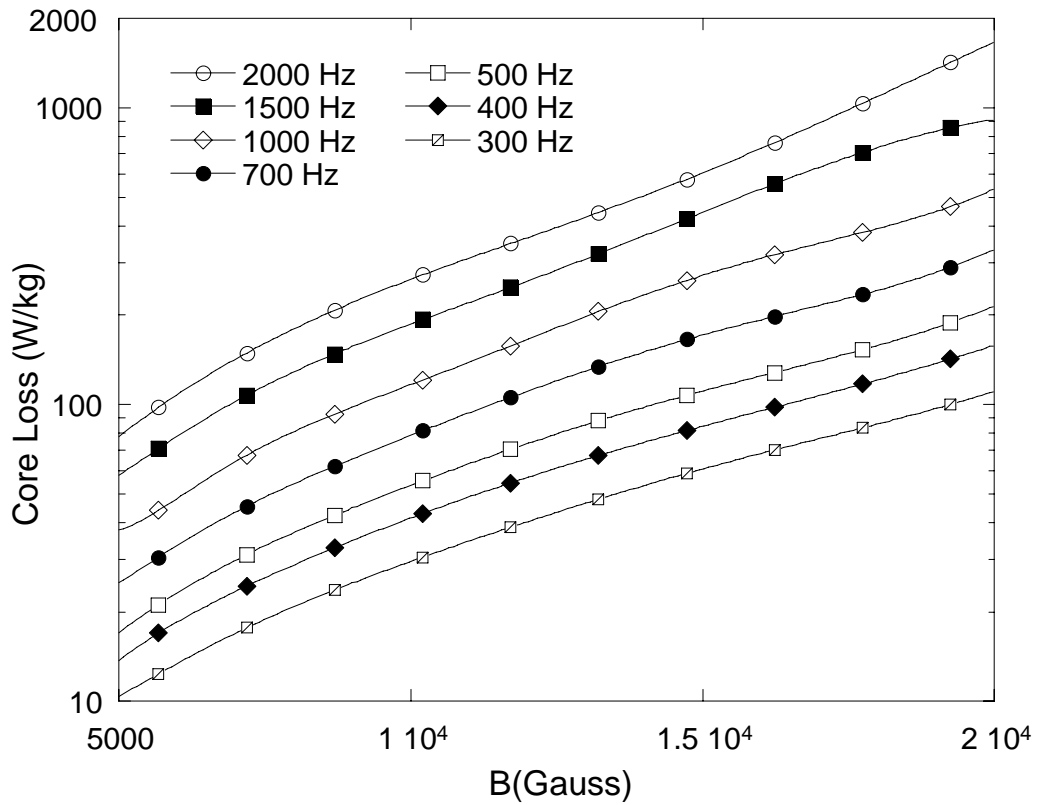


Figure 3.1.79 Core losses of 5000 hours-aged Hipercó 50 alloy taken at 300 °C

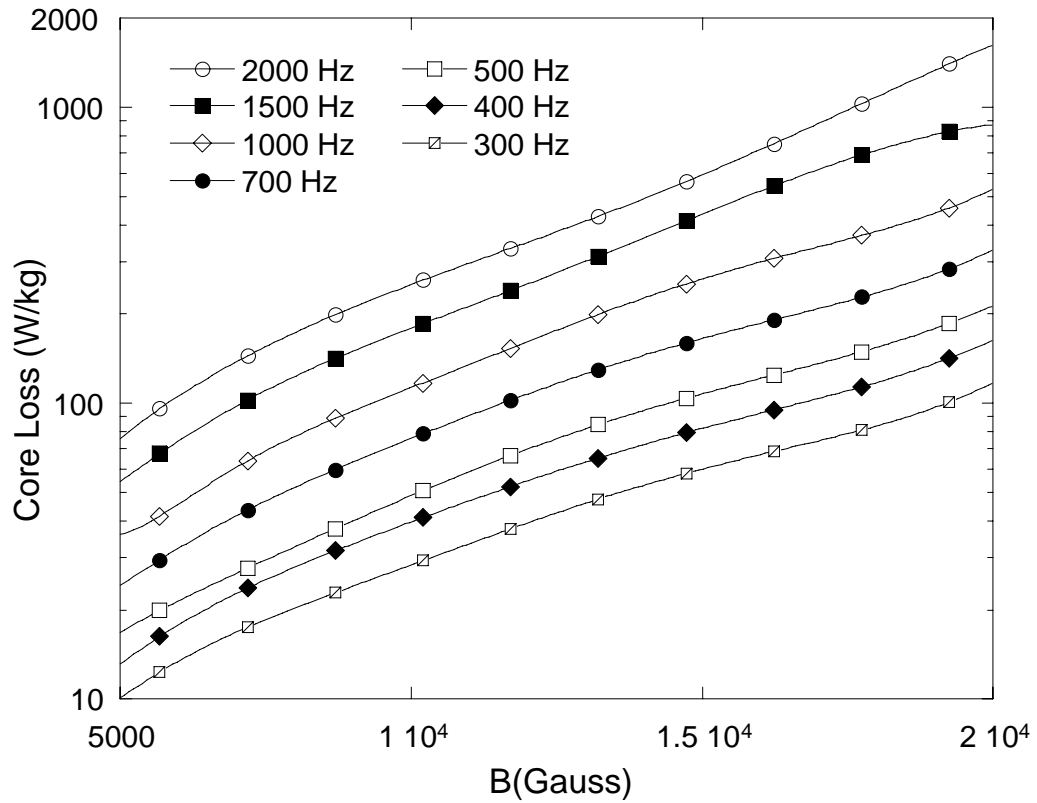


Figure 3.1.80 Core losses of 5000 hours-aged Hipercó 50 alloy taken at 400 °C

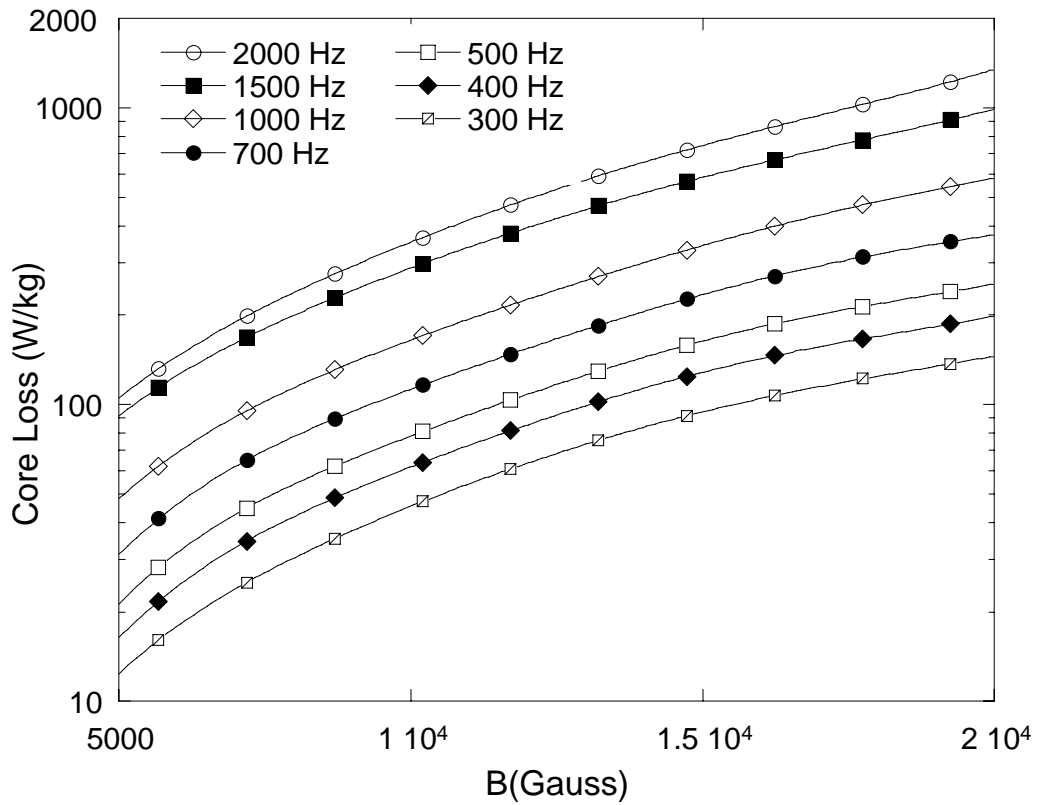


Figure 3.1.81 Core losses of 5000 hours-aged Hiperc 50 HS alloy taken at RT

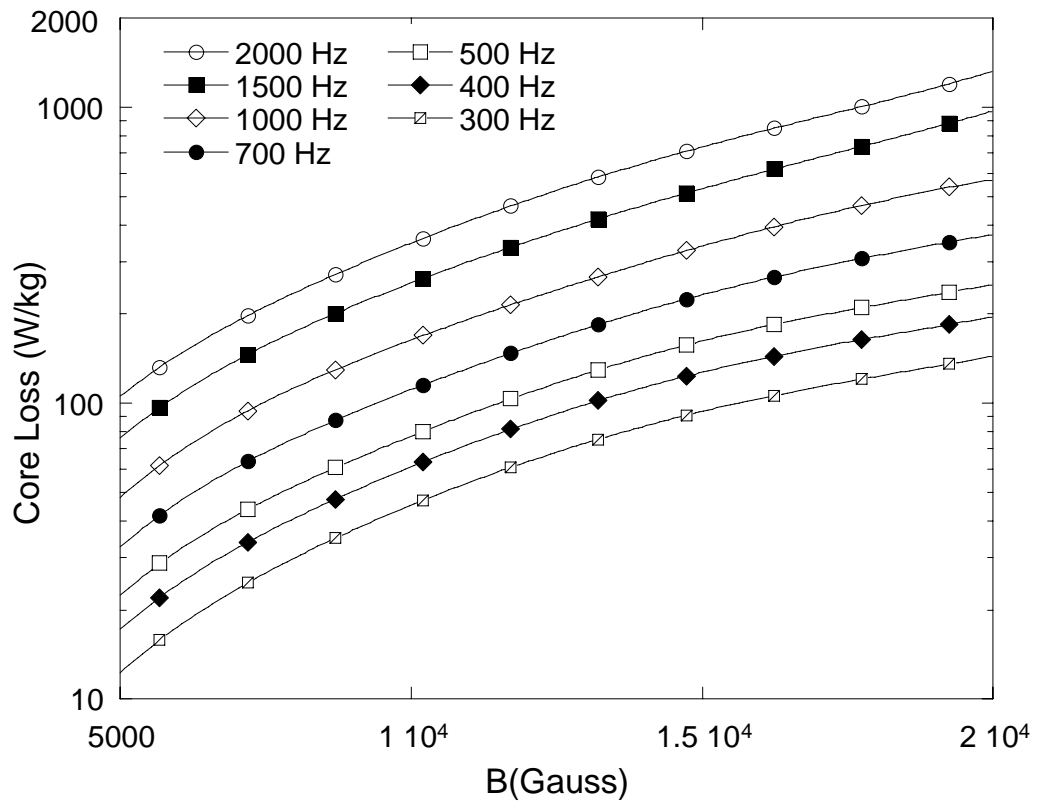


Figure 3.1.82 Core losses of 5000 hours-aged Hiperc 50 HS alloy taken at 100 °C

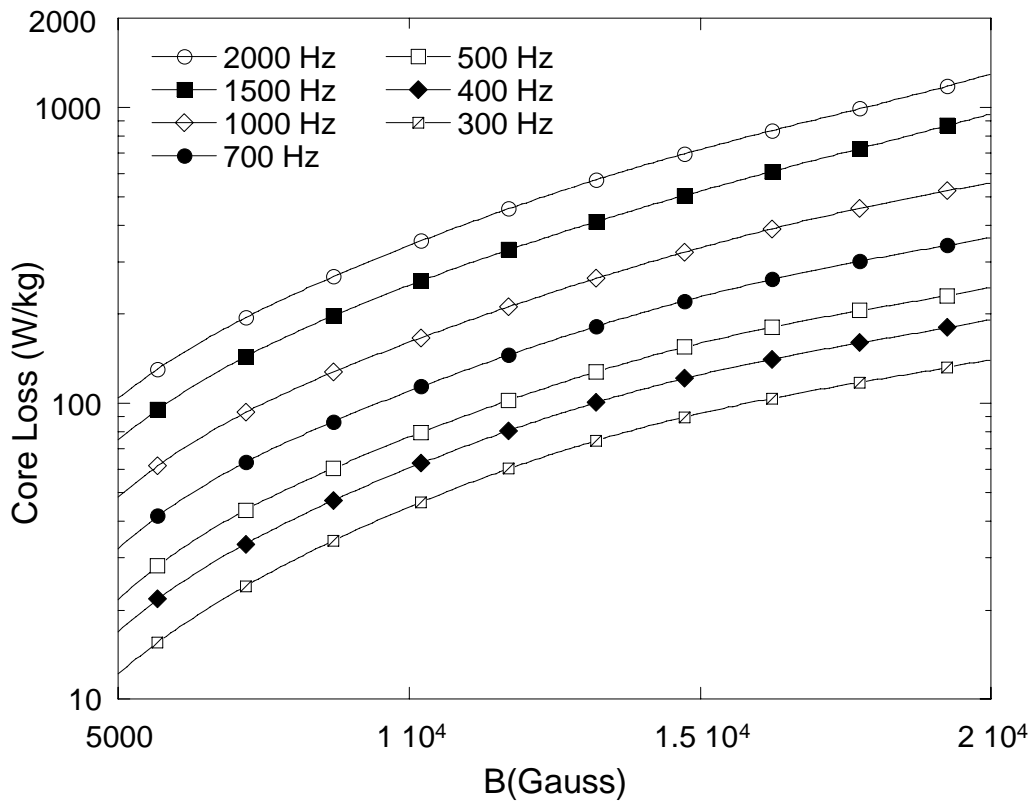


Figure 3.1.83 Core losses of 5000 hours-aged Hipercó 50 HS alloy taken at 200 °C

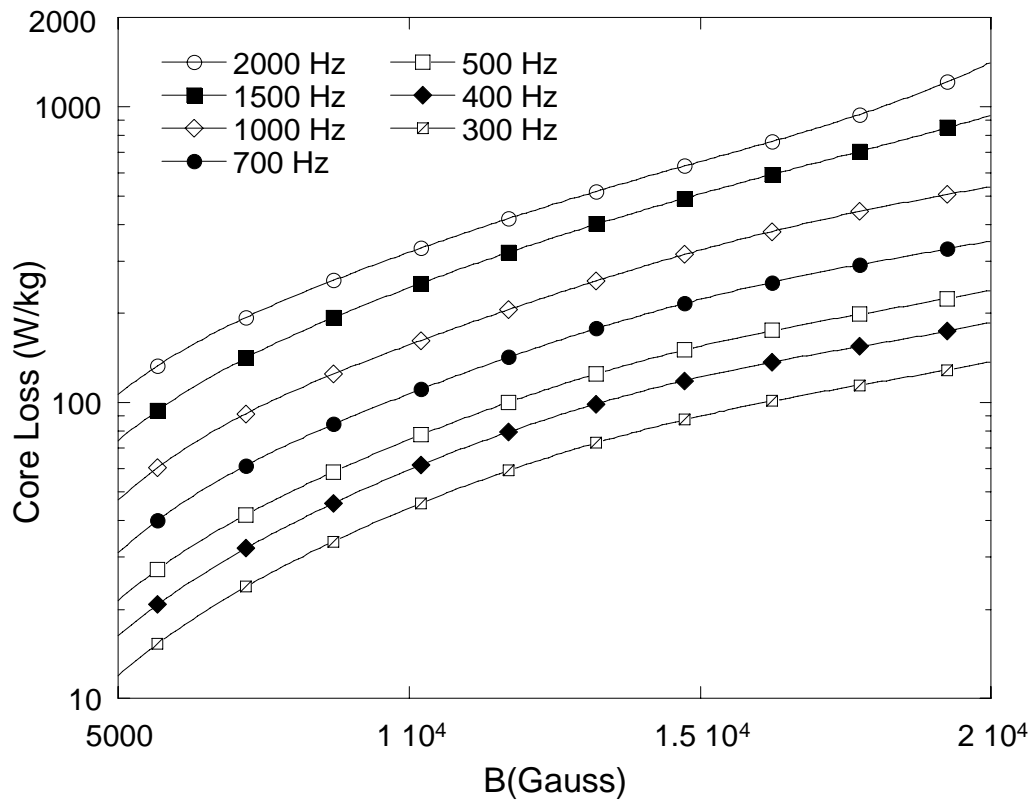


Figure 3.1.84 Core losses of 5000 hours-aged Hipercó 50 HS alloy taken at 300 °C

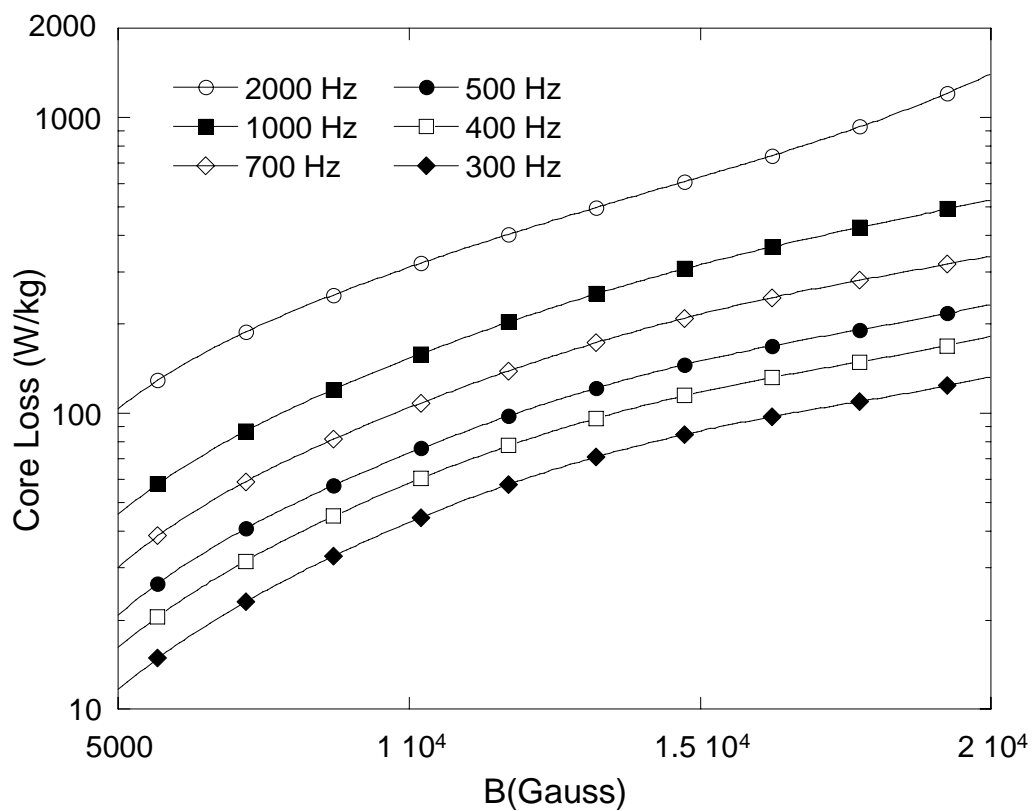


Figure 3.1.85 Core losses of 5000 hours-aged Hipercro 50 HS alloy taken at 400 °C

3.2 Mechanical Properties

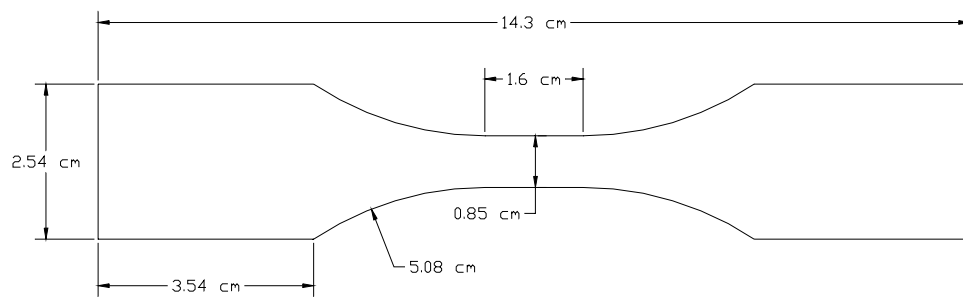
Until recently, many of the experimental and theoretical works have focused on magnetic properties of the Fe-Co alloy system since this class of alloys has satisfactory mechanical properties for applications at moderate temperatures. The manufacturer, Carpenter Specialty Alloys, specifies in their materials data sheet yield strengths of these alloys along with magnetic and electrical properties as a function of annealing time performed after cold deformation. Much of the earlier work done on the mechanical behaviors of the Fe-Co alloys was due to poor cold deformation ability of this alloy system. N. F. Stoloff and R. G. Davies [3.1]-[3.2] investigated the effects of long-range order on the deformation modes and dislocation motion of an equiatomic Fe-Co alloy containing 2 % vanadium. They reported a peak in yield stress at a critical degree of order. The fracture behavior of three compositions of Fe-Co alloys was studied by Zhao et al [3.3]. He concluded that all three alloys are more ductile in the disordered state than in the ordered state. Also, the stoichiometric alloy had less ductility than the two off-stoichiometric alloys, for both ordered and disordered states. Baker and Schulson [3.4] had suggested that partially disordered grain boundaries are needed for improved ductility. Glezer et al. [3.5] reported that ordered Fe-Co-2%V, which is more ductile than FeCo, had a higher impurity concentration along the grain boundaries than reported for FeCo. A niobium-containing variant of the commercial Fe-Co-2%V, which was introduced in the mid-nineties, received limited attention and only a few reports [3.6] have been published on the properties at elevated temperatures. No publications were found relating to high temperature performance as a function of time for the alloys Hiperco 50 and Hiperco 50HS.

Electromachines with high rotational speeds at high temperatures require a material not only with a combination of soft magnetic properties and high mechanical strength but also with a high creep resistance. Only the niobium-containing variant was explored [3.7]-[3.8] in terms of creep resistance and no publications were found relating to creep behavior as a function of aging time.

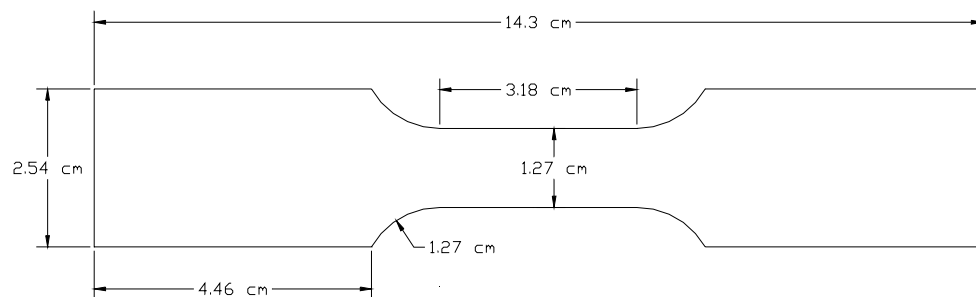
Specimens and Procedures

Flat “dog-bone” mechanical test specimens were cut with an electron discharge machine (EDM) oriented 45° to the manufacturer’s rolling direction. A 45° orientation was chosen based on previous studies indicating that it was the weakest direction. The specimens

were subsequently heat-treated in a dry hydrogen atmosphere at 730°C for 45 minutes, followed by cooling to room temperature at a rate of 177 ° C/h. The specimens used for tensile testing had a 1.6 cm gage length and a 0.85 cm gage width with a gage end blend radius of 5.08 cm. The specimens used for creep testing had a 3.18 cm gage length and a 1.27 cm gage width with a gage end blend radius of 1.27 cm. These specimen configurations are illustrated in Figure 3.3.1. Both specimen types were 14.3 cm in length and the tab ends were 2.54 cm wide. The specimens were then placed in a large capacity Applied Test Systems box furnace and subjected to an aging temperature of 500°C for 100, 1000, 2000 and 5000 hours under argon gas and air environments. Prior to testing, the specimen edges were hand-sanded with 600-grit paper and inspected for surface defects under an optical microscope to verify acceptable surface and edge conditions.



Tensile Specimen Configuration



Creep Specimen Configuration

Figure 3.2.1 Specimen Configurations

The small thickness and cross-sectional areas of both the tensile and creep specimens required particular attention to the measuring devices employed. An alignment fixture, specially designed and fabricated in-house, was used to clamp the grips in place while the specimens were inserted in order to prevent damage to the specimens. All of the data was recorded electronically. Yield strength as well as creep rates of all three alloys as a function of aging times and environments are reported in this document.

Tensile testing was performed in accordance with ASTM Standard E 8 for the room temperature tests and ASTM Standard E 21 for the elevated temperature tests. The tests were conducted on the Instron 4505 Tensile Machine at a cross-head speed of 1.0 mm per minute. These tests were performed at room temperature, 160°C, 320°C, and 480°C utilizing Class B-2 extensometers and bolt loaded compression grips with serrated faces. For the elevated temperature tests, the specimens were soaked at test temperature for 15 minutes prior to loading. Creep testing was performed in accordance with ASTM Standard E139 on a SATEC creep machine. The same grips, extensometer frame, class of extensometer, furnace, controller and thermocouples were used for creep testing as were used for the high temperature tensile tests.

Results: Tensile Testing

The following figure (3.2.2) gives the measured yield and ultimate strengths of the three alloys subjected to the initial common heat treatment and prior to any aging at an elevated temperature. As can be seen, the Hipercor 50HS material exhibits the highest yield strength at all temperatures tested, ranging from 550 MPa at room temperature to about 480 MPa at 480°C. Although the Hipercor 27 alloy had yield strength slightly higher than the Hipercor 50, it was less thermally stable at elevated temperatures, eventually exhibiting a yield strength 25% less than the Hipercor 50 at 480°C. The measured yield strengths are about 410 MPa for the Hipercor 50 and 430 MPa for the Hipercor 27 at room temperature. The yield strength is the same, about 380 MPa, for both alloys at 150 °C. At 480°C the Hipercor 27 and Hipercor 50 yield strengths are 280 MPa and 400 MPa, respectively.

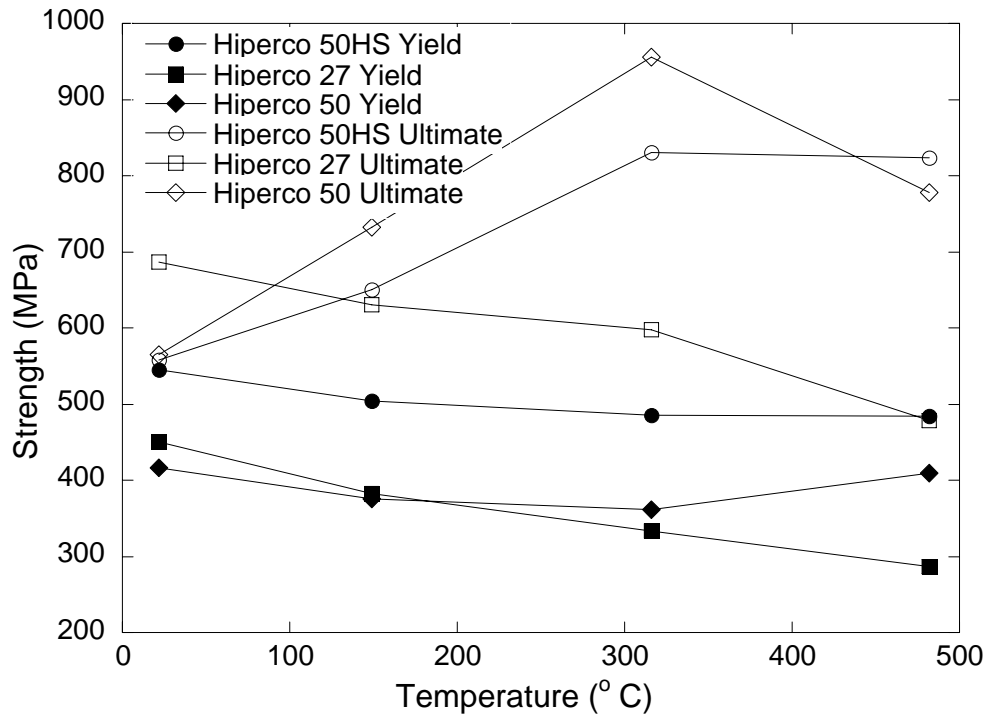


Figure 3.2.2 Strengths of Unaged Materials

Figures (3.2.3) through (3.2.5) illustrate the effect of aging on the yield strength of the three alloy compositions as a function of test temperature in both argon and air environments. The initial behaviors are also re-plotted from figure 3.2.2 as a reference for each respective alloy. The values for the air-aged specimens are included for comparison purposes and as an indication of the corrosion resistance of these alloys. In an actual rotor or stator assembly the area exposed to oxidation is much smaller than the conditions provided in this study.

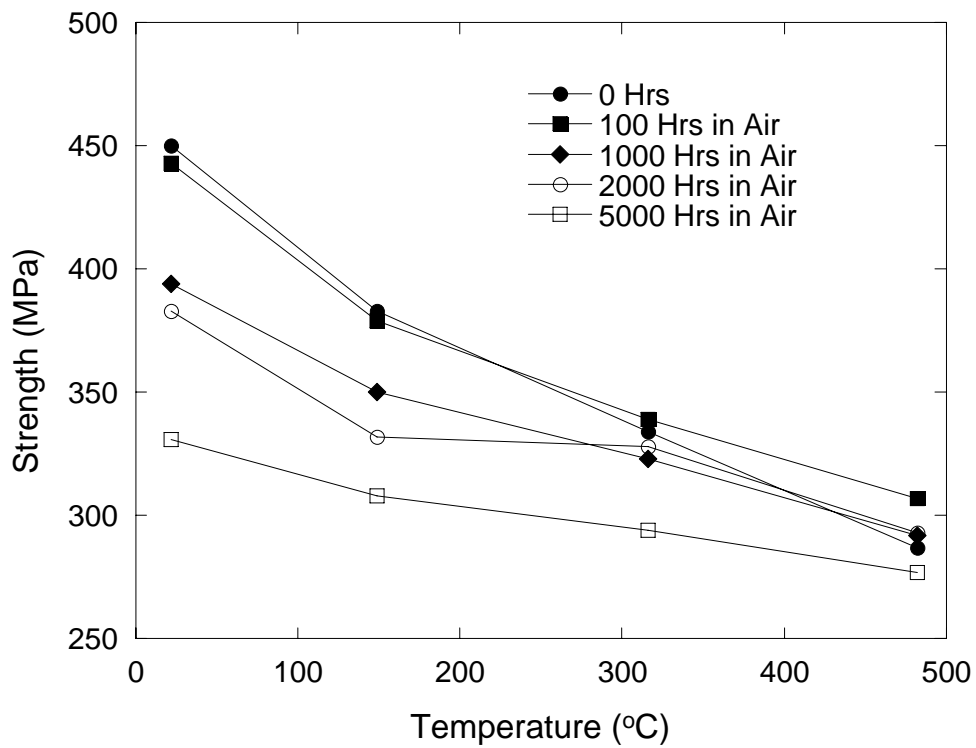
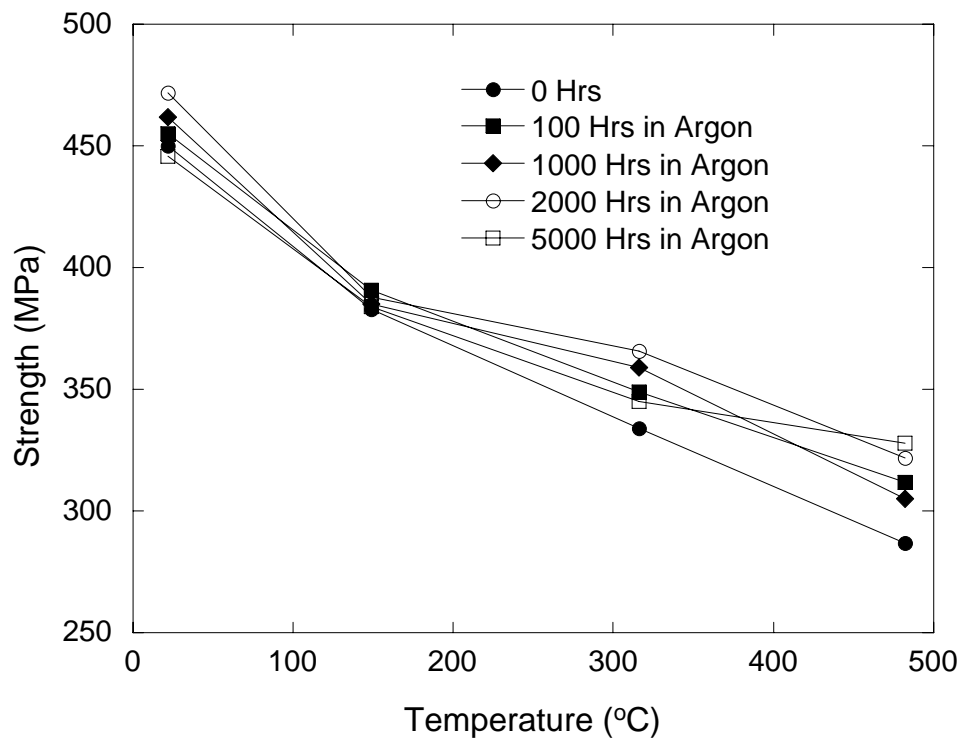


Figure 3.2.3 Effect of aging on the Yield Strength of Hipercor Alloy 27 aged in argon (top) and in air (bottom) as a function of test temperature

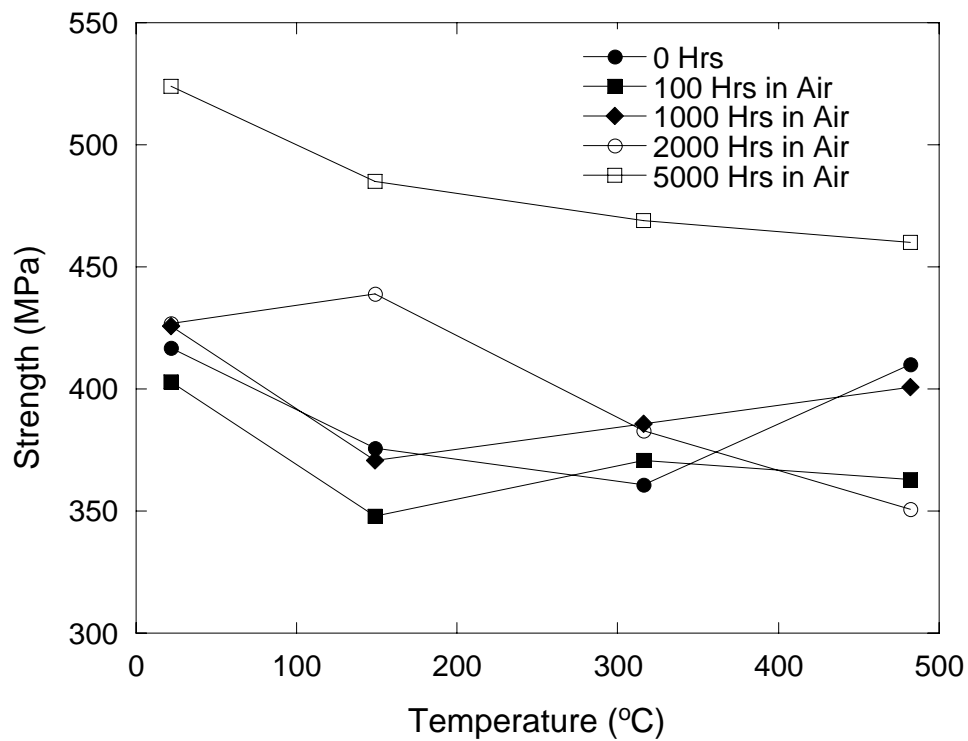
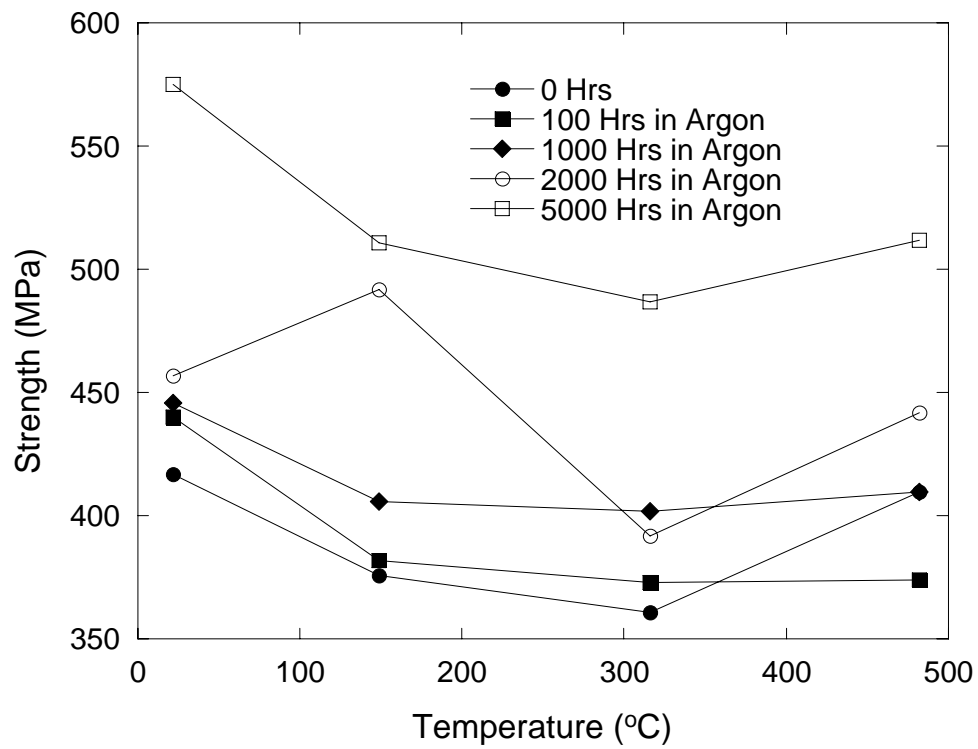


Figure 3.2.4 Effect of aging on the Yield Strength of Hipercor Alloy 50 aged in argon (top) and in air (bottom) as a function of test temperature

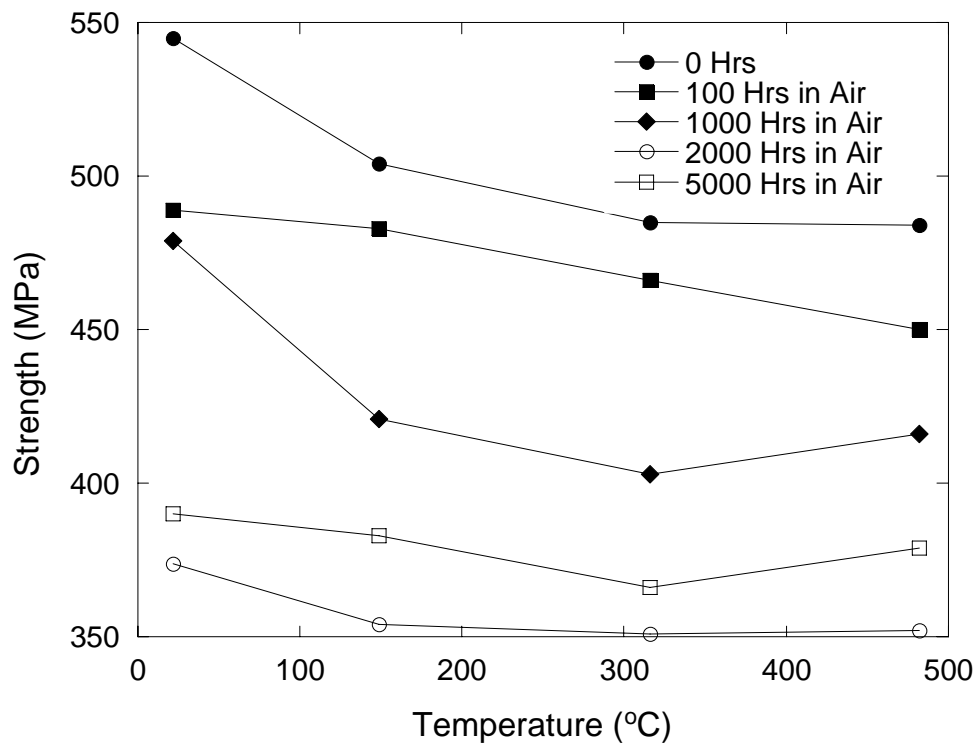
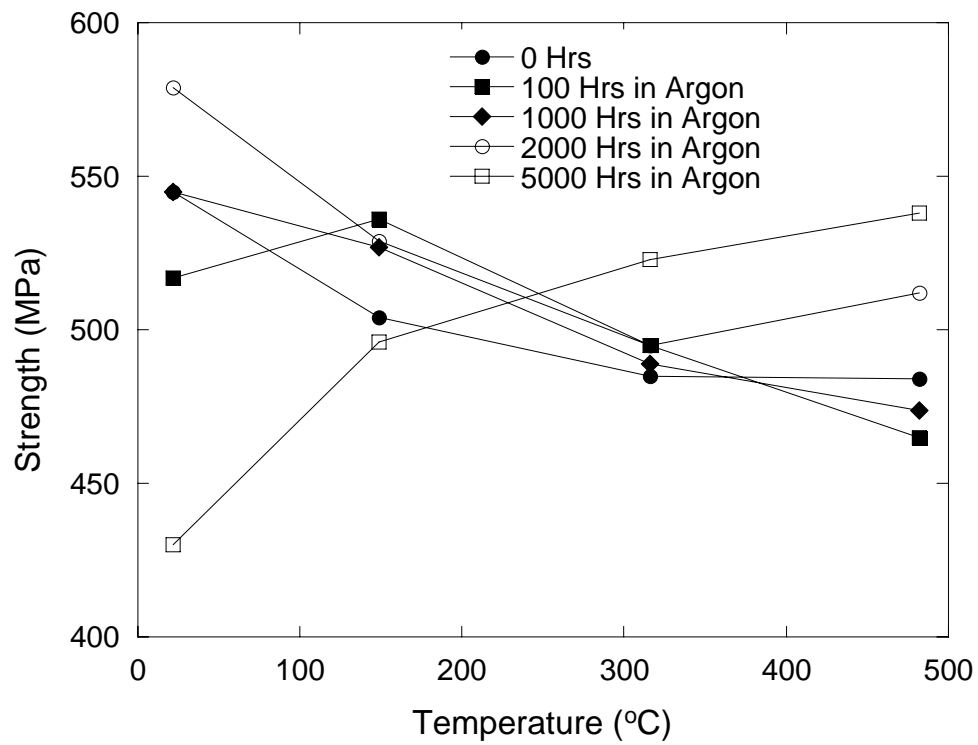


Figure 3.2.5 Effect of aging on the Yield Strength of Hipercor Alloy 50HS aged in argon (top) and in air (bottom) as a function of test temperature

There is little change of yield strength of the Hipercro 27 material when aged in argon. In fact, argon aging improved the yield strength of the Hipercro 27 material. Aging in air resulted in about 15% degradation at room temperature, gradually decreasing to zero degradation at 480°C. Also at the 480°C test temperature, the yield strength of the Hipercro 27 increased about 8% over the 2000 hour measurement when aged for 5000 hours in argon. As might be expected, the additional 3000 hours of aging in air resulted in a further decrease in yield strength at all test temperatures.

The data plotted in figure 3.2.4 shows a surprising amount of thermal stability and little dependence of Hipercro 50 yield strength on aging environment when aging time is 2000 hours or less. The yield strength plots of this Hipercro 50 material, with less than 5000 hours of aging, intersect throughout the test temperature range. After 1000 hours in the argon environment, the high temperature, 480°C, yield strength of the Hipercro 50 continued to improve to about 440 MPa at 2000 hours aged to about 510 MPa for the 5000 hour-aged specimen. The recorded strengths of the Hipercro 50 specimens indicated some data scatter up to 2000 hours with a surprising increase in strength being recorded for the 5000 hour specimens.

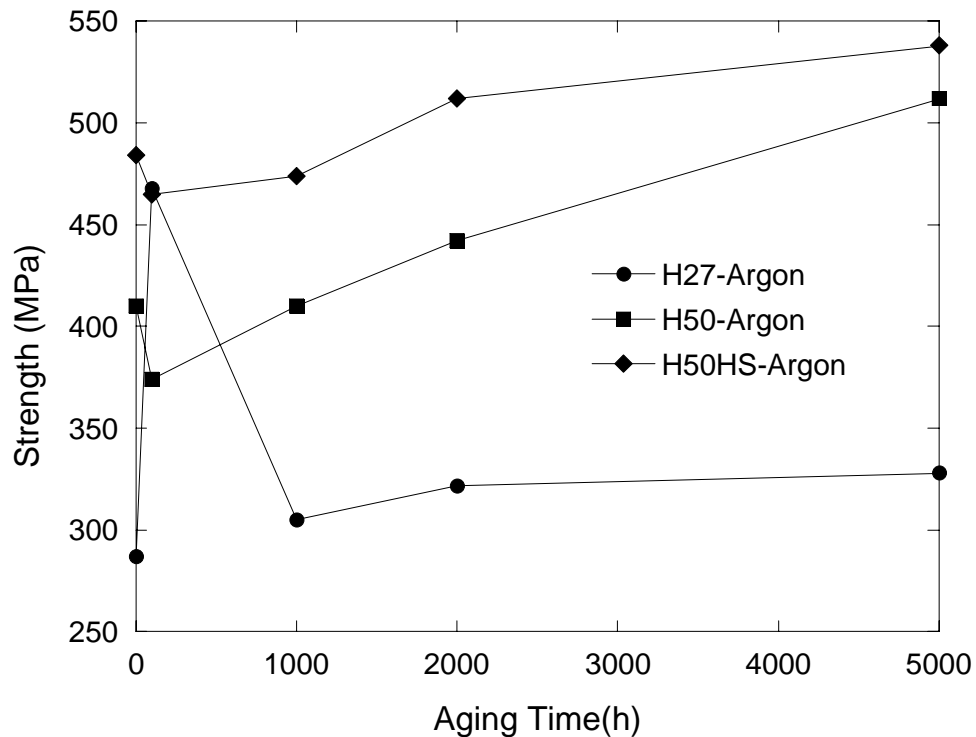


Figure 3.2.6 Yield strength of argon-aged materials as a function of time at test temperature of 482 °C

Figure 3.2.6 illustrates the data for all three alloys in an argon environment at aging lengths of 100, 1000, 2000 and 5000 hours at a test temperature of 482 ° C. As can be seen, the Hipercor 50HS alloy has the clear advantage of higher yield strength at all test temperatures.

Creep Testing

The effect of aging time and environment on creep behavior for these three alloys is not as clear as the impact on tensile performance due to a more complex set of test parameters. From the raw data, creep versus time, creep rates are determined and plotted versus test time for each of the three alloys in figures 3.2.7 through 3.2.9. A creep test temperature of 500 °C was selected for each alloy; however, an applied load of 300 MPa was used for only the Hipercor 50 and Hipercor 50HS specimens. Preliminary testing of the Hipercor 27 alloy at a load of 300 MPa resulted in almost immediate failures. A reduced loading of 180 MPa was used on the Hipercor 27 specimens. For the creep data, one specimen per parameter set was tested.

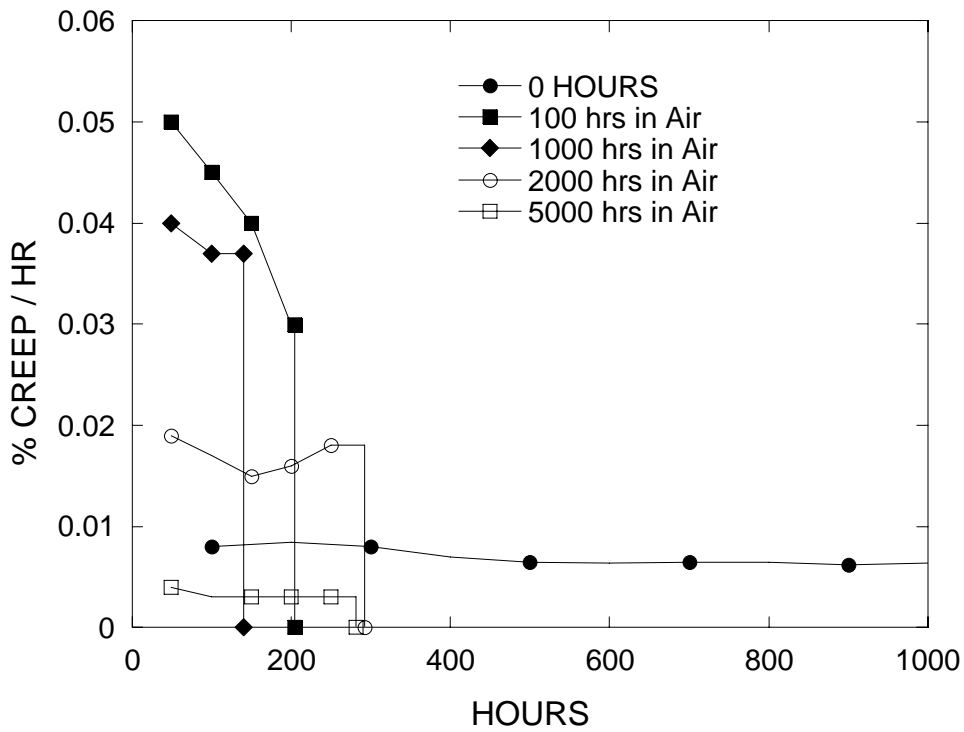
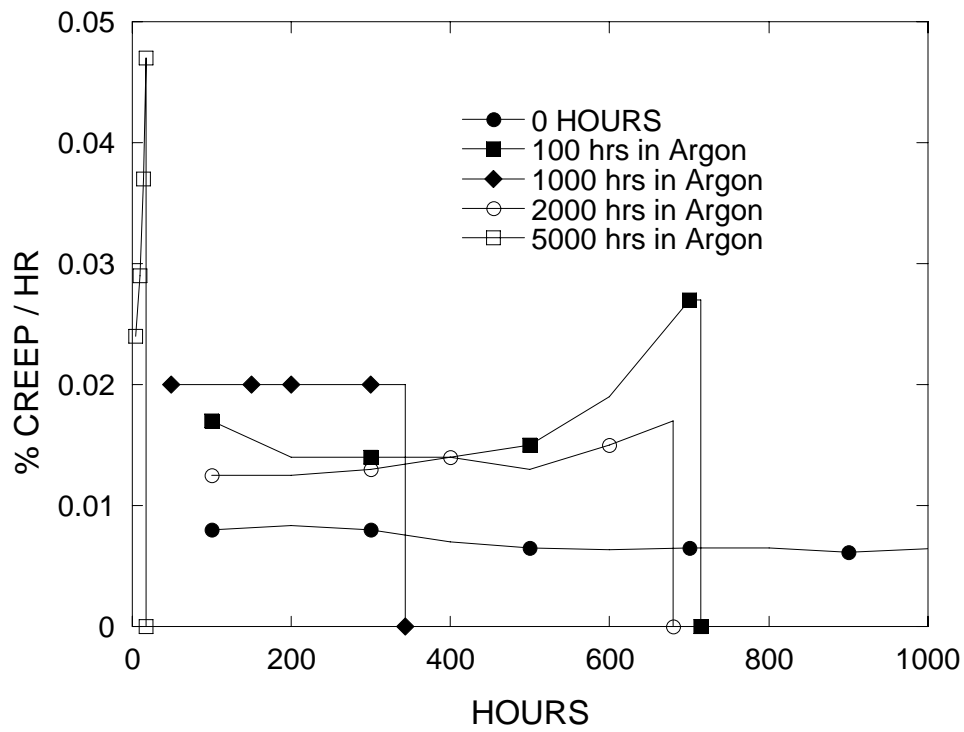


Figure 3.2.7 Effect of aging on the creep rate of Hiperc Alloy 27 at 180 MPa, 500 °C aged in argon (top) and in air (bottom)

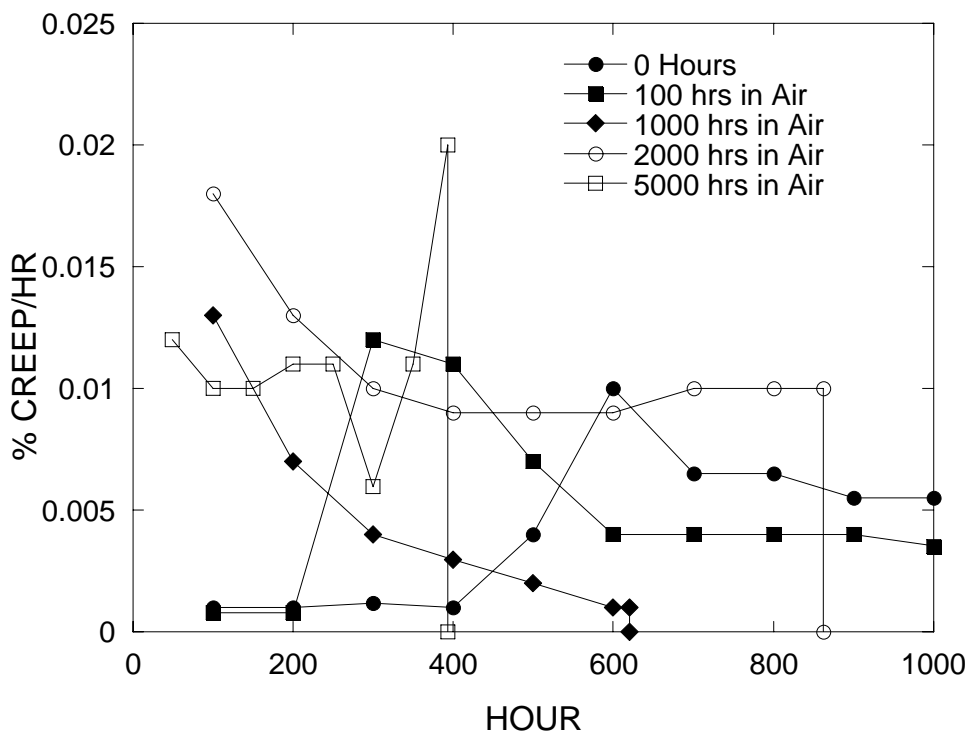
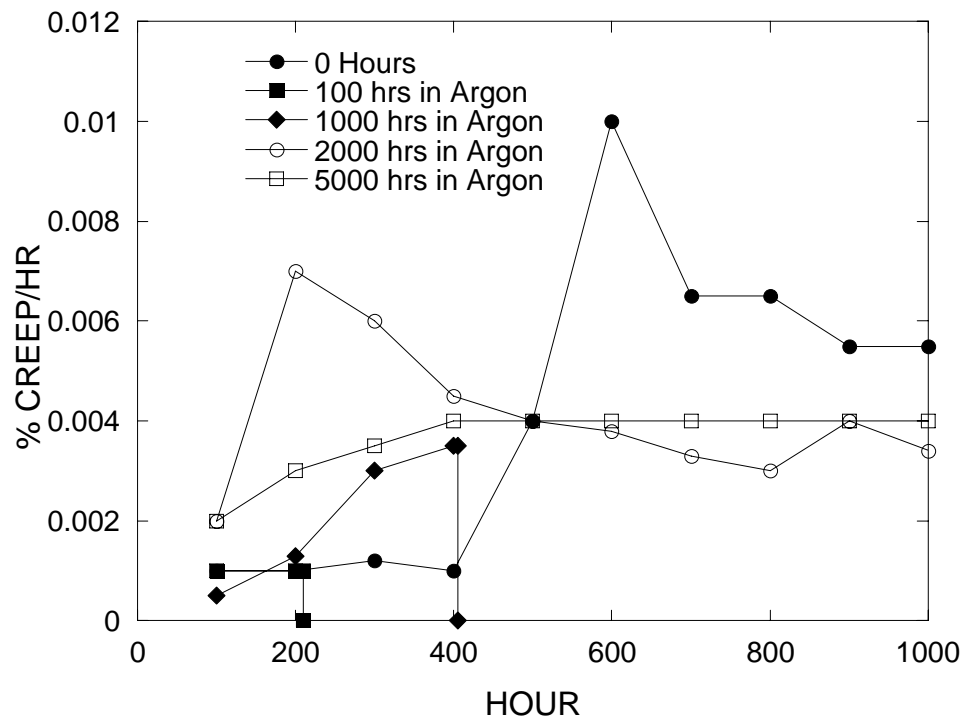


Figure 3.2.8 Effect of aging on the creep rate of Hipercro Alloy 50 at 300 MPa, 500 ° C aged in argon (top) and in air (bottom)

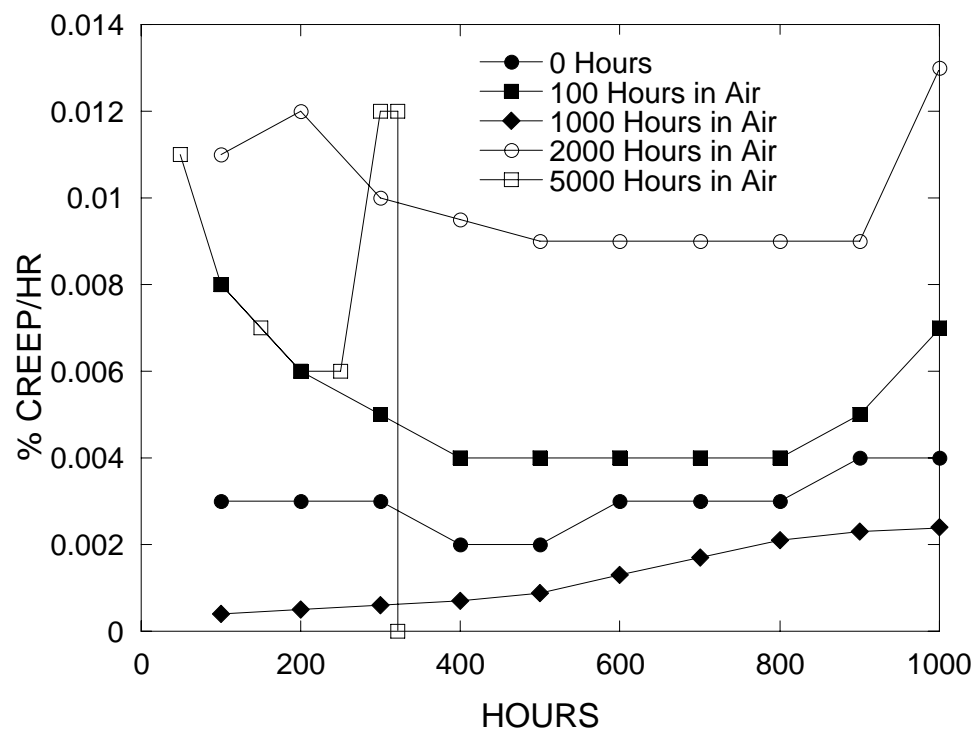
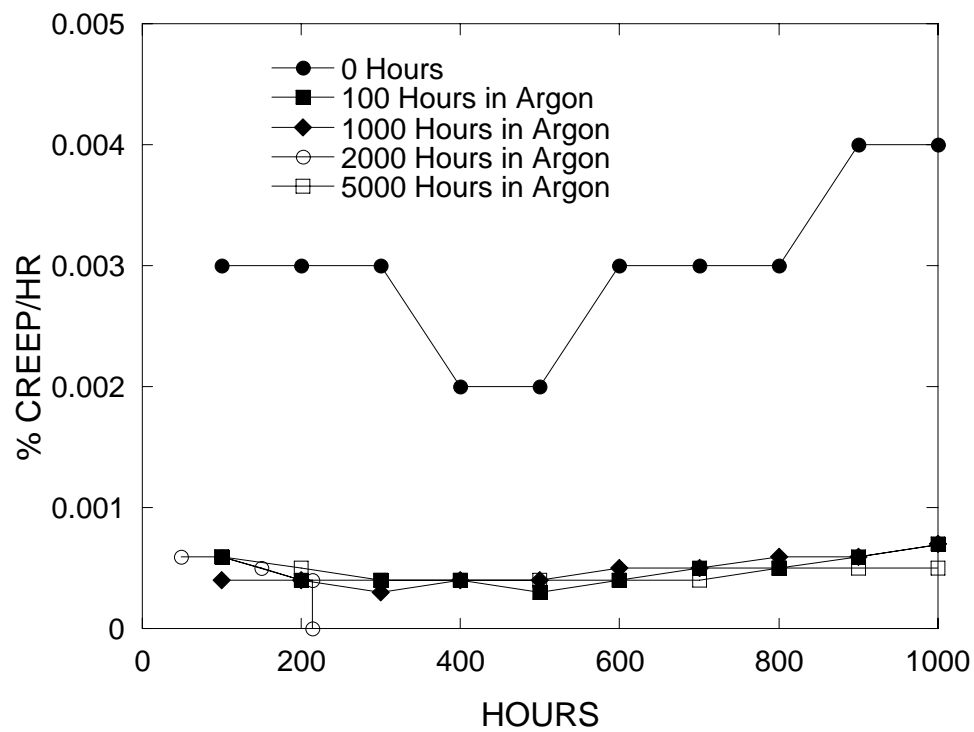


Figure 3.2.9 Effect of aging on the creep rate of Hipercro Alloy 50 HS at 300 MPa, 500 °C aged in argon (top) and in air (bottom)

One can easily conclude from the figures that the oxidation expected from being aged in an air environment had a significant impact on the life of the Hipercro 27 material. The argon-aged specimens also behaved with a much reduced creep strain rate as compared to the unaged specimens. Even though the applied loading was reduced to 180 MPa, all of the specimens failed by fracturing at less than the 1000 hour run out observed with the unaged data set. The specimens aged in argon did provide consistent data and the steady-state strain rates of the 1000 hour specimens can be estimated to be twice that of the unaged specimens, while the 2000 hour specimen data are closest to the unaged data. It appears as though the creep rates worsened up to 1000 hours at temperature when the Hipercro 27 specimens are aged in argon, but then improved to a level only slightly worse than observed for the unaged material. The data scatter and relatively short lives of the air-aged specimens make it difficult to make any substantiated observations other than the effect of the air environment is significant on the creep behavior of these materials.

The creep behavior observed for the Hipercro 50 material is less affected by aging at 300 MPa and 500°C than the Hipercro 27 alloy is at 180 MPa and 500°C. Some peculiarities illustrated in figure 3.2.8 include failures of some of the argon-aged specimens while the specimens aged in air for 100 hours and argon for 2000 and 5000 hours did not fail even after the 1000 hours of loading and temperature of the creep test. Little correlation can be drawn from these strain rate plots regarding the influence of aging times and environments for the Hipercro 50 specimens. One can possibly conclude only that aging in air or argon for times up to 5000 hours will not dramatically change the creep rate behavior of this Hipercro 50 FeCo alloy.

The Hipercro 50HS strain rate data set illustrated in figure 3.2.9 is the most consistent of the three materials. All of the creep tests of the Hipercro 50HS material, except the 5000 hour air-aged material, were terminated at about 1000 hours prior to specimen fracture. As can be seen in figure 3.2.9, the creep rate was reduced by aging in argon. When aged in air, the specimens exhibited an increase in creep rate after 100 hours aging; however, the rate for the 1000-hour specimens was reduced to a rate even better than the unaged value. Aging for 2000 hours did, however, increase the creep rates by nearly an order of magnitude over the unaged specimens. The creep specimens aged in air for 5000 hours failed after about 300 hours while the specimens similarly aged in argon maintained a consistent low strain rate for more than 1000 test hours.

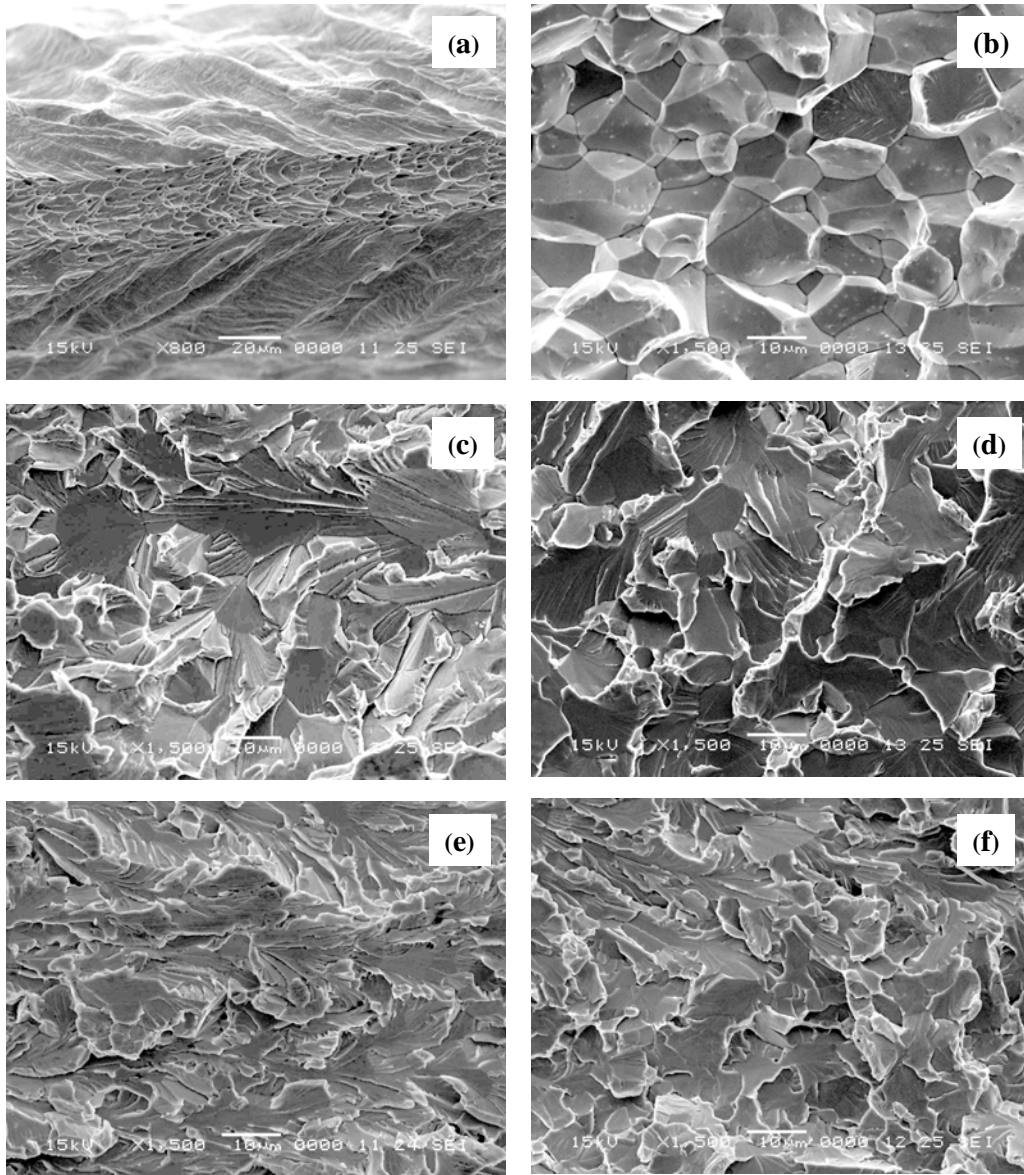


Figure 3.2.10 Fracture surfaces of tensile samples aged at: (a) Hipercor 27- 0 hours; (b) Hipercor 27- 5000 hours; (c) Hipercor 50- 0 hours; (d) Hipercor 50- 5000 hours; (e) Hipercor 50HS- 0 hours; (f) Hipercor 50HS- 5000 hours

Fracture surface images of tensile specimens are illustrated in Figure 3.2.10. The unaged Hipercor 27 alloy exhibited a ductile dimple failure (Fig. 3.2.10.a); however, after 5000 hours aging, the fracture mode changed to a brittle intergranular fracturing (Fig. 3.2.10.b). Regardless of their aging history, the Hipercor 50 and Hipercor 50HS alloys

failed by brittle cleavage fracture (Fig. 3.2.10.c through 3.2.10.f), and both of the alloys exhibited no significant change in the cleavage facet size after aging. Aging also had no effect on the grain sizes of the three alloys. The average grain sizes were 12 μm for Hipercor 27 alloy, 8 μm and 4 μm for the alloys Hipercor 50 and Hipercor 50HS respectively in unaged and aged states.

3.3 Electrical Properties

When a ferromagnetic body is magnetized by an alternating field, three different sources contribute to the observed energy losses. These are hysteresis losses, eddy current losses, and anomalous energy losses. While the mechanism behind the first two is well understood, the latter is usually pronounced to reconcile the discrepancy between the measured total energy losses and sum of the eddy current and hysteresis losses. Williams, Shockley and Kittel [3.9] ascribed this anomalous loss to inhomogeneous distribution of permeability throughout the material, but no comprehensive theory has emerged up to present.

Eddy current losses are due to electromagnetic forces (emf) induced by applied alternating fields. If the material is a good conductor, the induced emf will produce currents in the body known as eddy currents. These currents, driven through the finite resistance of the core material, constitute a net loss of energy, which is given away through Joule heating (I^2R) and is expressed by,

$$P_e = \frac{\omega^2 B_m^2 a^2}{6\rho} = \frac{2\pi^2 f^2 B_m^2 a^2}{3\rho}$$

Where f is frequency; $2a$ is sheet thickness; B_{\max} is maximum induction, and ρ is the electrical resistivity.

Although this formalism is an approximation, the main conclusion from the above equation is; the eddy current losses are proportional to the square of the frequency and sheet thickness and inversely proportional to the resistivity.

Equiatomic FeCo alloys exhibit poorer electrical resistivity than pure iron or pure cobalt (Fig. 3.4.1). Resistivity values can be improved by introduction of additive elements, but these metallic magnets still need to be rolled into thin sheets for alternating field applications. The cold workability becomes a critical step in processing of these alloys, and Vanadium serves very well in both improving electrical resistivity and cold workability.

Specimens and Procedures

Small strips averaging 0.15 x 2.3 x 8.3 mm in size were sanded with 240-grit sandpaper to remove a thin layer of oxide present on the surface. Gold contact pads were then sputtered onto the samples. For the low temperature measurements, gold wires were attached to the contact pads using silver paint to make electrical connections with the

samples. Later, for the high temperature measurements, gold wires were attached by arc-welding them to the contact pads. The sample dimensions were measured using a micrometer and an optical microscope.

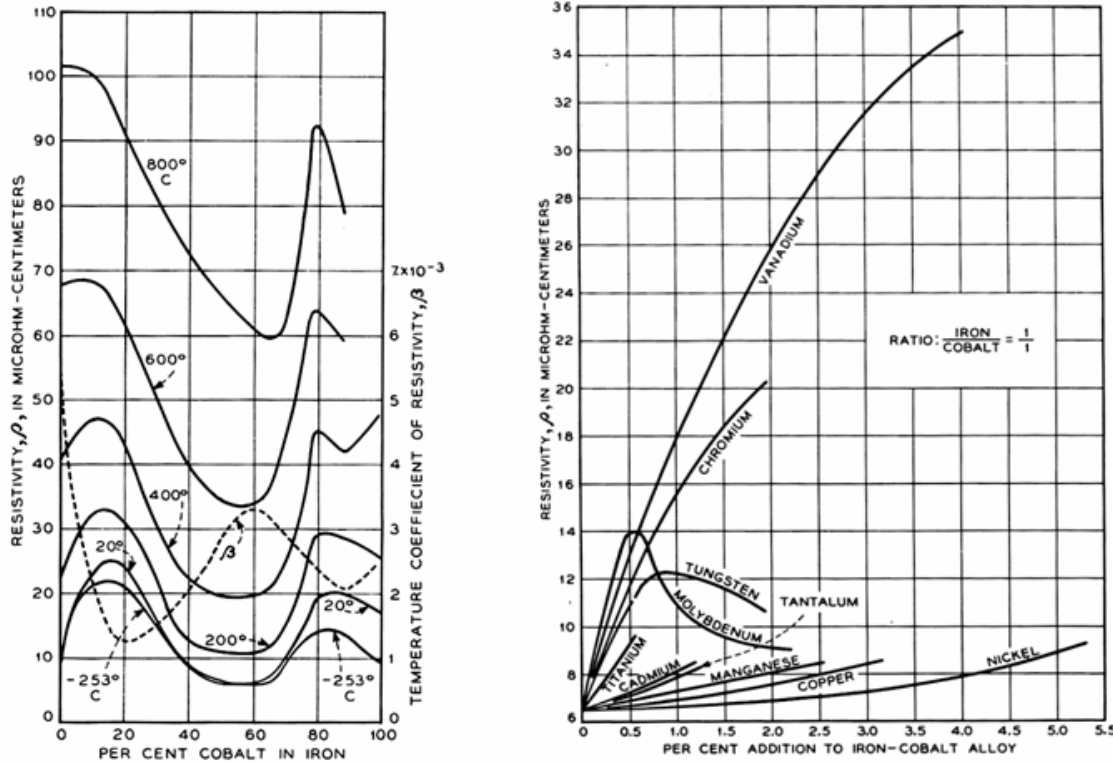


Figure 3.3.1 Electrical resistivity of FeCo alloys as a function of Co content (left) and alloying elements (right) [3.10]

For the low temperature measurements, (198 K to 298 K,) we mounted the samples on a high accuracy test head and placed them into a cryogenic variable temperature-dewar cooled to 77 K with liquid nitrogen. A helium gas environment was maintained in the sample chamber throughout the experiment. We cooled the samples to 198 K and took resistivity measurements at 198 K, 233 K, 273 K, and 298 K in the forward and reverse current directions. The sample was measured in the forward current direction and then measured in the reverse current direction. The formula $V_{\text{actual}} = (V_{\text{forward}} - V_{\text{backward}})/2$ was used to eliminate any offset voltages that might occur. Resistance was measured using a four point measuring system similar to the method described in the ASTM standard A712-75 [3.11]. A Keithley 228A Voltage/Current Source was used to provide a current through the sample with a Keithley 180 nano-voltmeter and a Keithley 195A Digital Multi-

Meter used to measure the sample voltage and current, respectively. A Lake Shore DRC-93C Controller was used to control the heating element to ensure proper temperatures for the measurements.

We took the high temperature measurements in a Dewar designed to withstand temperatures up to 1100K. We used this system to take measurements at 298K, 373K, 473K, 573K, 673K, 773K, and 873K. A silicon carbide heater was used to heat the samples and a nitrogen gas was maintained during the experiment runs to prevent oxidation. The current was supplied by a Keithley 238 High Current Source, which supplied current in the forward and reverse directions. Two Keithley 196 Digital Multi-Meters measured the current and voltage at each temperature point.

Results

Figure 3.3.2 depicts change in room temperature resistivity of the three Hipercó alloys as a function of aging time. Hipercó 50HS alloy was the most stable while degradation in resistivity of Hipercó 27 was also insignificant. After 5000 hours aging, electrical resistivity of Hipercó 50 alloy reduced by 34 %.

Figures 3.3.3 through 3.3.5 illustrates resistivities of the Hipercó alloys at test temperatures up to 600 ° C and aging times up to 1000 hours. The obtained non-linear behavior for all three alloys deviates from the textbook description of temperature coefficient of resistivity (α C⁻¹). If we were to subdivide the temperature range into segments where a linear fit can be applied, it would be obvious that α of Hipercó 27 is larger than that of Hipercó 50 and Hipercó 50HS. Even though Hipercó 50 and 50HS possess different RT resistivity values, their temperature coefficient of resistivity is relatively similar. It is also obvious from the figures that “ α ” does not change with aging. As it will be discussed in the next section, observed behaviors in electrical resistivity upon aging can be attributed to microstructural changes such as precipitation reactions that take place during aging.

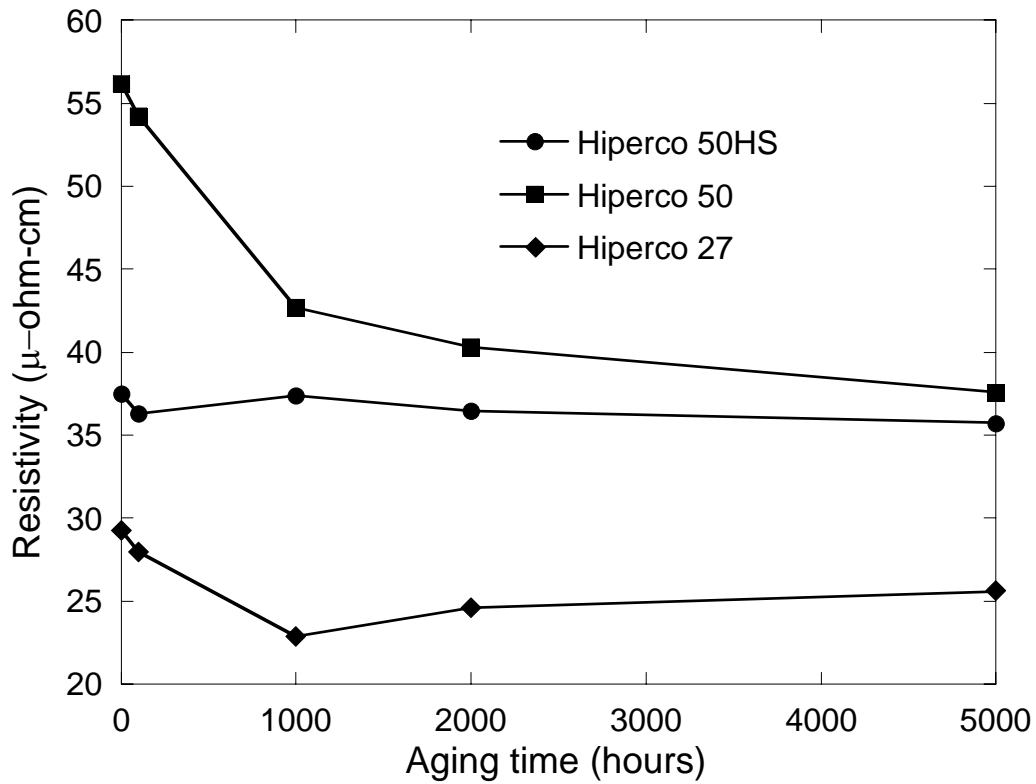


Figure 3.3.2 Room temperature resistivity versus aging time for FeCo alloys

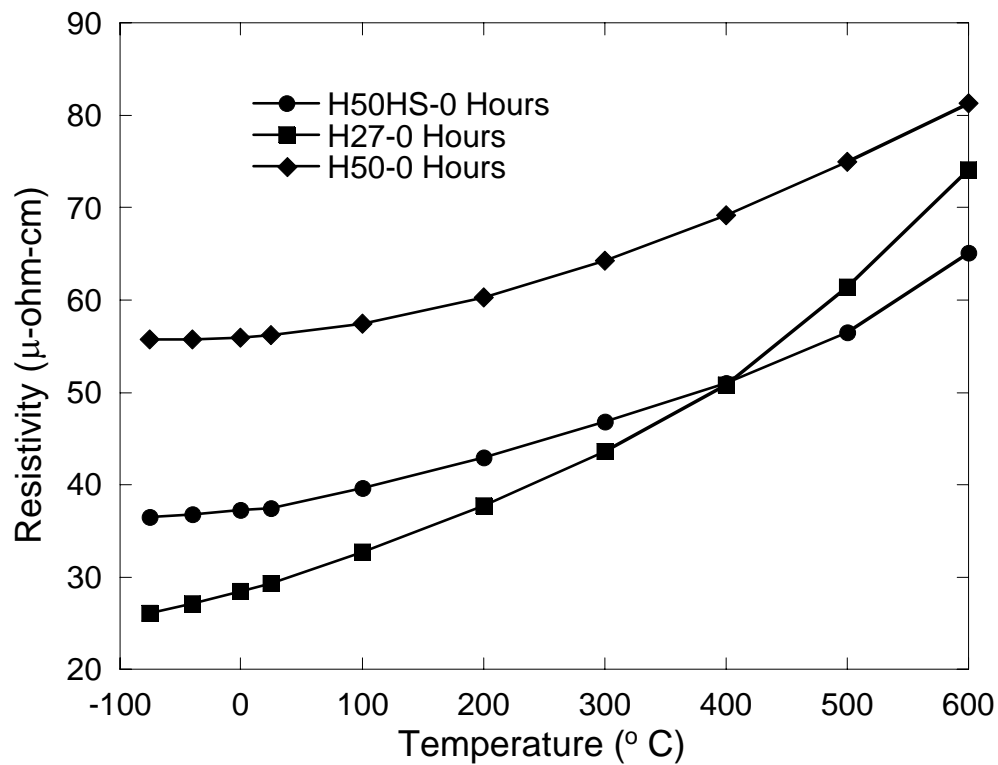


Figure 3.3.3 Resistivity of the Hipercó alloys as a function of temperature prior to aging

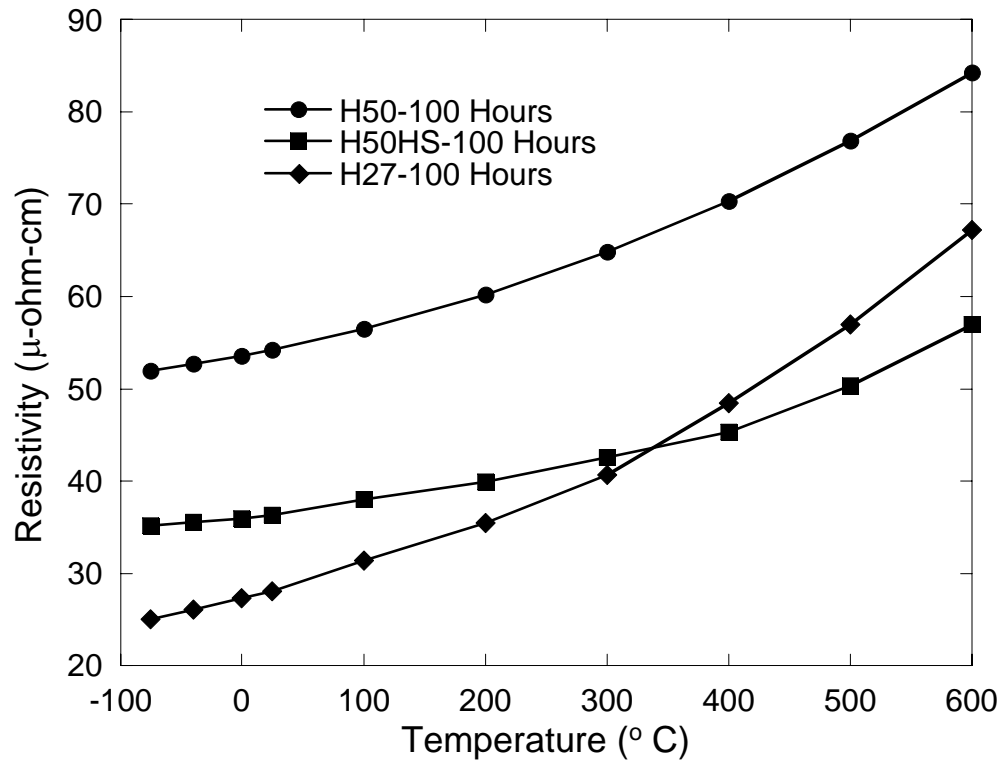


Figure 3.3.4 Resistivity of the Hiperco alloys versus temperature after 100 hours aging

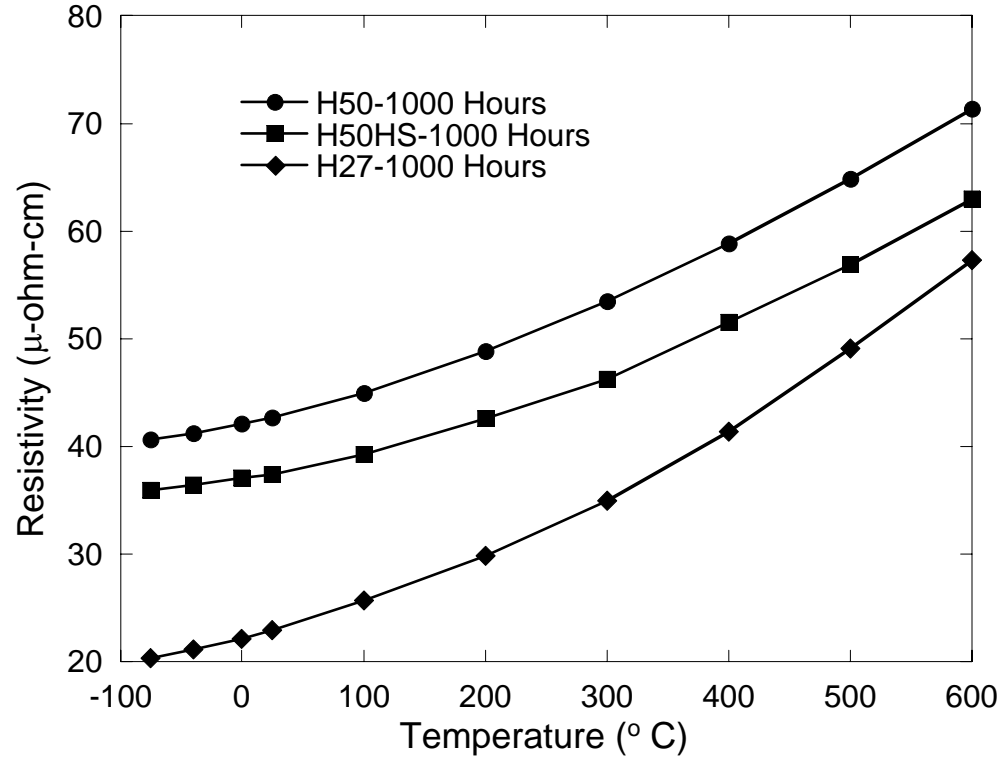


Figure 3.3.5 Resistivity of the Hiperco alloys versus temperature after 1000 hours aging

3.4 Microstructure

Extrinsic material properties ranging from magnetic to mechanical and electrical such as coercivity, permeability, yield and tensile strengths, electrical conductivity and related power losses are strongly depended on microstructure. Formation of new phases, grain growth, and precipitation reactions are some examples of structural changes that may occur at macro and/or micro scales during any type of heat treatment. Aging occurs at relatively low temperatures than grain growth, but there is enough thermal driving force for diffusion of atoms dissolved in a matrix in excess from their equilibrium values. These micro-scale evolutions may greatly impact the mentioned properties.

There are numerous investigations on microstructural characteristics of the FeCo system mostly focusing on heat treated materials after cold deformation [3.12-3.15]. There is also a limited amount of study on aging related property changes but no microstructural evidence had been given to relate those property changes to microstructural ones during aging. In V containing alloys, it is evidenced from the increased coercivities and reduced resistivities that during aging, there must be a precipitation reaction taking place involving Vanadium. Increased volumes of V rich phase (from ~0.3% to ~0.8%) upon aging were found by neutron diffraction studies [3.16], but their morphology and structure have never been explored up to date.

At aging temperatures employed in this study, FeCo alloys do not exhibit any grain growth even after 5000 hrs aging. The average grain sizes were ~12 μm for Hiperco 27 alloy, ~8 μm and ~4 μm for the alloys HA50 and HA50HS respectively in unaged and aged states. SEM characterizations also revealed that Vanadium containing alloys Hiperco 50 and Hiperco 50HS had spherical V rich precipitates (< 0.5 μm) that form during the post cold deformation heat treatment. Hiperco 27 alloy on the other hand exhibited small amount of carbide precipitates. Morphology of these inclusions was examined by SEM and TEM studies, and their structure was explored by selected area electron diffraction (SAD).

Figure 3.4.1 illustrates the bright field images of the three alloys along with the SAD patterns before these materials are subjected to any aging. All the alloys exhibited equiaxed grain structure with spherical inclusions. There was no indication of texture induced by cold deformation. Hiperco 27 and Hiperco 50 alloys were free from any dislocations; however Hiperco 50HS alloy did exhibit dislocations indicated by arrows in

Fig. 3.4.1.c. SAD patterns revealed super lattice reflections (for indexing please see figure 3.4.2) indicating that the final structure was ordered CsCl type structure.

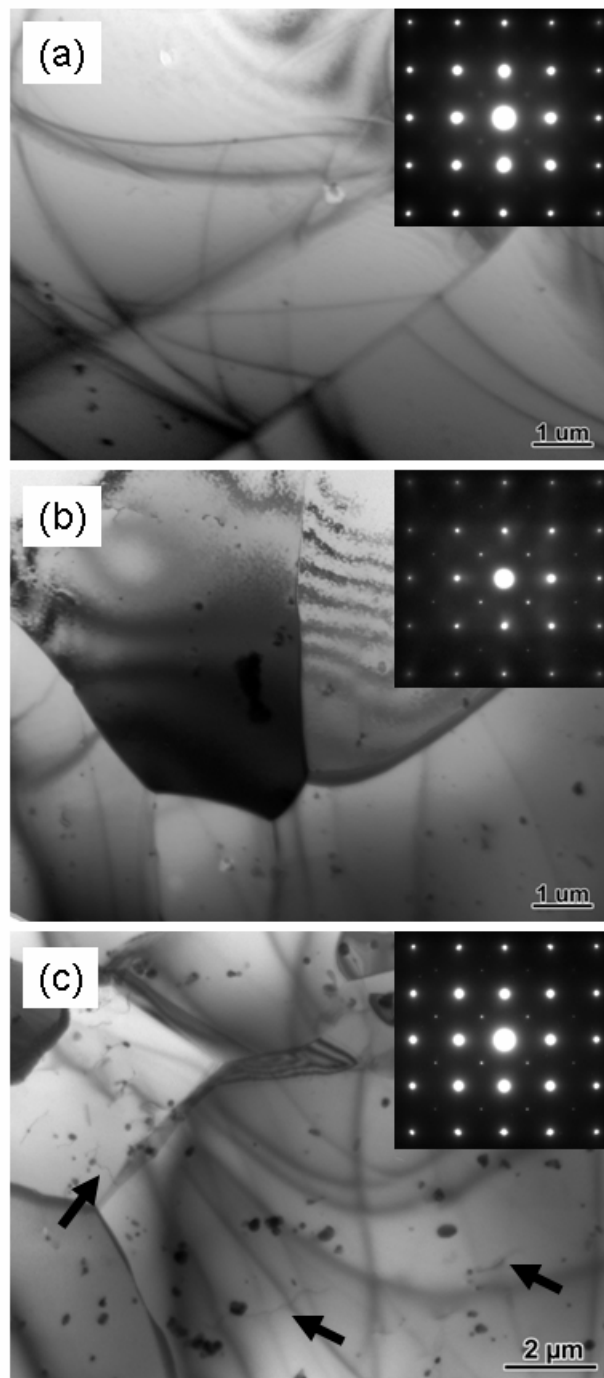


Figure 3.4.1 Bright field images of (a) Hiperco 27; (b) Hiperco 50 and (c) Hiperco 50HS alloys with corresponding SAD patterns before aging.

Population density of the spherical inclusions varied from one alloy to another; it was the highest for Hiperco 50 HS alloy. No preferential distribution of the spherical inclusions is observed; they were found along the grain boundaries as well as inside the grains of all the alloys.

Figure 3.4.2 shows bright field images and SAD patterns of Hiperco 27 alloy after 5000 hours aging. Even though we have not attempted to observe if there is a change in structural order parameter during aging, it is apparent from the intensity of the super lattice reflections that there is an increase in the structural order parameter for Hiperco 27 up on aging. Electron diffraction analysis on inclusions indicated that the spherical inclusions in Hiperco 27 alloy system were Fe_7C_3 .

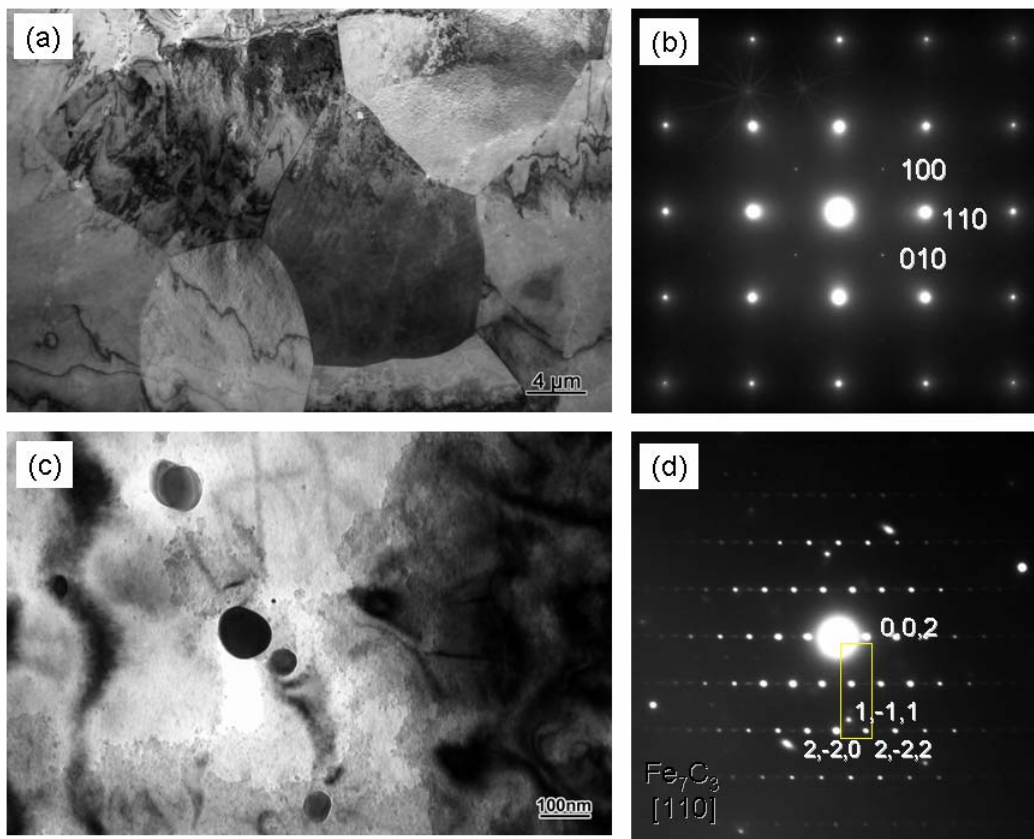


Figure 3.4.2 Bright field images of Aged Hiperco 27 Alloy (a and c) and SAD patterns of matrix (b) and spherical precipitates (d)

Bright field images of Hiperco 50 and Hiperco 50HS alloys containing vanadium (Fig. 3.4.3 and 3.4.4) exhibited very fine, plate-like precipitates of V rich phase with dimensions of ~50 nm long and 3-5 nm thick along with spherical V rich precipitates that

formed during the post-cold deformation heat treatment. SEM studies indicated that aging had no effect on population and size of the spherical precipitates that had MgZn_2 type hexagonal Laves structure (hP12) (Fig. 3.4.4.c-d). The plate-like precipitates a network resembling a sub-grain structure, and there is an obvious orientation relation between the matrix and these precipitates.

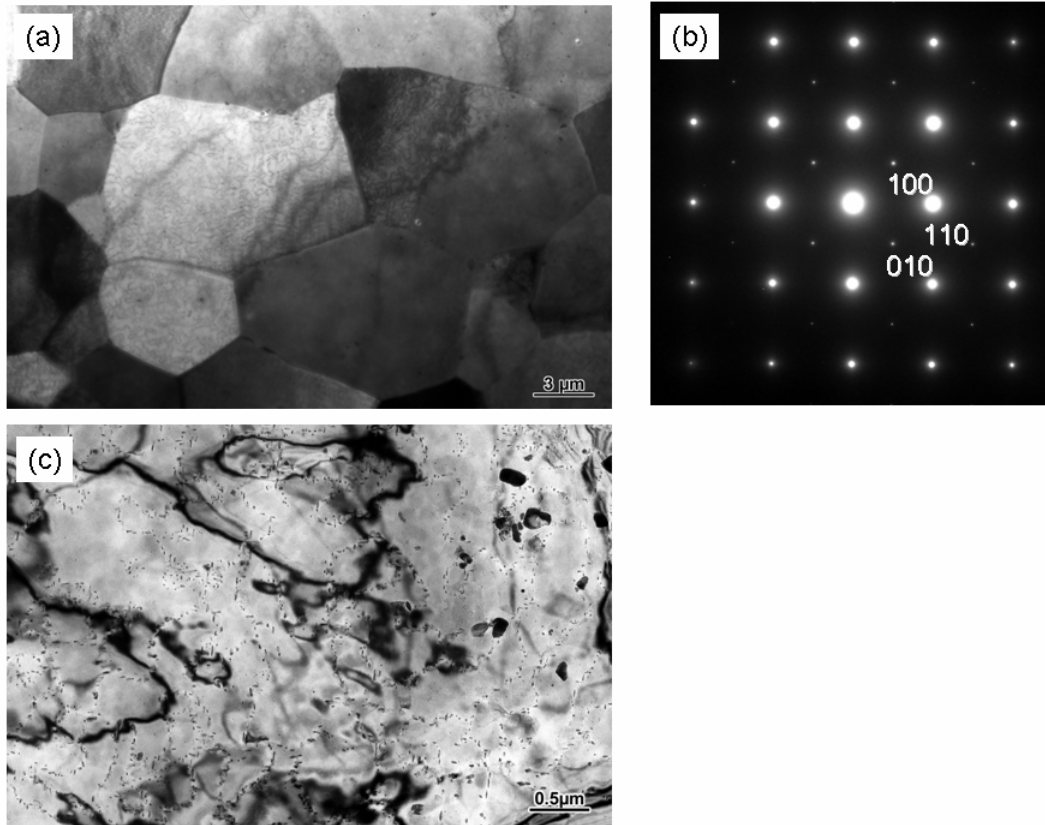


Figure.3.4.3 Bright field images (a and c) and SAD pattern of matrix (b) for aged Hipercor 50 Alloy

Energy Dispersive X-ray Spectroscopy (EDS) studies on Hipercor 50 HS alloy (Fig. 3.4.5) indicated that the fine platelets are rich in Vanadium with an undetermined structure. Surprisingly, neither matrix nor platelet precipitates contained any detectable Nb. All the niobium was concentrated in spherical inclusions. Since the formation of spherical inclusions are complete before any aging takes place, it can be interpreted that Nb does not contribute directly to the aging related property changes in Hipercor 50HS alloy system. Instead, it may be argued that niobium suppresses Vanadium's diffusion rate. This is evidenced from work of Yu *et al* [3.17] who determined that long-range order parameter differs by 0.1 ($S_{\text{Hipercor 50}} \sim 0.88$ and $S_{\text{Hipercor50HS}} \sim 0.76$) under the same

processing and annealing condition before any aging occurs. Since the amount of dissolved V contributes to the maximum degree of order attainable, the difference in order parameters between the two alloys can be explained by the amount of dissolved V that not precipitated out during post-cold deformation heat treatment. As these materials are subjected to aging, V continues to precipitate out at a greater rate in the Hipercor 50HS alloy system. This is also reasoned by the drastic change in the electrical resistivity of the Hipercor 50HS upon aging compared to that of Hipercor 50 alloy. Under this argument, one might expect that long-range order parameter also increases upon aging especially in Hipercor 50HS alloy systems. In fact, an increase in the structural order parameter upon aging was reported for Hipercor 50 [3.16] and Hipercor 50 HS [3.17] based on neutron diffraction studies.

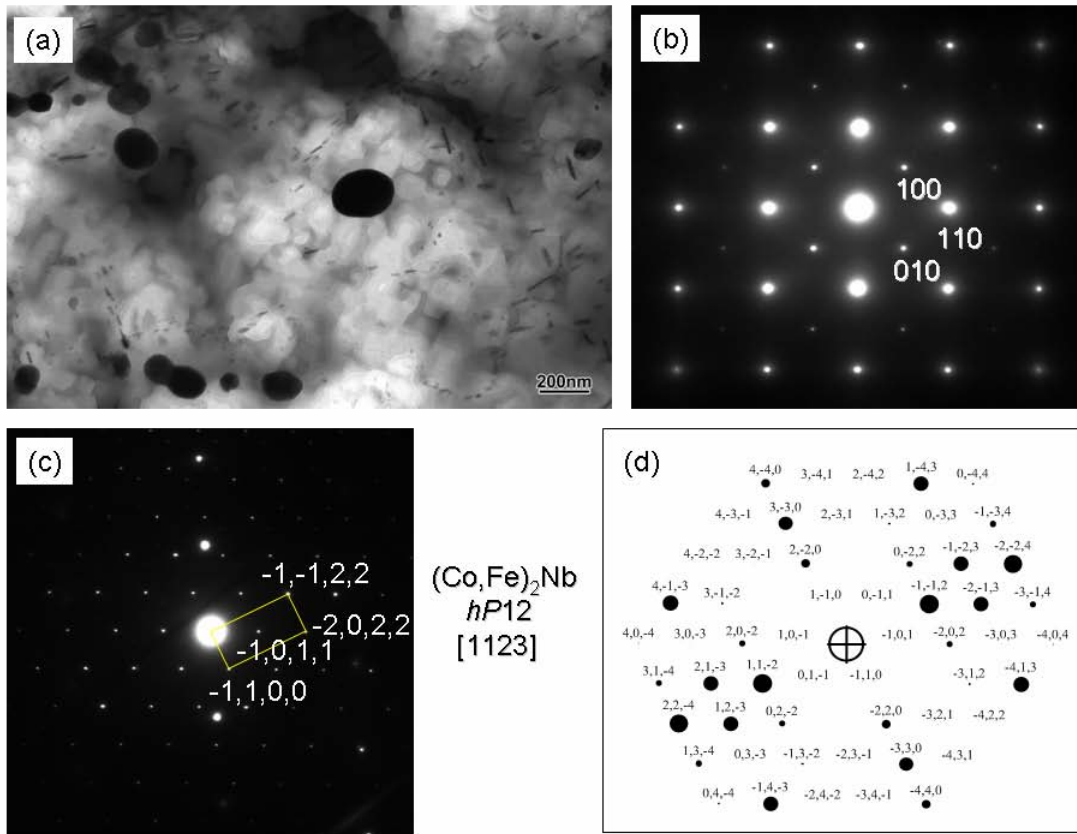


Figure 3.4.4 Bright field image (a) and SAD patterns of the matrix (b) and spherical precipitates (c) for aged Hipercor 50HS Alloy. (d) is the corresponding calculated SAD pattern

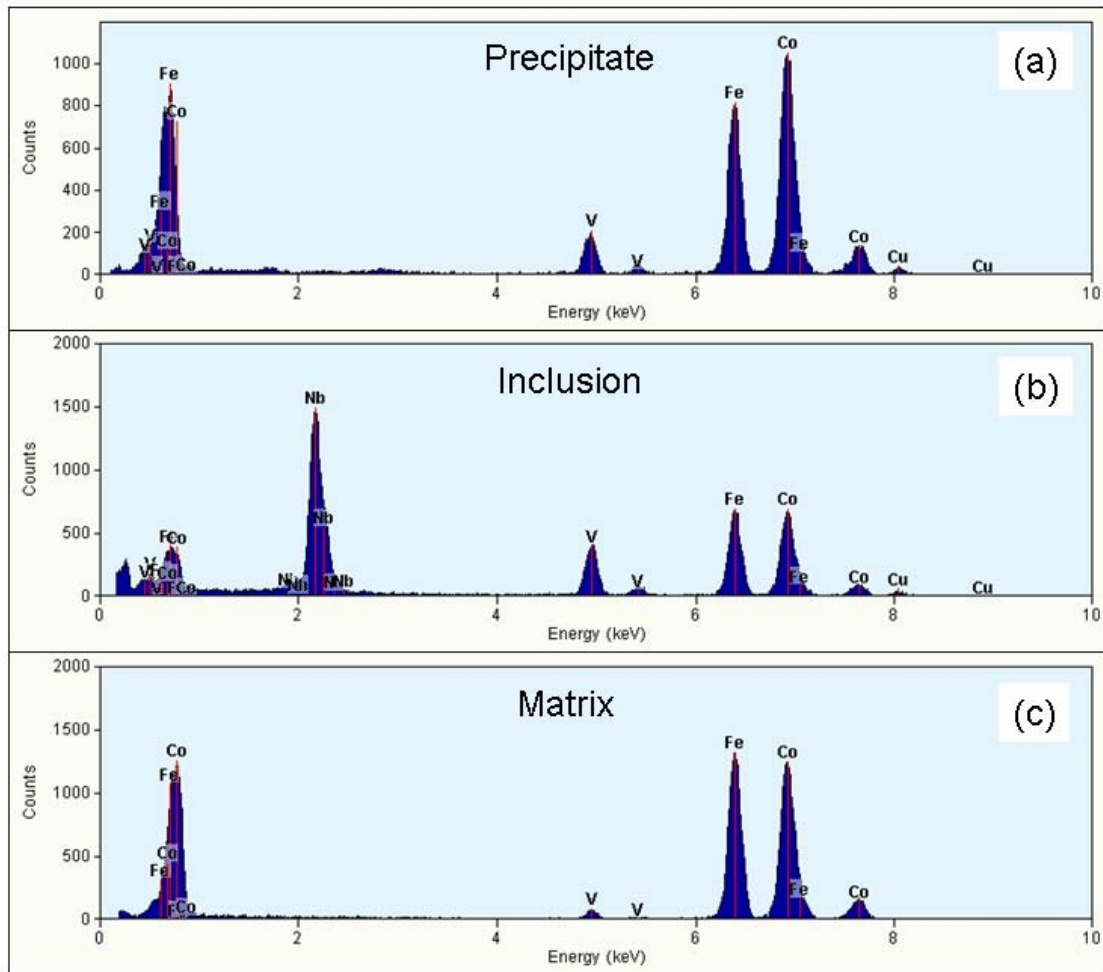


Figure 3.4.5 EDS patterns of aged Alloy 50HS

Formation of fine platelets during aging also explains the observed trends in mechanical and magnetic properties. Upon aging, magnetic properties are deteriorated while the yield strength is improved in both alloy systems. On the other hand, vanadium free Hipercor 27 composition was the most stable in terms of magnetic, mechanical and electrical properties.

CHAPTER IV

Effect of Stress on Magnetic Properties

Soft magnetic materials are known to be very sensitive to applied or internal stress, and their magnetic properties, specifically the magnetic losses under AC excitation, may change dramatically under stress. Current state-of-the-art technology utilizes stacks of 150-micron thick Fe-Co laminates. These laminates are stamped in desired shapes, and depending on the design, several hundreds of them are stacked onto a shaft. To increase the rigidity of the stack, they are held together by various clamp or shrink fits that exert a compressive stress on the stator or rotor core. Additionally, rotor cores experience tensile stress in the circumferential or radial direction during operation as a result of centrifugal forces. Therefore, nominal loss values of magnetic materials reported by manufacturers can be misleading when such cores are designed, and compensating factors are always employed to arrive at the desired machine performance. An earlier work [4.1] addressed these issues but focused mainly on a specific alternator design, which utilized FeCoV laminates. It is the purpose of this study to provide more detailed information on the stress related magnetic loss values of three commercial Fe-Co alloys and provide designers with better values for the compensating factors.

4.1 Effect of Tensile Stress

FeCo is usually provided by the manufacturer in the form of cold rolled sheets. Cold rolled materials often have a preferred orientation or texture in which certain crystallographic planes tend to be oriented preferentially with respect to the rolling direction and the plane of the sheet. A post-cold deformation annealing is always necessary to develop a stress free microstructure and good magnetic properties, at the expense of the mechanical strength of the material. This annealing is usually performed at or above the order-disorder phase transformation temperature of the FeCo alloys. The desired properties (mechanical versus magnetic) determine the annealing time and temperature, and a slow cooling to room temperature is necessary to obtain an ordered structure for optimum magnetic properties. Even after re-crystallization, which occurs during annealing, the magnetic properties reflect the presence of crystallographic texture. In this investigation we measured the directional dependence of the magnetic properties and the loss values of the three Hiperco[®] alloy compositions.

Specimens and Procedures

As noted above, annealing after cold deformation determines the magnetic and mechanical properties of these alloys. Therefore, the magnetic properties and loss values reported in this investigation apply only to alloys annealed at 730 °C for 2 hours.

All three Hiperco[®] alloy compositions tested were purchased from Carpenter Specialty Alloys as coils of cold-rolled 0.15-mm thick sheets. They were first machined into 12.7-mm×102-mm strips cut parallel, 45°, and perpendicular to the rolling direction. The strips were heat-treated in argon at 730 °C for 2 hours and cooled down to room temperature at 177 °C/hr. We used the Magnetic Instrumentation Inc. SMT 600 type hysteresisgraph for magnetic testing. This instrument was originally designed to test ring specimens, and had to be modified to allow the measurement of magnetic properties of strip samples under tensile stress while eliminating demagnetizing effects. A mild steel flux path annealed at 800 °C and slowly cooled to room temperature was employed for this purpose. Figure 4.1 shows the schematic of such a fixture. In order to minimize the errors that may arise from the windings, a single set of coil embedded in epoxy was used for all test specimens. We employed a maximum tensile stress of 200 MPa, which falls in the elastic region of the stress-strain curve for all the alloy compositions.

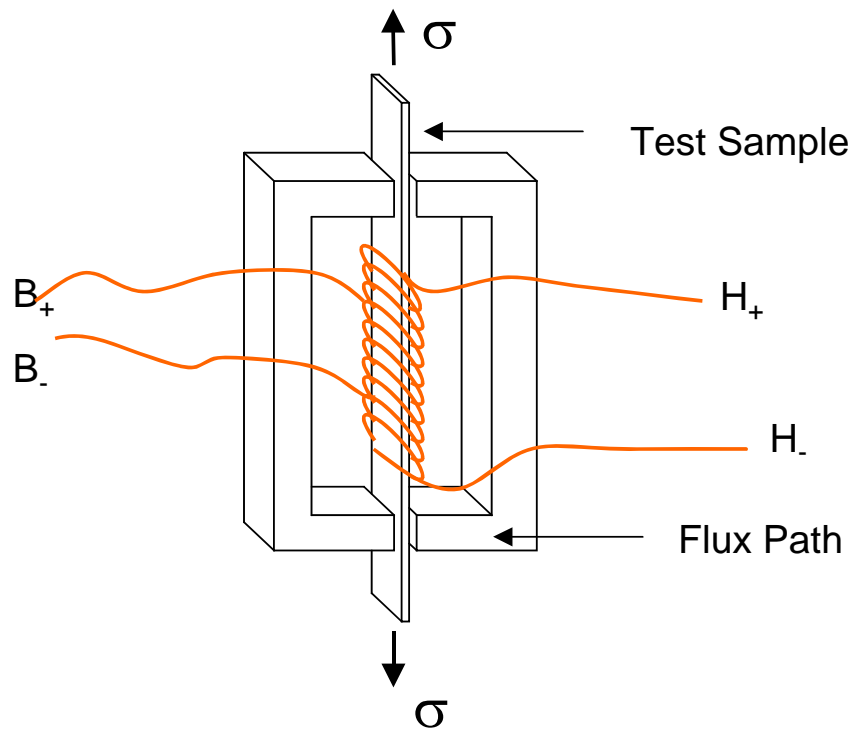


Fig. 4.1 Schematic representation of the fixture used for tensile stress testing

4.1.1 DC Magnetic Properties Under Tensile Stress

Following data covers the changes in the coercivity (H_c) and remanence ratio (B_r/B_s) with the application of tensile stress for Hipercro 27, Hipercro 50 and Hipercro 50HS alloys.

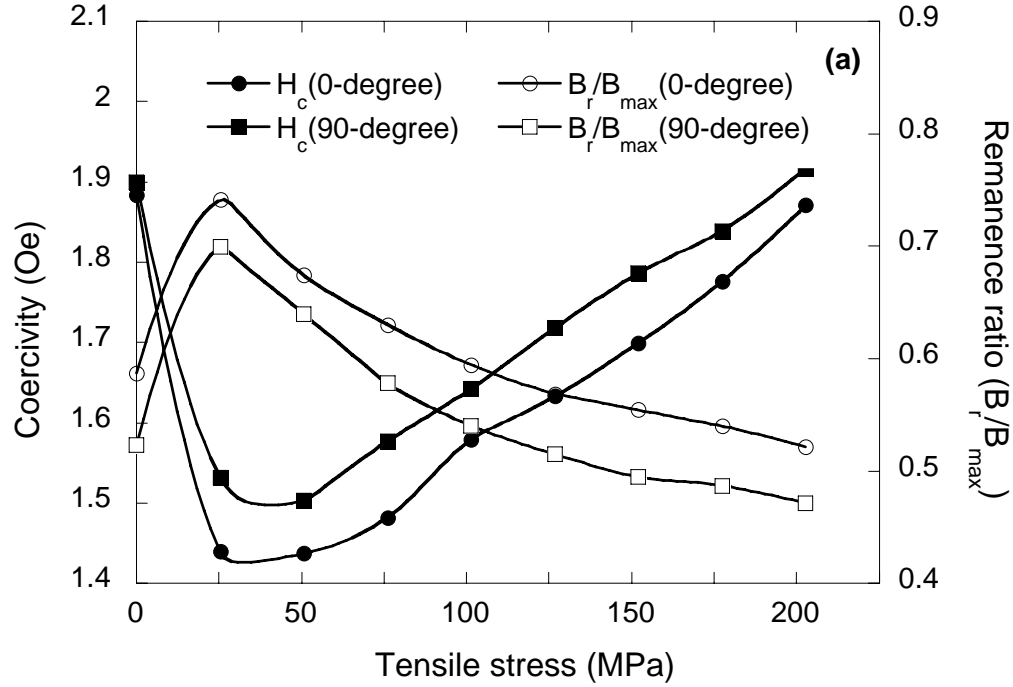


Fig. 4.2 DC coercivity and remanence ratio of Hipercro Alloy 27 at $B_{max}=18$ KG

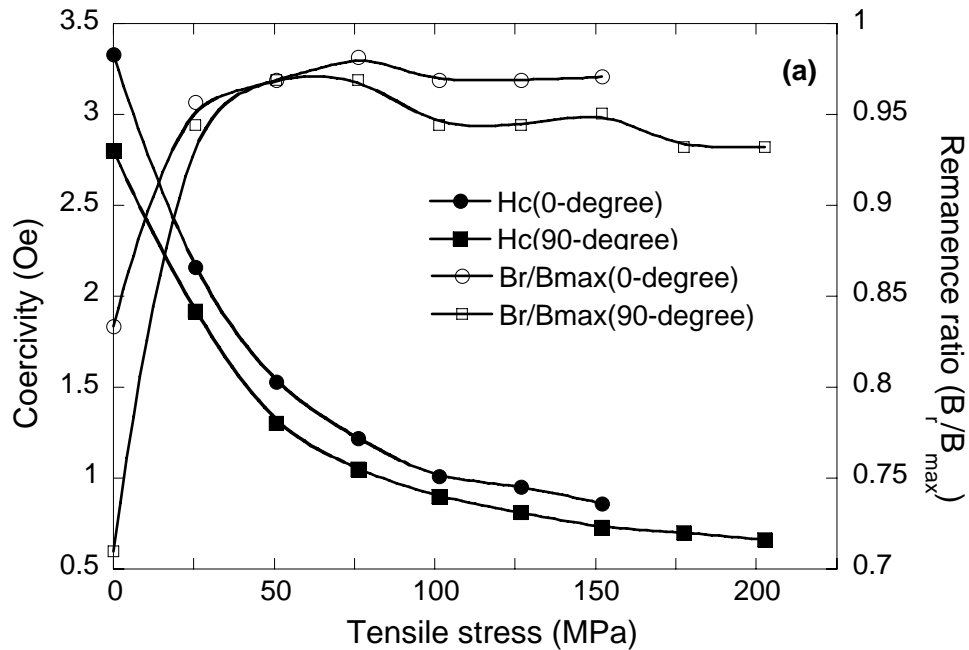


Fig. 4.3 DC coercivity and remanence ratio of Hipercro Alloy 50HS at $B_{max}=18$ KG

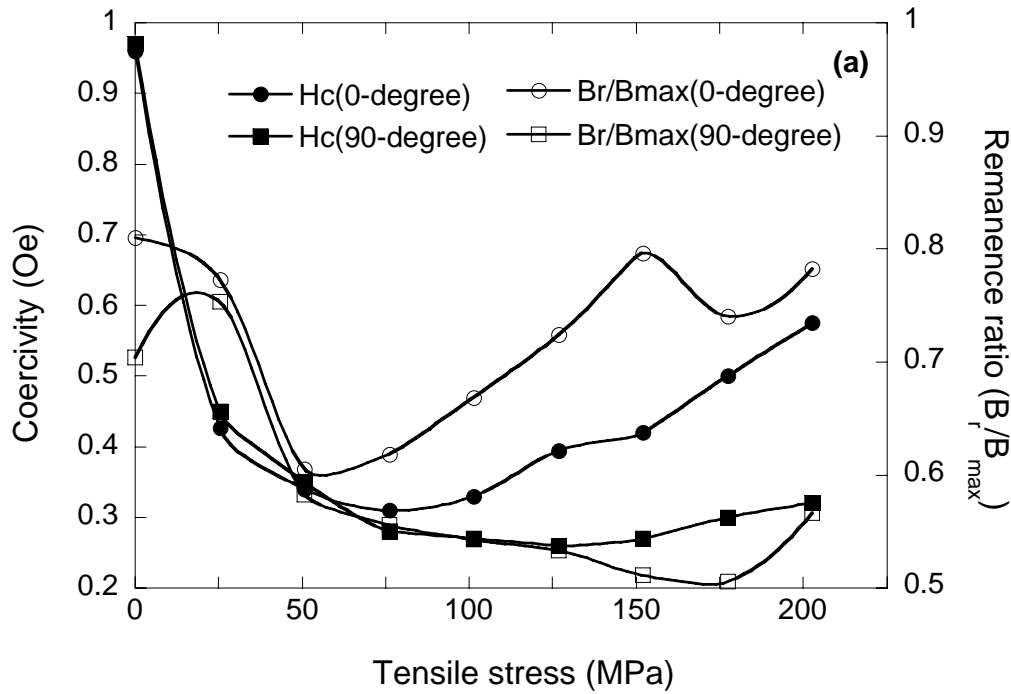


Fig. 4.4 DC coercivity and remanence ratio of Hipercro Alloy 50 at $B_{\max}=18$ KG

All the three alloys exhibited a steep decrease in the coercivity with the application of tensile stress, while a steep increase is observed in remanence ratio of the alloys Hipercro 27 and Hipercro 50 HS. For Hipercro 27 alloy above a stress of about 30 MPa, these trends are reversed, and at about 200 MPa the properties approach their zero-stress values. Hipercro 27 is magnetically softest in the rolling direction and hardest in the transverse direction. The Hipercro 50HS specimens exhibited continuously improving soft magnetic properties with increased tensile stress. The coercivity is still decreasing at a tensile stress of 200 MPa. However, the remanence ratio reaches a plateau at about 50 MPa, and the ratio has a very high value near 0.95. Hipercro 27 is magnetically softer in the rolling direction and harder in the transverse direction. The trend was reversed for Hipercro 50 HS. At zero stress, Hipercro 50 has the best soft magnetic properties of the three compositions. With applied tension, coercivity values are further reduced. After an initial drop, the coercivity of the specimen oriented in the rolling direction increased, while the transversely oriented specimen maintained lower coercivity values up to 200 MPa. This behavior was also apparent in the remanence ratios of the two specimens. This behavior is very different from the Hipercro 27 and Hipercro 50 HS alloys. In fact, applied tensile stress first decreased the remanence ratio of the Hipercro 50 alloy. While the remanence ratio of the sample cut parallel to the rolling direction recovered back to

its stress free values at high stress levels. The recovery was much less for the sample that was oriented perpendicular to the rolling direction.

4.1.2 Core Losses Under Tensile Stress

Total magnetic power losses of the three alloys followed the trend in coercivity and remanence ratio. Figures 4.5 through 4.58 depict the magnetic core losses as a function of applied tensile stress where RD, TD and DD are rolling, transverse and diagonal directions respectively.

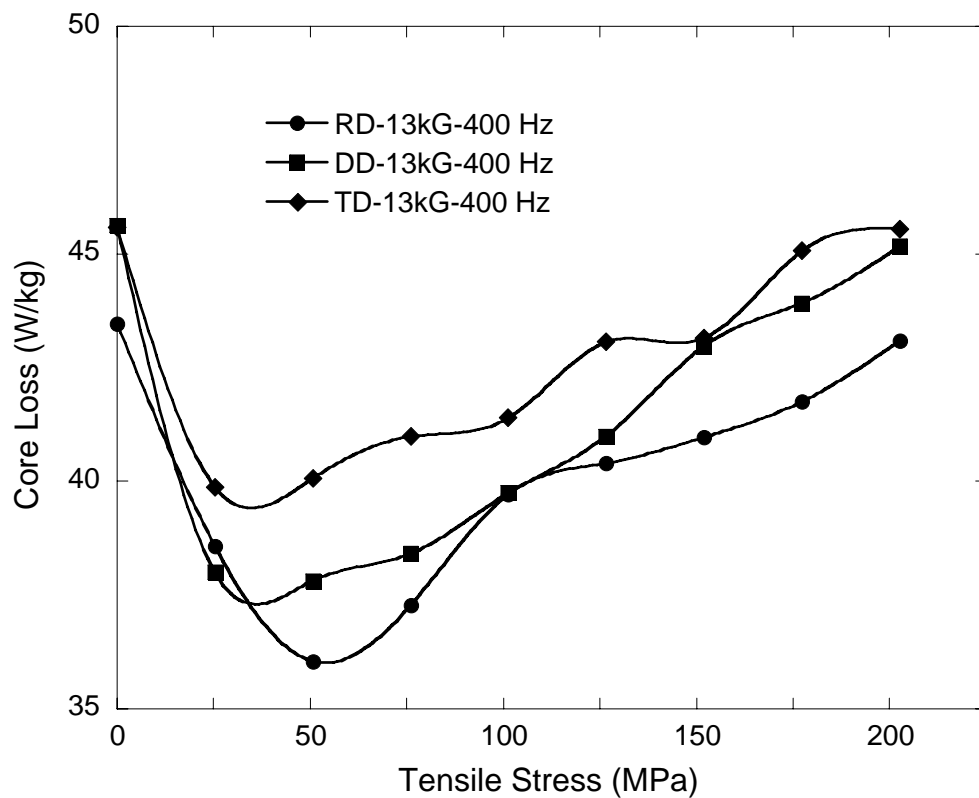


Fig. 4.5 Total core losses for Hiperco Alloy 27 at 13 kG B_{\max} and 400 Hz

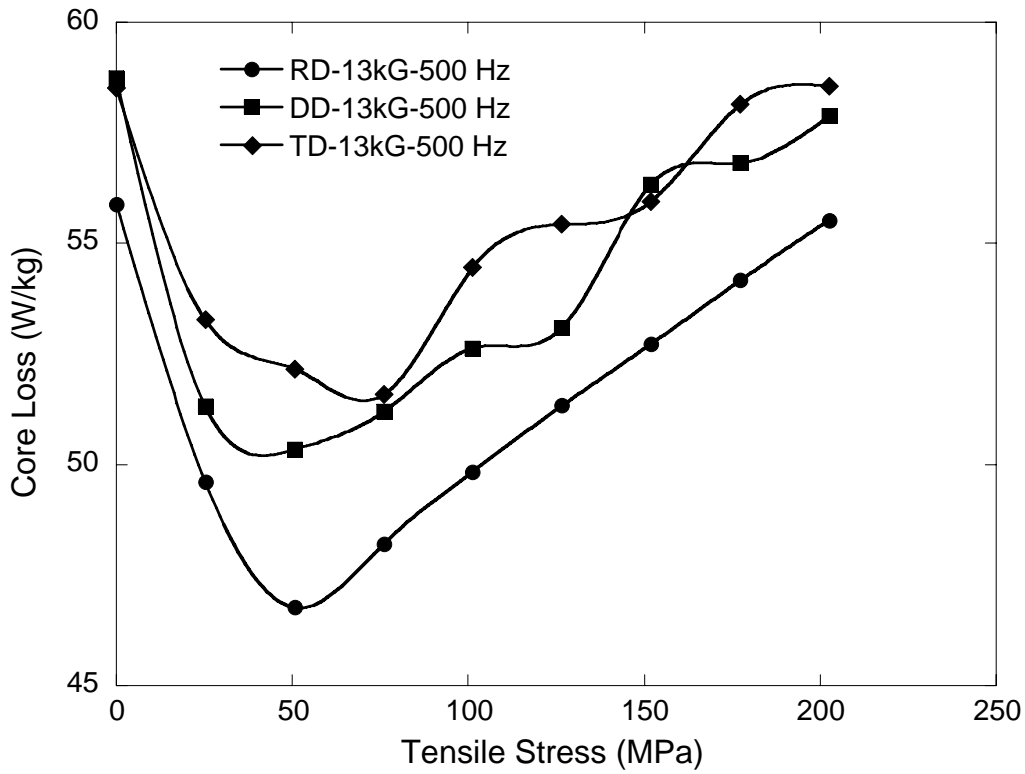


Fig. 4.6 Total core losses for Hiperco Alloy 27 at 13 kG B_{max} and 500 Hz

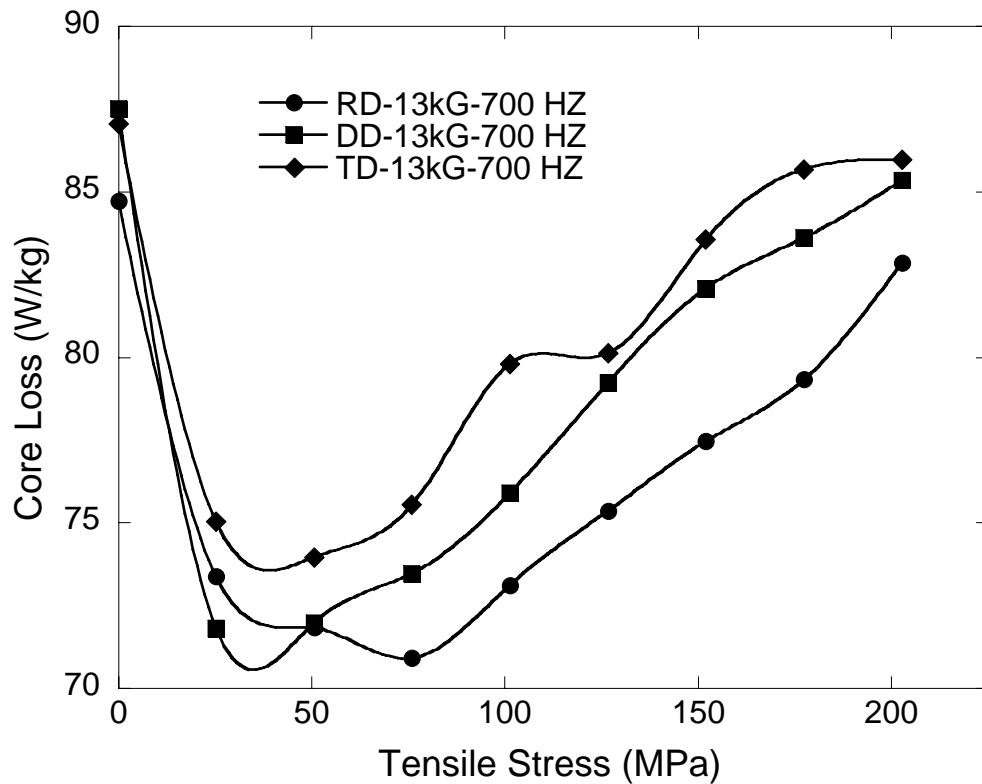


Fig. 4.7 Total core losses for Hiperco Alloy 27 at 13 kG B_{max} and 700 Hz

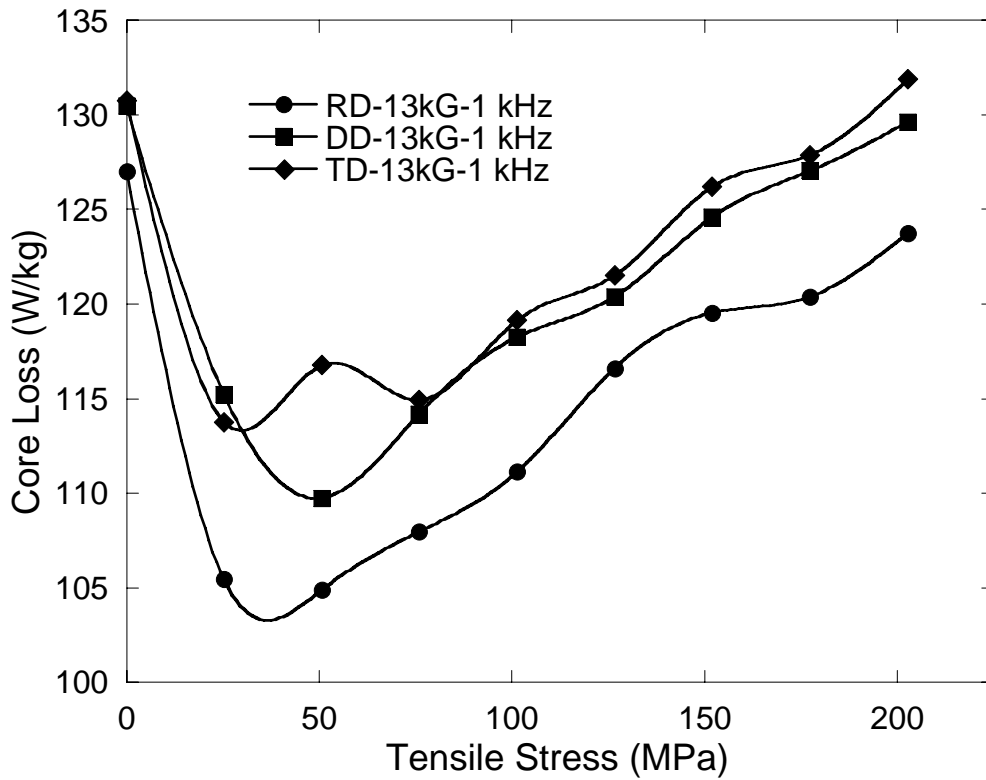


Fig. 4.8 Total core losses for Hiperco Alloy 27 at 13 kG B_{max} and 1000 Hz

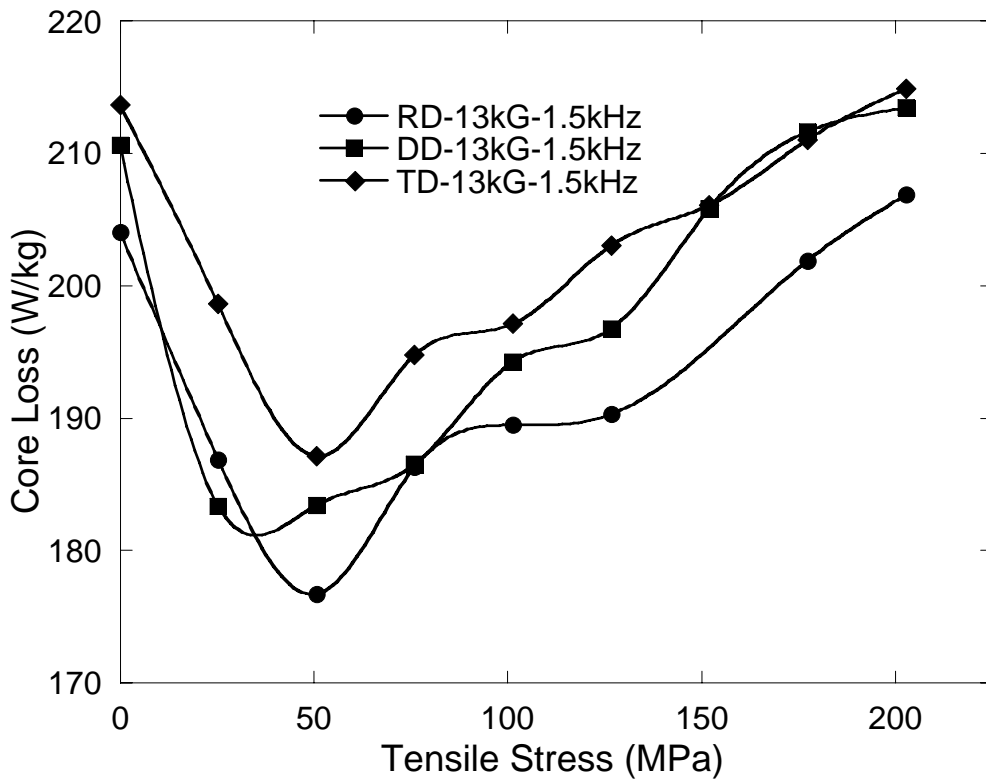


Fig. 4.9 Total core losses for Hiperco Alloy 27 at 13 kG B_{max} and 1500 Hz

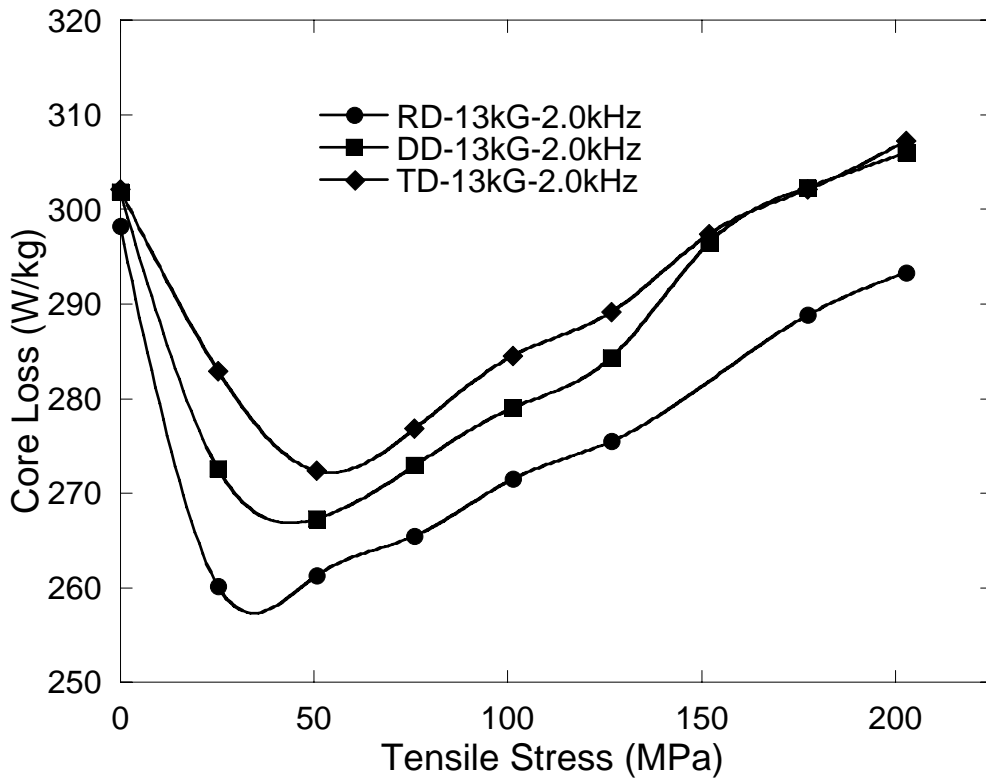


Fig. 4.10 Total core losses for Hiperco Alloy 27 at 13 kG B_{max} and 2000 Hz

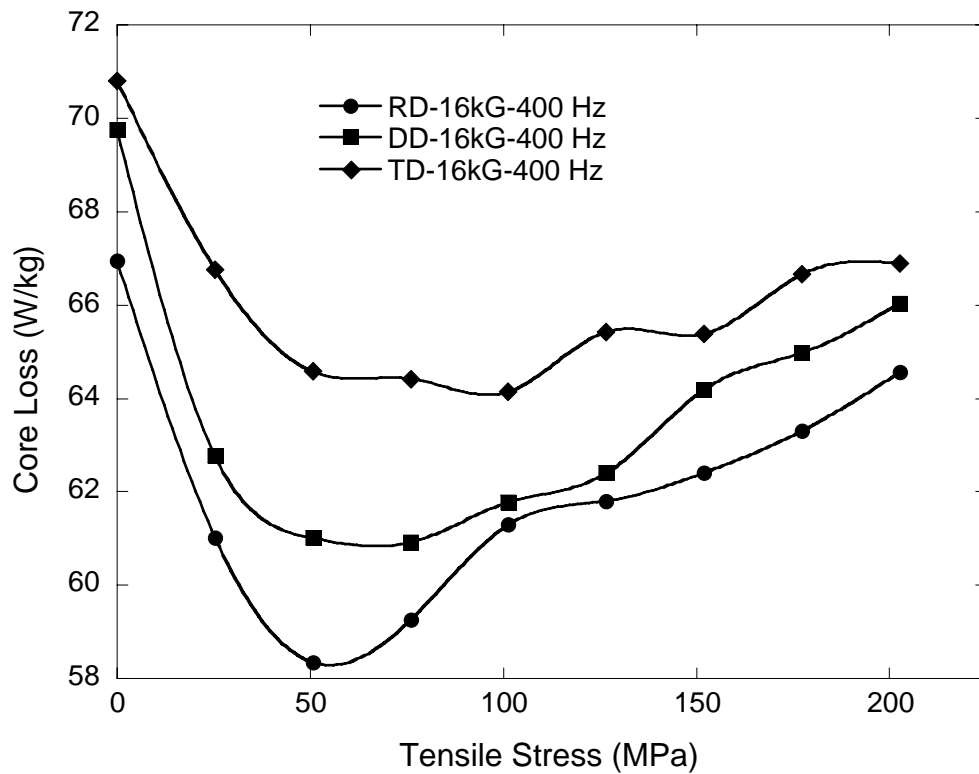


Fig. 4.11 Total core losses for Hiperco Alloy 27 at 16 kG B_{max} and 400 Hz

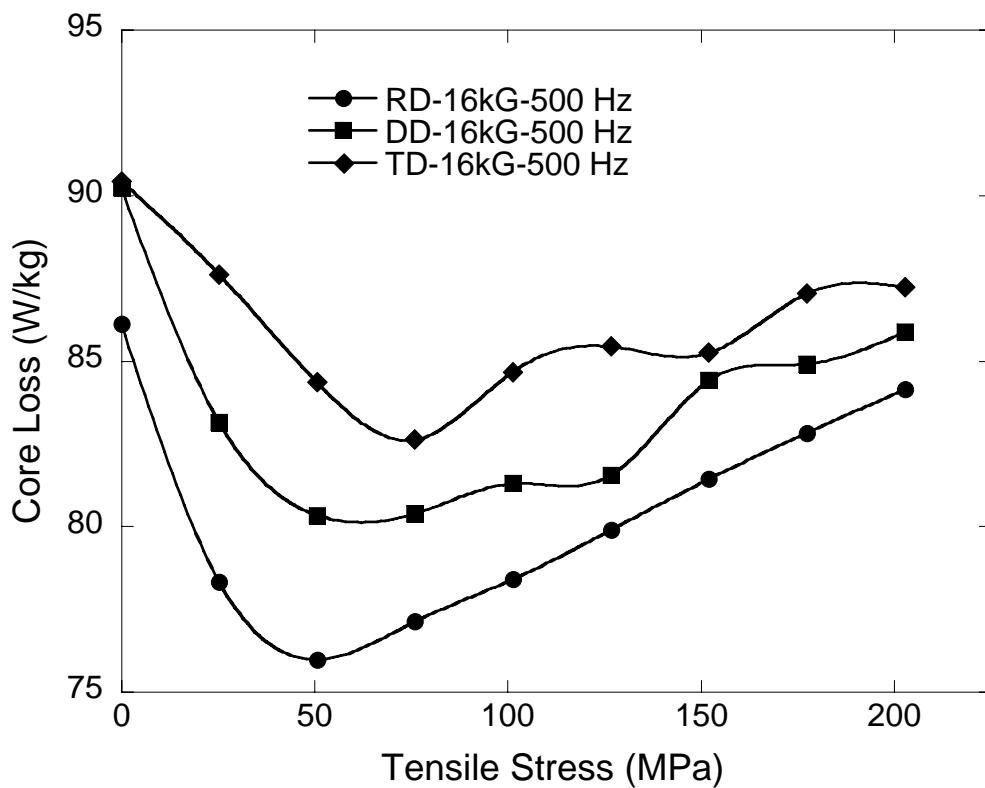


Fig. 4.12 Total core losses for Hiperco Alloy 27 at 16 kG B_{max} and 500 Hz

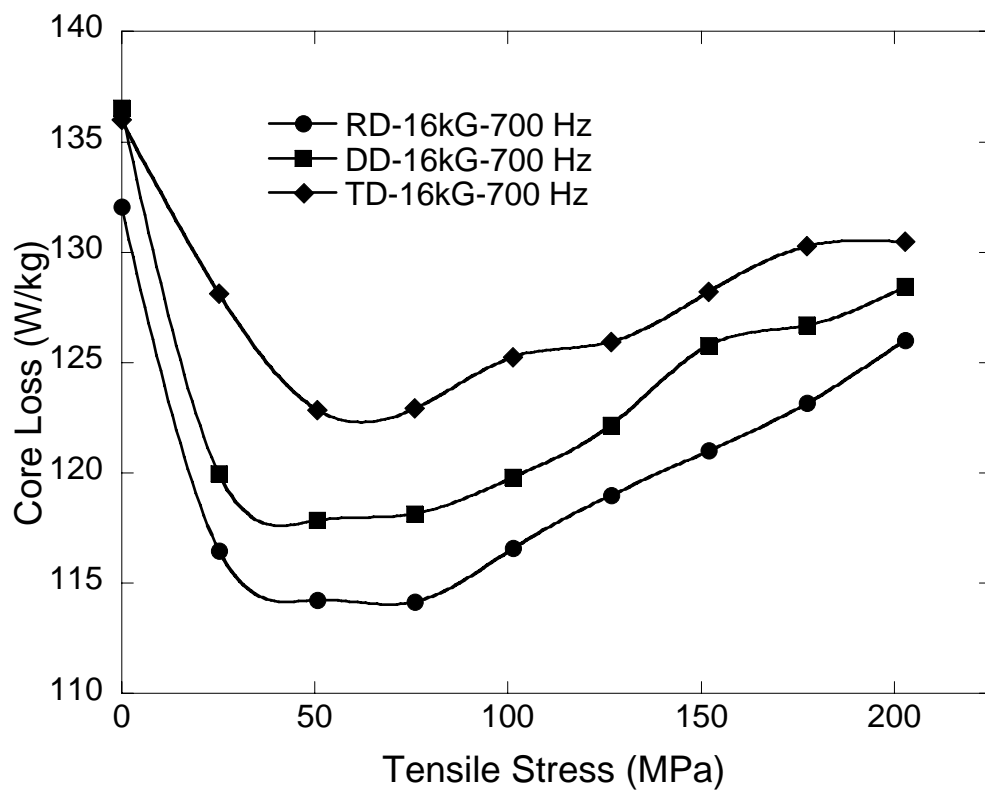


Fig. 4.13 Total core losses for Hiperco Alloy 27 at 16 kG B_{max} and 700 Hz

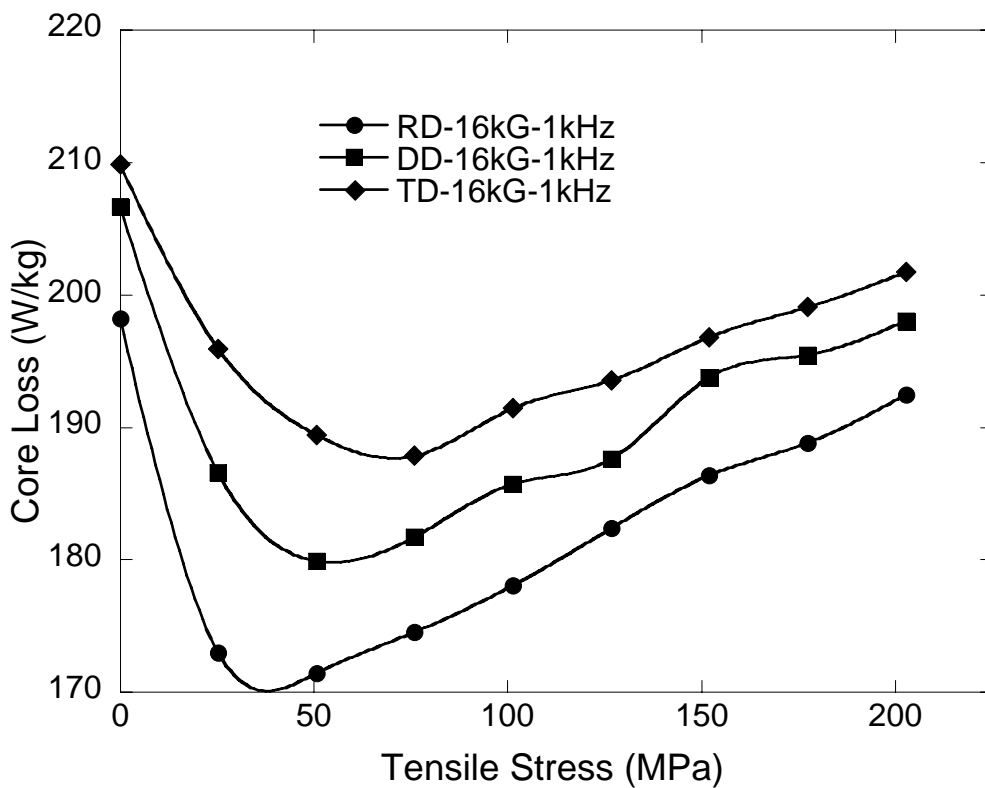


Fig. 4.14 Total core losses for Hiperco Alloy 27 at 16 kG B_{max} and 1000 Hz

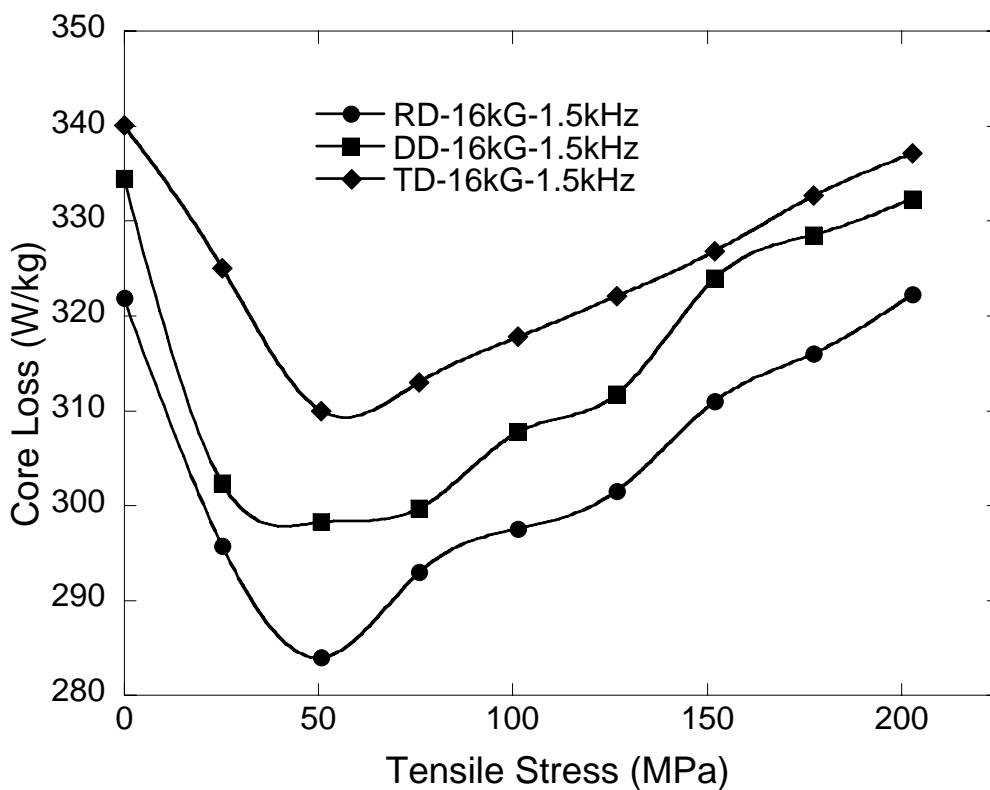


Fig. 4.15 Total core losses for Hiperco Alloy 27 at 16 kG B_{max} and 1500 Hz

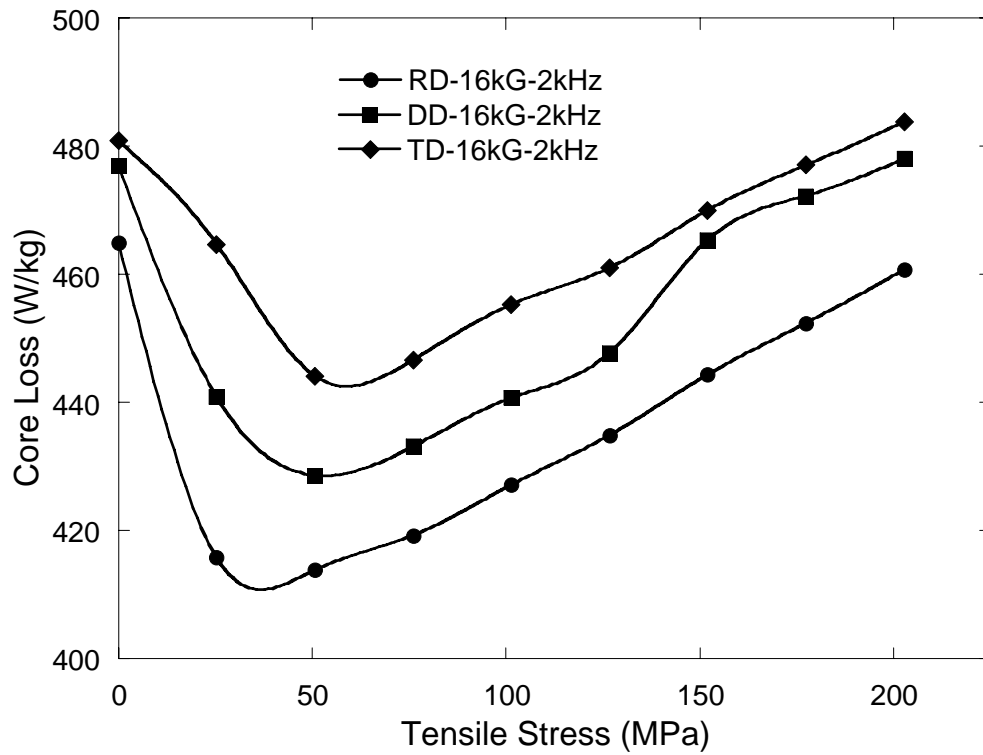


Fig. 4.16 Total core losses for Hiperco Alloy 27 at 16 kG B_{max} and 2000 Hz

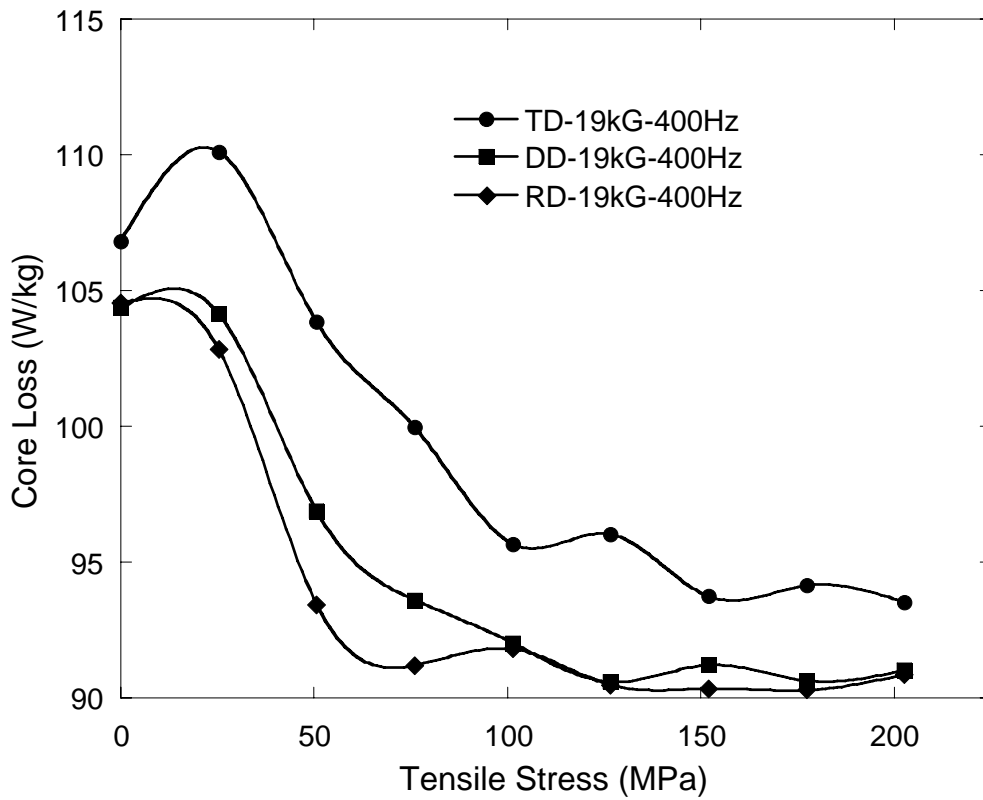


Fig. 4.17 Total core losses for Hiperco Alloy 27 at 19 kG B_{max} and 400 Hz

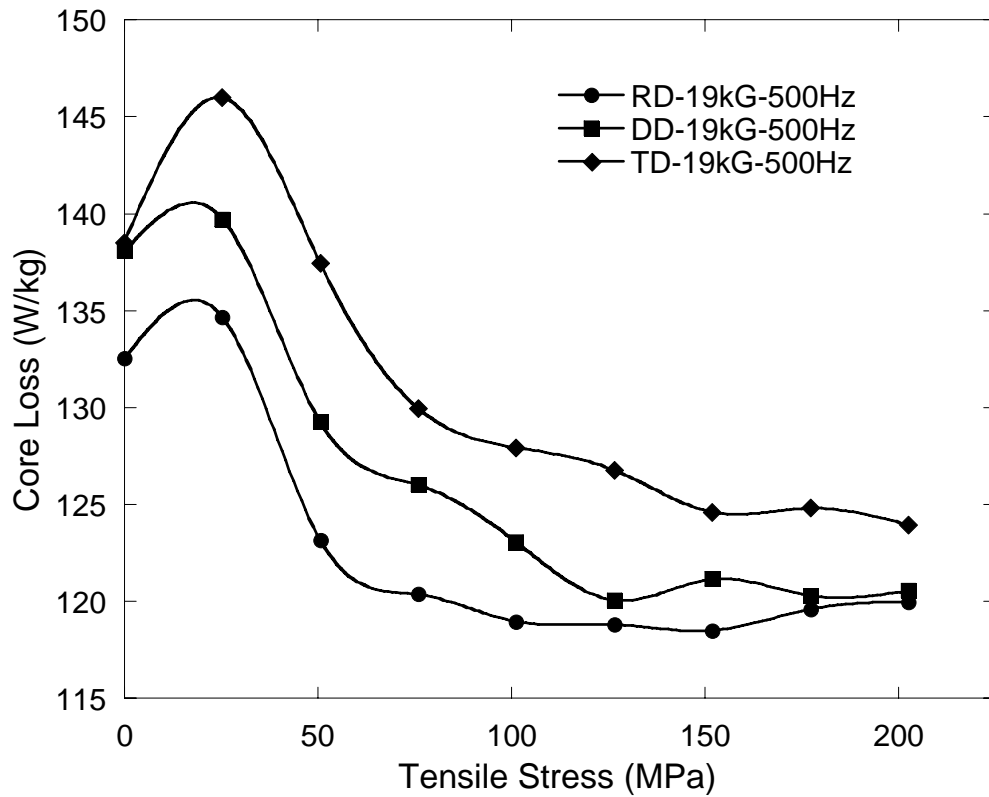


Fig. 4.18 Total core losses for Hiperco Alloy 27 at 19 kG B_{max} and 500 Hz

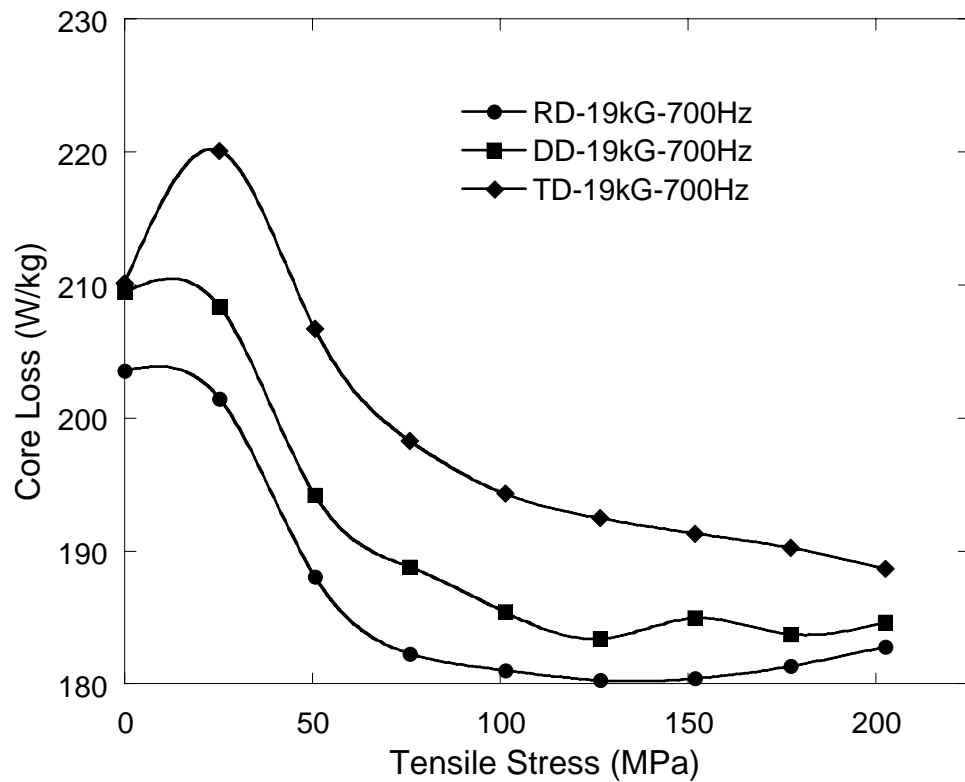


Fig. 4.19 Total core losses for Hiperco Alloy 27 at 19 kG B_{max} and 700 Hz

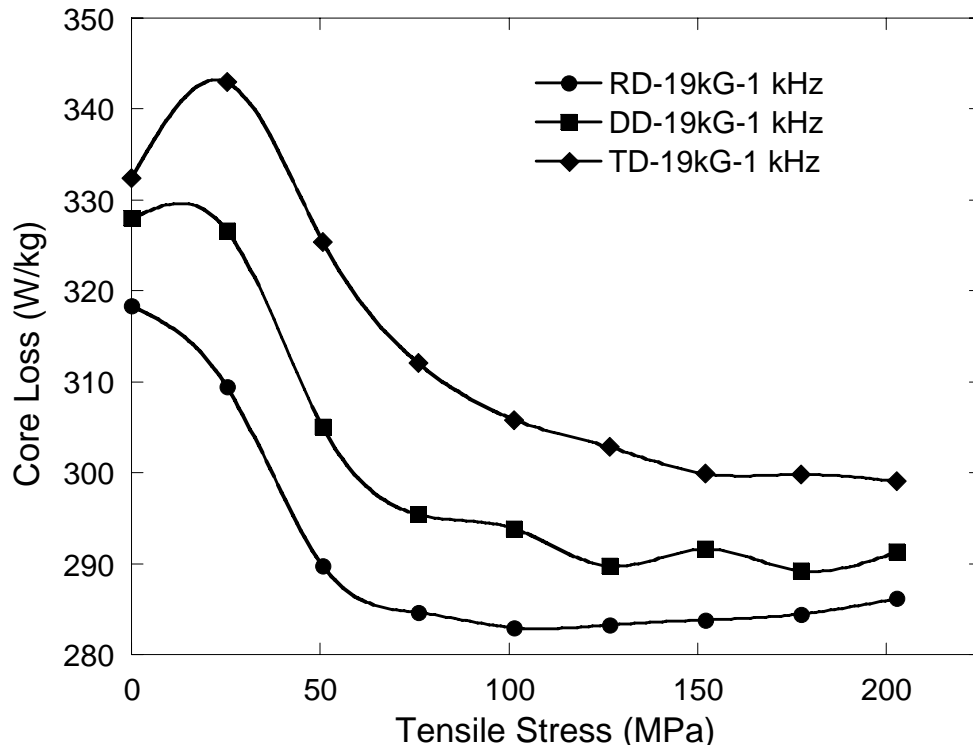


Fig. 4.20 Total core losses for Hiperco Alloy 27 at 19 kG B_{\max} and 1000 Hz

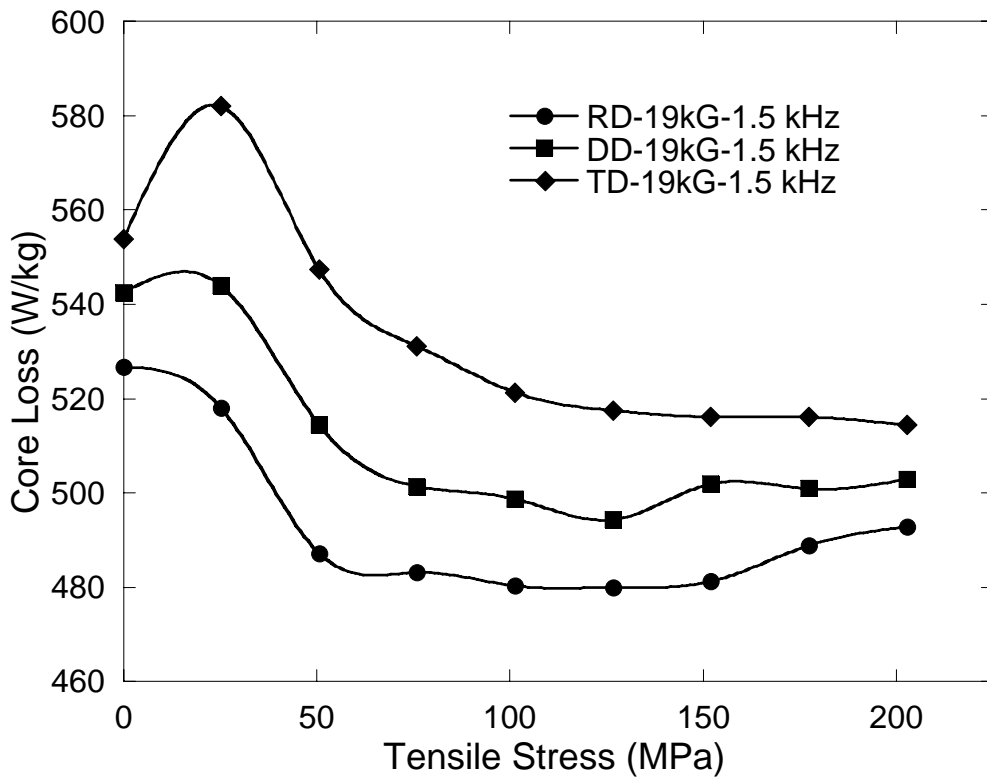


Fig. 4.21 Total core losses for Hiperco Alloy 27 at 19 kG B_{\max} and 1500 Hz

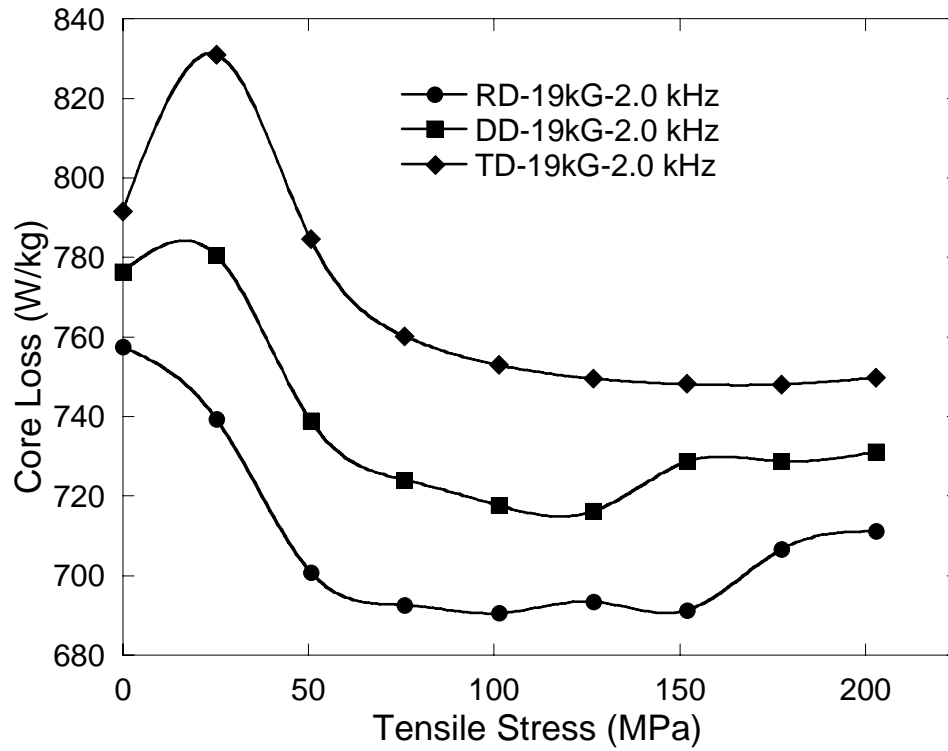


Fig. 4.22 Total core losses for Hipercro Alloy 27 at 19 kG B_{max} and 2000 Hz

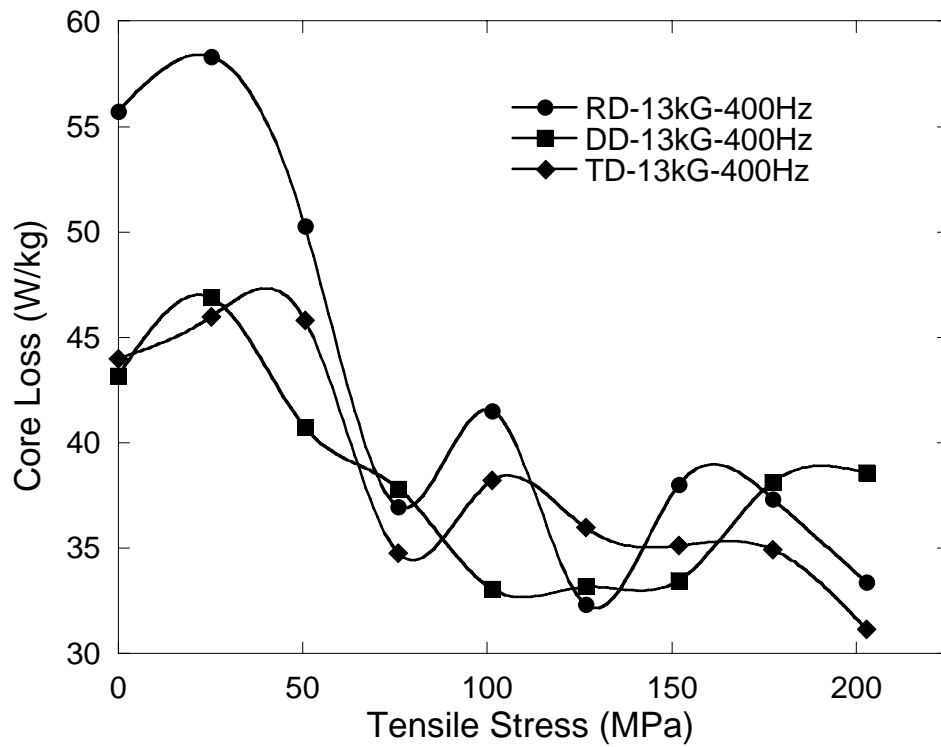


Fig. 4.23 Total core losses for Hipercro Alloy 50HS at 13 kG B_{max} and 400 Hz

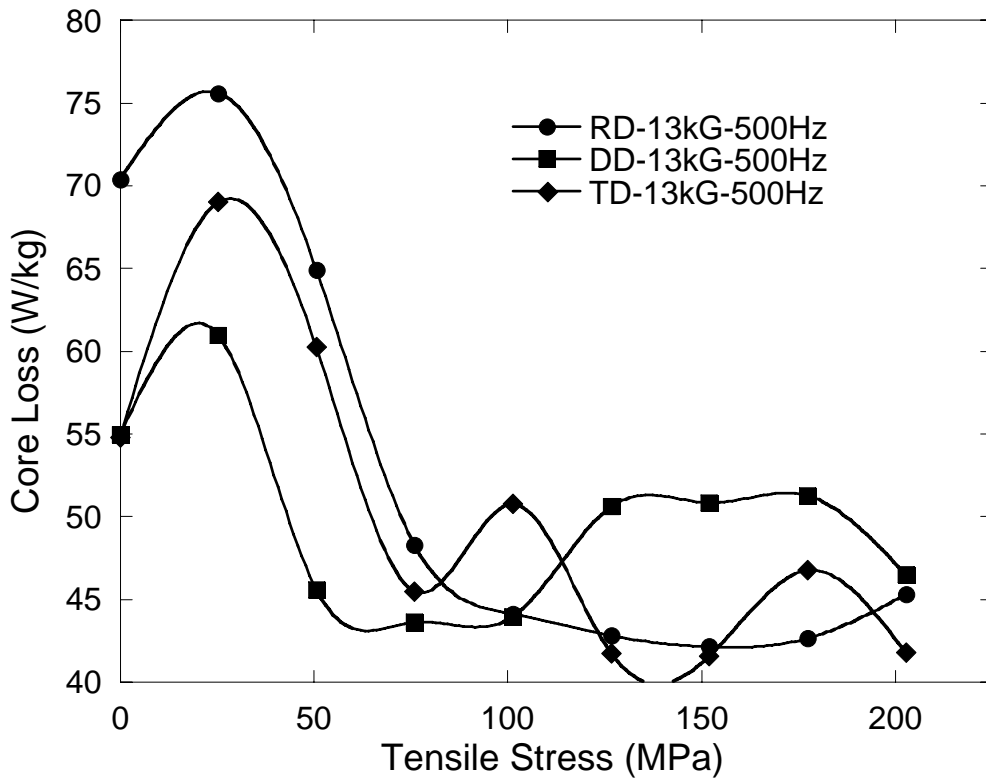


Fig. 4.24 Total core losses for Hiperco Alloy 50HS at 13 kG B_{\max} and 500 Hz

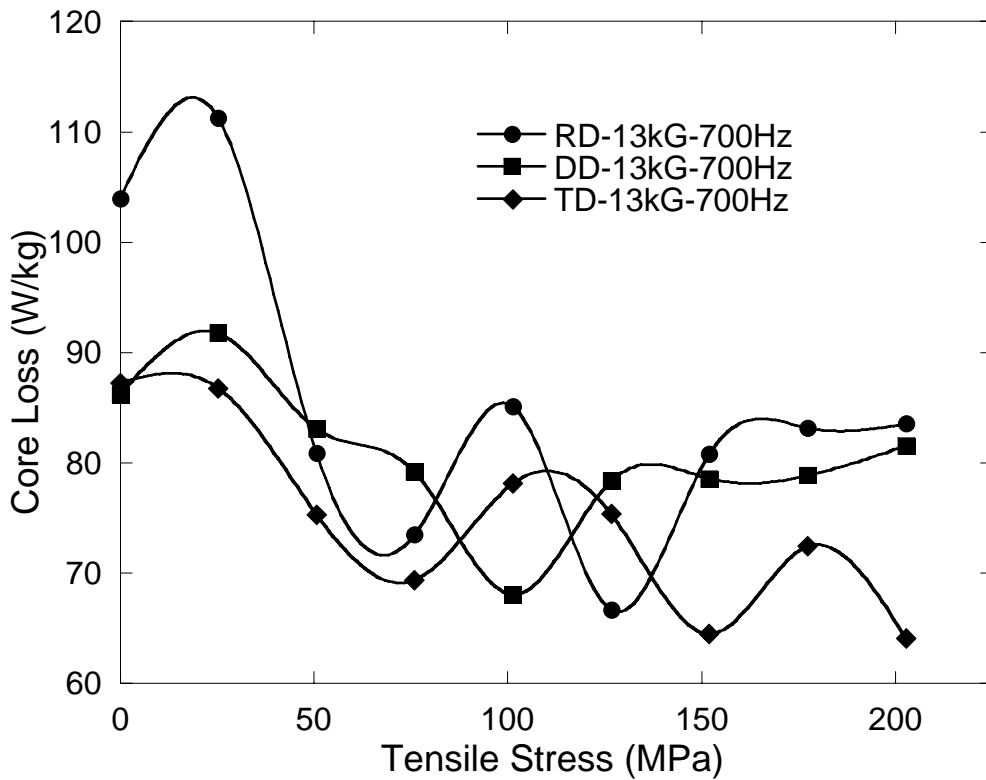


Fig. 4.25 Total core losses for Hiperco Alloy 50HS at 13 kG B_{\max} and 700 Hz

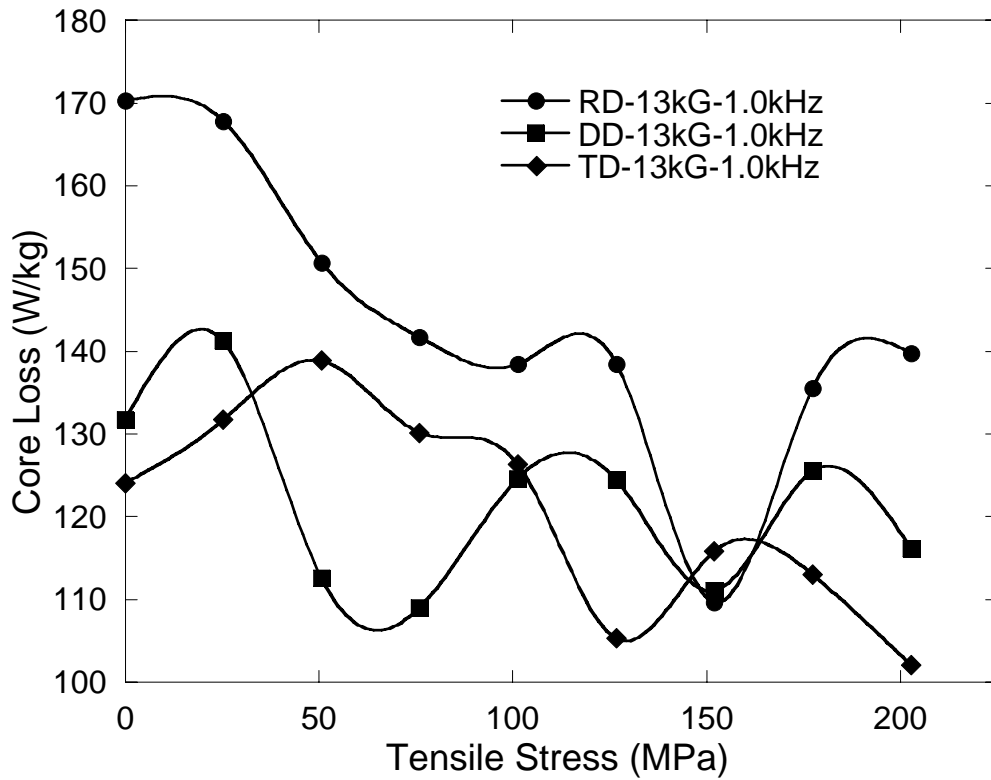


Fig. 4.26 Total core losses for Hiperco Alloy 50HS at 13 kG B_{\max} and 1000 Hz

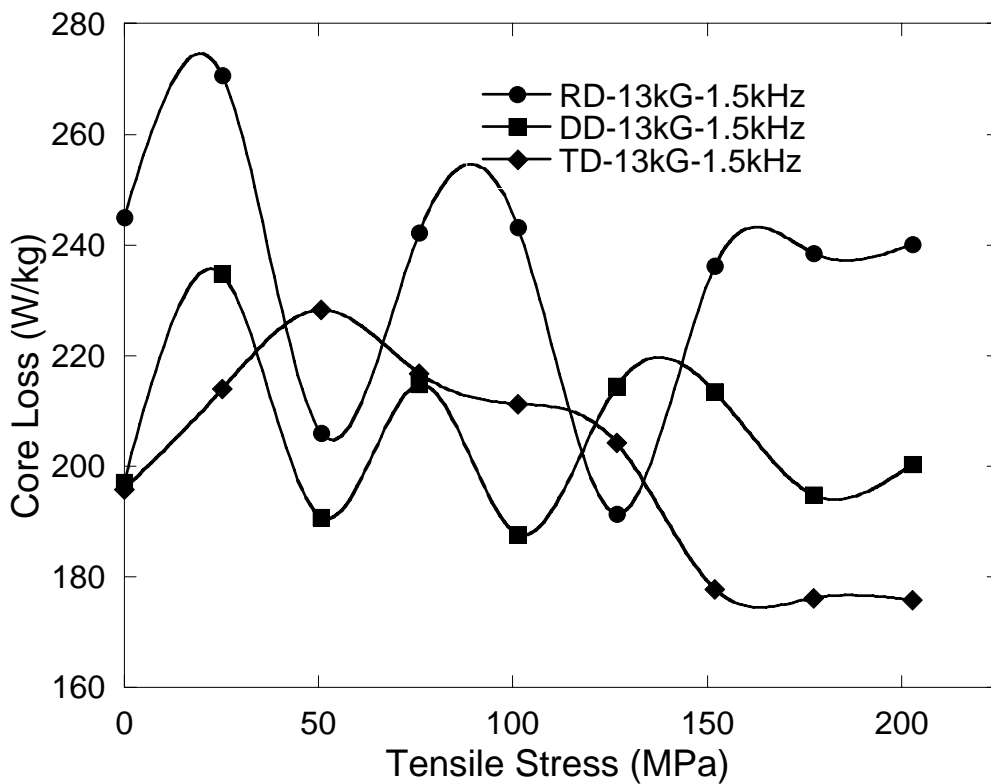


Fig. 4.27 Total core losses for Hiperco Alloy 50HS at 13 kG B_{\max} and 1500 Hz

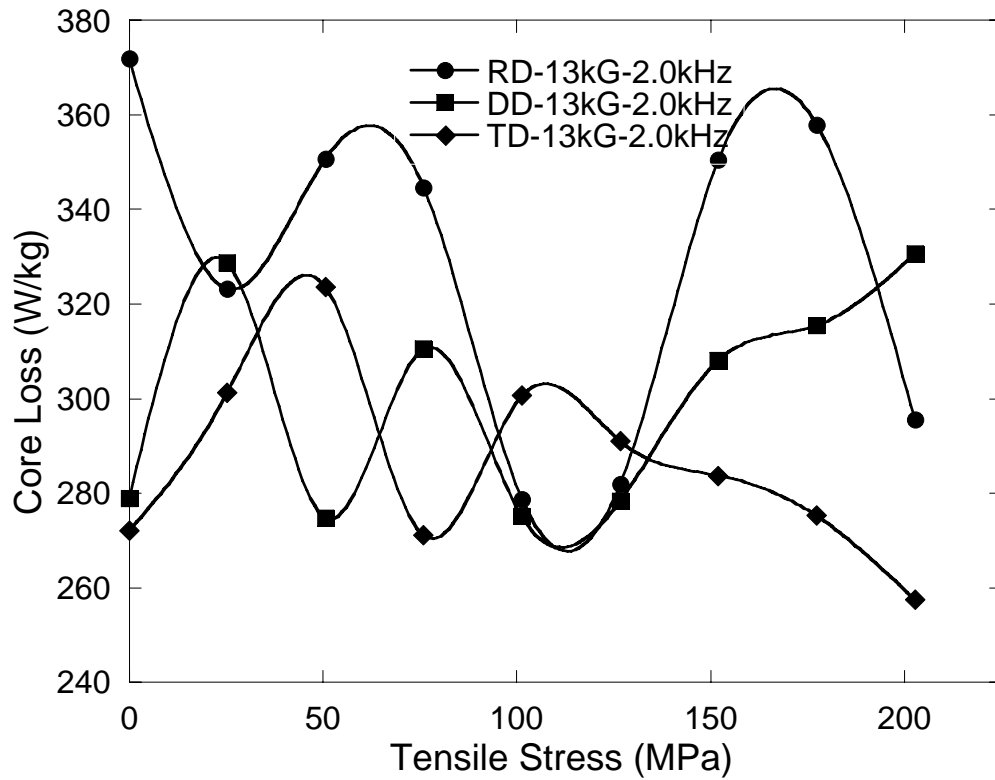


Fig. 4.28 Total core losses for Hipercro Alloy 50HS at 13 kG B_{\max} and 2000 Hz

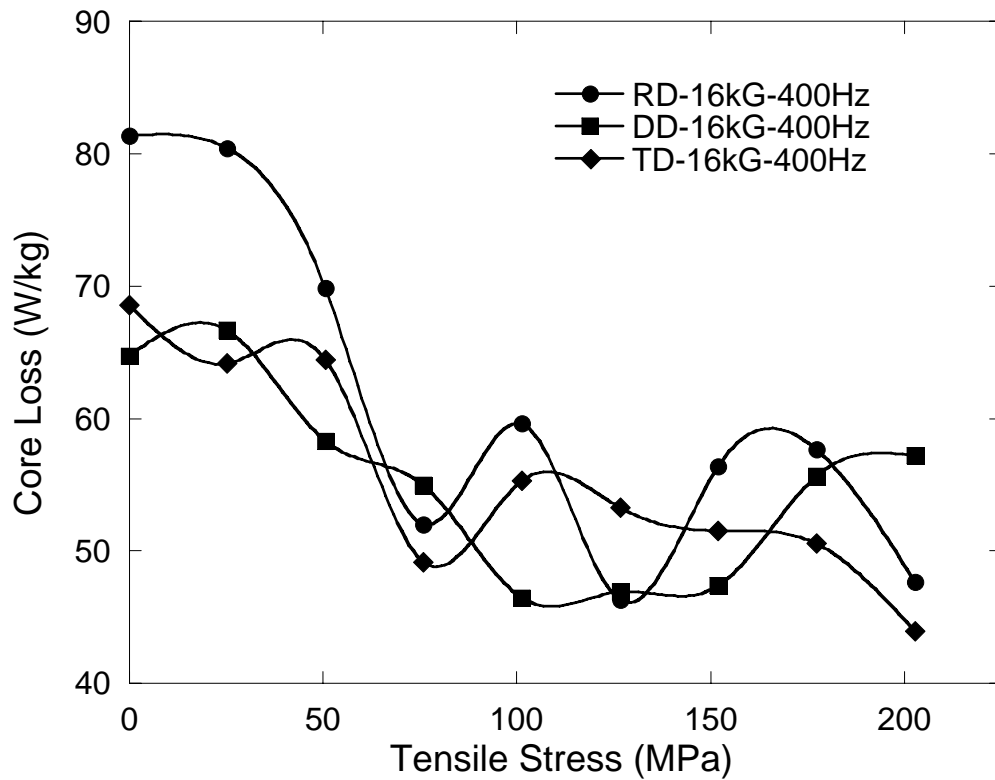


Fig. 4.29 Total core losses for Hipercro Alloy 50HS at 16 kG B_{\max} and 400 Hz

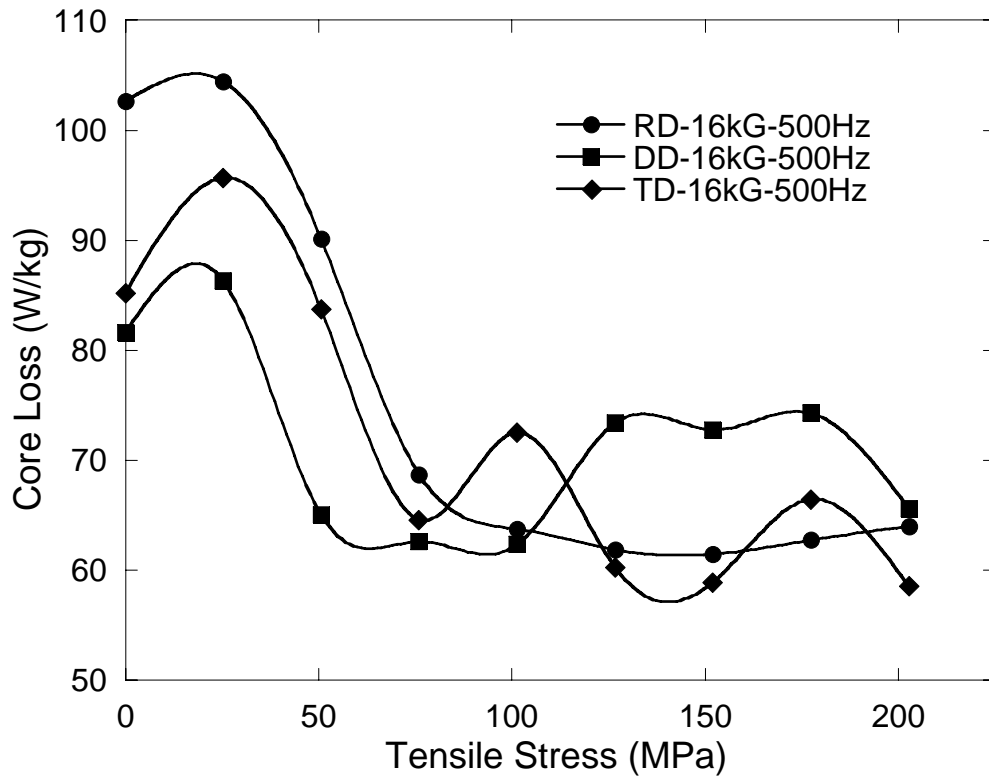


Fig. 4.30 Total core losses for Hiperco Alloy 50HS at 16 kG B_{\max} and 500 Hz

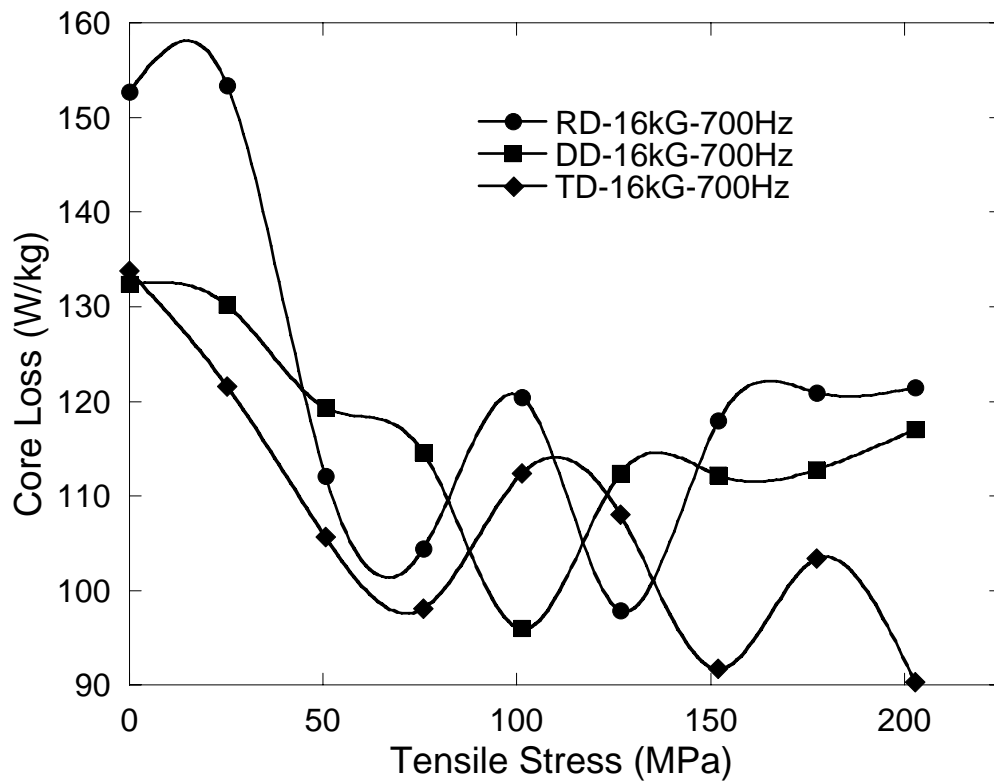


Fig. 4.31 Total core losses for Hiperco Alloy 50HS at 16 kG B_{\max} and 700 Hz

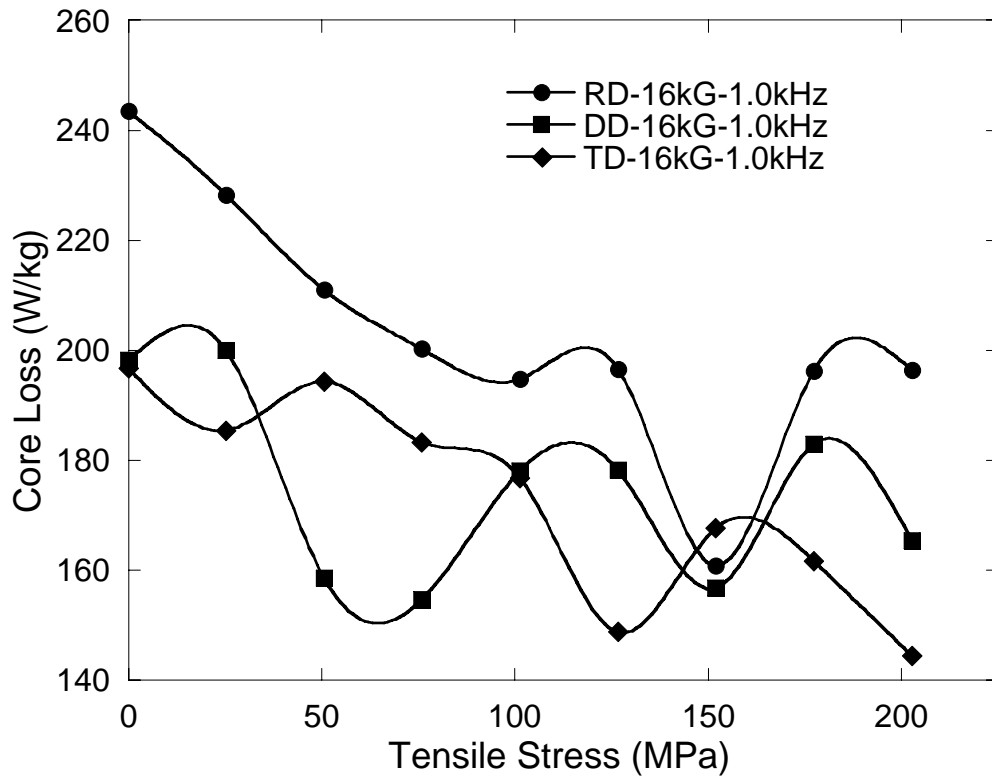


Fig. 4.32 Total core losses for Hiperco Alloy 50HS at 16 kG B_{\max} and 1000 Hz

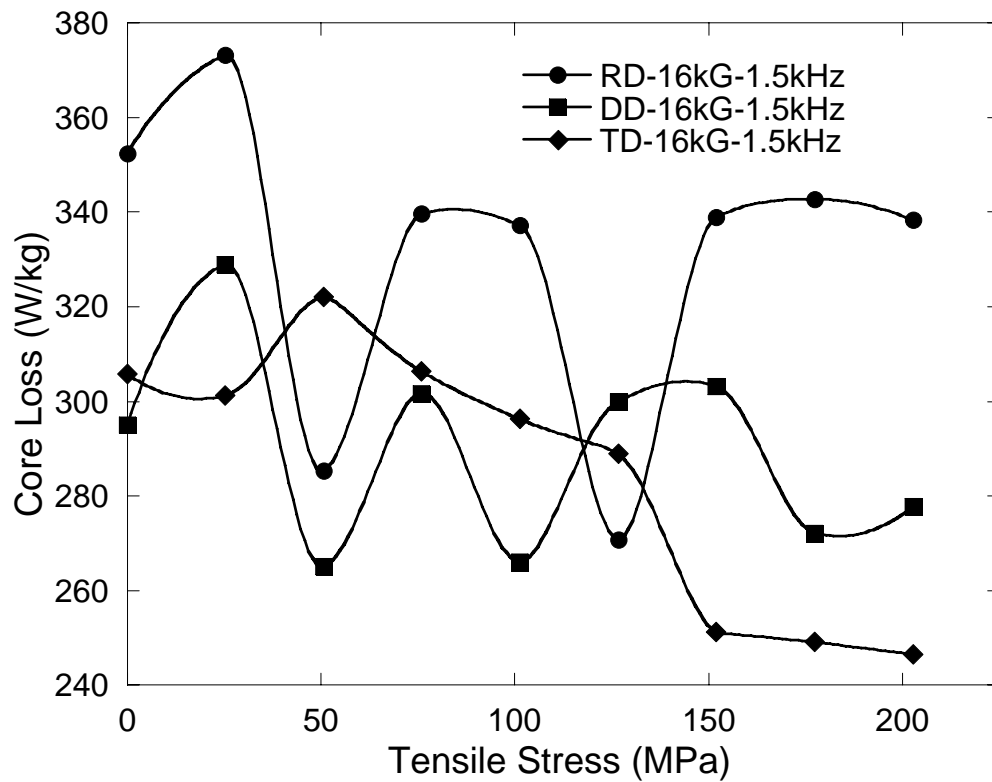


Fig. 4.33 Total core losses for Hiperco Alloy 50HS at 16 kG B_{\max} and 1500 Hz

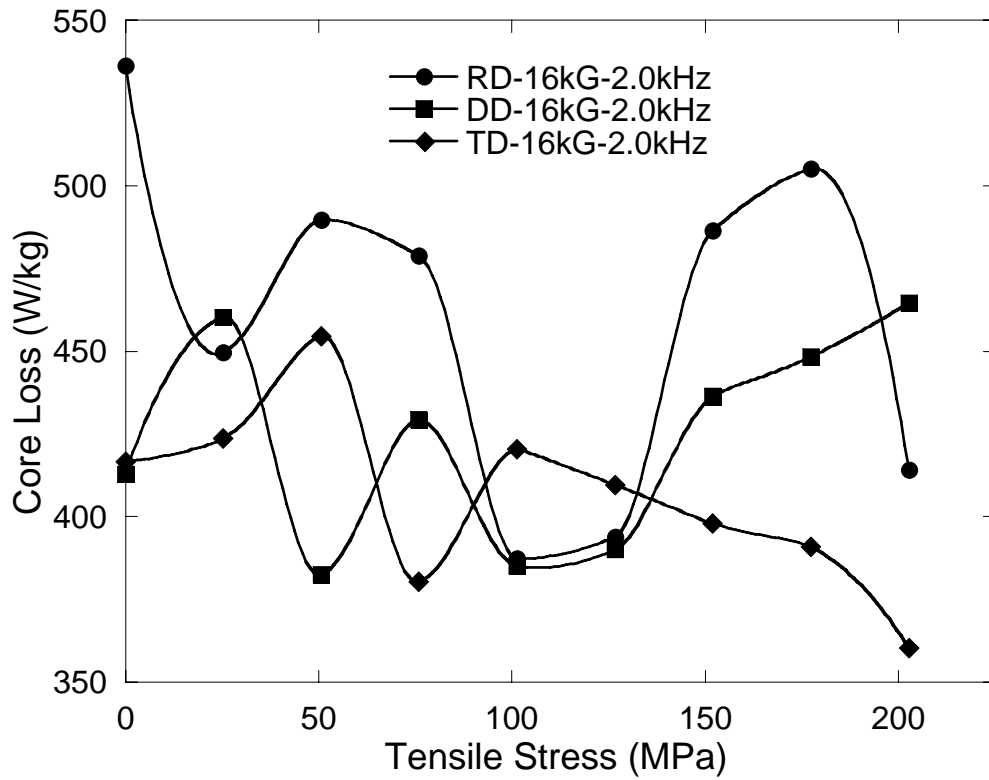


Fig. 4.34 Total core losses for Hiperco Alloy 50HS at 16 kG B_{\max} and 2000 Hz

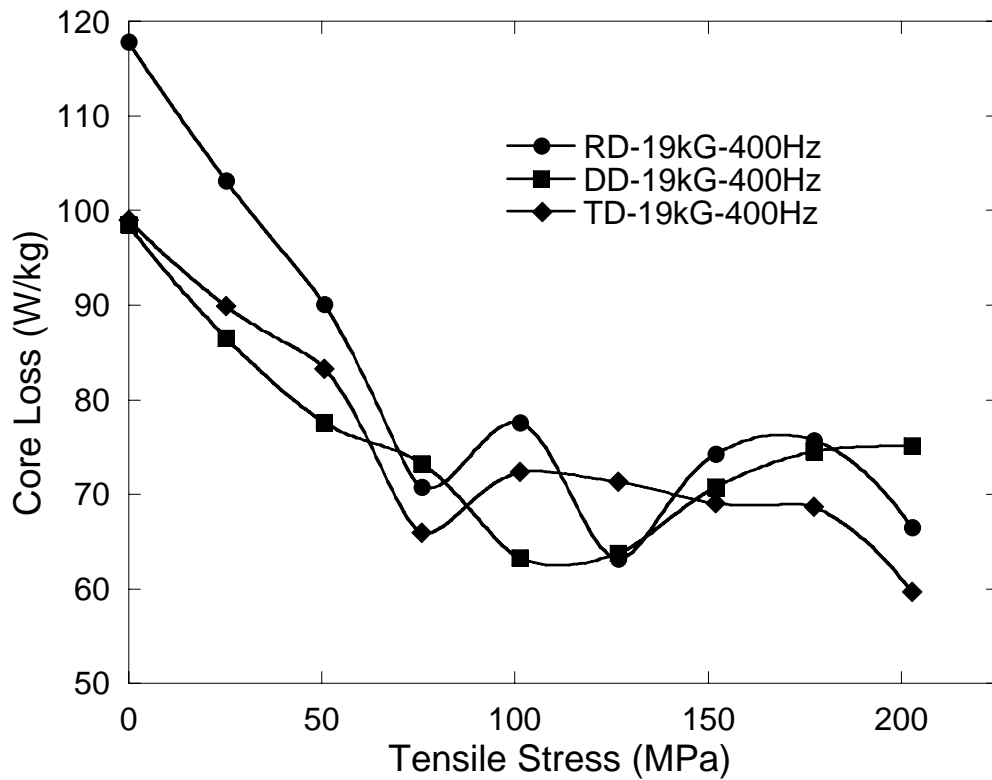


Fig. 4.35 Total core losses for Hiperco Alloy 50HS at 19 kG B_{\max} and 400 Hz

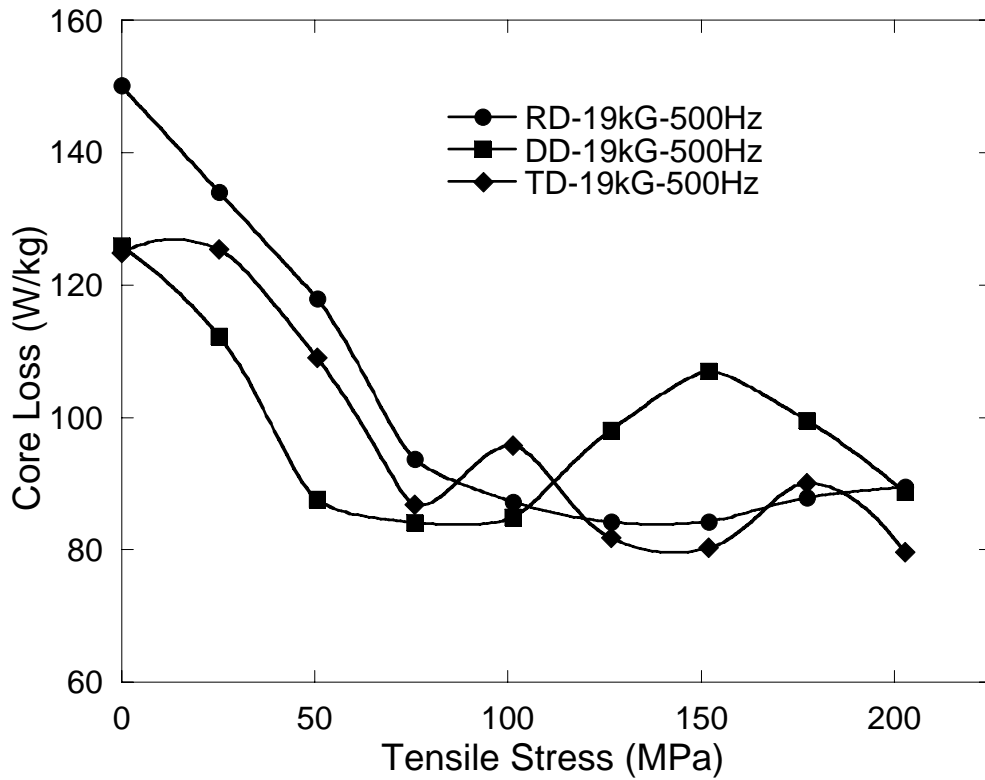


Fig. 4.36 Total core losses for Hiperco Alloy 50HS at 19 kG B_{\max} and 500 Hz

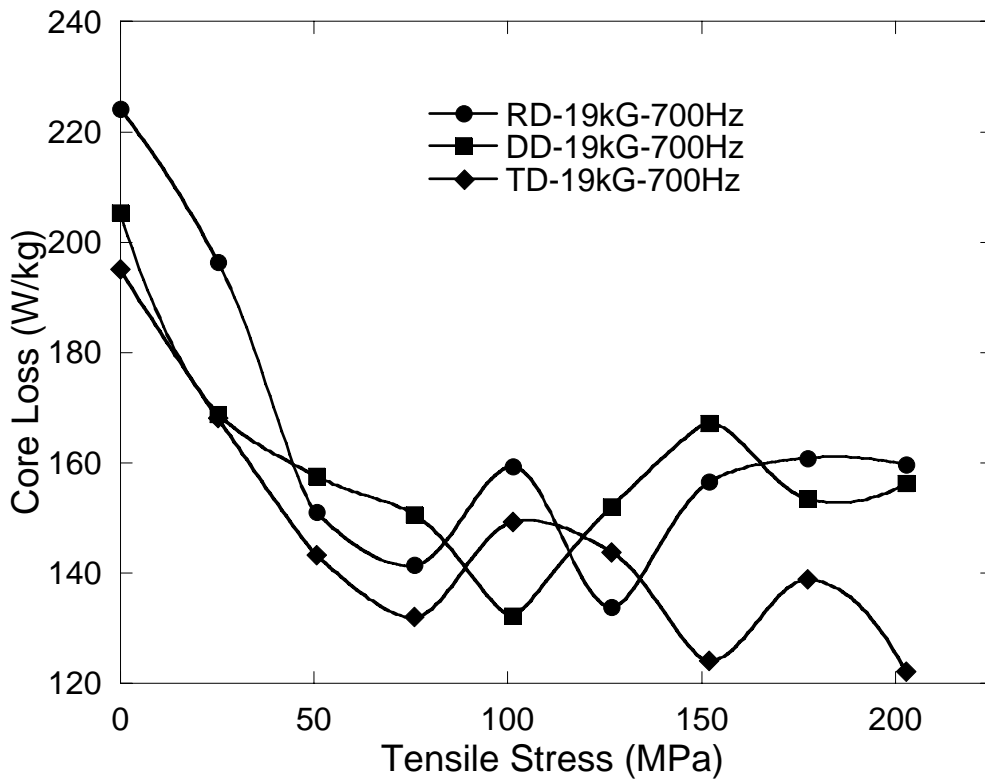


Fig. 4.37 Total core losses for Hiperco Alloy 50HS at 19 kG B_{\max} and 700 Hz

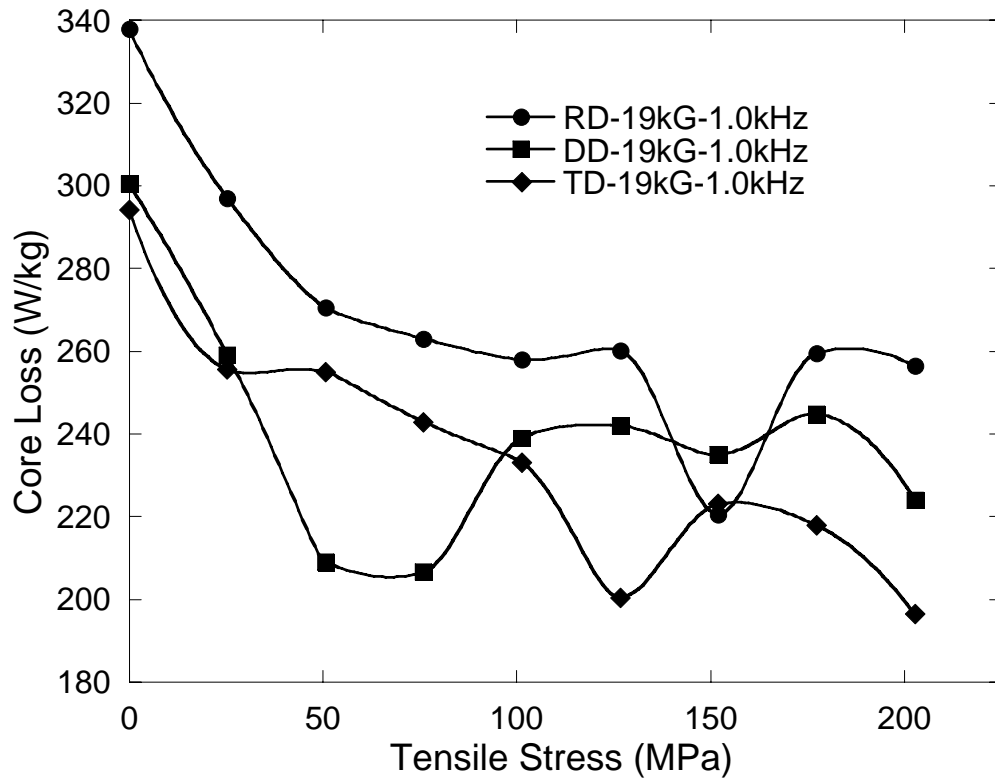


Fig. 4.38 Total core losses for Hiperco Alloy 50HS at 19 kG B_{\max} and 1000 Hz

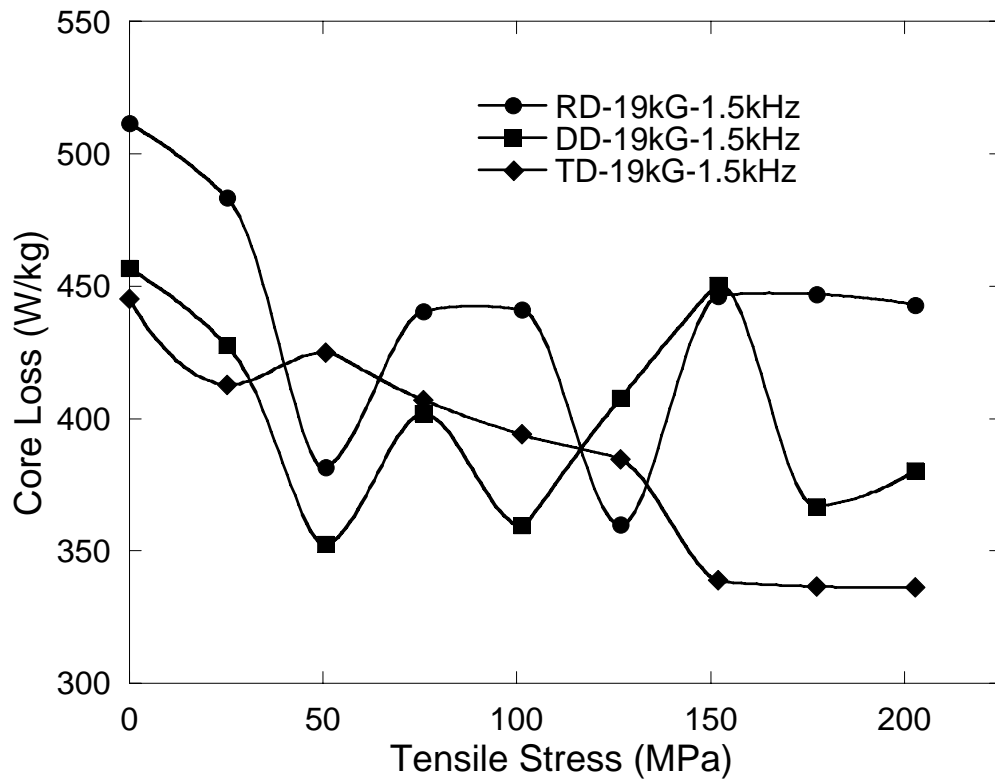


Fig. 4.39 Total core losses for Hiperco Alloy 50HS at 19 kG B_{\max} and 1500 Hz

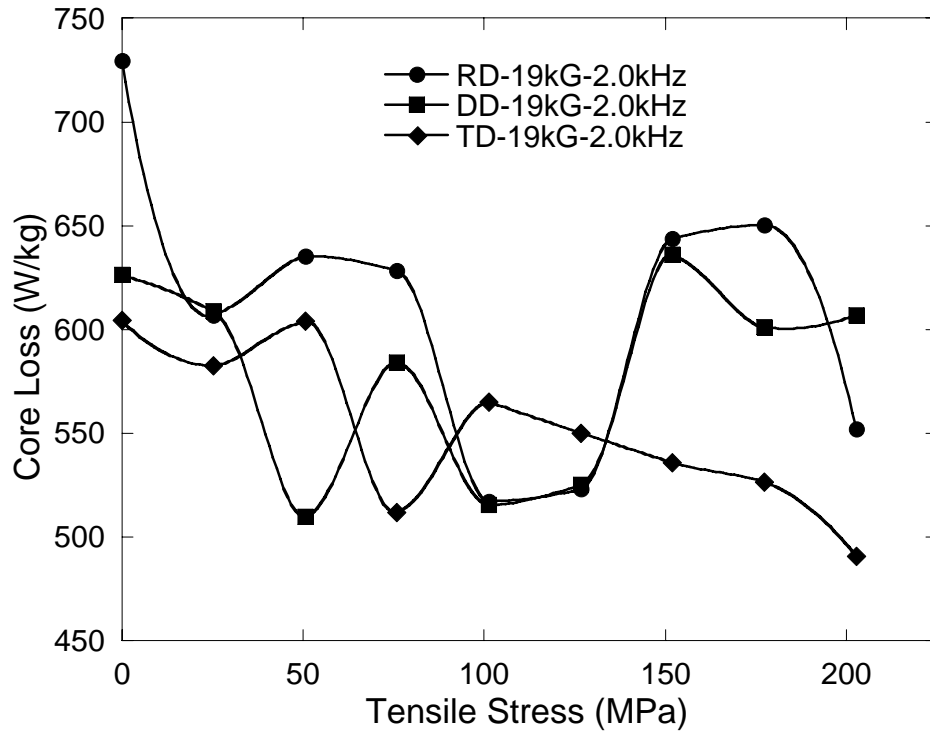


Fig. 4.40 Total core losses for Hiperco Alloy 50HS at 19 kG B_{\max} and 2000 Hz

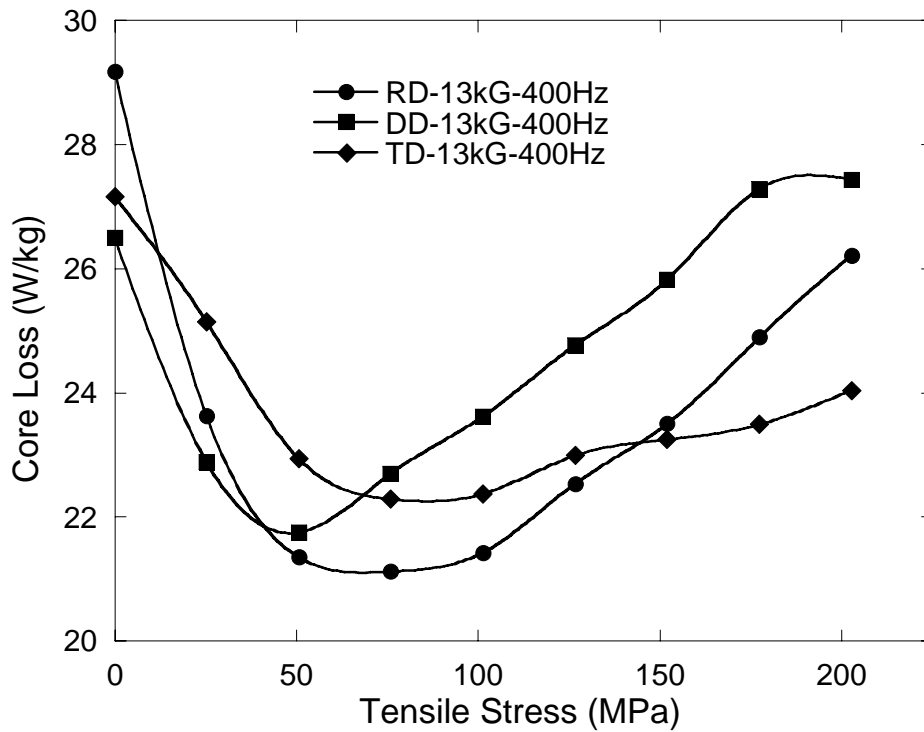


Fig. 4.41 Total core losses for Hiperco Alloy 50 at 13 kG B_{\max} and 400 Hz

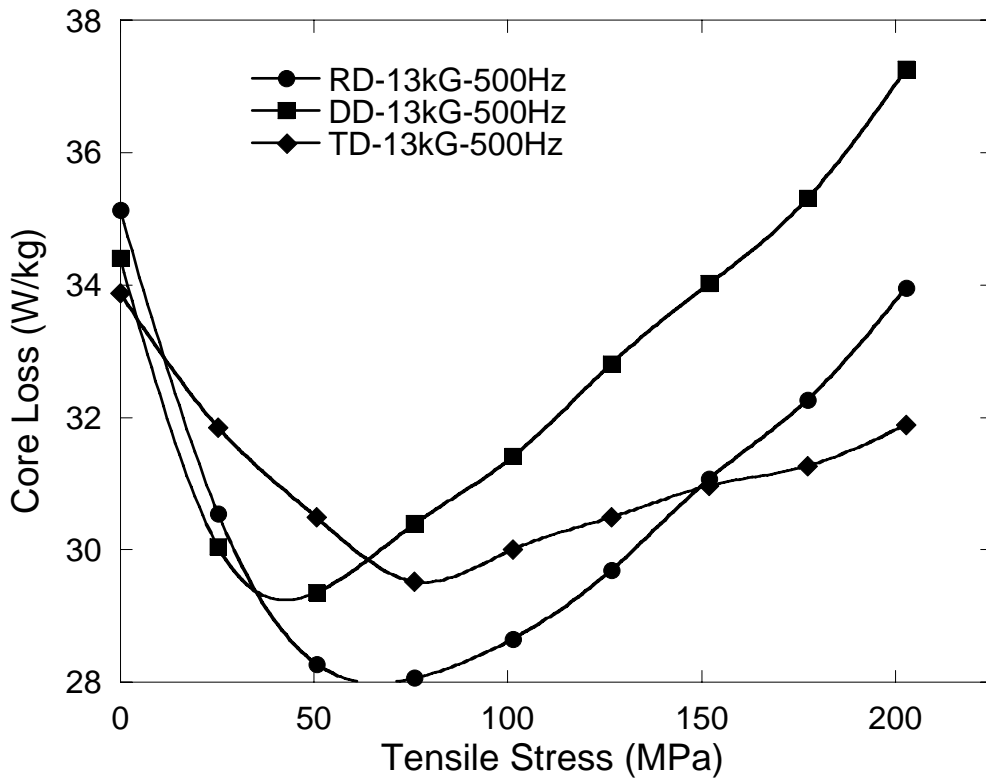


Fig. 4.42 Total core losses for Hiperco Alloy 50 at 13 kG B_{max} and 500 Hz

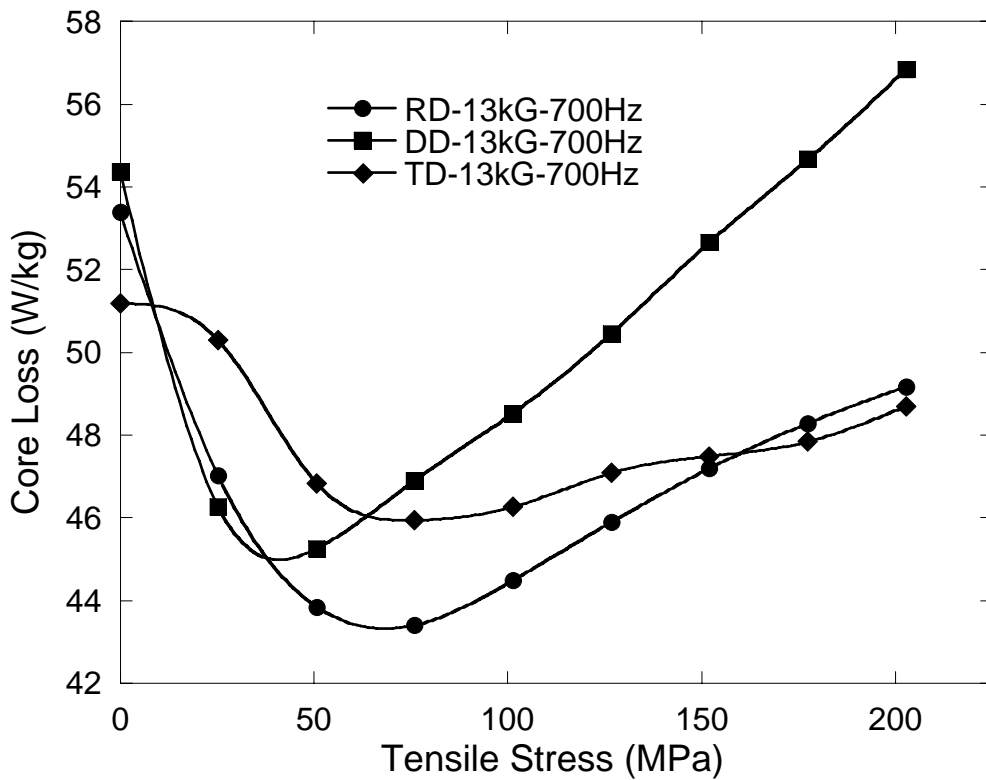


Fig. 4.43 Total core losses for Hiperco Alloy 50 at 13 kG B_{max} and 700 Hz

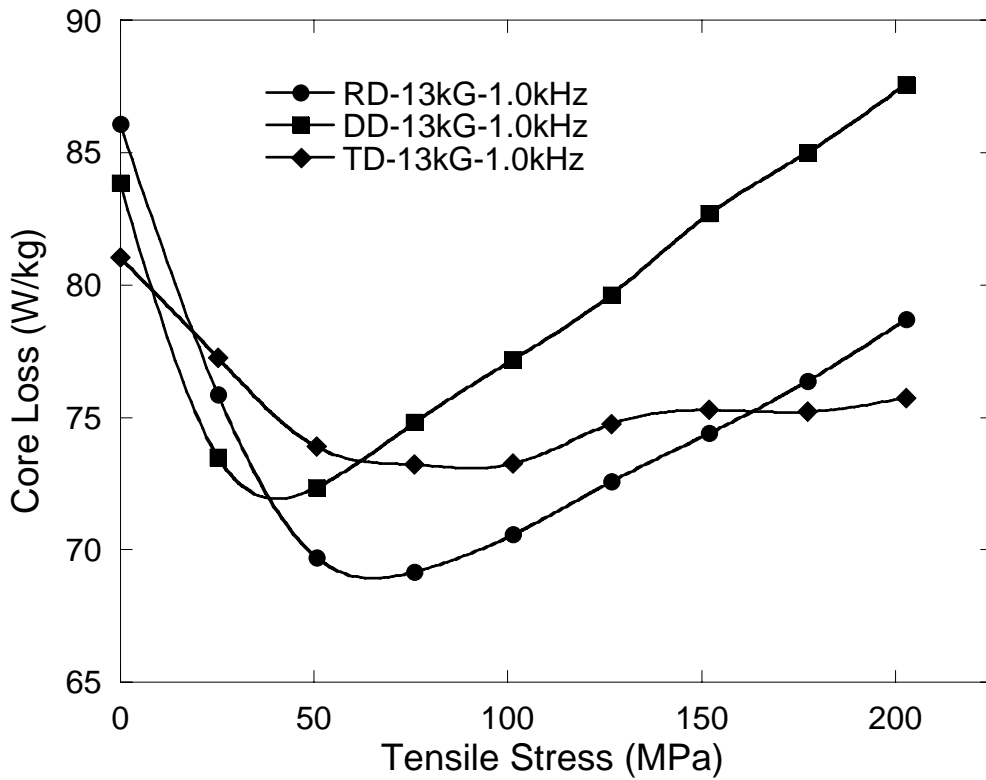


Fig. 4.44 Total core losses for Hiperco Alloy 50 at 13 kG B_{max} and 1000 Hz

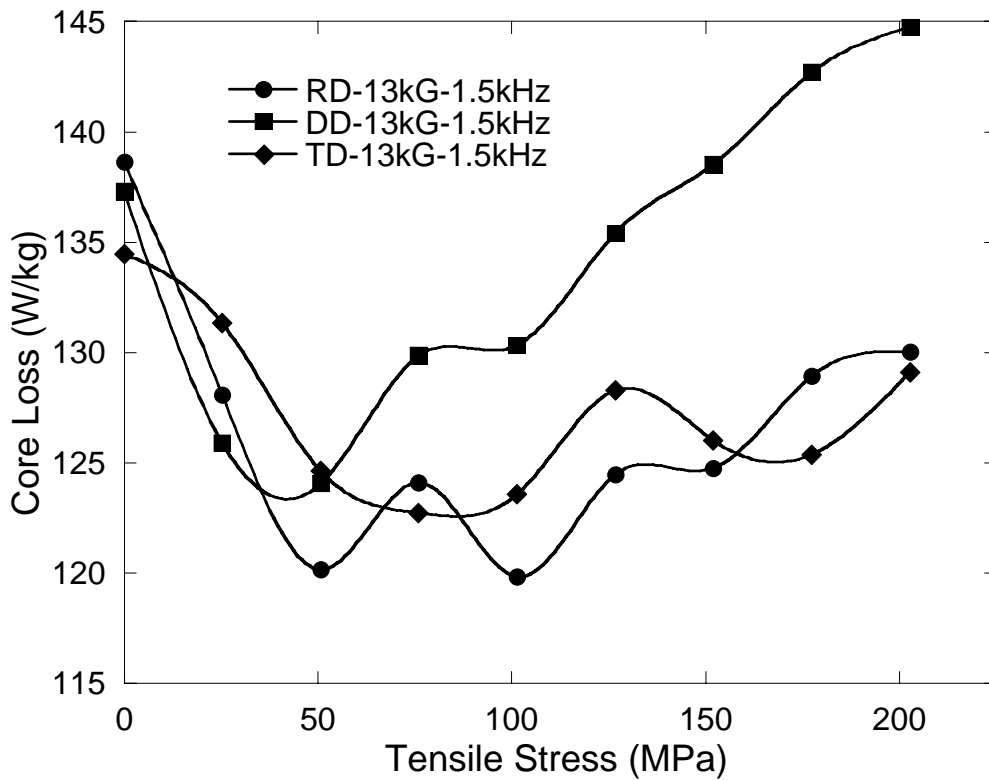


Fig. 4.45 Total core losses for Hiperco Alloy 50 at 13 kG B_{max} and 1500 Hz

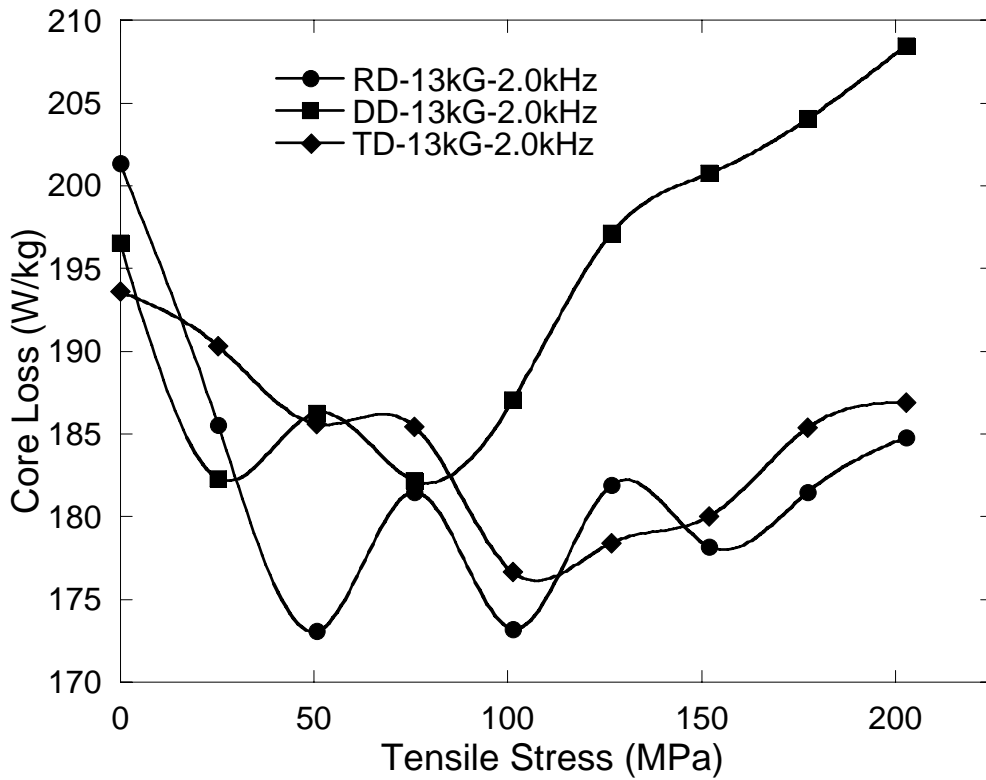


Fig. 4.46 Total core losses for Hiperco Alloy 50 at 13 kG B_{\max} and 2000 Hz

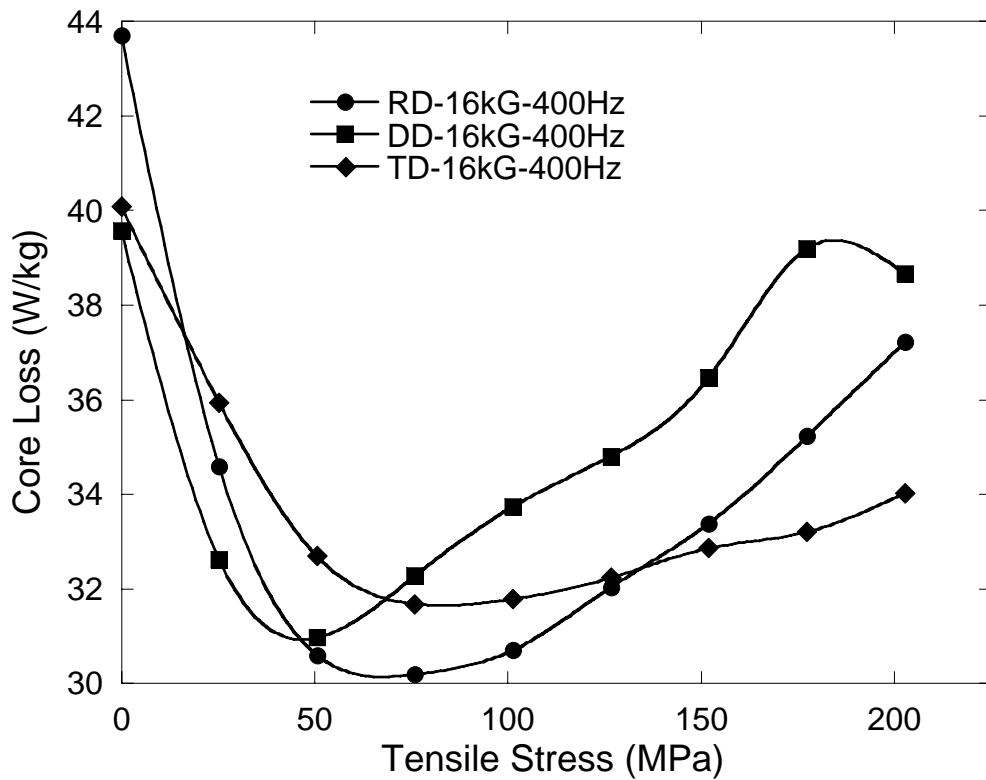


Fig. 4.47 Total core losses for Hiperco Alloy 50 at 16 kG B_{\max} and 400 Hz

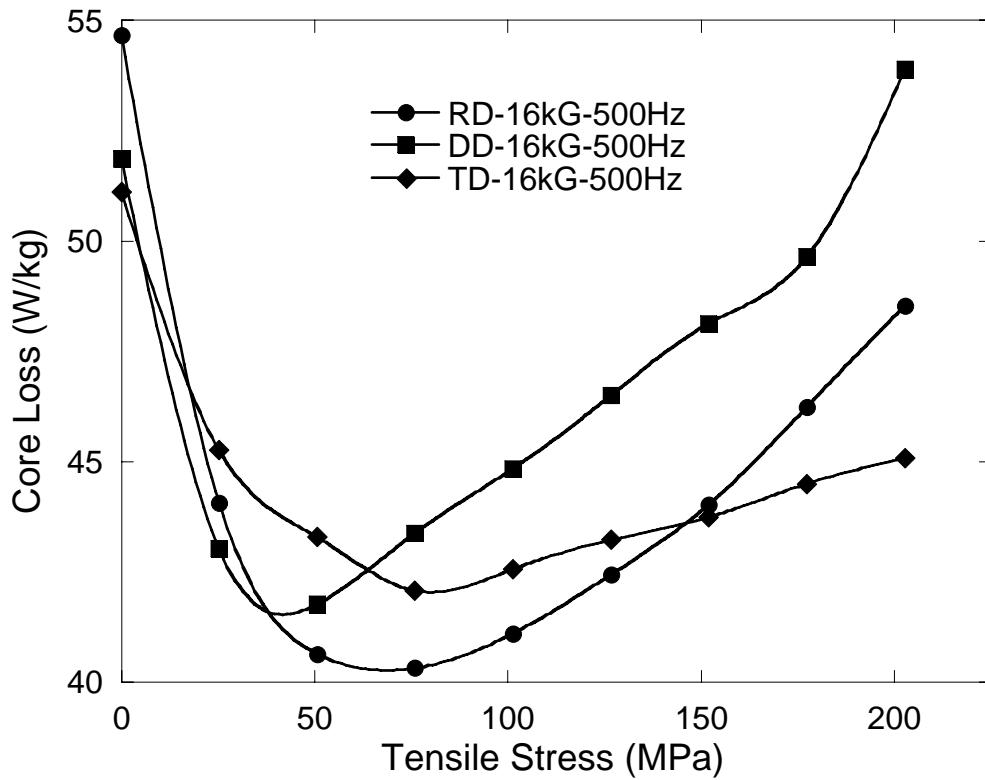


Fig. 4.48 Total core losses for Hiperco Alloy 50 at 16 kG B_{max} and 500 Hz

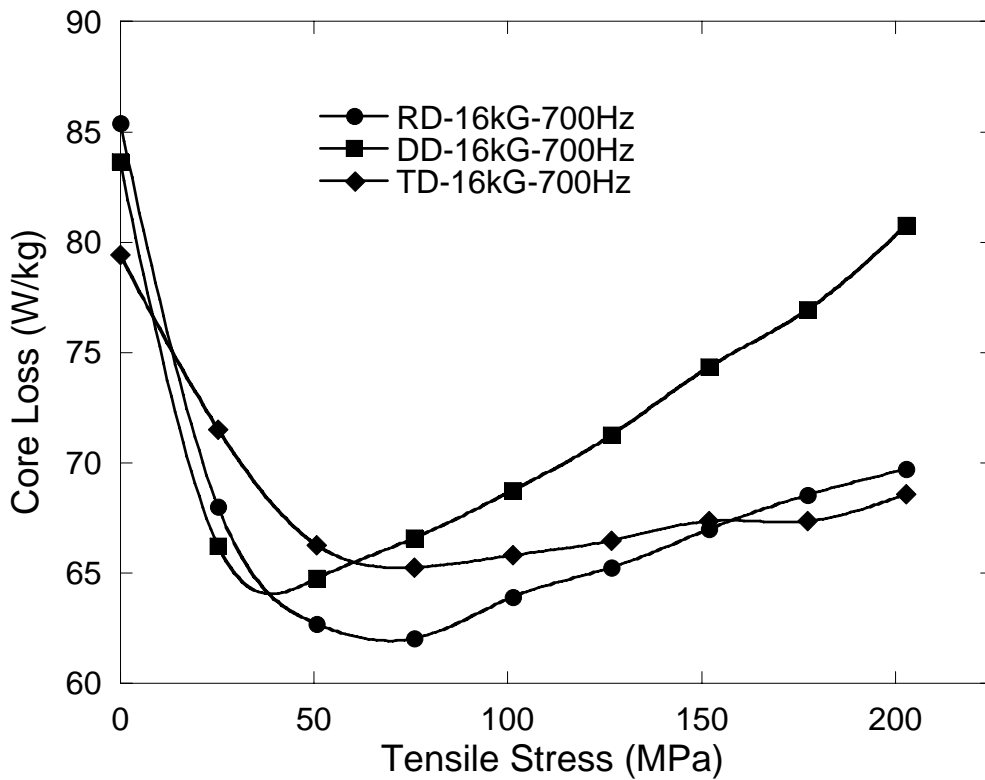


Fig. 4.49 Total core losses for Hiperco Alloy 50 at 16 kG B_{max} and 700 Hz

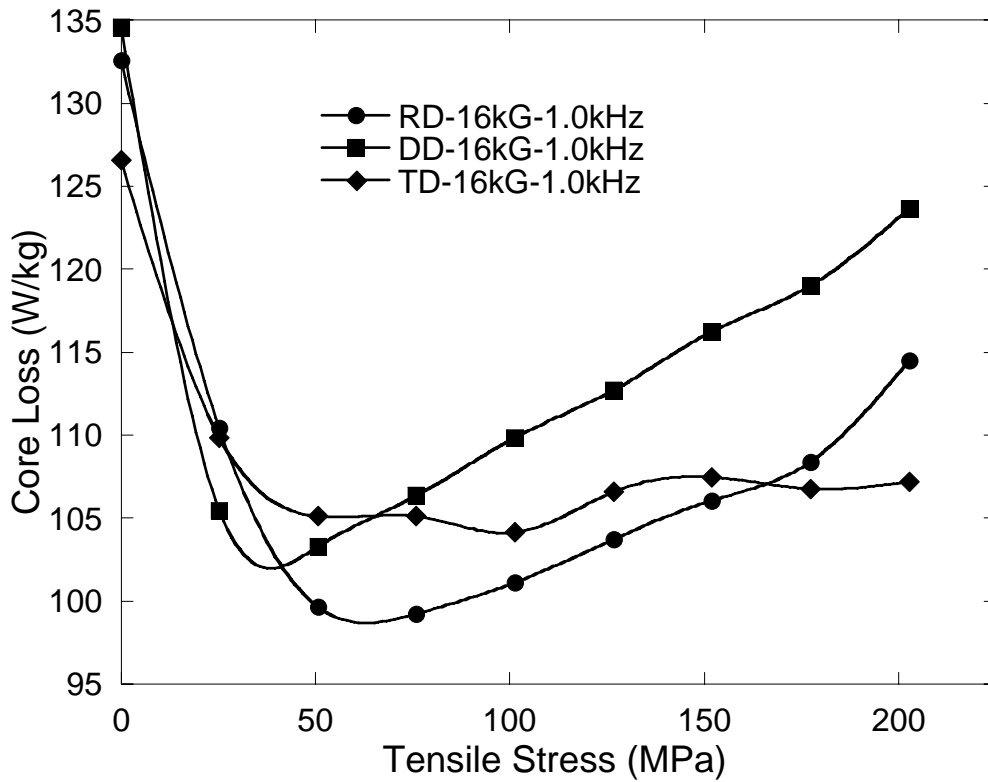


Fig. 4.50 Total core losses for Hiperc Alloy 50 at 16 kG B_{max} and 1000 Hz

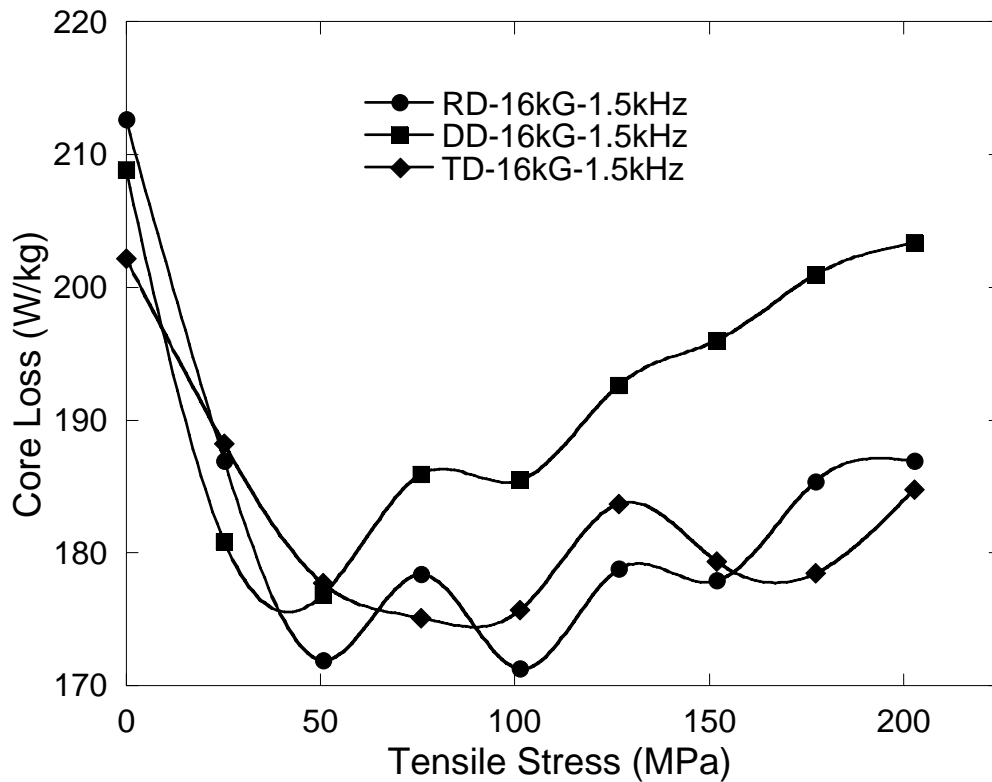


Fig. 4.51 Total core losses for Hiperc Alloy 50 at 16 kG B_{max} and 1500 Hz

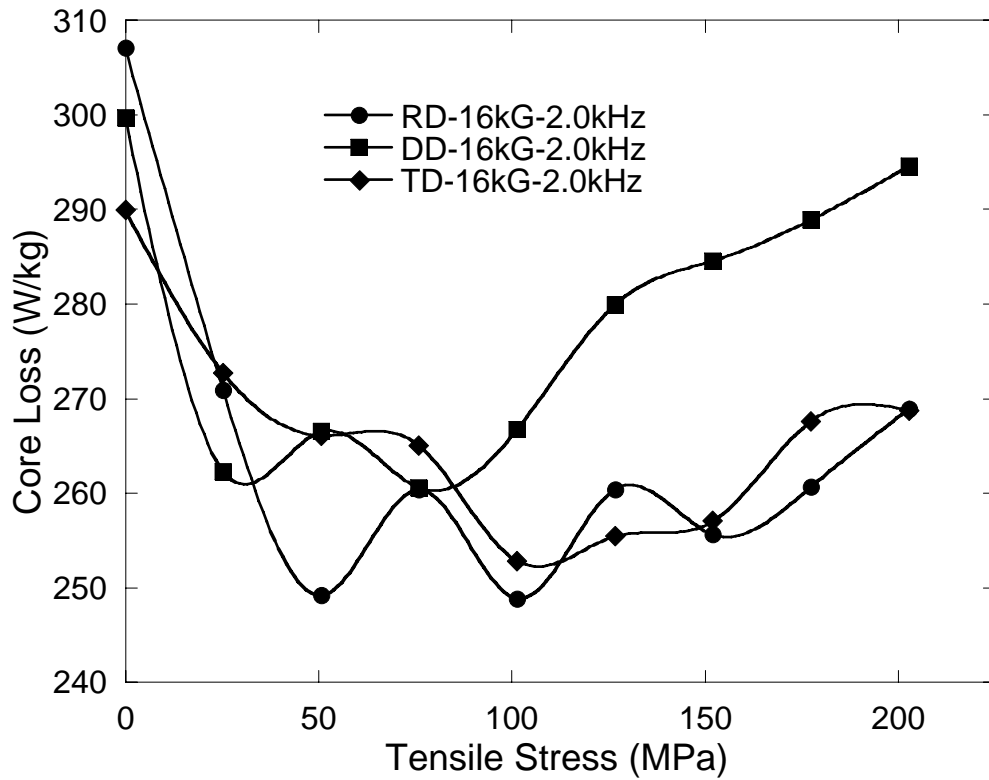


Fig. 4.52 Total core losses for Hiperco Alloy 50 at 16 kG B_{\max} and 2000 Hz

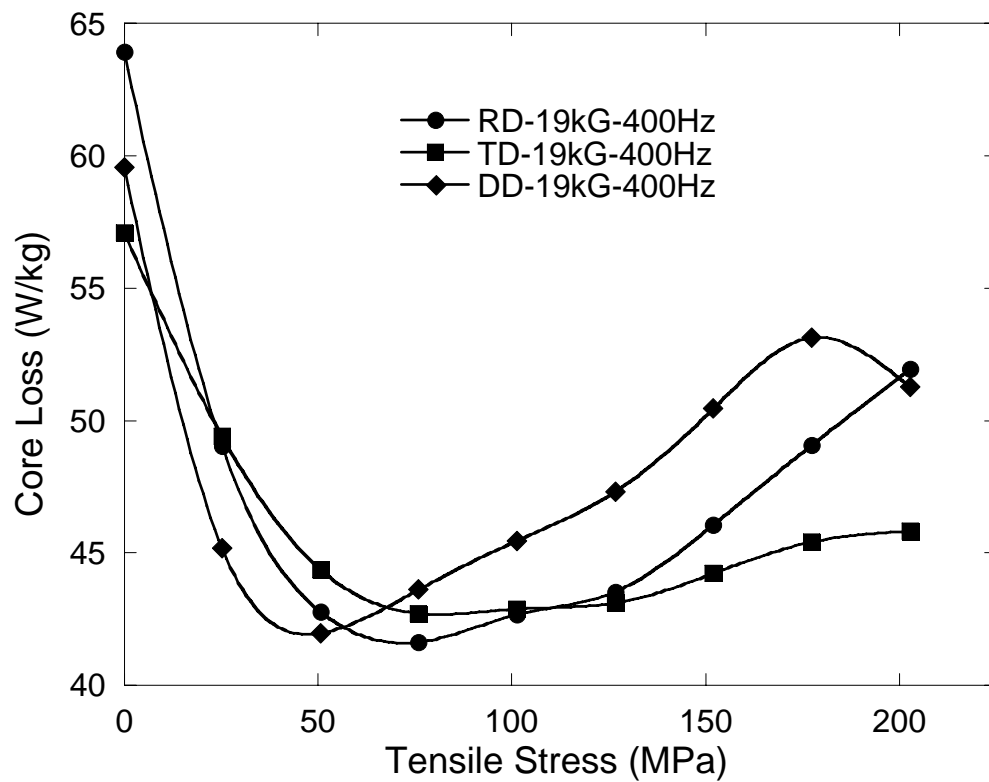


Fig. 4.53 Total core losses for Hiperco Alloy 50 at 19 kG B_{\max} and 400 Hz

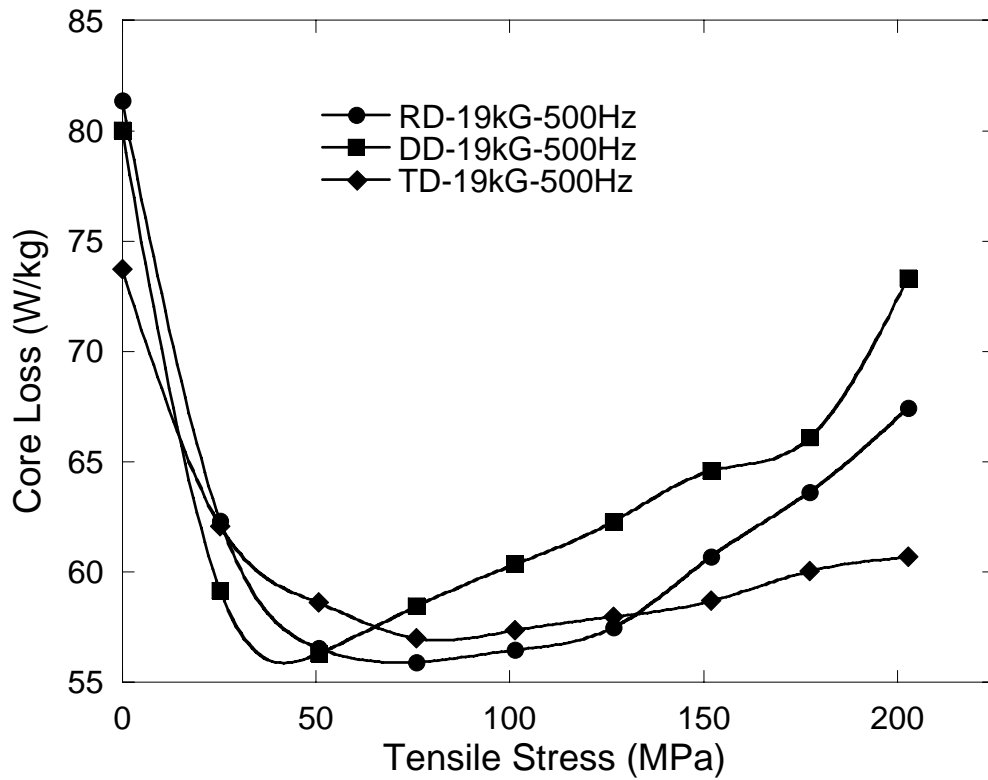


Fig. 4.54 Total core losses for Hiperco Alloy 50 at 19 kG B_{max} and 500 Hz

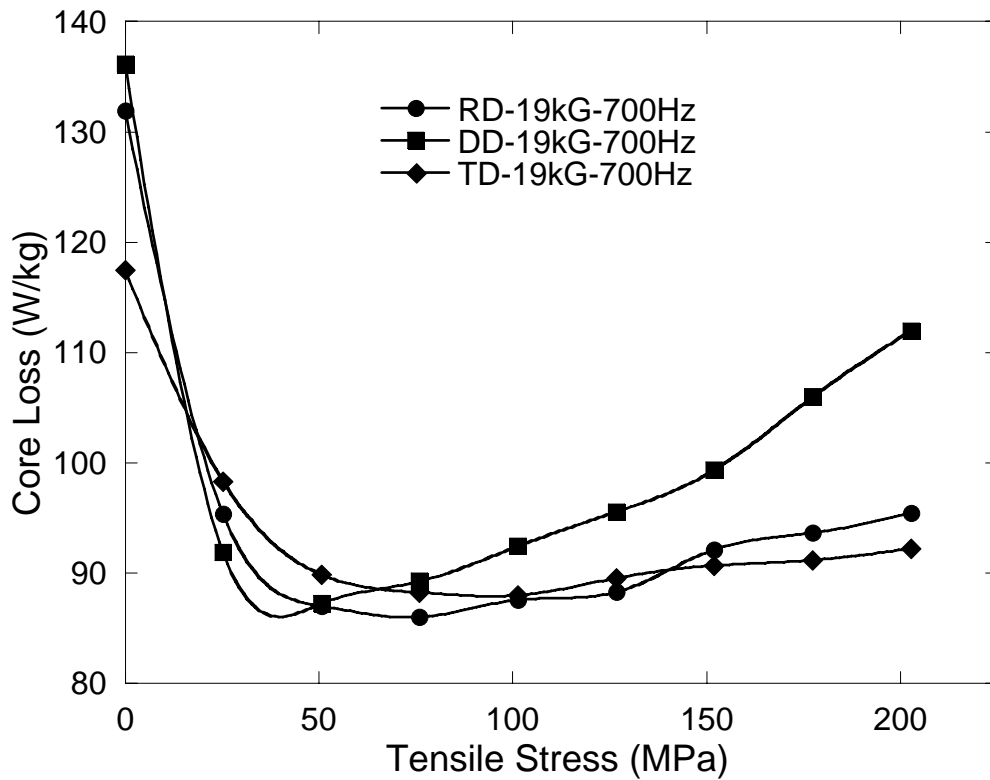


Fig. 4.55 Total core losses for Hiperco Alloy 50 at 19 kG B_{max} and 700 Hz

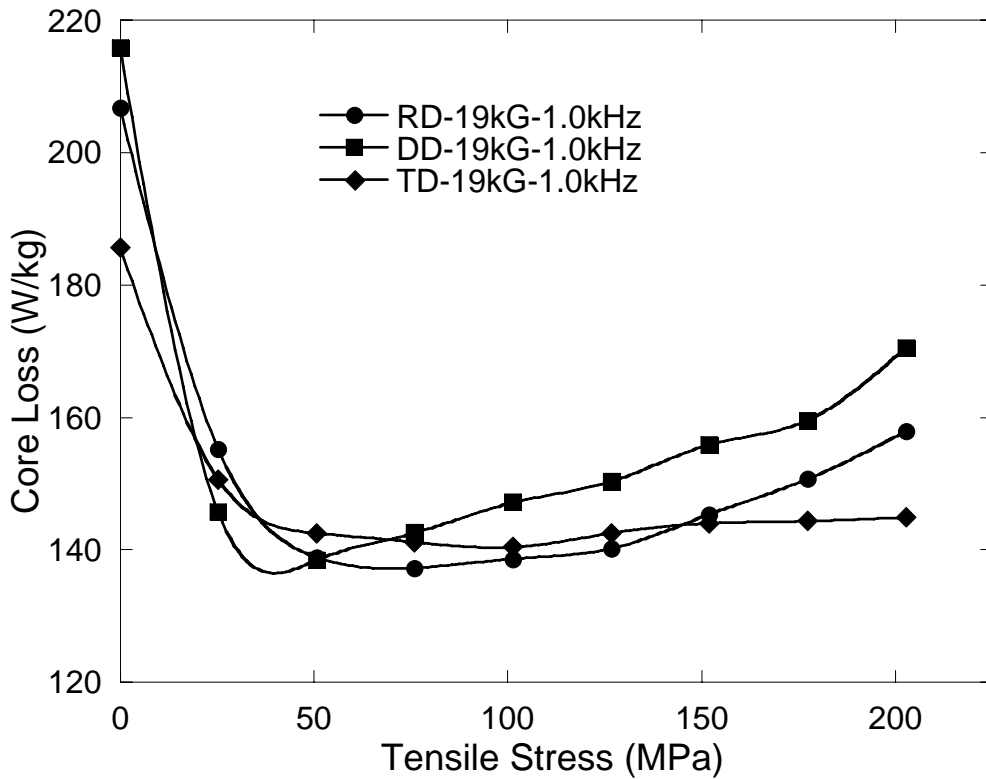


Fig. 4.56 Total core losses for Hiperco Alloy 50 at 19 kG B_{max} and 1000 Hz

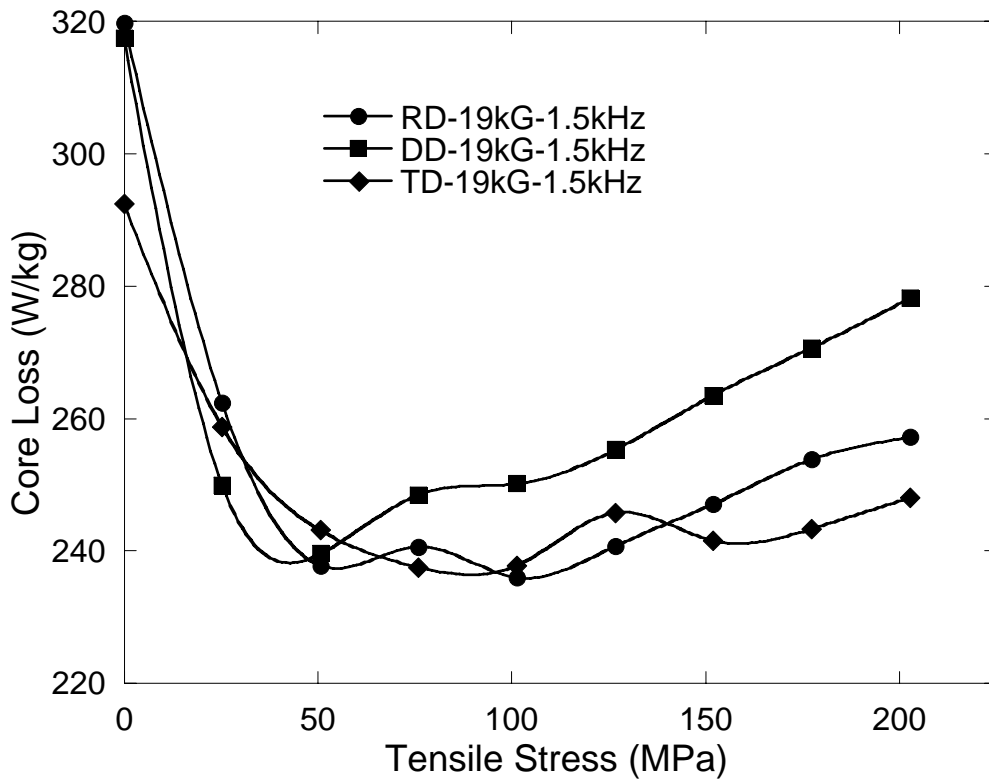


Fig. 4.57 Total core losses for Hiperco Alloy 50 at 19 kG B_{max} and 1500 Hz

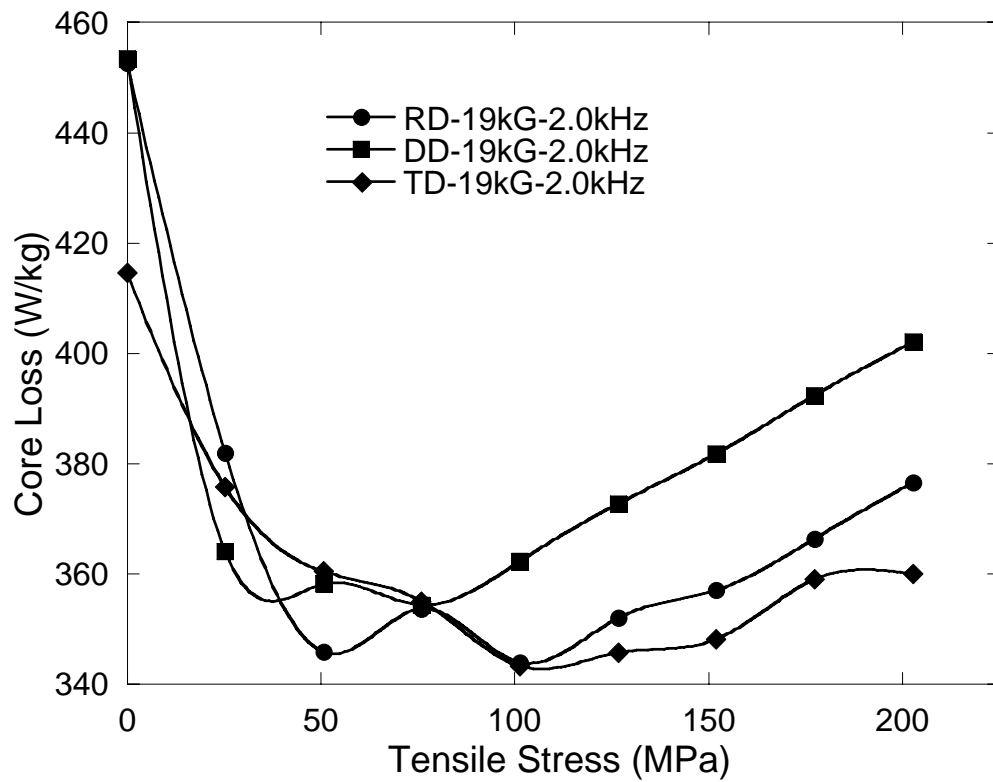


Fig. 4.58 Total core losses for Hiperco Alloy 50 at 19 kG B_{\max} and 2000 Hz

4.2 Effect of Compressive Stress

An applied stress exerted on a magnetic material alters the properties such as permeability, coercivity and remanence of that magnet. For a material i.e. nickel with a negative magnetostriction, a compressive stress greatly increases the permeability while an applied tensile stress reduces it. For materials with positive magnetostriction such as Fe-Co and Co, the effect of the compression and tensile stresses are just the opposite. The formalism for this magneto-mechanical effect is well established by numerous investigators [4.2]-[4.3].

If operated under an AC field, the property change due to an imposed axial load also reflects itself in the total power losses. The magnitude of these power losses is the interest of this work. We designed an experimental set up that is capable of measuring magnetic losses under applied compressive stress conditions. This axial loader enables core loss measurement to be made while the laminate stack is subjected to an axial load.

Among the Hiperco Alloys tested here, there is very limited data on the effect of stress on power losses for 49Co-49Fe-2V alloy by Moses [4.4]. The other two compositions are not explored yet in terms of compressive stress dependent core losses.

Specimens and Procedures

Ring specimens with dimensions, O.D = 5.08 cm, I.D = 4.242 cm, were heat-treated in an argon atmosphere at 750 ° C for two hours and cooled down to the room temperature at a rate of 177 ° C/h.

As an insulation layer, we used 20 (μm) thick paper between the laminates. We used a Magnetic Instrumentation Inc. SMT model 600 hysteresisgraph for magnetic testing. An axial loader to enable core loss measurements to be made while the laminate stack is subjected to an axial load has been designed (Figure 4.58). The apparatus and multi-layered slotted interface plates, allowing for the toroidal windings and simultaneous load application were used to evaluate the effect of compression on magnetic properties of commercially available Fe-Co based Hiperco® 50, Hiperco® 50 HS and Hiperco® 27 alloys. The ring specimens were subjected to a compression stress that was perpendicular to the plane of the rings up to 27.5 MPa.

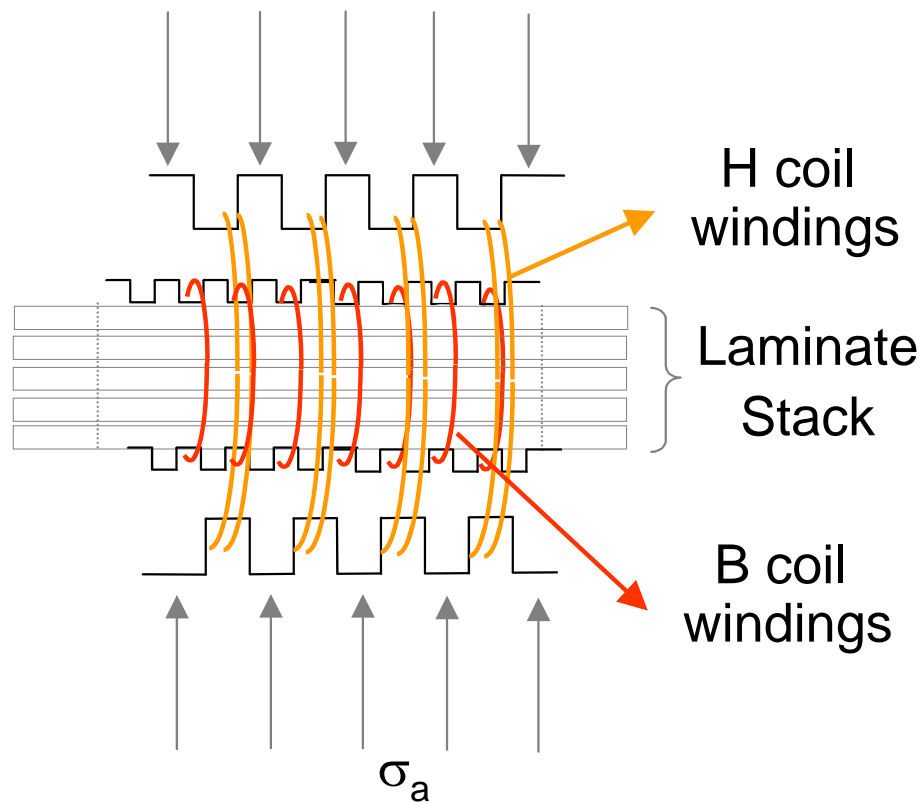


Figure 4.58 Schematic representation of compression apparatus.

4.2.1 DC Magnetic Properties Under Compressive Stress

In all DC measurements, the shape of the B-H loop changed during the application of the compressive stress. Permeability values showed a decreasing trend, while the coercivity values (Figure 4.59) first decreased with increasing load for Hiperco 50, Hiperco 50HS, and then increased gradually. The minima, where the lowest coercivities were observed are 7 and 4 MPa for the insulated alloys of Hiperco 50HS and Hiperco 50 respectively. Permikov [4.5] *et al.* reported the same type of minimum in the stress dependent coercivity of non-oriented fully processed V330-50A grade electrical steels under tensile stress. This anomaly, however, is absent for the Hiperco 27 alloy whose coercivity gradually increased from 2.5 Oe to 4.09 Oe at 27.5 MPa load.

An abrupt decrease in maximum permeability was observed for the Hiperco 50, Hiperco 50HS and Hiperco 27 alloys (Figure 4.60) with the application of the compressive stress of 3.4 MPa. Further increase in the compressive stress lowered the permeability almost linearly. Remanence (B_r) values (Figure 4.61) followed the same decreasing trend with

the permeability. The lack of information on the grain orientation and the measured specimens' polycrystalline structure prevents us from making a strong argument about the origin of the observed trends. But the way coercivity behaves may be attributed to a preferred domain orientation in the demagnetized state induced by the applied stress. In the absence of an applied stress, the direction of the magnetization is controlled by the crystal anisotropy. But, as a stress is applied, both stress and crystal anisotropy control the direction of the magnetization. As a result, some preferred domain orientation may occur which favors an easy wall movement. As the stress level gets higher, now the magnetization vector has to overcome the anisotropy induced by the stress, and coercivities are further increased.

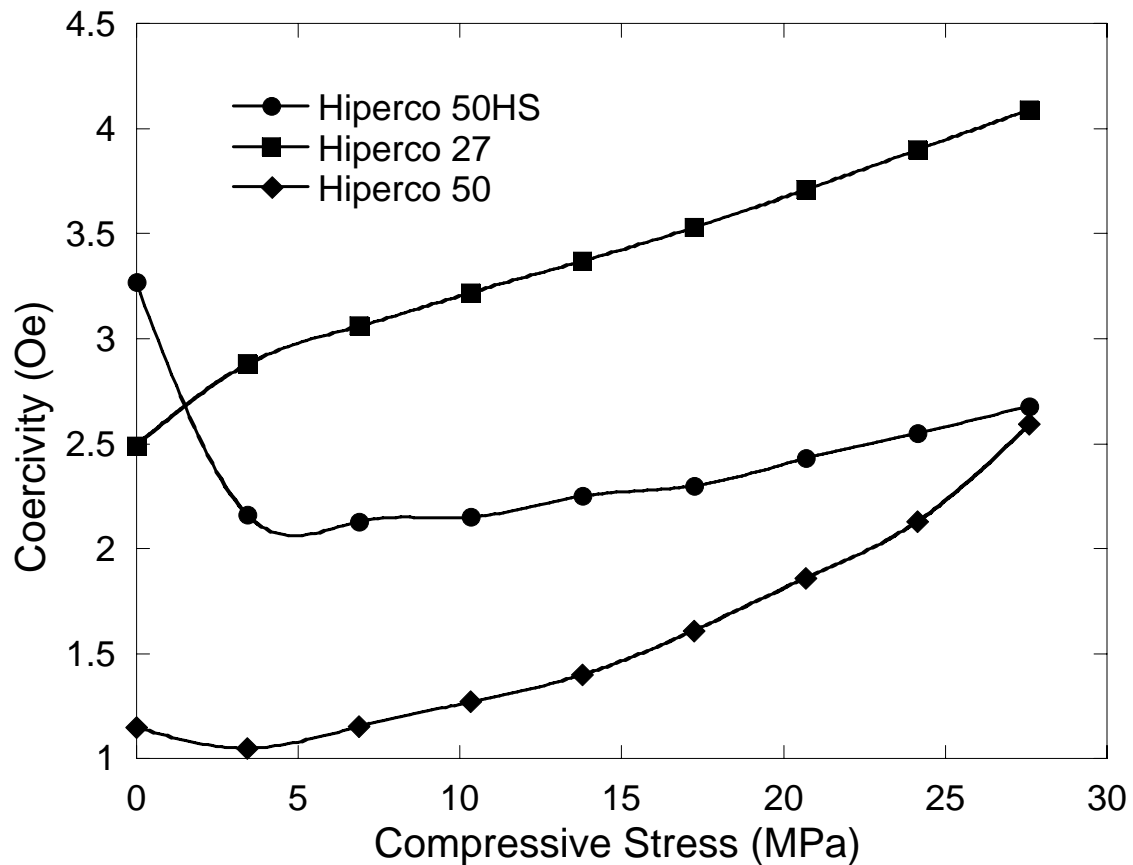


Figure 4.59 Change in coercivity of the Hiperco Alloy 50, Hiperco Alloy 50HS and Hiperco Alloy 27 with applied compressive stress.

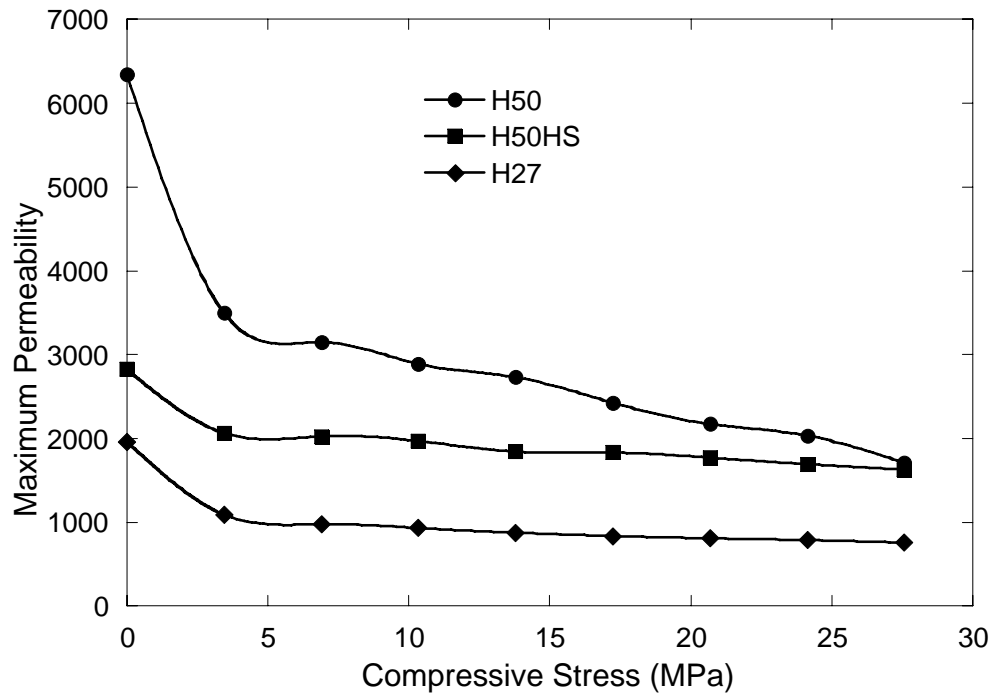


Figure 4.60 Maximum permeability (μ_{\max}) versus applied compressive stress for the Hiperc Alloy 50 , Hiperc Alloy 50HS and Hiperc Alloy 27.

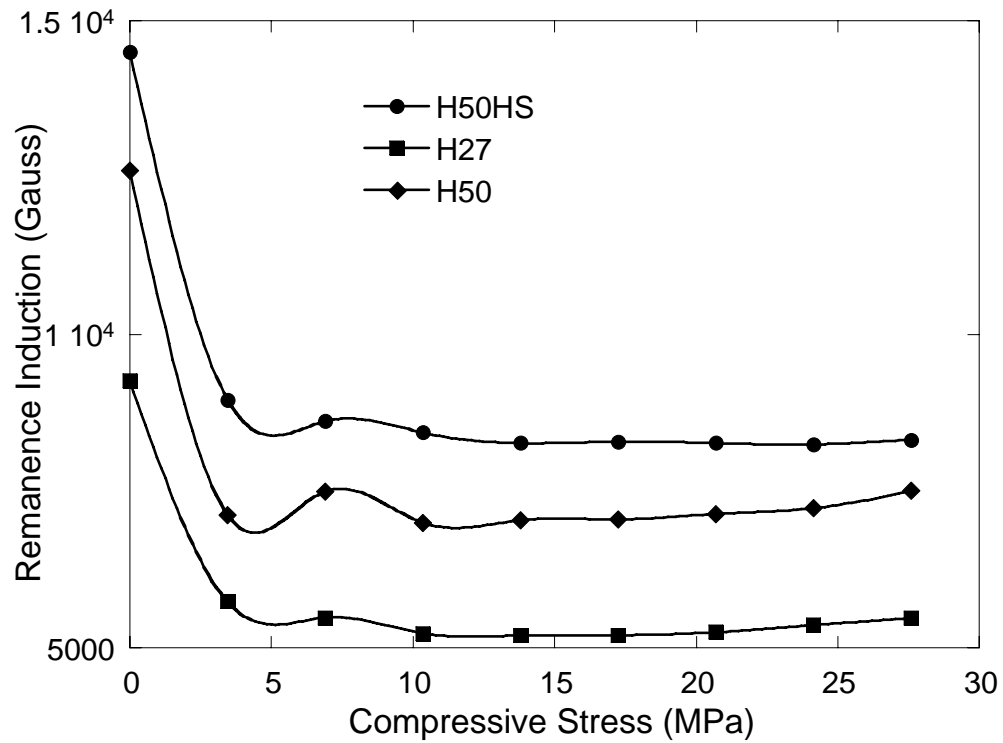


Figure 4.61 Remanence (B_r) of Hiperc Alloy 50, Hiperc Alloy 50HS and Hiperc Alloy 27 at different compression stresses.

The positive saturation magnetostriction (λ_s) values of equiatomic FeCo alloys may be responsible for these observations. One can realize the correlation between the magnitude of the λ_s and the coercivity change by compression. The Hiperco 27 Alloy with a relatively small but still positive saturation magnetostriction does not exhibit the minimum in the stress dependence of the coercivity.

4.2.2 Core Losses Under Compressive Stress

Core loss measurements performed on stacks of insulated laminates of the three alloys exhibited the same trend in which the total power losses increased with an increased amount of applied stress (Figures 4.62 through 4.79). However, the lower coercivities that occurred with the application of small stresses for the Hiperco 50 and Hiperco 50HS alloys are not reflected on the total power losses. We measured the hysteretic losses, $W_h = \oint H \cdot dB \text{ (J/m}^3\text{)}$ and found that they follow the same trend as the coercivity with the application of a stress. It was also experimentally observed that the electrical resistivity remains unchanged during the compression, indicating that eddy current losses are constant. Since the total power losses are composed of hysteresis, W_h , eddy-current, W_e , and anomalous, W_a losses, increased power losses with the application of a stress are dominated by the anomalous losses.

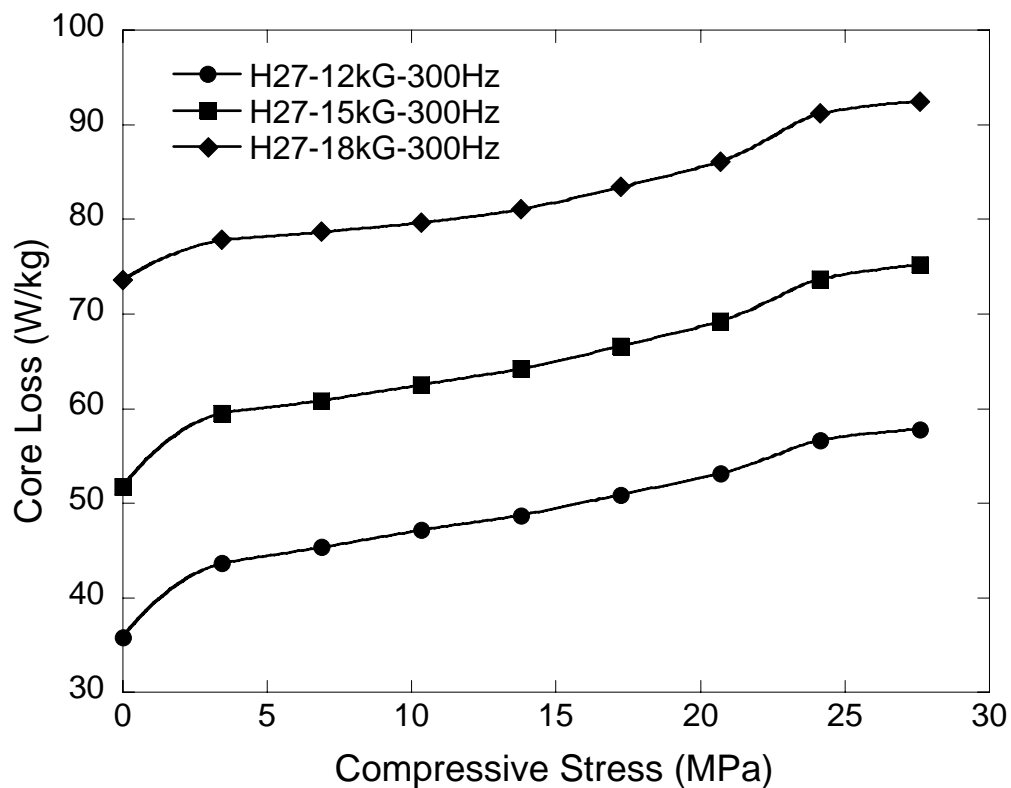


Figure 4.62 Total core losses of Hiperco Alloy 27 at B_{\max} of 12-15-18 KG and 300 Hz.

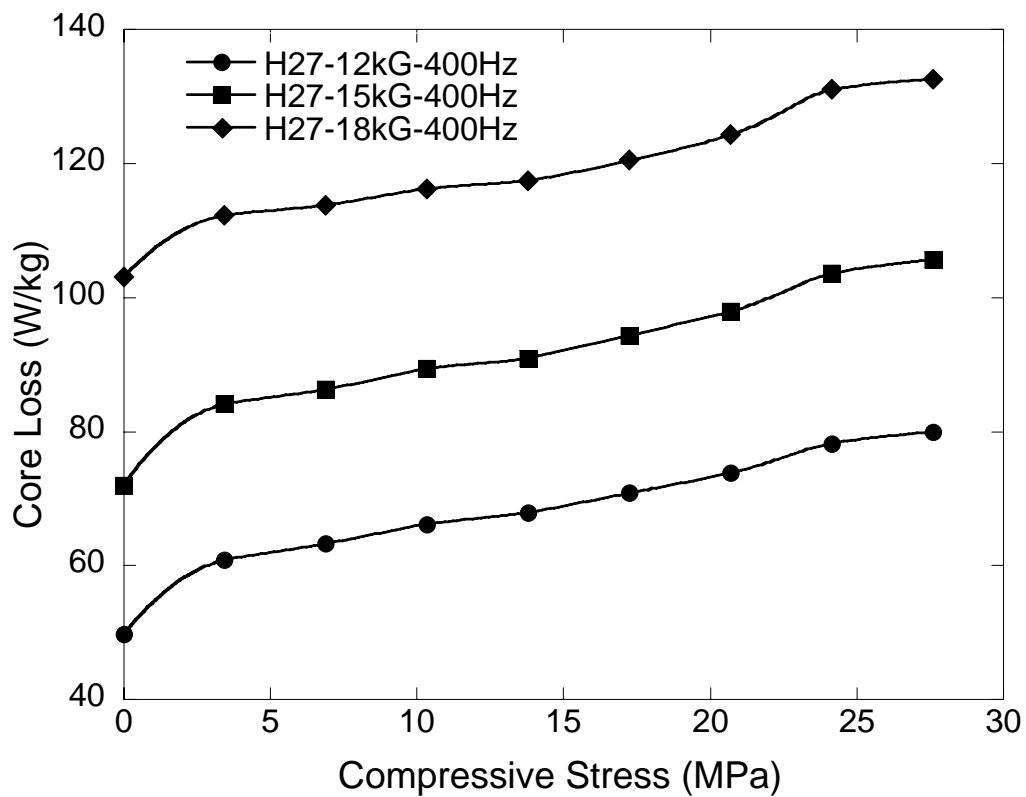


Figure 4.63 Total core losses of Hiperco Alloy 27 at B_{\max} of 12-15-18 KG and 400 Hz.

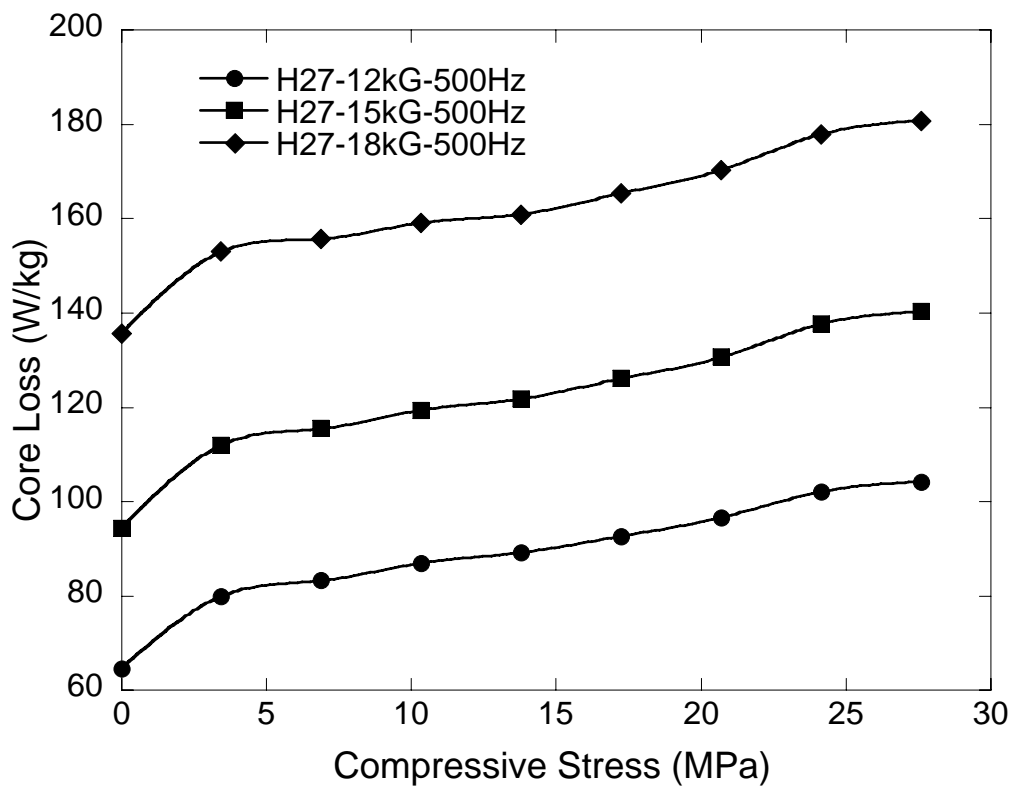


Figure 4.64 Total core losses of Hiperco Alloy 27 at B_{max} of 12-15-18 KG and 500 Hz.

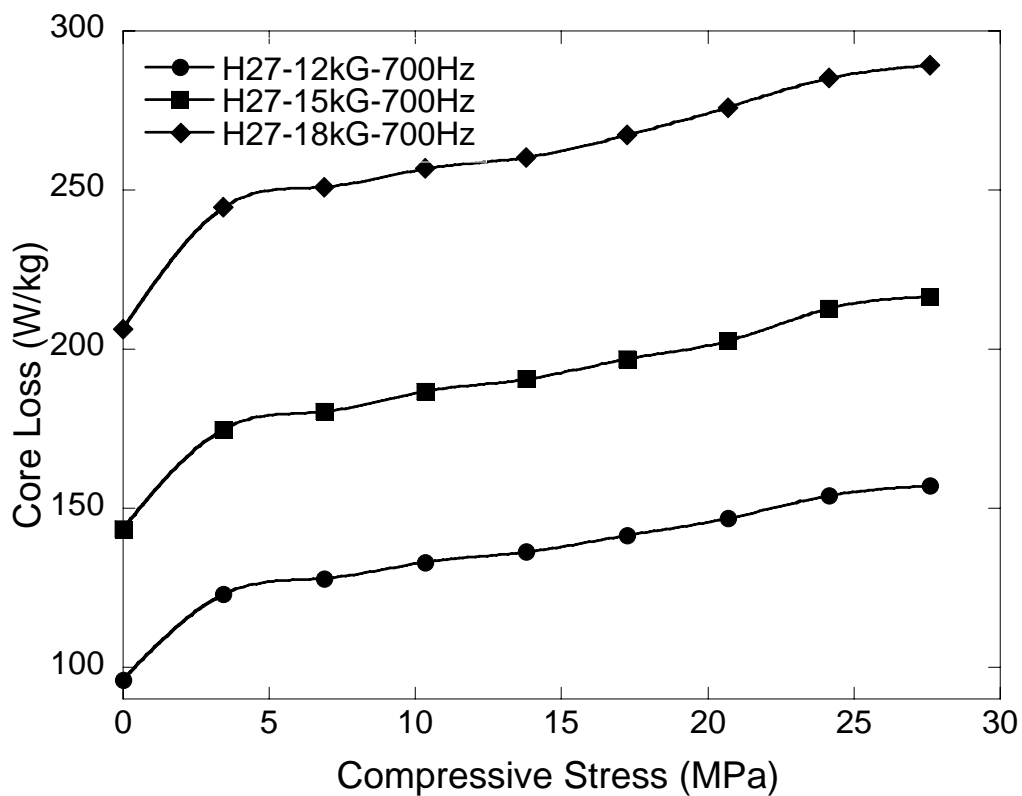


Figure 4.65 Total core losses of Hiperco Alloy 27 at B_{max} of 12-15-18 KG and 700 Hz.

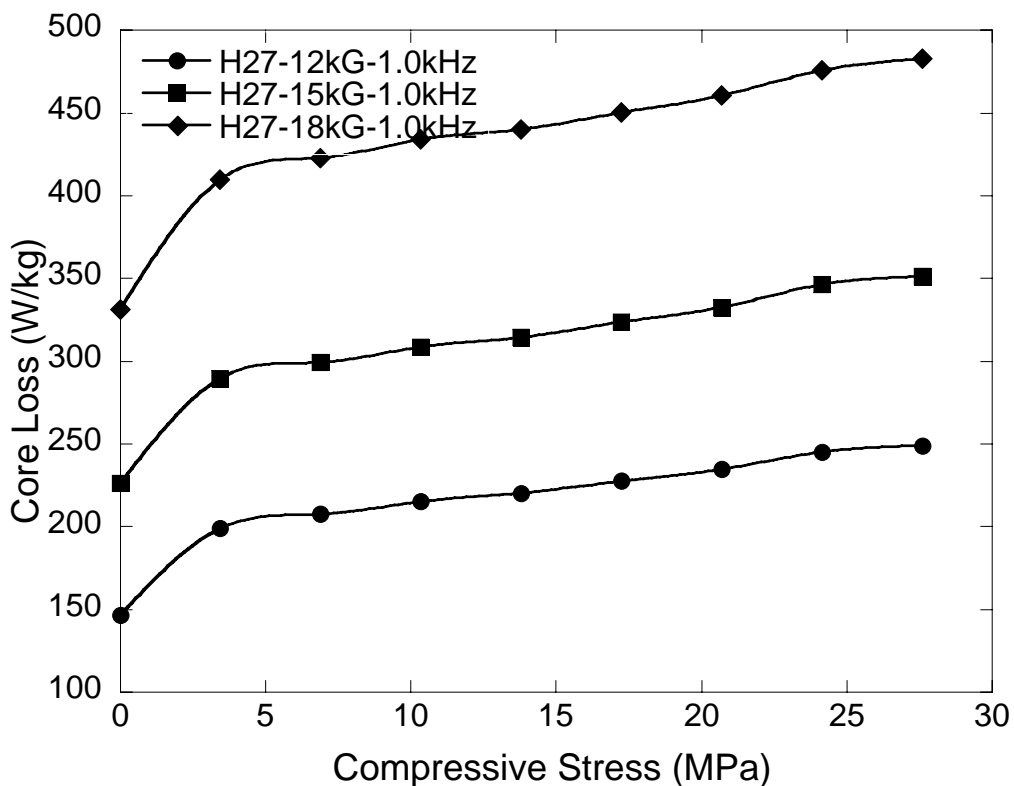


Figure 4.66 Total core losses of Hipercro Alloy 27 at B_{max} of 12-15-18 KG and 1 kHz.

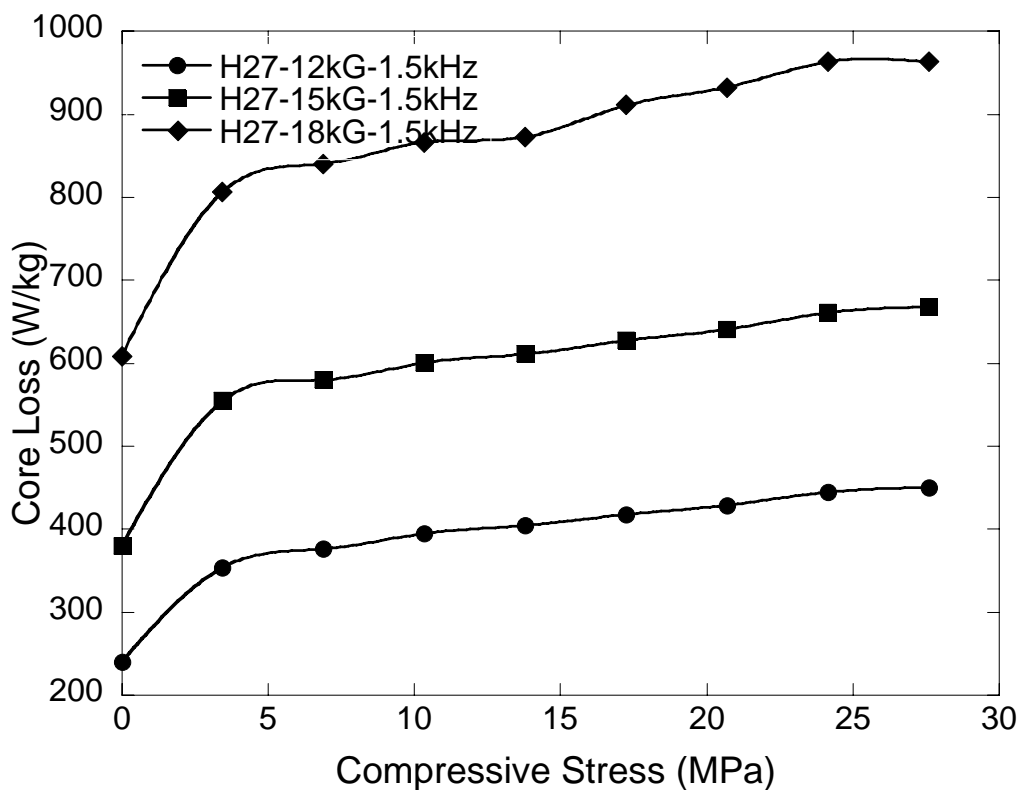


Figure 4.67 Total core losses of Hipercro Alloy 27 at B_{max} of 12-15-18 KG and 1.5 kHz.

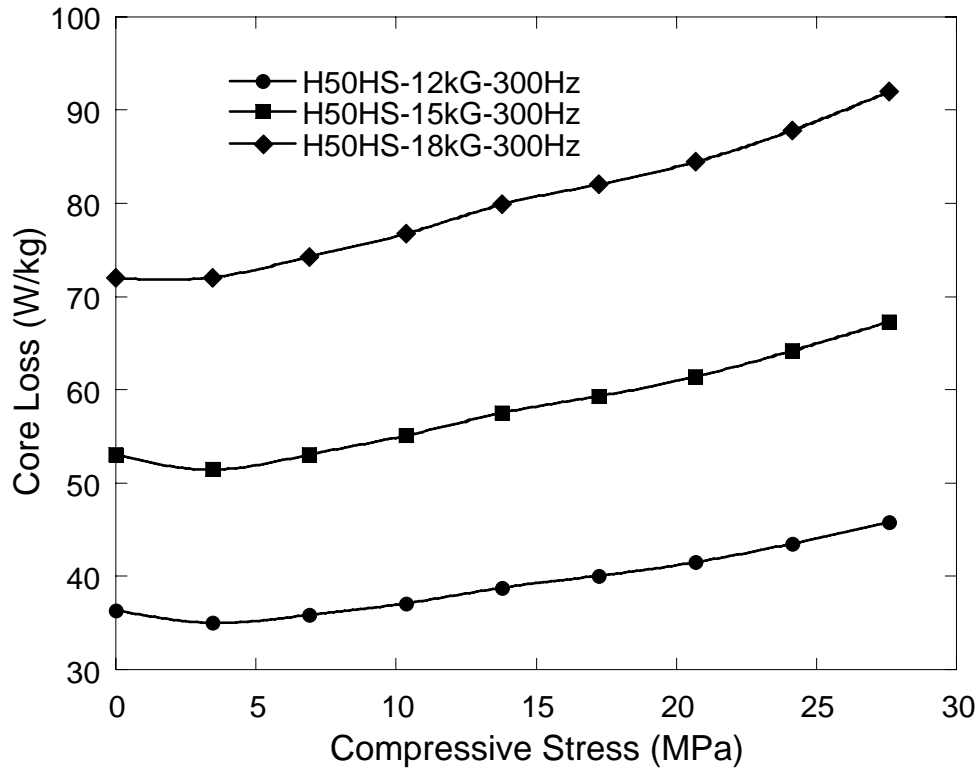


Figure 4.68 Total core losses of Hiperco Alloy 50HS at B_{\max} of 12-15-18 KG and 300 Hz.

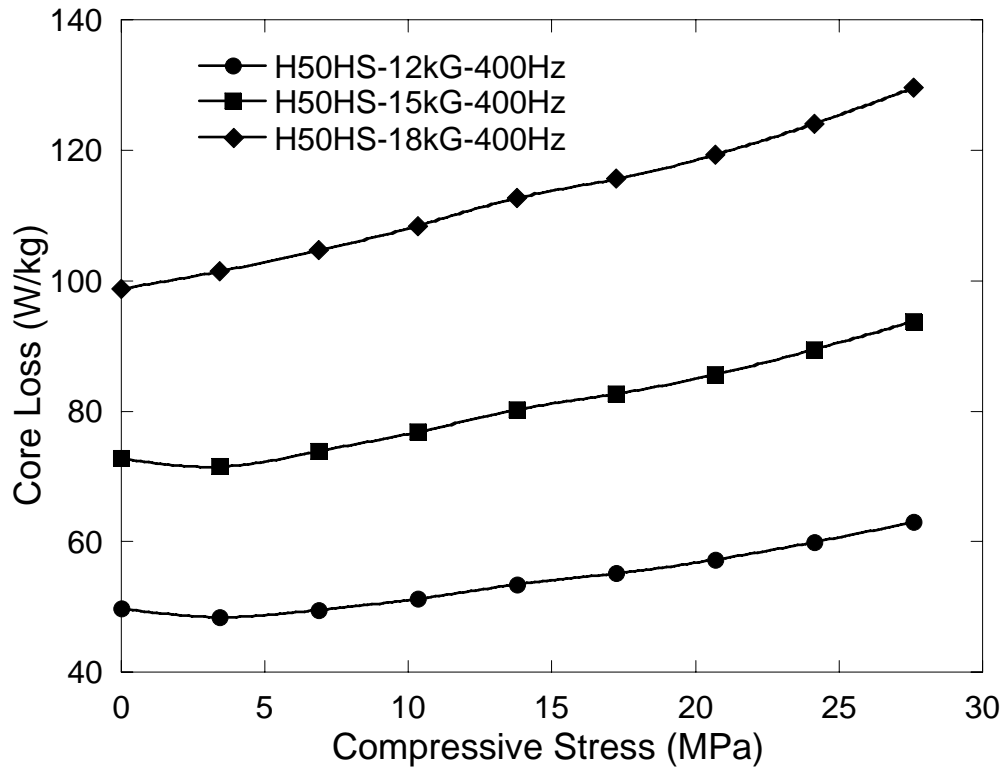


Figure 4.69 Total core losses of Hiperco Alloy 50HS at B_{\max} of 12-15-18 KG and 400 Hz.

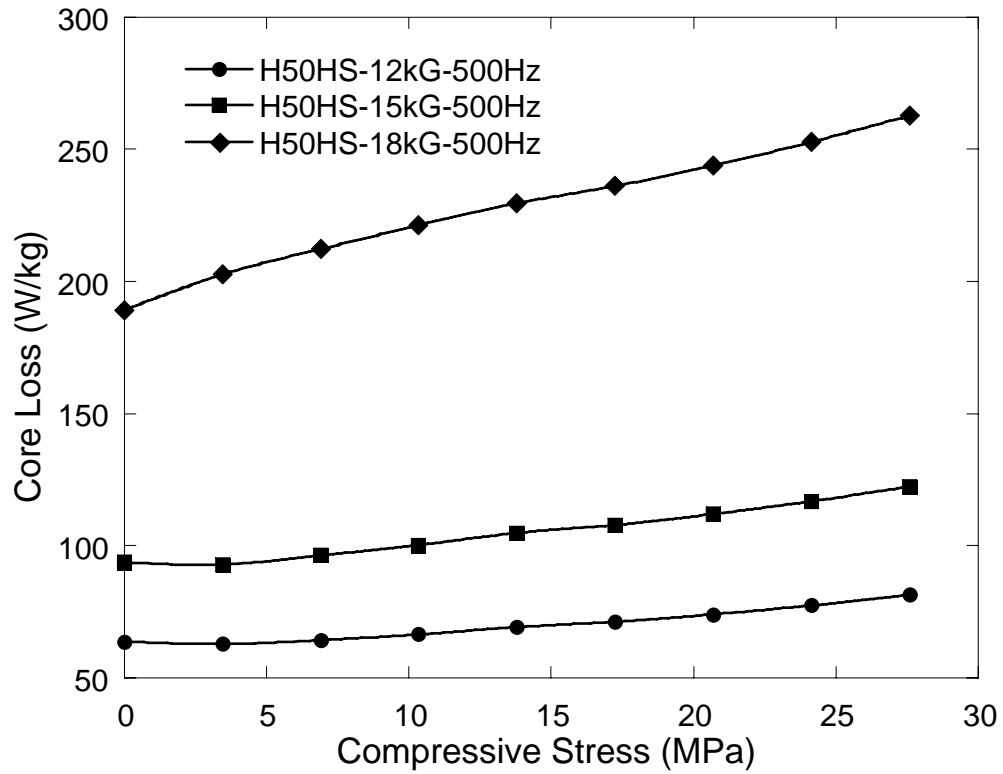


Figure 4.70 Total core losses of Hiperco Alloy 50HS at B_{\max} of 12-15-18 KG and 500 Hz.

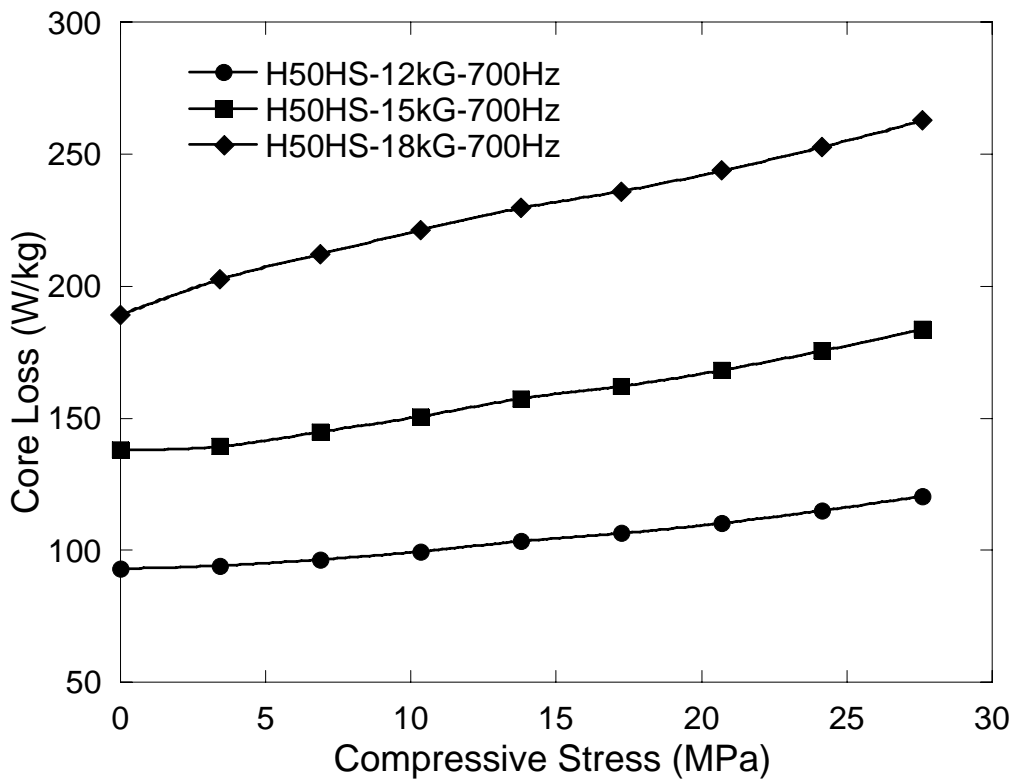


Figure 4.71 Total core losses of Hiperco Alloy 50HS at B_{\max} of 12-15-18 KG and 700 Hz.

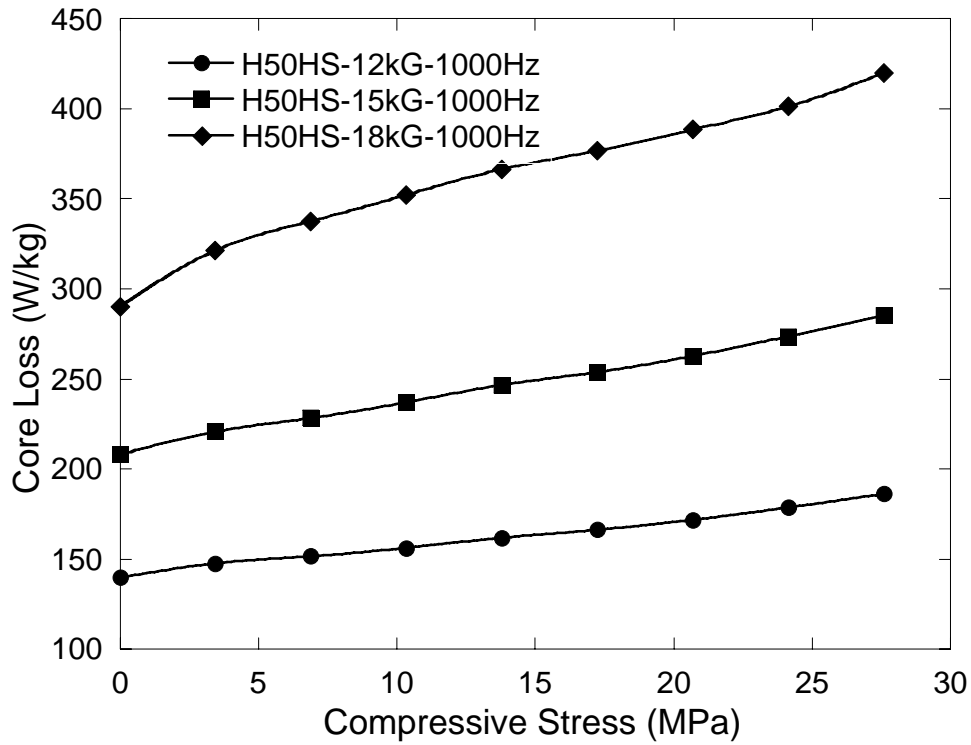


Figure 4.72 Total core losses of Hiperco Alloy 50HS at B_{\max} of 12-15-18 KG and 1kHz.

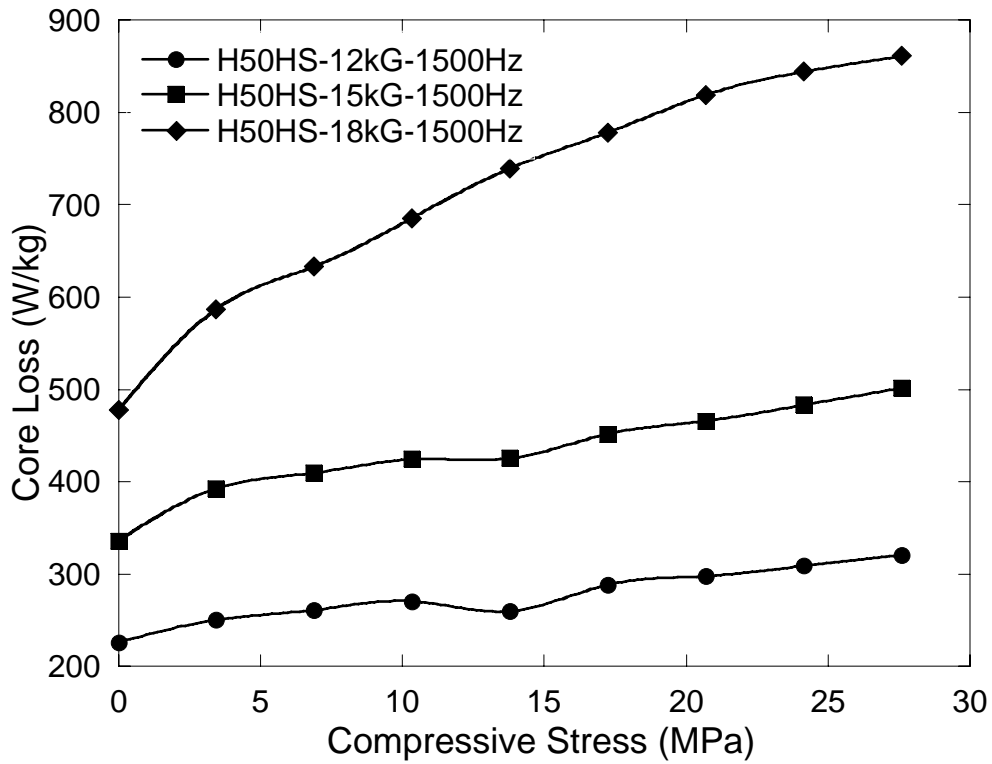


Figure 4.73 Total core losses of Hiperco Alloy 50HS at B_{\max} of 12-15-18 KG and 1.5 kHz.

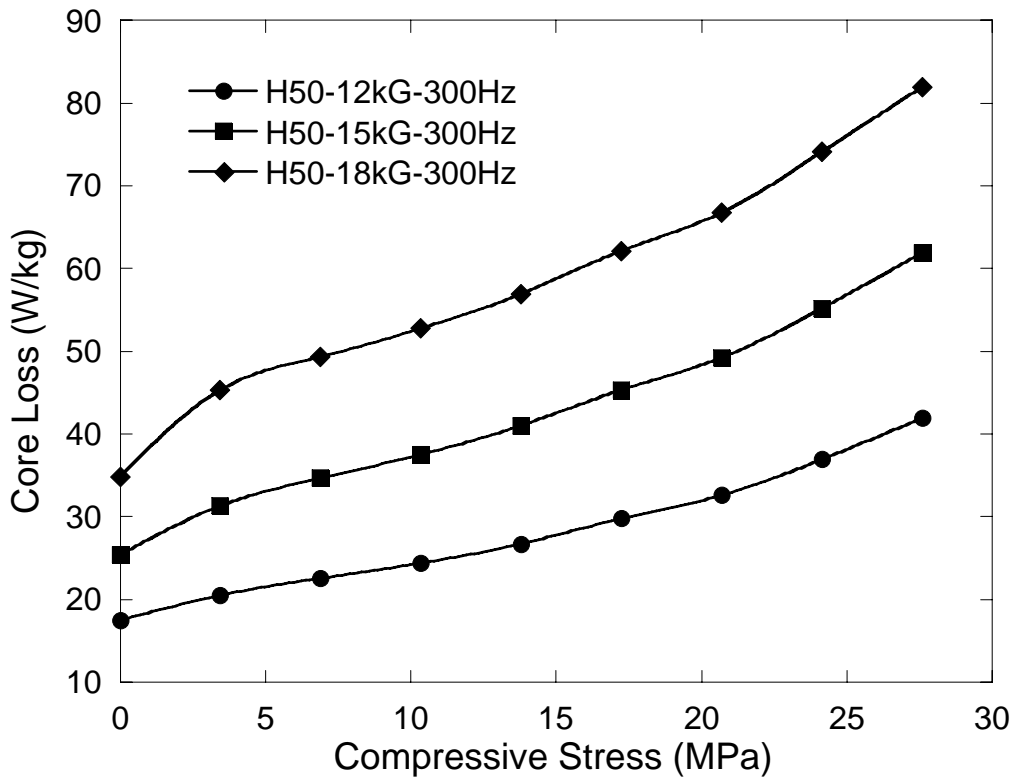


Figure 4.74 Total core losses of Hiperco Alloy 50 at B_{\max} of 12-15-18 KG and 300 Hz.

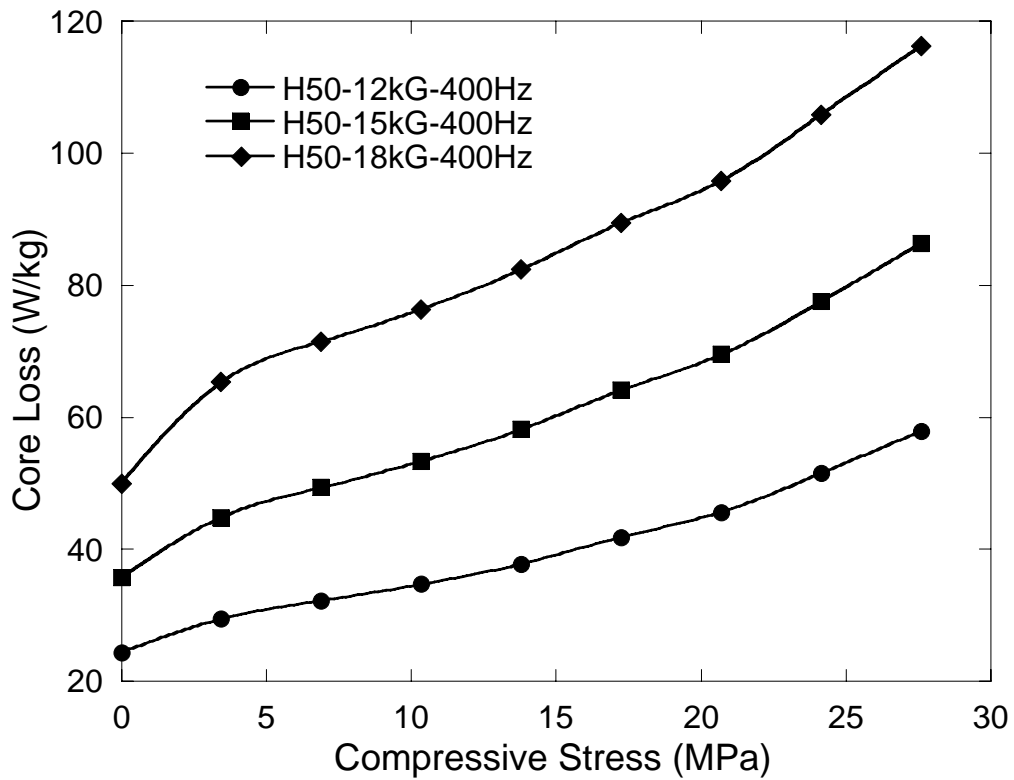


Figure 4.75 Total core losses of Hiperco Alloy 50 at B_{\max} of 12-15-18 KG and 400 Hz.

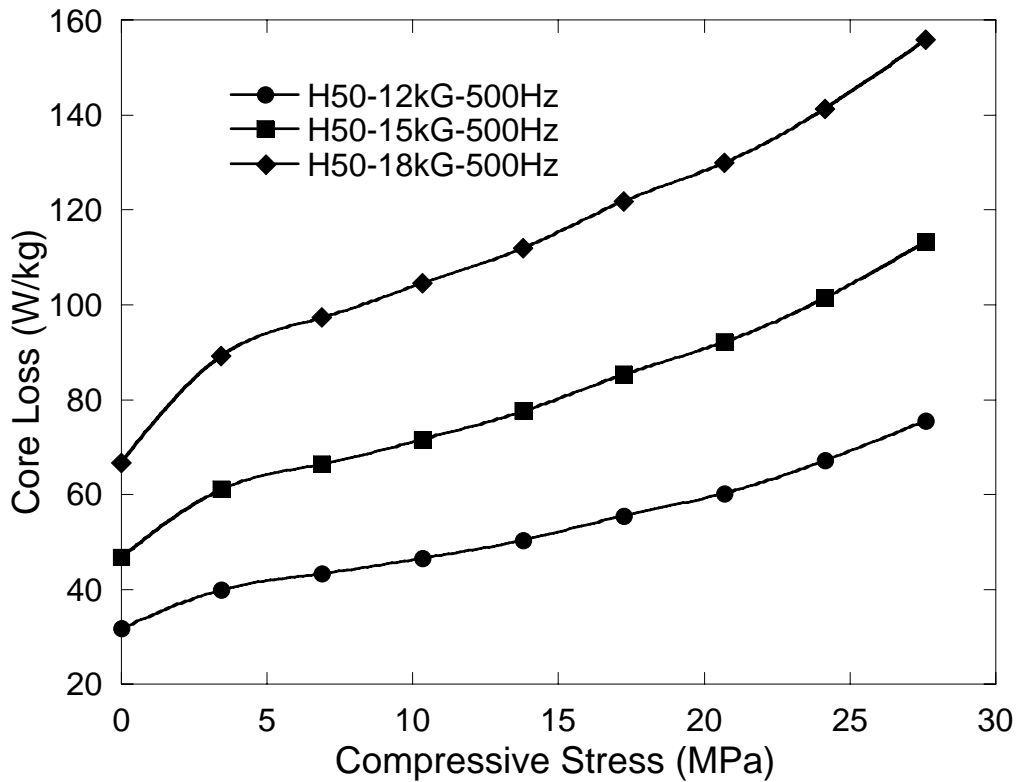


Figure 4.76 Total core losses of Hiperco Alloy 50 at B_{\max} of 12-15-18 KG and 500 Hz.

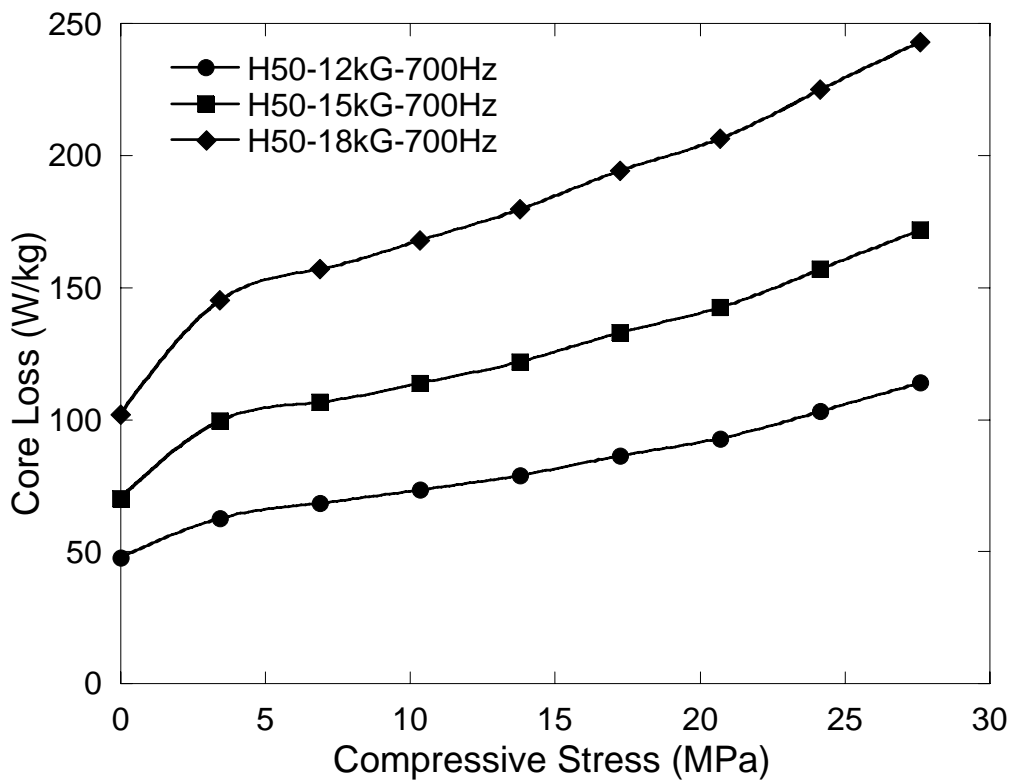


Figure 4.77 Total core losses of Hiperco Alloy 50 at B_{\max} of 12-15-18 KG and 700 Hz.

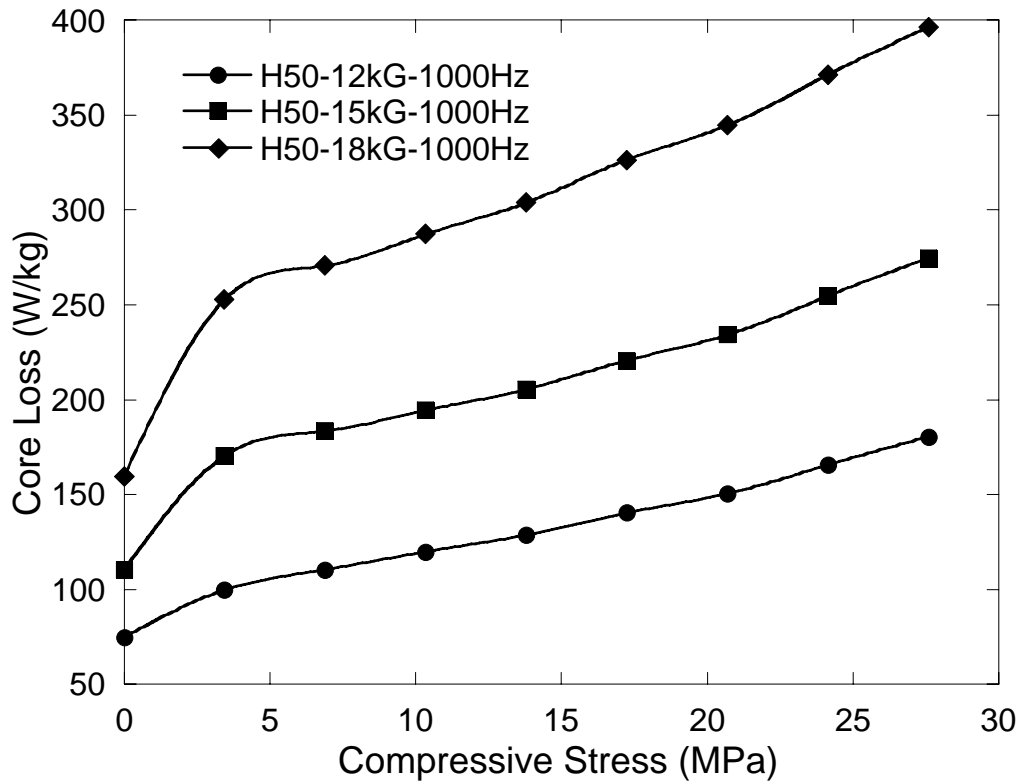


Figure 4.78 Total core losses of Hiperco Alloy 50 at B_{max} of 12-15-18 KG and 1 kHz.

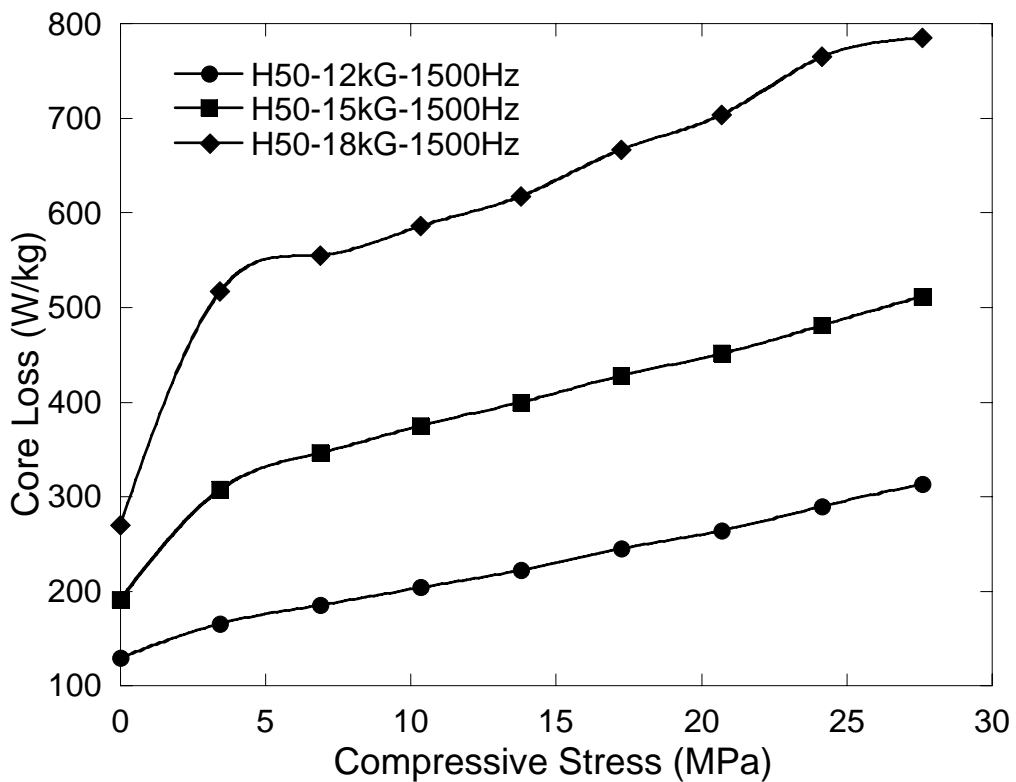


Figure 4.79 Total core losses of Hiperco Alloy 50 at B_{max} of 12-15-18 KG and 1.5 kHz.

CHAPTER V

SUMMARY

This publication was intended to provide a guideline to the designers of high temperature electromachines using Fe-Co materials. Three commercial alloys were studied; Hipercor 27, Hipercor 50 and Hipercor 50HS. The alloys were aged at a temperature of 500 ° C, which was carried out for 5000 hours. For a complete material assessment, magnetic, mechanical and electrical performance needed to be considered over the anticipated lifetime of a component. Materials' properties were documented from room temperature up to 500 ° C for 0-1000-2000-5000 hrs intervals. This work also correlates those property changes to microstructural changes that occur during aging process.

A 5000 hours aging study should sufficiently be long enough to extrapolate the trends in materials' properties for real-life applications. Information contained in this publication is only specific to the alloys with given annealing conditions since; magnetic and mechanical properties are greatly depended on the annealing conditions performed after cold deformation. The processing of each of these FeCo alloys can be altered to achieve a range of final properties that are perhaps targeted for specific applications. However, absence of any grain growth during 500 ° C aging up to 5000 hours indicates that the observed trends should be representative for the same alloy compositions with different annealing histories.

We also documented room temperature magnetic properties of above mentioned alloys under compressive and tensile stresses. These stress conditions were intended to simulate the forces that a stator or rotor may experience during assembly and/or operation.

It is hoped that the information provided in this document is used to predict trends and magnetic, electrical and mechanical behaviors for real-life, long-term applications.

REFERENCES

- [2.1] R. M. Bozorth, "Ferromagnetism", Van Nostrand, 197 (1951).
- [2.2] F. Pfeifer, and C. Radloff, J. Magn. Magn. Mater. **19**, 190 (1980).
- [2.3] H. Asano, Y. Bando, N. Nakanishi and S. Kachi, Trans. J.I.M., **8**, 180 (1967).
- [2.4] J. A. Oyedele and M. F. Collins, Phys. Rev., **B**, 16, 3208 (1977).
- [2.5] C. G. Shull and S. Siegel, Phys. Rev., **75**, 1008 (1949).
- [2.6] M. F. Collins and J. B. Forsyth, Phil. Magn., **8**, 401 (1963).
- [3.1] N. S. Stoloff, and R. G. Davies, Acta Metallurgica, **14**, 473 (1964).
- [3.2] N. S. Stoloff, and R. G. Davies, Progress in Material Sciences, **13**,1 (1966)
- [3.3] L. Zhao, I. Baker, and E. P. George, Mater. Rese. Soc. Proc., **228**, 501 (1993).
- [3.4] I. Baker, and E. M. Schulson,, Scripta Metallurgica, **23**, 345 (1989).
- [3.5] A. M. Glazer, and I. V. Maleyeva, Phys. Metals and Metallography, **68**, 65 (1989).
- [3.6] R. T. Fingers, "Creep Behavior of Thin Laminates of Iron-Cobalt Alloys for use in Switched Reluctance Motors and Generators", Ph.D. Thesis, Virginia Tech., (1998).
- [3.7] J. E. Coate, R. T. Fingers, and N. E. Dowling, J. Appl. Phys., **85** (1999).
- [3.8] R. T. Fingers and J. E. Coate, "Tensile and Creep Data for Carpenter Technology Corporation's Soft Magnetic Hiperco Alloy 50HS Material," Materials Directorate Evaluation Report, No. MLS-99-022 (1999).
- [3.9] H. J. Williams, W. Shockley and C. Kittel, Phys. Rev. **80**, 1090 (1950).
- [3.10] *Ferromagnetism*, Bozorth
- [3.11] *Standard Test Method for Electrical Resistivity of Soft Magnetic Alloys, Standard A712- 75*. American Society for Testing and Materials, Philadelphia (1991)
- [3.12] M. R. Pinnel and J. E. Bennett, Metallurgical Trans., **5**, 1273 (1974)
- [3.13] S. Mahajan, M. R. Pinnel and J. E. Bennett, Metallurgical Trans., **5**, 1263 (1974)
- [3.14] J. A. Ashby, H. M. Flower and R. D. Rawlings, Metal Science, 91 (1977)
- [3.15] C. D. Pitt and R. D. Rawlings, Metal Science, **15**, 369 (1981)
- [3.16] Q. Zhu, L. Li, M. S. Masteller and G. J. Del Corso, Appl. Phys. Lett. **69**, 3917 (1996)
- [3.17] R. H. Yu and J. Zhu, J. Appl. Phys., **97**, 539005 (1999)
- [4.1] B. Thomas, IEEE Trans. Magn., **16**,1299 (1980).
- [4.2] C. Kittel, Rev. Mod. Phys., **21**, 541 (1949).
- [4.3] E. W. Lee, Reports on Prog. In Phys., **18** 184 (1955).
- [4.4] A. J. Moses, AIP Conference Proceedings, **24**, 741 (1975).
- [4.5] V. Permiakov, L. Dupre, D. Makaveev and J. Melkebeek, J. Appl. Phys. **91**, 7854 (2002).